Defining the mechanism of small molecule inhibition of amyloid fibril formation using ion mobility spectrometry – mass spectrometry

Lydia Mary Young

Submitted in accordance with the requirements for the degree of PhD

The University of Leeds

Astbury Centre for Structural Molecular Biology

September 2015

The candidate confirms that the submitted work is her own, except where work which has formed part of jointly-authored publications has been included. The contribution of the candidate and the other authors to this work has been explicitly indicated overleaf. The candidate confirms the appropriate credit has been given within the thesis where reference has been made to the work of others. This copy has been supplied on the understanding that it is copyright material and that no quotation from this thesis may be published without proper acknowledgement.

Jointly Authored Publications

Throughout this thesis the work directly attributable to the candidate is as follows:

    (i)   Literature research and compilation of the manuscript stated above.

    (ii)   The candidate performed all the experimental work and data analysis unless otherwise stated.

Details of jointly authored publications and the contributions of other authors to these manuscripts:

Results Chapter 1 contains work from the following manuscript published in *Int J Ion Mobil Spectrom*, 2013:

Young, L.M., Ndlovu, H., Knapman, T.W., Harris, S. A., Radford, S.E. and Ashcroft, A.E. Monitoring oligomer formation from self-aggregating amylin peptides using ESI-IMS-MS.

In this work, TWK performed preliminary experiments and helped in designing the project. I carried out all ESI-IMS-MS experimental work, ThT and TEM analysis and wrote the manuscript along with AEA. HN performed molecular modelling of oligomeric structures. SAH, SER and AEA provided help with scientific discussions, data interpretation and manuscript preparation.

Results Chapter 2 contains work from the following manuscript published in *J Am Chem Soc,* 2014:

Young, L.M., Cao, P., Raleigh, D.P., Ashcroft, A.E., and Radford, S.E. Ion Mobility Spectrometry–Mass Spectrometry Defines the Oligomeric Intermediates in Amylin Amyloid Formation and the Mode of Action of Inhibitors.

In this work, I designed and carried out all ESI-IMS-MS experimental work, data interpretation, ThT and TEM analysis and wrote the manuscript. PC synthesised

the hIAPP and rIAPP peptides. DPR, SER and AEA provided help with scientific discussions, data interpretation and manuscript preparation.

Results Chapter 3 contains work from the following manuscript published in *Nat Chem*, 2015 and *Methods*, 2015:

Young, L.M.*, Saunders, J.C.*, Mahood, R.A., Revill, C.H., Foster, R.J., Tu, L.-H., Raleigh, D.P., Radford, S.E. and Ashcroft, A.E. Screening and classifying small molecule inhibitors of amyloid formation using ion mobility spectrometry-mass spectrometry.

Young, L.M.*, Saunders, J.C.*, Mahood, R.A., Revill, C.H., Foster, R.J., Ashcroft, A.E. and Radford, S.E. ESI-IMS–MS: A method for rapid analysis of protein aggregation and its inhibition by small molecules.

*These authors contributed equally to this work.

In this work, I designed and carried out all ESI-IMS-MS experimental work, data interpretation and TEM analysis and wrote the manuscript, together with JCS. JCS also provided background information on the small molecules and their published interactions with human islet amyloid polypeptide (hIAPP) and amyloid β peptide residues 1-40 (Aβ40), and provided all the small molecules for *in vitro* analysis. JCS reviewed and selected the small molecules to be used for seeding the virtual screening library, and calculated LogP values of all 40 small molecules screened. RAM purified the Aβ40 peptide and performed TEM of the sample. CHR and RJF performed the virtual screen. LHT synthesised the hIAPP peptide. RJF, DPR, SER and AEA provided help with scientific discussions, data interpretation and manuscript preparation.

Acknowledgements

These past 4 years have been challenging, rewarding and life changing and I would like to whole-heartedly thank all the people who have carried me through and put up with me.

Firstly, thank you to my supervisors, **Prof. Alison Ashcroft** and **Prof. Sheena Radford** for their insight, guidance, and encouragement throughout my PhD. Both have experienced first-hand with me the highs and lows of my PhDs – from papers being accepted to sickness bugs at conferences.

To my amazing friends and collaborators **Janet Saunders** and **Rachel Mahood**, the final 18 months of my PhD were so greatly enriched by your presence and input, both inside and outside of work, thank you! I will miss you like the desert misses rain. To my bestie **Anton Calabrese,** we have had THE best times and I'm not sure how I'd have coped without you, please stay in Leeds forever!!

Big up to all the magnificent members of the Ashcroft and Radford groups. It is a total pleasure to work with people that I consider to be such close friends. LGI Costa trips played a large part in getting me through a good deal of the 4 year PhD, thank you **Helen Beeston** for fuelling my caffeine addiction. Thanks to the Berry lab beauties **Claire Windle** and **Sasha Derrington** (and **Alex Moloney**) for all the cocktails, fun times and dancing! Sincere thanks to **Lucy Woods** and **James Ault** for your patience, training and spoon feeding. You are both stars and I am forever grateful for your valuable input. We had some great fun along the way too!

Most importantly my deepest gratitude goes to my crazy but wonderfully amazing family **Matthew** (my hero)**, Sarah** (my inspiration)**, Grace** (my best mate)**, Aaron** (my lovely bro)**, Dan** and **Leah** (my babies), never a dull or lonely moment! My family are THE best, fact. Special thanks to **Grandma Debs** for being by my side through all of my university years, you've been amazing!! I would be nowhere without the love and support of you all and I consider myself so deeply blessed that God chose you to be my family. I'm sorry for being a 'controllious freakious' and I hope to make you proud. This is for you!

iv

Table of Contents

List of Figures

X

List of Tables

List of Abbreviations

Amino acids are abbreviated according to their standard three-letter or single-letter codes. Other abbreviations are as follows:

μg	Microgram
1*H*-B-SA	1*H*-benzimidazole-2-sulfonic acid
Å	Ångström
AD	Alzheimer's disease
AFM	Atomic force microscopy
AFM	Atomic force microscopy
ALS	Amyotrophic lateral sclerosis
APP	Amyloid precursor protein
ATD	Arrival time distribution
Aβ	Amyloid beta
Aβ40	Amyloid beta residues 1-40
Aβ42	Amyloid beta residues 1-42
CCS	Collision cross-sectional area
CID	Collision induced dissociation
CRM	Charge residue model
Da, kDa	Dalton, kiloDalton
DC	Direct current
DMSO	Dimethyl sulphoxide
DOPA	3,4-dihydroxyphenylalanine
DRA	Dialysis related amyloidosis
ECD	Electron capture dissocation
EGCG	Epigallocatechin gallate
EM	Electron microscopy

ESI	Electrospray ionisation
ESI-IMS-MS	Electrospray ionisation-ion mobility spectrometry-mass spectrometry
ETD	Electron capture dissociation
FT-ICR	Fourier transform ion cyclotron resonance
HD	Huntington's disease
HDX	Hydrogen-deuterium exchange
HFIP	Hexafluoroisopropanol
hIAPP	Human islet amyloid polypeptide
HD	Huntington's disease
IAPP	Islet amyloid polypeptide, *or* Amylin
IEM	Ion evaporation model
IMS	Ion mobility spectrometry
MALDI	Matrix assisted laser desorption ionisation
mg	Milligram
mL	Millilitre
mol	mole
MS/MS	Tandem mass spectrometry
NMR	Nuclear magnetic resonance
NMR	Nuclear magnetic resonance
PD	Parkinson's disease
PDB	Protein Data Bank
RF	Radio frequency
rIAPP	Rat islet amyloid polypeptide
rpm	Rotations per minute
SOD1	Superoxide dismutase 1
TEM	Transmission electron microscopy

xvi

ThT	Thioflavin T
ToF	Time of flight
TTR	Transthyretin
T2DM	Type 2 Diabetes Mellitus
UV	Ultraviolet
β2m	Beta-2 microglobulin

List of Amino Acid Abbreviations

A	Ala	alanine
C	Cys	cysteine
D	Asp	aspartate
E	Glu	glutamate
F	Phe	phenylalanine
G	Gly	glycine
H	His	histidine
I	Ile	isoleucine
K	Lys	lysine
L	Leu	leucine
M	Met	methionine
N	Asn	asparagine
P	Pro	proline
Q	Gln	glutamine
R	Arg	arginine
S	Ser	serine
T	Thr	threonine
V	Val	valine
W	Trp	tryptophan
Y	Tyr	tyrosine

Abstract

The study of protein/peptide folding, misfolding, structure, and interactions are vital to understanding complex biological problems. The work presented in this thesis describes the development and application of mass spectrometry -based techniques to investigate protein structure, aggregation and interference with aggregation, providing insights into the self-assembly and inhibition of several disease-related peptides.

Mass spectrometry has evolved significantly over the past decade, its applications varying from small molecules to macromolecules. Travelling wave ion mobility spectrometry (TWIMS), when combined with mass spectrometry (MS), has the unique and unrivalled capability of separating molecular ions based on their collision cross-sectional area in addition to their mass-to-charge ratio, thus facilitating structural studies of co-populated protein conformations and structural isomers of protein complexes that cannot be separated by molecular weight alone. One biological system that has benefitted enormously from such advances is the study of *in vitro* amyloid formation.

The ability of amyloidogenic protein/peptides to assemble into insoluble fibrils is the basis of a vast array of human disorders. Human islet amyloid polypeptide (hIAPP) is one such peptide able to readily assemble into amyloid fibrils *in vitro* at neutral pH, despite being intrinsically disordered. Identifying oligomeric states occupied between monomer and final fibrils creates an enormous challenge, given that few techniques are able to separate and characterise such lowly-populated and transient species. In addition to characterisation of fibril precursors, recent research has focussed on the identification of small molecule inhibitors of the amyloid cascade and understanding their mechanism of action is of great interest to this field.

In the work presented here, the power of TWIMS-MS has been harnessed to achieve the separation and characterisation of oligomeric precursors of the type-2 diabetes-related peptide hIAPP along with IAPP mutants and peptides corresponding to its core sequence. In addition, the effects of small molecule inhibitors on oligomer population and fibril formation have been studied and

described in detail. Further, an experimentally simple, *in vitro* MS-based screen has been developed and implemented that provides rapid and accurate analysis of protein aggregation and its inhibition. All of the results highlight the powers of MS to provide important insights into the mechanism of amyloid formation and demonstrate the potential of this approach for screening for novel inhibitors of disease-related amyloid assembly.

Aims

The propensity of proteins to aggregate into amyloid has severe consequences in human disease. Little is known about the nature of these toxic amyloid states and current screening techniques used in the search for potential inhibitors are expensive, time consuming and require large quantities of protein.

There is an urgent need for detailed analysis of all potentially toxic amyloid intermediates and the generation of a high-throughput, highly sensitive, and cost-effective assay for inhibitors of amyloid formation. Therefore, the aim of this thesis is the observation and characterisation of oligomeric states of amyloid systems followed by the development of an *in vitro*, automated, MS-based screen for inhibitors of aggregation that could be applied to multiple aggregating systems.

The screen should; enable the selection of small molecule inhibitors of protein aggregation of various sequences, have a low false positive and false negative rate, have the ability to rule out self-aggregating small molecules and allow determination of the usefulness of inhibitory compounds based upon spectral fingerprints.

These above requirements are all been achieved using the MS-based screen for identifying amyloid inhibitors. **Chapter 3** and **Chapter 4** detail the initial characterisation of the peptide that was chosen for use in proof-of-principle screening. **Chapter 5** describes the development of the screen and its capacity to differentiate between inhibitors and non-inhibitors of amyloid assembly, with a classification system for compounds based on spectral fingerprints being demonstrated. The high-throughput potential and diversity of the screen is demonstrated by the use of automation and a second peptide system, respectively. Finally, **Chapter 6** demonstrates the application of the MS-based screen to other, disease related aggregating proteins.

1 Introduction

1.1 History of mass spectrometry

Mass spectrometry (MS) is an analytical technique used to measure the mass/charge ratio (m/z) of ions in the gas phase within a mass spectrometer. It is a technique used for determining mass, composition and structures of samples. The sample is first ionised by a choice of methods, its ions are separated in an analyser according to m/z and their relative abundances are recorded by a detector, see **Figure 1-1**.
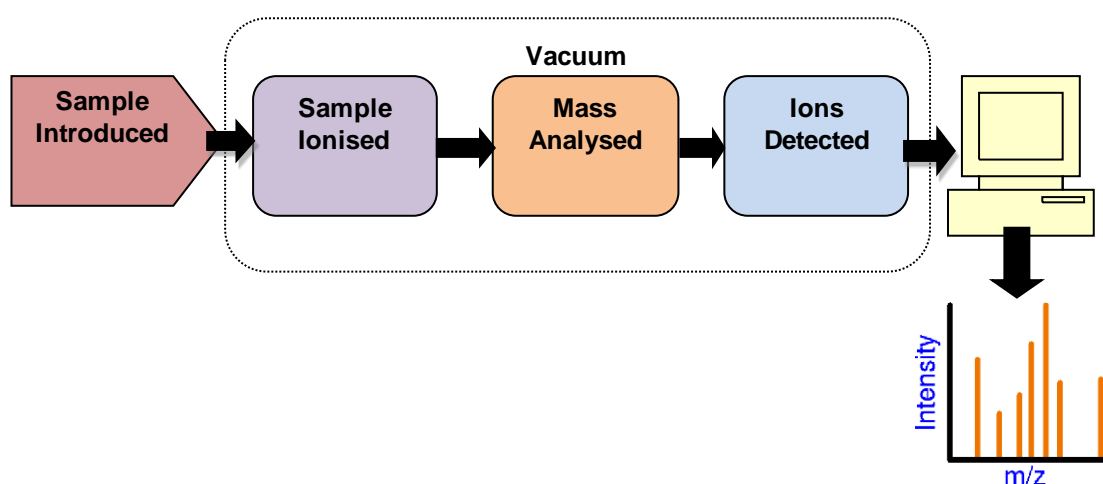
Figure 1-1. *Schematic of a mass spectrometer. The sample is introduced, ionised in the ion source, and the ions separated according to m/z. The detector measures ion count detected at each m/z. A computer system converts information from the detector into a mass spectrum.*

MS has been a widely accepted tool utilised in the analysis of biological systems for more than twenty years, since the pioneering development of electrospray ionisation (ESI)(1, 2). ESI, along with other soft ionisation techniques, for example matrix assisted laser desorption ionisation (MALDI)(3), have been revolutionary in their ability to reveal new insights into protein structure and macromolecular assemblies using MS. Not only can ESI-MS experiments of biological

macromolecules provide accurate molecular mass measurements (2), the technique enables structural information about proteins and their biomolecular complexes to be acquired. Recent advances have meant that information about protein/ligand binding, structure, stability, dynamics and post-translational modifications can be obtained (4-6).

1.2 Synapt HDMS

The work presented in this thesis was carried out using a Synapt HDMS mass spectrometer (Waters UK Ltd)(**Figure 1-2**). Samples are introduced using nano-electrospray ionisation (ESI) (**Section 1.3**) and guided into the instrument which incorporates travelling wave ion mobility spectrometry (IMS) (**Section 1.4**) with Time of flight (ToF) mass spectrometry (**Section 1.5**) (7). Within this device, three travelling wave ion guides (TWIGs) are situated between a quadrupole (Q) mass analyser and a ToF analyser. The first TWIG is known as the trap region, the second as the mobility cell and the third as the transfer region. The final electrode of the trap TWIG is direct current (DC) only and its voltage is adjusted in order for it to act as a gate through which ion packets move into the IMS cell to be separated. In the mobility cell, a wave voltage is applied to the 1st and 7th pair of electrodes followed by the 2nd and 8th pair and so on. The transfer region has a constant travelling wave voltage applied to it to maintain temporal separation between the mobility cell and the ToF analyser. The ToF pusher is synchronised with the gate of the trap region and for each gate pulse, 200 pushes of the ToF analyser are recorded for every IMS experiment. Additionally, the trap and transfer regions can function as MS/MS collision cells for fragmentation experiments (**Section 1.6**).
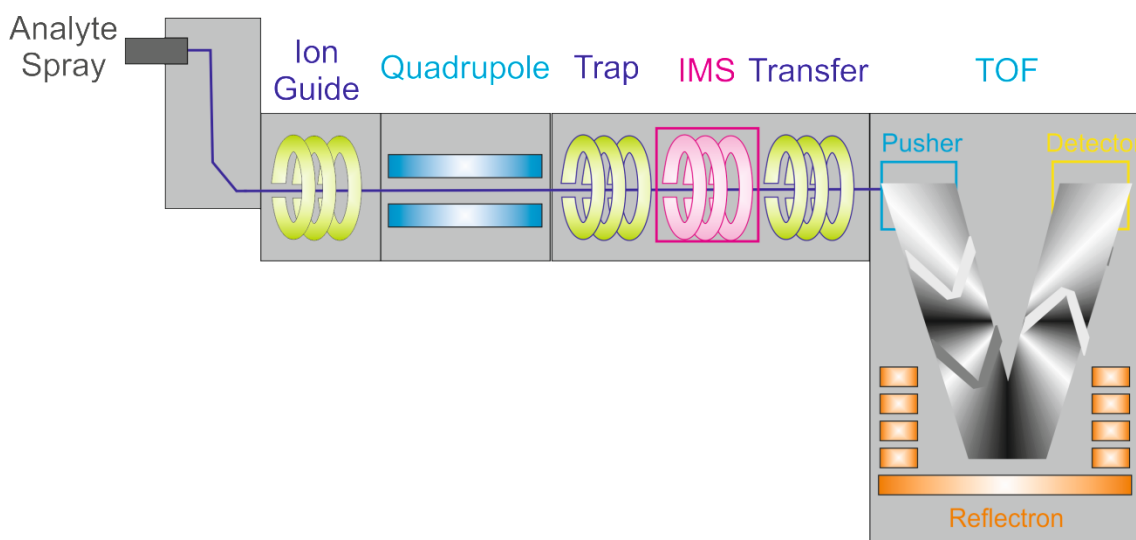
Figure 1-2. *Schematic showing the layout of the Synapt G1 HDMS Figure adapted from (7).*

1.3 Ionisation of biological molecules

Ions can be generated by a number of methods for use in MS. In the past, electron impact and chemical ionisation were most commonly used to generate ions from a sample. These methods require the sample to be in the gas phase, and thus were only suitable for the mass determination of small volatile organic molecules. More modern, 'soft ionisation' methods, MALDI (3) and ESI (2), developed ~27 years ago, have allowed mass analysis of polar and thermally labile biomolecules without prior derivatisation (8). MALDI ionisation can be used for biological samples, however, it results in the formation of predominantly singly charged ions (9), meaning that valuable information about the native protein conformation is lost. ESI results in the formation of non-fragmented, multiply charged gas phase ions.

ESI, a very gentle ionisation technique, is performed at atmospheric pressure and is suitable for the analysis of polar molecules with a mass range of 100 Da to >1 MDa. First, the sample is dissolved in the appropriate solvent, depending on the sample's features, which also determine the ionisation mode (positive or negative) of the MS. Next, the sample is sprayed through a narrow stainless steel capillary needle into a heated evaporation chamber. The needle is held at a high potential, with a voltage of 3-4 kV being applied to its tip. The analyte emerges from the

capillary in the form of an aerosol of highly charged droplets. Nebulising gas, usually nitrogen, flows around the outside of the capillary and aids formation of such droplets. The charged droplets are attracted by a voltage to a sampling cone at the opposite end of the desolvation chamber and move towards it. Warm nitrogen gas, used as a drying gas, passes orthogonally across the front of the ionisation source and aids solvent evaporation leading to decreased size of charged droplets as they move across the chamber. When the size of the droplet has diminished below a certain threshold for a given charge, a 'Coulombic explosion' occurs. The charge repulsion at a certain radius exceeds the surface tension and droplets split into smaller droplets, each carrying a proportion of the charge. This cycle continues, leading to the formation of a fine spray of analyte ion-containing samples (**Figure 1-3**). Eventually, charged sample ions are free of solvent and pass through the sampling cone into the vacuum chamber. Two opposing models exist for the formation of gas phase ions: the 'Ion Evaporation Model' (IEM) states that when a droplet reaches a certain radius the field strength at the surface of the droplet becomes large enough to cause direct emission of ions into the gas phase (10). The 'Charge Residue Model' (CRM) states that electrospray droplets undergo cycles of evaporation and fission until no more solvent remains and droplets contain, on average, one analyte ion or less (1). Despite these two proposals, the precise mechanism of ion liberation is unknown and neither model is able to explain all observations. It is probable that the proposed mechanisms may operate individually or in tandem, depending on the analyte, to invoke ion formation (11). It is thought that the IEM model may apply to ions originating from relatively small molecules, while ions with multiple charges are likely to be formed via the CRM model. A third, alternative mechanism for unfolded proteins has been proposed recently by Konermann *et al.* (12). This chain ejection model (CEM) states that proteins are expelled from the droplet long before complete solvent evaporation has taken place (12).
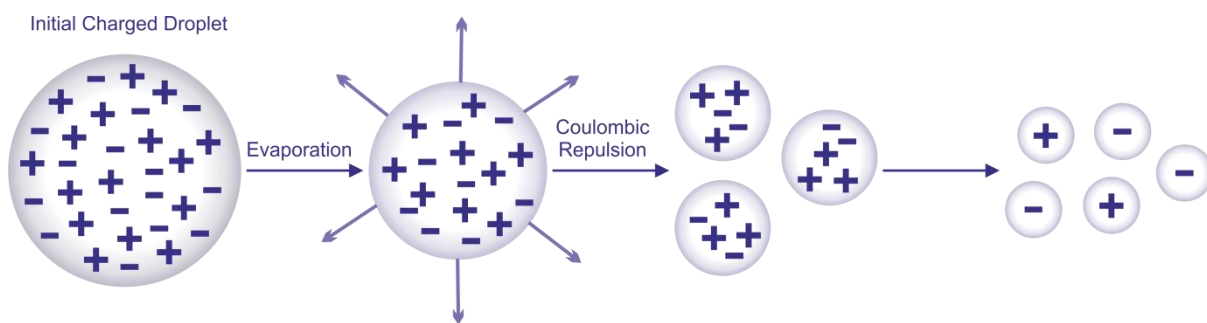
Figure 1-3. *The mechanism of electrospray ionisation*.

The efficiency of ESI has been improved by use of volatile buffers in the presence of acids, which increase the ionic strength of the solution, therefore enhancing droplet formation. The sensitivity of ESI can be improved by decreasing the flow rate, which causes smaller droplets to be formed usually with few salt adducts on the sample ions. Nano-ESI is a low flow rate version of ESI (13), in which ions are formed and desolvated using electrostatic charging. A small amount of sample is added to an appropriate volatile solvent (concentration 1-10 pmol/µL). A high voltage (ca. 1000 V) is applied to a gold plated narrow, borosilicate vial which initiates a low flow rate of 30-1000 nL/min. This means that far less sample is consumed with respect to ESI and therefore multiple experiments can be performed on very small volumes of sample. In 2002 John Fenn, who developed ESI, received the Nobel Prize (14) together with Koichi Tanaka, who developed Laser Desorption Ionisation. The greatest application of ESI is the study of proteins and protein complexes whose functions are vitally dependant on non-covalent interactions that can be maintained in the gas phase using ESI. When performing ESI, peptides of molecular mass <1200 Da usually give rise to singly charged, protonated species, whereas a polypeptide of molecular mass >1200 Da is likely to acquire multiple charges. The number of charges that a protein picks up during the electrospray process is thought to be directly related to its solvent-exposed surface area. Basic residues are most likely to become protonated however protons are able to migrate to other sites of high gas-phase bascicity within the mass spectrometer. The mass of multiply-charged protonated ions can be determined using the equation: $m/z = (M + nH^+)/n$. Nano-ESI has the ability to provide effective desolvation to high mass samples of low concentrations, in the nanomolar to picomolar range. Consequently, samples in highly aqueous solvents containing a low salt concentration can be effectively introduced into the mass spectrometer. A

novel method of ionisation is the Advion TriVersa Nanomate (Advion Biosciences Inc., Ithaca, NY USA)(15). This is an automated chip-based nano-ESI device, which uses a chip consisting of an array of 400 nanospray needles, or nozzles. The analyte solution is sprayed from a conducting pipette tip aligned against the rear of the chip and a small gas pressure is then used to aspirate the sample. A new nozzle is used for each sample.

1.4 Ion mobility spectrometry-MS

One key technical advance, the pairing of MS to ion mobility spectrometry (IMS), has seen MS emerge as a central component of the structural biology tool kit (16-18). MS coupled to IMS allows detailed analysis of complex systems via determination not only of their masses, but also their rotationally-averaged collision cross-sectional areas (CCS). IMS is an analytical technique that separates gas phase ions on the basis of their mobility through a carrier buffer gas under the influence of an electric field. Separation of ions depends on two fundamental principles: the CCS of the ion and the charge of the ion (as well as gas temperature and pressure) (19). Larger, more extended ions will experience a greater number of collisions with the buffer molecules gas and, as a result, will take longer to traverse through the drift tube. Conversely, smaller, more compact ions of the same *m/z* will undergo fewer collisions with the buffer gas molecules and hence have a higher mobility and therefore a shorter drift time. Separation depends also on charge, with more highly charged ions being accelerated through the drift cell and therefore having higher mobility than ions of the same *m/z* but carrying fewer charges. The many applications of IMS-MS include: separating isomers, separating protein monomer conformations, separating protein oligomers and calculating ion CCS (19).

When using conventional IMS in determination of drift time (tD), the equation below is used to calculate an ion's CCS (Ω) (**Equation 1.1**): (20, 21).

6

Equation 1.1: *Calculation of cross sectional area in conventional IMS*

$$\Omega = \frac{(18\pi)^{\frac{1}{2}}}{16} \frac{ze}{(k_b T)^{\frac{1}{2}}} \left[\frac{1}{m_I} + \frac{1}{m_N} \right]^{\frac{1}{2}} \frac{760}{P} \frac{T}{273.2} \frac{1}{N} \frac{t_D E}{L}$$

Where z is the charge of the ion, e is the charge of an electron (1.602×10^{-19} C), K_b is Boltzmann's constant (1.381×10^{-23} m^2 kgs^{-2} K^{-1}), T is temperature in K, t_D is the drift time of the ion, N is the number density of the buffer gas, P is pressure, m_I and m_N are the molecular masses of the ion and the buffer gas respectively. A ratio of actual pressure (P) and temperature (T) are taken against standard temperature and pressure values (273.2 K and 760 torr). The electric field is denoted by E, and L is the length of the drift tube in meters (20, 21). **Equation 1.1** allows the collision cross-sectional area of any species to be determined providing temperature and pressure and the drift time (t_D) can be measured accurately.

The term below (**Equation 1.2**) is the reciprocal for reduced mass between the analyte ion and the buffer gas. Reduced mass is the effective inertial mass of a molecule, also described as the mass of an object measured by its resistance to acceleration.

Equation 1.2: Calculation of Reduced mass

$$\text{Reduced mass } = \left[\frac{1}{m_I} + \frac{1}{m_N} \right]$$

The major drawback of conventional IMS-MS is its poor sensitivity, with approximately just 1 % of ions produced being transmitted through the IMS-MS to the detector (22). The major cause of this insensitivity is the length of the drift tube and the fact while a particular packet of ions is being separated, no other ions can enter the drift cell.

Over the past decade, much effort has been directed at producing commercially viable instrumentation. This has led to the development of ion mobility separation based on a travelling-wave IMS system (22) (**Figure 1-4**). Travelling-wave ion mobility spectrometry mass spectrometry (TWIMS-MS) uses the same basic

principles as conventional IMS-MS except that ions are trapped until they can all be pushed into the drift cell together, giving much higher sensitivity, with >80 % ions being transmitted (22). TWIMS-MS has been shown to be promising for protein analysis, being highly sensitive and having good separative power for analysis of multiply-charged ions, and it can be used to calculate CCS values for each component in a sample. Unlike conventional IMS experiments, drift time values are not linearly related to Ω in the TWIMS-MS system, therefore cross-sectional area must be defined by a calibration approach. The determination of peptide cross-sectional areas can be achieved due to the abundance of known IMS-MS cross-sectional areas available within the literature (these can be found on Professor David Clemmer's website: www.indiana.edu/~clemmer) (23). For peptide analysis, the TWIMS-MS device can be calibrated by measuring drift times of peptides derived from commercially available proteins following tryptic digest. Readily available proteins such as cytochrome c and alcohol dehydrogenase (ADH) can be used and IMS-MS data for the calibrant protein are acquired under exactly the same instrument conditions that will be used for the target protein (24). Tryptic digests of such proteins result in a wide range of peptide sizes that are observed as singly and doubly charged ions and a wide range of cross-sectional areas is covered by the calibration (23).
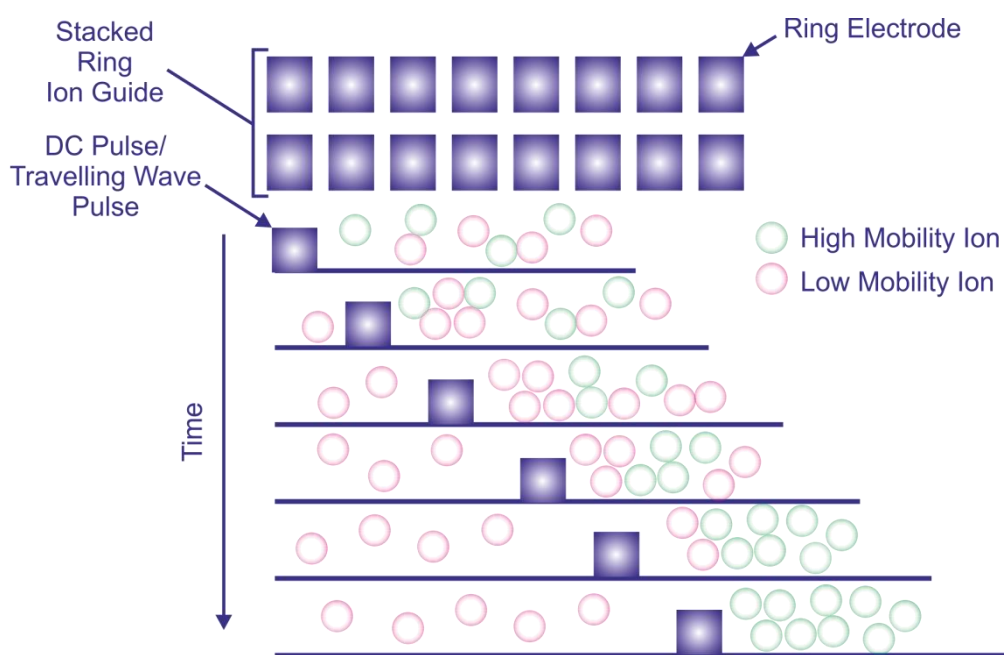
Figure 1-4. Schematic of separation of ions in a TWIMS-MS device. Ions of a low mobility fall off the top of the travelling wave and therefore have a longer drift time. Figure adapted from (Giles et al., 2004)(22).

Because the electric field (E) is not uniform in a TWIMS cell, the conventional IMS equation does not apply. The equation for calculating Ω must take into account the wave functions of the TWIMS-MS system. This TWIMS-MS equation contains constants A and B that describe TWIMS-MS characteristics rather than electric field density. A is the correction factor for the electric field parameters and B is to compensate for the non-linear effect of the TWIMS cell, shown in **Equation 1.3:**

Equation 1.3: Calculation of Ω when using TWIMS

$$\Omega = \frac{(18\pi)^{\frac{1}{2}}}{16} \frac{ze}{(K_bT)^{\frac{1}{2}}} \left[\frac{1}{m_I} + \frac{1}{m_N}\right]^{\frac{1}{2}} \frac{760}{P} \frac{T}{273.2} \frac{1}{N} At_D{}^B$$

The collision cross-sections can also be stated as a charge and mass independent value. **Equation 1.3** is divided throughout by absolute charge (*ze*) and reduced mass giving rise to **Equation 1.4**, shown below: (20)

Equation 1.4: Calculation of reduced cross section, Ω'

$$\Omega' = \frac{(18\pi)^{\frac{1}{2}}}{16} \frac{1}{(K_bT)^{\frac{1}{2}}} \frac{760}{P} \frac{T}{273.2} \frac{1}{N} At_D{}^B$$

The calculation can be further simplified when the correction for pressure, temperature, electric field and other constants are transformed into a single value, *A'*, resulting in **Equation 1.5**, shown below: (20)

Equation 1.5: Use of single constant for the correction of temperature, pressure and electric field

$$\Omega' = A't_D{}^B$$

Equation 1.3 can be then be simplified greatly by the incorporation of reduced cross-section, Ω', giving **Equation 1.6**, shown below; (20)

> ***Equation 1.6:*** Use of reduced cross section for the calculation of cross-sectional area

$$\Omega = ze\left[\frac{1}{m_I} + \frac{1}{m_N}\right]^{\frac{1}{2}} A't_D{}^B$$

$$= ze\left[\frac{1}{m_I} + \frac{1}{m_N}\right]^{\frac{1}{2}} \Omega'$$

For calibrant peptides, Ω and drift times are known and can be used to determine values for constants A and B under defined instrument conditions. A plot of reduced Ω, (Ω') against t_D fitted allometrically will give A and B values and enable determination of unknown peptide Ωs. The calculations from **Equation 1.6** can be input into an Excel spreadsheet for rapid determination of unknown peptide Ωs from experimental drift times (20). Once the CCS of an ion is known, then additional modelling tools can be used to predict its structure. For example, modelling of protein structures can be achieved using MOBCAL (25, 26) and/or the more recently developed Leeds (20) and PSA methods (27) to calculate theoretical cross sections from PDB files. These CCS values can then be compared with those obtained experimentally. From this, it can be deduced whether a protein is in a native-like compact state, or if a different conformer is observed.

1.5 Mass analysers used in a Synapt HDMS

A mass analyser separates ions according to their *m/z* after the ionisation step. The most commonly used analysers for biomolecular studies are the quadrupole (Q) and time-of-flight (ToF) analysers, or combinations of the two. The Q analyser detects ions of each *m/z* sequentially by scanning the *m/z* range (**Figure 1-5**), while the ToF mass analyser detects all ions simultaneously (**Figure 1-6**). Mass

analysis aims to achieve high resolution, accuracy and a wide mass range and sensitivity.

Quadrupole mass analysers are composed of four rods in parallel to one another in a circular arrangement (**Figure 1-5**)*.* The four rods are arranged as two pairs that are connected electrically. The electric field between the pairs consists of a static DC potential and an oscillating radio frequency (RF). Ions travel between the rods through the centre of the quadrupole and as they travel through the mass analyser they undergo a complex oscillating motion. This motion is a result of the oscillating component of the electric field causing the polarity of the rods to change with time, the ions being attracted to rods of opposite polarity. Unlike ToF analysers, where all ions are analysed simultaneously, Q mass analysers allow ions of a particular *m/z* to be detected for a given ratio of RF and DC voltages. Ions with a certain *m/z* will have a stable trajectory at a given ratio of voltages and will reach the detector. All other ions will have unstable trajectories and either collide with the rods or become lost in the walls of the analyser (**Figure 1-5**). Continually varying the voltages applied to the rods allows ions with a range of *m/z* values to be analysed and detected. A Q can be operated as a selection device for a particular ion(s) so that tandem MS (MS/MS) can be carried out. Also, a Q can be used as an ion guide to transmit all ions (above a lower mass cut-off) by operating in RF mode only.
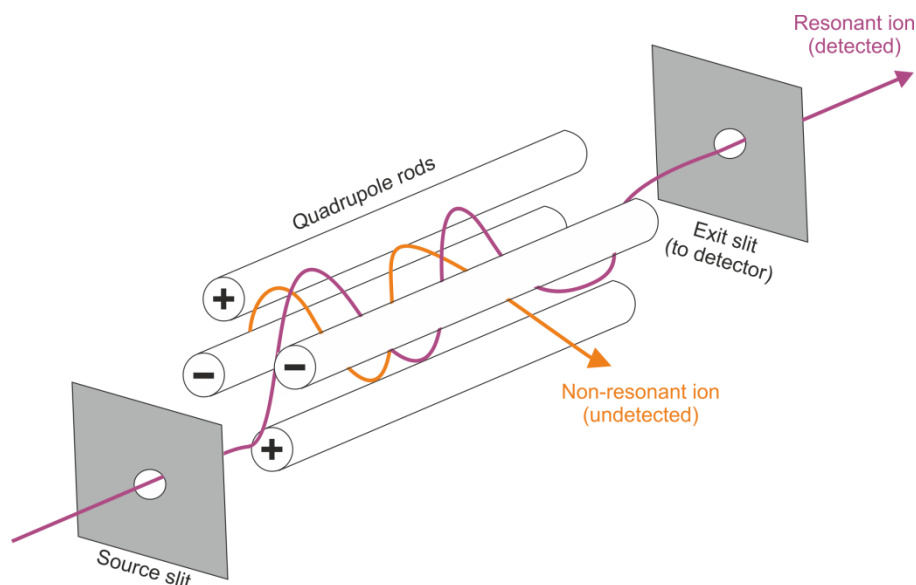
Figure 1-5. *Schematic representation of a quadrupole mass analyser. Ions with a specific m/z (purple) will traverse through the quadrupole and reach the detector*

whilst all other ions with unstable trajectories (orange) will be deflected into the rods. Voltages can be adjusted to transmit different m/z values.

ToF mass analysers measure the time taken for an ion to traverse a field-free region and reach a detector, this time is then converted to *m/z* (28, 29). The time taken (t) for an ion to travel a given distance, d, can be defined as t=d/v where v is the average velocity of the ion. All ions are given a fixed kinetic energy (K_e) when they exit the ionisation source but have different velocities (v) corresponding to their different masses (m) ($K_e=1/2mv^2$). ToF analysers have a theoretically unlimited *m/z* range, making them suitable for use in the analysis of large biomolecules such as proteins. These analysers also have high sensitivity due to the parallel detection of ions, i.e. all of the time is spent looking at all of the ions. A pulsed ion beam is used in combination with an orthogonal series of ion filters that couple ion flow from the ESI source to the high vacuum analyser. Historically, the major disadvantage of ToF analysers was their poor mass resolution, occurring as a result of the range of kinetic energies produced by the source for ions of the same *m/z*. However, this drawback has been overcome by several improvements including orthogonal geometry, two-stage acceleration, delayed pulsed extraction and the use of reflectron lenses. Delayed extraction is achieved by allowing ions to initially move in the field-free region with velocities determined by their kinetic energy. An extraction pulse, applied at an optimised delay time, then provides ions with low initial kinetic energy with more kinetic energy hence decreasing the kinetic energy spread and peak width (30). The reflectron lens system, is a feature of modern ToF mass analysers which also enhances resolution (31). The reflectron consists of a series of ring electrodes stacked on top of one another in the path of the ion (**Figure 1-6**). It acts as a mirror and doubles the flight distance by reflecting ions back through the flight tube towards the detector and focuses ions of the same *m/z* that have slightly different kinetic energies. The reflectron circumvents the need for extra lab space or more vacuum pumps, by doubling the ion path length, whilst keeping the TOF dimensions (hence pumping/vacuum system) the same. Certain analysers with dual reflectrons can be set to operate in V or W mode, which represent ions being reflected once or twice by the reflectron respectively. V mode allows enhanced sensitivity with respect to W mode which

becomes important for the detection of minor species with high resolution within co-populated ensembles.
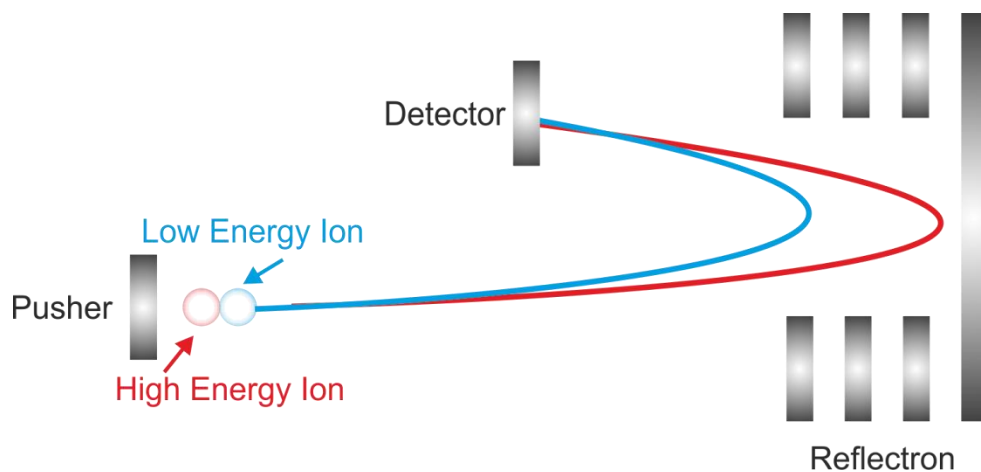
Figure 1-6. *Schematic representation of a TOF mass analyser. Ions represented in red and blue have the same m/z value, but slightly different kinetic energies. The presence of the reflectron compensates for this, as higher energy ions penetrate the reflectron deeper and have a longer flight path.*

1.6 MS/MS in a Synapt HDMS

The use of hybrid instruments, such as the Synapt HDMS, allows additional characterisation of protein or peptide samples using tandem mass spectrometry (MS/MS). Here, MS/MS can occur most commonly via a collisional induced dissociation (CID) mechanism (32, 33). During CID-MS/MS experiments, precursor ions of a specific *m/z* are selected in the first mass analyser before being accelerated into a region filled with an inert gas, commonly argon. The accelerated ions collide with the buffer gas molecules, during which the kinetic energy of the ion is converted into vibrational energy. If the vibrational energy is sufficient, the ion will fragment. Fragmentation yields a charged and neutral ion, of which only the charged ion is detected. In the Synapt HDMS, both the Trap and Transfer regions can act as collision cells, with parent ions of a specific *m/*z isolated on the Q mass analyser and subsequent daughter fragment ions being detected on the ToF

mass analyser. CID-MS/MS can be applied to the study of protein/ligand and protein/protein complexes (34, 35). Fragmentation of peptides or proteins typically occurs via the cleavage of the peptide amide bonds, (predictably yielding b- and y- type ions) (8, 36), where the charge can reside on either ion type depending on the exact sequence of the peptide. The sequence of the peptide or protein can be identified when fragmentation occurs at adjacent amide bonds along the peptide backbone, allowing determination of the mass, and therefore identity, of adjacent amino acids. Only one isobaric pair of amino acids exist :- Leu/Ile, with Gln/Lys also being very close in mass.

1.7 Mass spectrometry for protein structure elucidation

Early ESI-MS studies of proteins revealed that the extent of ionisation was related to structure (37). More compact protein structures, such as those containing multiple disulphide bonds, acquired fewer charges during ESI with respect to more expanded proteins (37). When a folded protein is in its native state, it has a smaller solvent-accessible surface area therefore few sites are accessible to protonation, therefore the ESI mass spectrum will show a narrow charge state distribution that appears at a relatively high m/z value. On the contrary, when proteins are denatured under acidic conditions, they have a larger solvent-accessible surface area therefore they acquire higher charge states. This occurs because as a protein unfolds, it becomes more accessible to the protonated solvent therefore will have a higher charge and therefore a lower m/z. Additionally, the mass spectrum of an unfolded protein will show a wider charge state distribution due to the increased variety of charge states that can occur. The number of experimentally determined charges on a native protein can therefore help to give an estimate of its surface area and can help towards the structural characterisation of protein complexes (38). Although protein structure estimates are possible, they are not conclusive given the elusive nature of the relationship between structure and charge (5, 38).

Relatively few techniques are available that allow elucidation of residue-specific information about the structure of proteins. NMR and X-ray crystallography have

14

proved useful in providing atomic resolution structures of many protein systems, that have been deposited in the PDB. However, such techniques are not applicable to all protein systems i.e. NMR is restricted to proteins $<\sim40$ kDa in size for full structural determination whilst dynamic samples usually elude crystallisation. Both NMR and X-ray crystallography require mg quantities of pure protein samples for analysis. NMR of intrinsically disordered, dynamic protein assemblies leads to challenging data interpretation as a result of signal averaging. MS overcomes the caveat of requiring pure protein samples required for NMR or X-ray crystallography by 'purifying' samples as they are separated by their *m/z,* allowing characterisation of whole species distributions, providing information relating to both conformation and equilibria. Monomeric protein can be distinguished easily from oligomeric species given that the charge allows determination of the mass of each species thus defining oligomer order. Non-covalent assemblies, such as virus capsid assembly (39-43) and amyloid intermediates (6, 44-49), that function as complexes rather than monomeric protein can be studied in detail using MS. Complementary techniques such as covalent labelling (50, 51) and hydrogen-deuterium exchange (HDX) (52, 53) can be used in combination with MS. By combining MS with these methods, high-resolution information on the structure of protein assemblies can be gained. Of particular interest is the study of transient, lowly populated, heterogeneous amyloid intermediates, discussed below.

1.8 Protein Folding, Misfolding and Aggregation

The protein folding process is, for the most part, spontaneous and therefore determined by the protein's primary structure (54). However, the exact mechanism by which the final folded conformation of a protein is encoded in the amino acid sequence, and how the folding process is achieved, remains elusive. Funnel-shaped energy landscapes can be used to describe the transition from high energy unfolded structures towards functional native states, at local minima of folding profiles (**Figure 1-7**) (55-57).
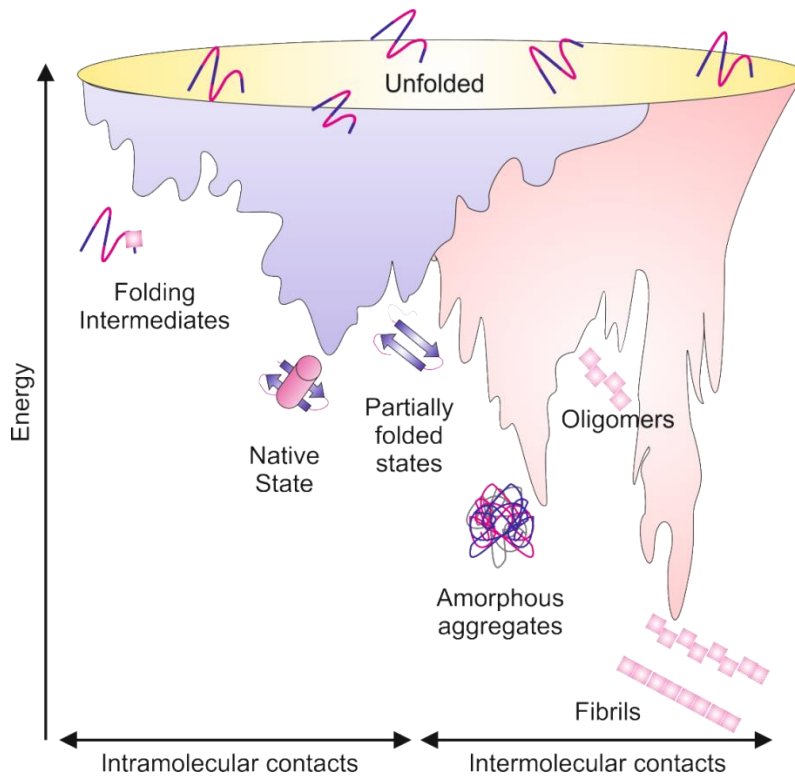
Figure 1-7*. The energy landscape of both protein folding (purple) and aggregation (pink). The purple surface shows that many intermediate conformations can lead to to the native state (which is in a local energy minimum) by the formation of intramolecular contacts. The pink surface shows the conformations that can lead to amorphous aggregation or amyloid fibril formation through intermolecular contacts. Figure adapted from references (57).*

Most peptides and small proteins (<100 residues) achieve their native structure via a one-step folding process, with only the unfolded and native state being populated significantly (57). On the contrary, folding of large multi-domain proteins (>100 residues) is achieved via an array of intermediate non-native states (57, 58). Such intermediate structures may be on-pathway i.e. towards the native state, or alternatively may be stable, misfolded conformations that are trapped in local energy minima that have to be reorganised before the native state can be revealed (**Figure 1-7**).

Aggregation is the association of two or more non-native protein molecules that can occur due to exposure of hydrophobic amino acid residues that are buried in the native state (56, 59). Misfolding can occur during or after folding, as a result of cellular stress conditions (55, 59-61). Proteins can leave the folding pathway and

enter alternative aggregation pathways, driven by hydrophobic interactions between folding intermediates (**Figure 1-7**). Off-folding pathways include both the amorphous aggregation pathway leading to the formation of disordered aggregates and the fibril forming pathway resulting in formation of highly ordered, thermostable assemblies (55, 57, 59). Amorphous aggregates are non-toxic and can be cleared by the proteasome (57), however oligomeric species formed on the fibril forming pathway are considered to be highly toxic and are associated with the aetiology of numerous devastating pathologies (**Table 1.1**).

1.9 Amyloid formation and the study of amyloid intermediates

Aberrant aggregation of proteins and peptides into amyloid fibrils contributes to more than 50 human disorders (62). Amyloid diseases can be divided into three broad classes: neurodegenerative diseases, where amyloids are deposited in the brain and spinal cord (this class includes Alzheimer's disease (AD), Parkinson's disease (PD) and Huntington's disease (HD)); non-neuropathic localised amyloidosis, where aggregation occurs in a single tissue (not the brain); or systemic amyloidoses where aggregation occurs in multiple tissues (**Table 1.1**).

Some of these conditions arise in individuals with a genetic predisposition, or alternatively can occur sporadically. The location of protein aggregates varies between disease states and the proteins contained within such plaques share no obvious sequence, function, or structural similarity and result in a wide variety of symptoms (56, 63, 64). In each case, normally soluble proteins that may be folded, partially folded or intrinsically disordered embark on alternative aggregation energy landscapes (65) (**Figure 1-7**) leading to the formation of β-sheet rich, fibrillar assemblies. The association between amyloid formation and disease pathogenesis is common for all amyloidoses and the cytotoxic properties of amyloidogenic peptides may also be similar (66). Identifying and characterising the structures and dynamics of prefibrillar oligomers is vital to understanding the mechanism of protein aggregation in amyloid diseases, identifying the specific culprits of toxicity and designing therapeutics to prevent aggregation.

Disease class	Disease	Protein involved	Location of aggregates	Clinical features	Ref.
Neuro-degenerative	Transmissible spongiform encephalopathies	Prion protein	Extracellular amyloid fibrils in CNS	Dementia, ataxia, psychiatric problems	(67)
	Alzheimer's (AD)	Amyloid-β and tau	Extracellular amyloid plaques, cytoplasmic neurofibrillar tangles	Progressive dementia	(68)
	Parkinson's (PD)	α-synuclein	Cytoplasmic Lewy bodies	Movement disorder	(69)
	Amyotrophic lateral sclerosis (ALS)	Superoxide dismutase	Cytoplasmic and axon inclusions	Movement disorder	(70)
	Huntington's (HD)	Huntingtin	Intranuclear neuron	Dementia, motor and	(71)

			inclusions	psychiatric problems	
Non-neuropathic localised amyloidoses	Type II diabetes mellitus (T2DM)	hIAPP (amylin)	Pancreatic amyloid plaques	Hyperglycaemia, insulin deficiency and resistance	(72)
	Injection-localised amyloidosis	Insulin	Injection localised plaques	Sub-therapeutic levels of insulin	(73)
	Apolipoprotein A1 amyloidosis	Apo A-1 fragments	Renal, hepatic, cardiac, laryngeal or cutaneous fibrillar deposits	Progressive renal and/or hepatic disease	(74)
Non-neuropathic systemic amyloidosis	Amyloid light chain amyloidosis	Immuno-globulin light chain fragments	Fibrillar deposits in various organs, most commonly kidneys	Renal failure	(75)
	Amyloid A amyloidosis	Serum amyloid A1 protein fragments	Kidney, liver and spleen	Renal failure	(76)
	Dialysis-related amyloidosis (DRA)	β_2-micro-globulin	Amyloid plaques in joints	Paraplegia	(77)
	Lysozyme amyloidosis	Lysozyme	Fibrillar deposits in leukocytes and macrophages	Renal failure	(78)

Table 1.1. *Amyloid diseases (56, 79). Table courtesy of Dr. Janet Saunders.*

Several *in vitro* techniques have been implemented successfully in order to gain molecular and mechanistic insights into amyloid formation. Imaging techniques such as electron microscopy (EM) (**Figure 1-8**a) and atomic force microscopy (AFM) are used routinely to confirm the presence of amyloid (80, 81). Additionally, X-ray fibre diffraction enables detection of the cross-β structure, common to amyloid fibrils (**Figure 1-8**b)(56). Small molecules such as Congo red (**Figure 1-8**c) and thioflavin T (ThT) (**Figure 1-8**d), known to bind to amyloid fibrils, are used commonly to detect the presence of fibrils both *in vitro* (82, 83) and *in vivo* (84, 85). Congo red exhibits apple-green birefringence upon excitation with plane-polarised light when bound to the regular array of β -strands within the cross-β structure of amyloid. Binding of ThT to amyloid fibrils can be monitored by excitation of the dye with light at 444 nm, upon which fluorescence emission can be measured at 480 nm (86). Although little is known about the specificity of this interaction, it is thought that the ThT binds with its long axis parallel to the

hydrogen bonded network within fibrils (86). *In vitro*, ThT fluorescence can be monitored in real-time and is therefore routinely used in determination of fibril formation kinetics. Typically, ordered amyloid assembly proceeds via a nucleated assembly mechanism (87). Such an assembly mechanism begins with a lag-phase in which a critical nucleus forms, followed by an elongation phase and ending with a stationary phase (**Figure 1-8**d). Identification of species in each of these phases is crucial for understanding the mechanism(s) of amyloid formation and for identifying all potentially toxic species as targets for inhibition by ligand binding. The latter could pave the way for the development of therapeutics to circumvent amyloid-associated toxicity in numerous pathologies (**Table 1.1**).
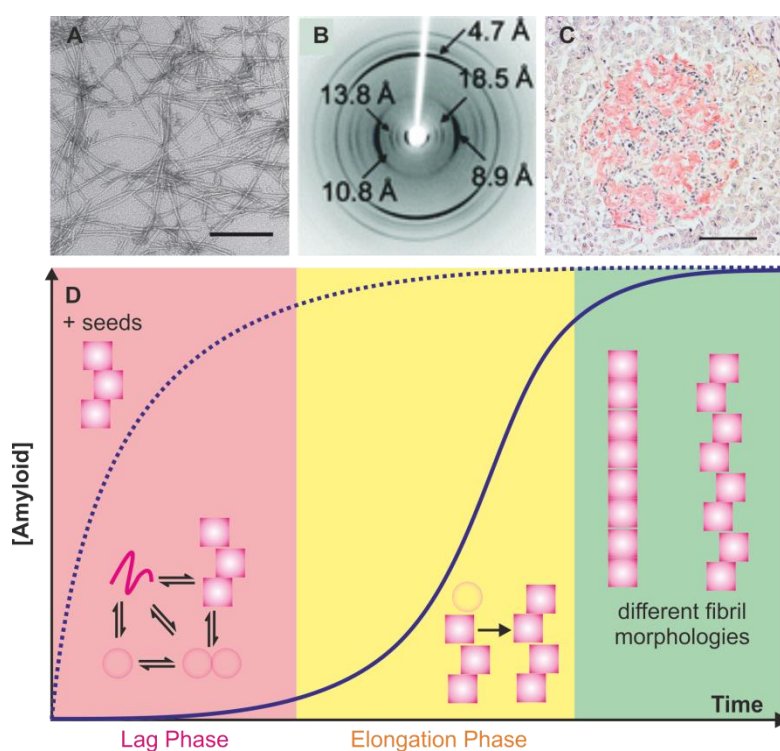
Figure 1-8. *Techniques for characterisation of in vitro amyloid formation. (a) Negative Stain EM image of long, straight hIAPP fibrils (scale bar = 100 nm); (b) X-ray fibre diffraction of long, straight hIAPP (20-29) fibrils (88) showing the hallmark amyloid pattern; (c) Congo red staining of hIAPP amyloid from a diabetic subject (89) (scale bar: 50 μm); (d) Schematic representation of amyloid fibril formation starting from monomer (pink circles) and proceeding via oligomers (pink squares) along seeded (dotted line) and unseeded (solid line) assembly pathways to produce fibrils of different morphologies.*

Protein aggregation is thought to be initiated by a misfolding or unfolding event that allows oligomerisation to proceed followed by either structural rearrangement or assembly directly into amyloid fibrils (90). Identifying oligomeric species both on- and off-pathway to the final fibrillar structure creates an enormous challenge, yet is crucial to understanding the molecular mechanisms of amyloid assembly. Whilst much attention has focussed on blocking fibril formation using small molecules that target on-pathway oligomers, recent studies have suggested that off-pathway oligomers are equally as interesting and exhibit toxicity against numerous cell-lines (91, 92). Therefore, it is essential to identify and characterise all species present within these heterogeneous ensembles. In order to identify such species, techniques are urgently required that enable the interrogation of different amyloid systems in great detail. To this end, systems including beta-2 microglobulin (β_2m) (44, 93, 94), α-synuclein (49, 95-97), Aβ (45, 98-100) and IAPP (47, 48, 101, 102) have been studied using a range of biophysical approaches including IMS-MS (**Table 1.2**).

Amyloid System	References
IAPP	(47, 48, 101, 102)
Aβ40 and Aβ42	(45, 98-100)
α-synuclein	(49, 95-97)
β2-microgloblin	(44, 93, 94)
Transthyretin	(103)
Insulin	(104, 105)
NNQQNY, VEALYL and SSTNVG peptides	(46)
Prion protein fragment PrP106-126	(106)

Table 1.2. *Amyloid systems studied by IMS*

1.10 hIAPP amyloid assembly *in vivo*

IAPP is a highly amyloidogenic 37 residue peptide hormone synthesised by beta cells of the pancreas as an 89 residue pre-prohormone. Removal of the 22 residue signal sequence leads to the 67 residue pro-IAPP, which is further processed in the

Golgi and in the insulin secretory granule to produce the 37 residue mature hormone (107) (**Figure 1-9**). Additional post-translational modifications include formation of an intramolecular disulfide bridge between cysteine residues at positions 2 and 7, and amidation of the C-terminus (**Figure 1-9**). The mature, 37 residue peptide is stored in the insulin secretory granule at a ratio of 1:50 -1:100 relative to insulin and is co-secreted with insulin. The physiological roles of IAPP are not completely understood in humans, however rodent models have suggested that the peptide plays a part in the inhibition of insulin secretion, glucose homeostasis and calcium metabolism and also affects feeding behaviour (89, 108, 109).

Figure 1-9. Comparison of human IAPP (hIAPP) and rat IAPP (rIAPP) sequences. Both peptides have a disulfide bridge between Cys-2 and Cys-7 and have an amidated C-terminus. Residues that differ from those of the human peptide are coloured pink in the rat sequence.

IAPP was discovered during post mortems of patients with T2DM due to its aggregation into insoluble amyloid deposits in pancreatic islets (109). IAPP amyloid deposits have been reported to occur in up to 95 % of Type 2 Diabetes Mellitus (T2DM) patients compared with less than 15 % of non-diabetic individuals (89). T2DM is characterised by insulin resistance and beta cell failure. Insulin resistance leads to increased insulin production by beta cells, and when these cells fail to produce sufficient insulin, then T2DM develops (110). Elevated glucose levels in T2DM cause increased amounts of IAPP to be secreted, concomitant with increased insulin secretion, eventually resulting in the formation of large extracellular beta sheet-rich aggregates. IAPP's exact role in T2DM remains elusive but its misfolding is thought be a pathogenic factor in the disease as there is strong correlation between the degree of amyloid present and disease severity (109). Amyloid formation by IAPP is thought likely to induce apoptotic cell death of pancreatic islets (110) thus leading to the observed decrease in beta cell

mass and function (111). Such proteinaceous deposits are restricted to the islet area, not spread throughout the pancreas (109).

IAPP amyloid forms via a nucleation-dependent mechanism possibly via binding to beta cell membranes (112). IAPP amyloidosis is thought to begin intracellularly; however, deposits are extracellular leading to the following hypothesis for IAPP amyloid: amyloid first forms intracellularly and causes cell death leaving a small amount of extracellular amyloid to act as a seed for progressive amyloid formation leading to development of the proteinaceous plaques observed in T2DM patients, shown in **Figure 1-10** (109).

1. Intracellular accumulation of amyloid in membrane-bound compartments.

2. Membranes are compromised and small deposits fuse to form larger ones.

3. Amyloid fills cell cytosol and apoptosis is induced.

4. Amyloid is not degraded and remains as extracellular deposits.

5.Extracellular deposits act as seeds for amyloid propagation.
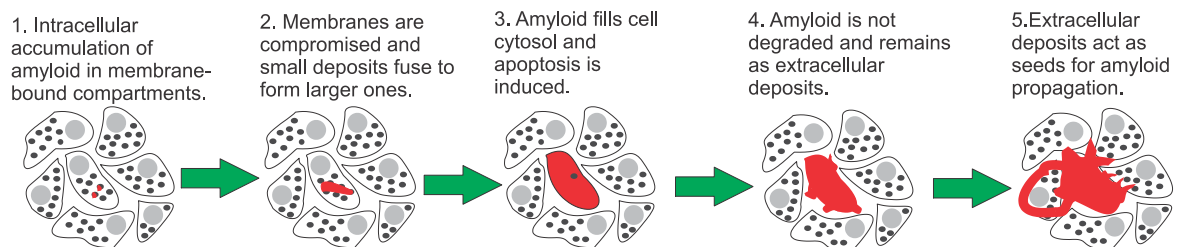
Figure 1-10. Hypothesis of IAPP fibril formation during the progression of T2DM. Figure adapted from (109).

1.11 Sequence dependence of IAPP amyloid formation

Amyloid formation by IAPP is highly sequence specific (113). Mice and rats do not develop islet amyloid, but cats, non-human primates and humans do. Whilst the human polypeptide is extremely amyloidogenic, rat IAPP does not form amyloid *in vivo* or *in vitro*, despite differing in sequence at only six amino acid positions (three being Pro residues in rat IAPP, leading to disruption of secondary structure formation) (**Figure 1-9**) (114). Much attention has been focused on the sequence within the 20–29 region and the role it plays in controlling amyloid formation. This region (SNNFGAILSS) forms amyloid-like fibrils readily in isolation *in vitro* (101, 115) and is considered to be one of the major determinants of the ability of IAPP variants to form amyloid. The shortest IAPP sequence capable of forming fibrils is

NFGAIL, whereas FGAIL forms short ribbon-like structures and GAIL is not capable of fibril formation (115). The characterisation of designed variants of IAPP support the significance of residues 20-29; analogs of IAPP which contain prolines or N-methylated residues within this portion of the polypeptide are considerably less amyloidogenic than wild type IAPP (116, 117). Although there is a strong correlation between the primary sequence of the 20–29 segment and rate of *in vitro* amyloid formation (118), mutations outside of this region significantly impact amyloid formation, indicating other factors are involved in controlling IAPP's amyloid propensity.
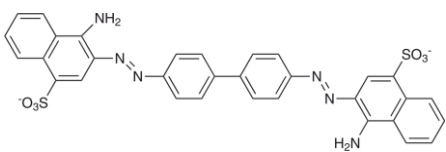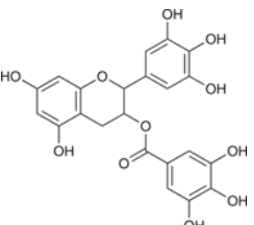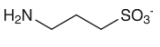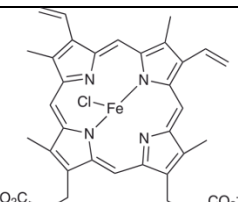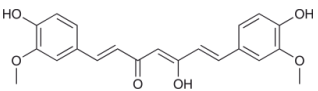
A variety of single point mutants and a free C-terminal mutant exhibit altered rates of amyloid formation with respect to the wild-type peptide sequence (119). The missense S20G mutation of the human IAPP gene, known to occur *in vivo,* is associated with a history of an early onset, more severe type of T2DM (120). This substitution also enhances amyloid formation *in vitro* (120). A H18L mutant, in which His-18 is replaced by Leu, a neutral residue of a similar volume, has a significantly increased rate of amyloid formation with respect to wild-type human IAPP (121). On the contrary, an IAPP variant with a free acid at its C-terminus forms amyloid much more slowly (121) and the 'non-amyloid', single-point mutant I26P has been shown previously to be a moderately effective inhibitor of amyloid formation by wild-type human IAPP (116). Studies of the monomeric and oligomeric species populated by mutant IAPP sequences over time would give key insights into the amyloid competence and possible toxicity of distinct states.

1.12 Inhibitors of amyloid formation

Given the multifaceted nature of the mechanisms involved in amyloid diseases, alarmingly few therapies are available currently (122-126). The toxic species in many of these disorders remains elusive, therefore any available therapies target the symptoms rather than culprits of the disease (127). The use of small molecule inhibitors (low molecular weight organic compounds) to bind to amyloid species and block and/or re-direct amyloid assembly is one promising therapeutic avenue
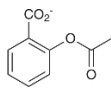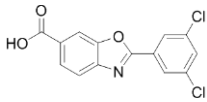
(125, 126). This inhibition approach was first introduced upon observations that aromatic compounds such as ThT and Congo red could bind to and inhibit the formation of amyloid structures, for example formed from the Aβ peptide, when present at high enough concentrations (122, 128-130). Small molecule inhibitors have numerous advantages over peptide inhibitors; they are able to cross the blood-brain barrier, avoid an immunological response, and are more stable in biological fluids and tissues (131). A vast arrays of compounds have since been demonstrated to interfere with the aggregation pathways of many proteins associated with amyloid disease. **Table 1.3** contains examples selected to highlight the structural and chemical diversity of small molecules that bind to amyloid suggesting that they may be binding to different sites and/or have different binding modes to the proteins of interest.

Small Molecule	Structure	Protein Target
Congo red		Aβ (129, 132), insulin (133), Ig domain (134)
EGCG (epigallocatechin-3-gallate)		Aβ (135), hIAPP (136-138), TTR (139), κ-casein (140), α-syn (141)
Tramiprosate		Aβ (142)
Hemin		Aβ (143, 144)
Curcumin		Aβ (145, 146), hIAPP (147, 148), α-syn

		(149), lysozyme (150)
Aspirin		Aβ (151)
Tafamadis		TTR (126)

Table 1.3 *Select examples of small molecule inhibitors of protein aggregation. Table courtesy of Dr. Janet Saunders.*

The most common family of small-molecule inhibitors of aggregation are polyphenol compounds (139, 152-155) found naturally at high concentrations in wine, tea and many plants. The compounds play protective roles including disease prevention and protection from ultraviolet radiation damage and their human consumption has been proposed to have potential antibacterial, antiviral, anticancer and neuroprotective benefits (155).

Polyphenols are believed to interact with amyloid and interfere with aggregation by means of competitive interactions with key aromatic residues within the peptides and proteins (156-158). Aromatic rings of polyphenols can compete and prevent stacking of aromatic residues ('π-stacking'), believed to be pivotal for formation of amyloid fibrils (156-158). The prevention of π-π interactions subsequently blocks further self-assembly (155, 159, 160). This has been demonstrated by structural analysis of the interaction between Congo red and the aromatic moieties of insulin, an interaction which subsequently abolishes fibril formation by insulin (133). Aromatic stacking is, however, not the sole determinant of aggregation, as demonstrated recently with the Aβ peptide in which replacement of aromatic side chains with leucine or isoleucine enhances amyloid formation (161).

One of the most intensively studied small molecules, is the tea-derived flavanol (-)-epigallocatechin-3-gallate (EGCG) (**Figure 1-11**). EGCG has been shown to interact with multiple amyloid systems and is capable of preventing oligomerisation and fibrillation as well as disaggregating preformed fibrils both *in vivo* and *in vitro* (102, 128, 135, 136, 138, 140, 141, 162-164). The numerous phenolic hydroxyl groups, as well as the aromatic rings, of EGCG (**Figure 1-11**) are believed to play a central role in aggregation inhibition, potentially via hydrogen bonding to the peptide backbone of the amyloidogenic protein (135, 137). When these hydroxyl groups are removed sequentially, the ability of the molecule to inhibit aggregation decreases sequentially (137).

Upon incubation with EGCG, fibril formation from α-synuclein and Aβ40 is ablated and small spherical species result in the place of fibrils (141, 156). Characterisation of the spherical off-pathway species formed when EGCG is

incubated with α-synuclein or Aβ40 has shown that the species formed reduce cellular toxicity when compared with fibrillar species (162). However, the point at which the assembly pathways switch from fibril formation to off-pathway oligomer formation and the mechanism by which such spherical aggregates form remains to be deduced.
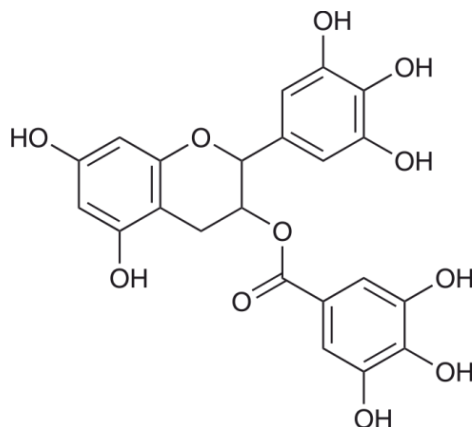
Figure 1-11. *Chemical structure of the polyphenol (-)-epigallocatechin-3-gallate (EGCG).* The high number of phenolic hydroxyl groups is pivotal to its broad anti-amyloidogenic properties (135, 137)

One possible disadvantage of polyphenol compounds as aggregation inhibitors is their lack of specificity. The generic structure of the final amyloid fibril formed by a wide variety of protein sequences enables polyphenol compounds to interact with a vast array of systems. This could be disadvantageous given that not all amyloid sytems are disease-related. Interference with functional amyloid (56, 165, 166), such as the fibrils formed by PMel17 in mammalian melanocytes that assist in melanin deposition (167), would be of great detriment. Additionally, the lack of understanding of the nature of the toxic species makes inhibitors of fibril formation and/or fibril disaggregates potentially harmful. Each non-native species on the aggregation pathway could potentially contribute towards the toxicity therefore molecules that bind to monomers and prevent all stages of misfolding and aggregation are desirable as therapeutics. Techniques for determining the mode of action of potential inhibitors and the exact species with which they interact is of great interest and importance to this field.

1.13 IMS-MS for studying amyloid assembly

IMS-MS is ideally suited to the study of amyloid formation (6, 97). It allows separation of multiple conformations of the same protein monomer with the same *m/z* ratio that differ in size and/or shape, thus enabling all of the non-native states occupied *en route* to fibril formation to be identified and characterised in detail.

Several studies have shown that the ESI process is capable of conserving a protein's solution-phase characteristics in the gas-phase and that by performing ESI-MS alone, observation and characterisation of the different conformational states of folded proteins is possible (95, 168). A protein's charge state distribution alone can provide useful information on the protein's conformation, given that unfolded conformations expose more ionisable sites than the more folded/ compact conformations (95, 168). This means that unfolded conformers of the same protein will exhibit higher charge states than their folded counterparts during the ESI process (**Section 1.7**). For protein systems that exhibit multiple conformations, Gaussian distributions can be fitted to charge state envelopes to estimate the number of conformers present (95, 168). Although fitting charge state distributions to ESI-MS *m/z* spectra helps in determining the number of conformations present, and their relative abundances, it does not allow separation and/or detailed interrogation of these species. By contrast, using IMS-MS, conformers of distinct CCS are separated and characterised individually. These approaches have been demonstrated for both α-synuclein (α-syn), an intrinsically disordered amyloidogenic protein associated with Parkinson's disease (169) and β$_2$-microglobulin (β$_2$m), a protein with an immunoglobulin fold that forms amyloid fibrils associated with DRA (170), a debilitating osteoarticular complication of long-term hemodialysis. In the case of α-syn, Gaussian fitting allowed identification of four distinct conformational states, ranging from a highly structured one to a random coil (95). The use of IMS-MS later allowed a highly amyloidogenic fragment of α-syn (residues 72–140) to be separated from the intact protein according to its CCS and subsequently individually characterised (171). In the case of β$_2$m, under low pH conditions (pH 2.5) three different conformeric families

(compact, partially compact and expanded) of the protein monomer were first identified by fitting the charge state distributions (168) and later separated using IMS-MS (172). A variety of proteins and peptides that assemble into amyloid have been studied using IMS and are listed in **Table 1.2**.

After IMS-MS separation and subsequent CCS determination, it is possible to use molecular dynamics simulations and/or coarse-grain modelling to reveal potential structures of protein conformers observed using IMS-MS and to understand the mechanism of oligomer growth. Molecular dynamics (MD) simulations have been utilised in conjunction with IMS-MS in the analysis of several amyloid systems including IAPP (47), α-syn (49) and a short prion fragment (residues 106-126) (106). In the case of IAPP (discussed in detail in **Section 1.11**), a distinct change in monomer conformation associated with amyloid propensity was identified using IMS-MS. IMS-MS revealed that human IAPP populates a more expanded conformation than its non-amyloidogenic rat counterpart (48). MD simulations confirmed that the expanded conformation identified in the IMS-MS analyses was likely populated by a β-hairpin structure. Similarly, NMR data suggested that fibril formation of hIAPP is initiated through a β-hairpin intermediate (173), validating the use of IMS-MS in combination with MD for study of early amyloid intermediates. In a similar study, Dupuis *et al.* suggested a β-hairpin human IAPP dimer structure with CCS values consistent with this species containing two β-hairpin IAPP monomers bound side-to-side (47) (**Figure 1-12**).
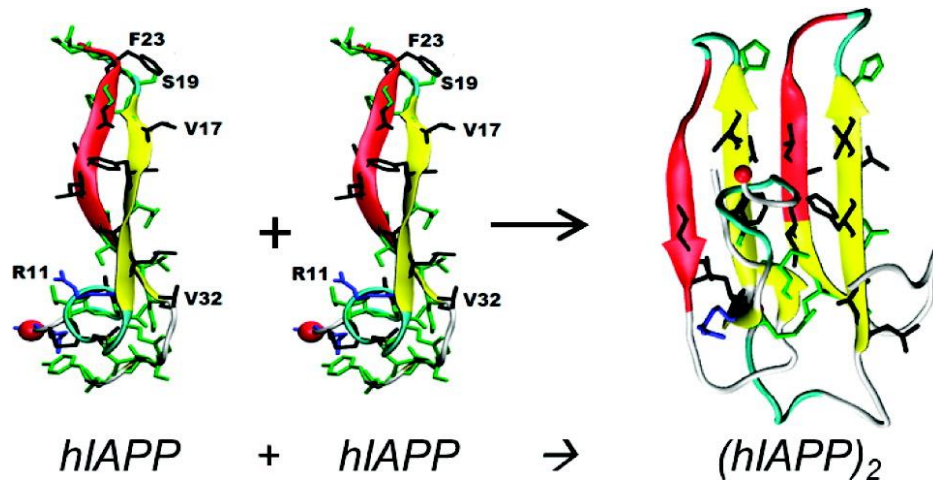
Figure 1-12*. Mechanism of dimer formation by hIAPP: dimers have β-strand monomer-monomer interfaces. IMS-MS and simulation data support a route to the fibril state through an "early conformational transition" to a β-stranded conformer. Figure take from (47).*

Using the same approach, a mechanism of the prion fragment 106-126 oligomer formation was proposed (106). An expanded conformer observed using IMS-MS was shown likely to have a β-hairpin-like structure according to MD simulations. This β-hairpin-like conformation decreased in relative intensity over time, concomitant with an increased intensity of a peak in the IMS spectra corresponding to oligomeric species (**Figure 1-13**). Increased β-sheet content over time, measured using CD (106), was additional evidence for this conformational change.
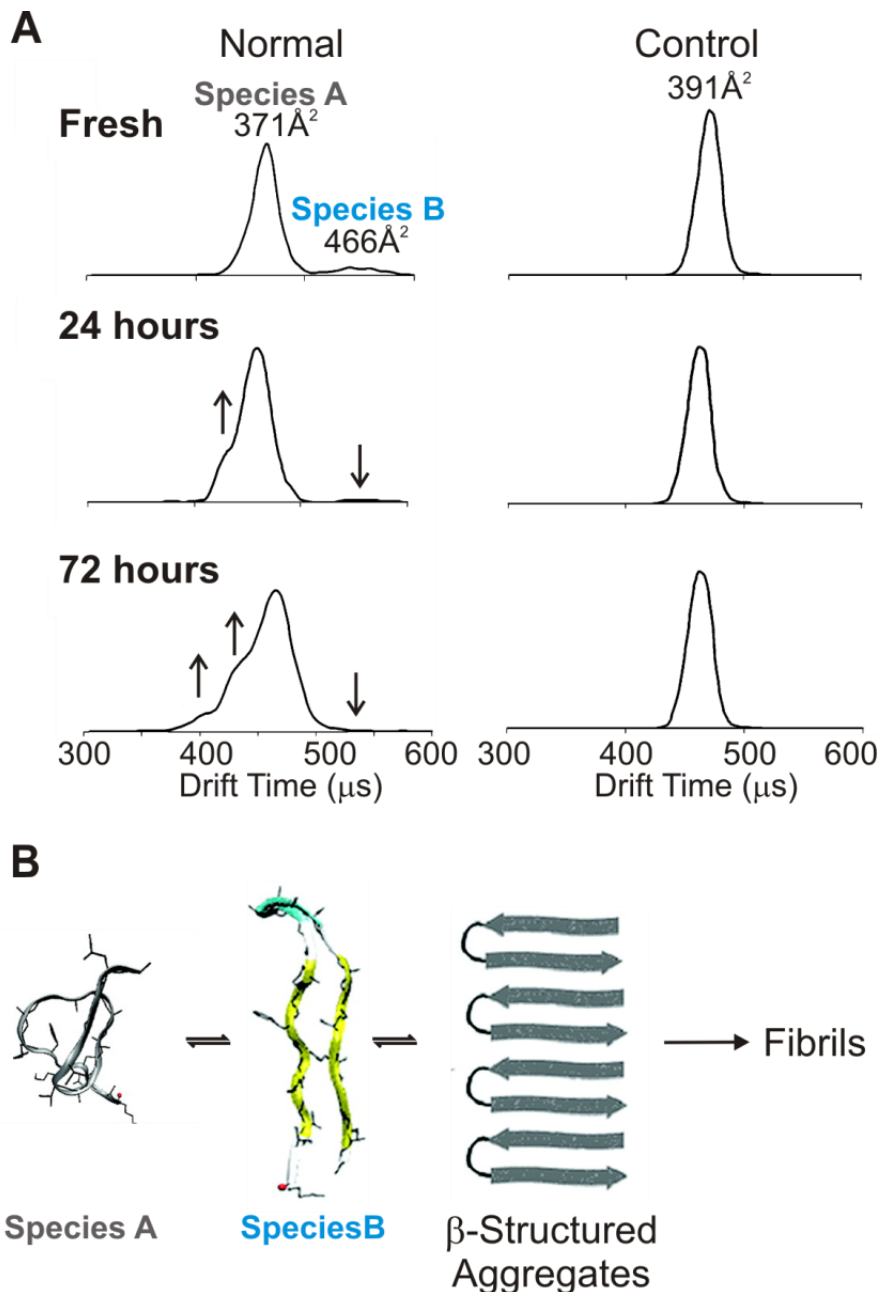
Figure 1-13. *Ion mobility spectrometry-mass spectrometry of the assembly pathway of the prion protein fragment 106-126. a) Ion mobility traces for the +2 charge state monomeric ions of the prion fragment 106-126 showing the presence of Species A (CCS = 371 Å²) together with Species B, an expanded β-sheet conformation with a CCS of 466 Å², at early time-points. Species B is absent in the "Control" sample, a non-amyloidogenic peptide of the same amino acid composition but with a scrambled sequence (CCS = 391 Å²). The population of expanded conformers in the "Normal" prion protein fragment 106-126 decreases over time as species with drift times of 390 μs and 425 μs appear. These peaks are presumed to be oligomeric as the CCS values are too small to belong to a monomeric conformer with +2 charges. b) Schematic showing the proposed mechanism of PrP106-126 oligomer formation involving the assembly of Species A and Species B into ordered small aggregates. Figure taken from (106).*

Although IMS-MS is a relatively new addition to the structural biology tool kit, it is now accepted as a powerful method for the interrogation of the conformational properties of proteins which may be folded, partially folded or intrinsically unfolded (6, 97). Given that amyloid fibril formation can be initiated via the formation of lowly populated and highly dynamic, transient species, this is especially useful.

1.14 Studying oligomeric intermediates using IMS-MS

A significant challenge in the study of amyloid assembly is the identification and characterisation of oligomeric intermediates. In the early stages of amyloid assembly multiple, rapidly-converting, transient and lowly-populated species are co-populated in solution, so the detection and characterisation of individual species is extremely difficult. In contrast to rival biophysical techniques, such as light-scattering or fluorescence, IMS-MS can individually identify and characterise oligomers that are present, rather than simply providing information on the average properties of the species populated. ESI-IMS-MS lends itself to the study of amyloid systems for a number of reasons. Firstly, MS enables the detection of multiple ions within the same sample at femtomolar concentrations, and their identification, based on their m/z. Secondly, nESI-MS allows preservation of large, non-covalently bound biomolecular species in the gas phase that are reflective of species populated in solution (174-177). Thirdly, IMS-MS allows ion species of the same m/z but different CCSs to be separated, enabling different protein conformational states and oligomeric species to be distinguished confidently (178, 179), all within a single experiment. Amyloid formation can be followed over time and any changes in oligomer distribution and/or protein conformation can be monitored (180).

In the past, using ESI-MS without IMS, high order oligomers occupied during fibril formation of proteins including β_2m and insulin have been identified based upon m/z alone (94, 105). Using this approach, oligomer charge states were identified based on the observed ^{13}C isotope spacing or through the identification of unique,

odd numbered charge states (94, 105). More recently, using IMS-MS, it has been possible to establish unequivocally which species are present in solution, given that at a particular *m/z* different oligomeric ions may contribute to the peak in the ESI-MS spectrum. Oligomeric states that have coincident *m/z*, but different size/shapes can be separated based on their mobility through an inert gas under the influence of a weak electric field, as they travel through the IMS drift cell.

Multiple amyloid systems have been interrogated by IMS-MS (**Table 1.2**) including the Aβ40 (98, 100) and Aβ42 (45) peptides that form extracellular plaques in AD and contribute to cell death associated with memory loss (123). Both peptides are aggregation prone, however Aβ42 is more highly amyloidogenic and considered to be significantly more neurotoxic (123). The discrepancy in amyloid propensity of the two peptides has been proposed to be in part due to a difference in the oligomeric states occupied during fibril formation. Bernstein *et al.* (98) employed negative mode ESI-IMS-MS in order to show significant differences in the oligomeric states populated by Aβ40 and Aβ42 (**Figure 1-14**). IMS-MS data revealed that the key structure in the aggregation pathway of Aβ40 is a 'closed' tetramer that is not amenable to further oligomerisation by monomer or dimer addition. In contrast, Aβ42 occupies 'open' tetramers *en route* to a planar hexamer which stacks to form a dodecamer, proposed to be a potential candidate for the primary toxic species in AD (**Figure 1-14**).
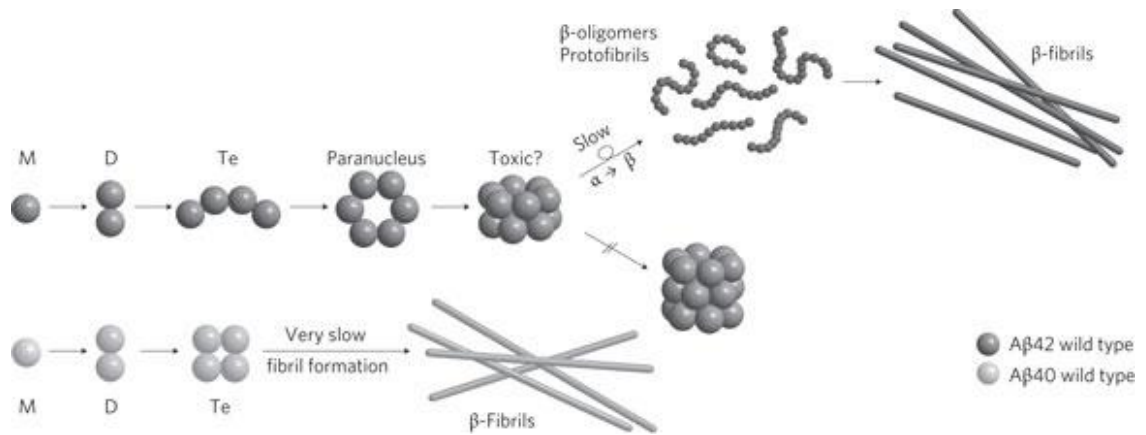
Figure 1-14. *Differences in Aβ40 /Aβ42 fibril formation determined by ESI-IMS-MS. For Aβ40 the key structure is the tetramer that does not undergo further monomer or dimer addition. For Aβ42 an 'open' tetramer promotes the formation of the planar hexamer (paranucleus) and the stacked dodecamer. The Aβ40 tetramer is suggested to go on to forms fibrils, but these were not observed in this study. For Aβ42 a rate-limiting slow α- to β-sheet transformation was suggested for the dodecamer, but this was not explicitly demonstrated. Fibril formation was indirectly detected through macroscopic clogging of the spray tips used for Aβ42. Figure taken from reference (98).*

Using positive mode ESI with travelling wave IMS-MS and improved *m/z* resolution, however, Kłoniecki *et al.* observed higher order species (monomer to 13-mer) formed by the Aβ40 peptide (100) demonstrating the possible instrument and settings dependence of data produced.

Comparison of IMS-MS-derived CCS values with coarse grain modelled oligomer structures enables estimations of the mechanism by which protein monomers assemble into fibrils. For example, theoretical isotropic and linear growth models can be estimated by the use of equations and compared with measured CCS values. In an isotropic growth model, $\sigma_n = \sigma_{monomer}*n^{2/3}$, where n = oligomer number, σ_n is the CCS of the oligomer number n and $\sigma_{monomer}$ is the monomer CCS (98). Similarly, linear growth in one direction (fibril growth) can be estimated by $\sigma_n = a*n + k$, where a describes the CCS of a monomer within a fibril and k is the size of the fibril cap. Such modelling has been employed in the study of oligomers formed during the assembly of the small highly amyloidogenic peptides sequences NNQQNY, VEALYL and SSTNVG (46) derived from the yeast prion protein Sup 35, human

insulin and IAPP, respectively. Self-assembly of these amyloid fragments proceeds rapidly *in vitro*. Comparisons with modelled structures reveal that fibrillation proceeds via stacking of extended, fibril-like conformers. For each peptide sequence, a transition of soluble oligomers from globular conformations into β-strand structures occurs at different points in the aggregation pathway, as early as dimer (**Figure 1-15**). In contrast, a non-amyloidgenic control sequence leucine enkephalin (YGGFL) forms an isotropic distribution of compact oligomers and does not transition toward β-strand structures as aggregation proceeds (46).
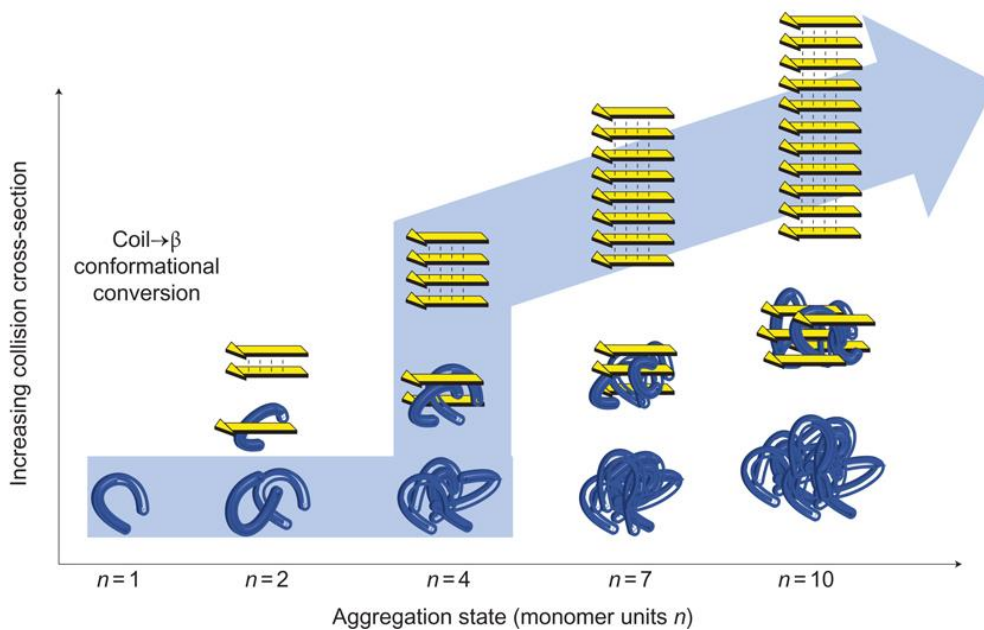
Figure 1-15. *The in vitro self-assembly of peptide monomers into mature, insoluble β-sheet fibrils. A distinct transition of IMS-detectable oligomeric states (horizontal axis) from globular conformations into β-strand structures occurs during the lag phase of fibril formation. Self-assembly begins with a folded monomer (n=1) and proceeds to soluble oligomers of increasing size (n=2, 4, 7, and 10, right). Soluble peptide oligomers with identical mass (i.e. the same n) can occupy different conformations such as globular (blue structures) or β-strand conformations (flat yellow arrows) with different CCS. CCS determination of the oligomeric states reveals the nature of the self-assembly pathway that is taking place in solution (large, pale blue arrow). The oligomer size at which the divergence from compact to extended conformers occurs differs for peptides of different sequences. Figure taken from (46).*

1.15 IMS-MS can be used to unravel the mechanism of inhibition of fibril assembly by small molecules

Over the past decade IMS-MS has been utilised successfully to gain information on the inhibition of amyloid assembly by small molecules. The first example of a study of this kind was performed by Robinson *et al.*, who used ESI-MS to identify inhibitors of transthyretin (TTR) amyloidosis (103). TTR, a native homotetramer, is active in the serum and cerebroserum wherein it functions to transport vitamin A and the hormone thyroxine, respectively. Upon dissociation from its tetrameric state, however, TTR mis-folds and aggregates into amyloid fibrils (103). Stabilisation of the native tetramer by ligand binding and therefore prevention of the initiation of amyloid assembly is a possible therapeutic strategy. The ESI-MS-based study demonstrated the stabilisation of the native state via binding of small molecule ligands (103). These ligands have subsequently been evolved leading to production of tafamadis, the first small molecule therapeutic for an amyloid disease (126).

More recently, by combining IMS separation with ESI-MS analysis, the detection of ligand binding to specific monomeric conformations and oligomeric species has been shown to be possible. Several amyloid-small molecule interactions have been probed to this extent, including Aβ42, IAPP, α-synuclein and β2m (44, 96, 181). Bowers and co-workers, for example, studied the changes in the well-characterised oligomerisation pathway of Aβ42 (98) in the presence of a known inhibitor, Z-Phe-Ala-diazomethylketone (PADK) (99). ESI-IMS-MS data demonstrated the binding of PADK to monomeric and oligomeric forms of Aβ42 resulting in both the inhibition of assembly from monomer and the dissociation of potentially toxic high order oligomers. The same group revealed that insulin, a potent inhibitor of hIAPP self-assembly, interacts with the compact hIAPP monomer conformation and shifts the equilibrium away from the extended, aggregation-prone conformation (48), thus preventing initiation of β-sheet formation and subsequent amyloid assembly (182).

The changes in the conformational properties of monomeric α-synuclein in the presence of the known amyloid inhibitor EGCG (141, 162) have also been probed using ESI-IMS-MS (183). The results revealed that addition of EGCG to the disease related A53T α -synuclein variant results in the formation of a ligand-bound off-pathway conformer as opposed to a compact conformer previously described and attributed to an amyloid competent state. The reverse effect can be observed in the presence of spermine, an amyloid accelerator, that initiates the formation of a compact state of α-synuclein (184) thereby increasing the rate of fibrillation.

The conformer-specific mechanism of inhibition of β_2m fibrillation by the antibiotic rifamycin SV was demonstrated by Woods *et al.* using ESI-IMS-MS. At pH 2.5, β_2m occupies several monomeric conformations, i.e. compact (thought to be native like) partially compact, and extended (20, 93). Rifamycin SV was observed to bind all three monomeric conformers and inhibit amyloid assembly by β_2m (44). By contrast, other antibiotics from the rifamycin family with very similar structures, for example rifaximin, bind only to the most compact conformations and fail to inhibit amyloid formation. The data suggested that the unfolded and partially folded conformers are amyloid competent, thus revealing key insights into the self-assembly mechanism of β_2m.

Identifying amyloid inhibitors is difficult given that many protein precursors of aggregation are partially folded or intrinsically disordered. The level of disorder of such systems means that they are not amenable to structure-based design. Together, the studies reviewed above clearly demonstrate the power of IMS-MS to identify binding of ligands to specific amyloid species and to reveal the mechanism of action of small molecules that interfere with the amyloid cascade. Furthermore, the role of different conformers in the amyloid assembly route can be determined.

2 Materials and methods

2.1 Materials

2.1.1 Technical equipment

Equipment	Manufacturer
Microplate readers	
FLUOstar OPTIMA plate reader	BMG Labtech, Aylesbury, Bucks, UK
NEPHELOstar Galaxy laser-based nephelometer	BMG Labtech, Aylesbury, Bucks, UK
Electron microscope	
JEOL JEM-*1400* transmission electron microscope	JEOL Ltd., Tokyo, Japan
Other equipment	
Grant JB1 Unstirred Waterbath	Grant Instruments, Shepreth, UK
Jenway 3020 Bench pH Meter	Bibby Scientific, Stone, UK

Mass spectrometer

Synapt High Definition Mass Spectrometry (HDMS) quadrupole-time-of-flight mass spectrometer (Micromass UK Ltd., Waters Corpn., Manchester, UK), equipped with a Triversa automated nano-electrospray ionisation (ESI) interface (Advion Biosciences, Ithaca, NY, USA).

2.1.2 Chemicals

A

Acetic acid, glacial	Fisher Scientific, Loughborough, UK
Acetonitrile	J.T.Baker, Deventer, The Netherlands
Acid fuchsin	Fisher Scientific, Loughborough, UK
Acridine orange	Fisher Scientific, Loughborough, UK
Alcohol dehydrogenase	Sigma Life Sciences, St. Louis, USA
Ammonium Acetate	Sigma Life Sciences, St. Louis, USA
Ammonium bicarbonate	Sigma Life Sciences, St. Louis, USA
Aspirin	Sigma Life Sciences, St. Louis, USA
Azure A	Sigma Life Sciences, St. Louis, USA
Azure C	Alfa Aesar, Heysham, UK

B

1H benzimidazole-2-sulfonic acid	Sigma Life Sciences, St. Louis, USA
Benzimidazole	Sigma Life Sciences, St. Louis, USA
Bromophenol blue	Sigma Life Sciences, St. Louis, USA

C

Caffeic acid	Sigma Life Sciences, St. Louis, USA
Caesium iodide	Sigma Life Sciences, St. Louis, USA
Congo red	Sigma Life Sciences, St. Louis, USA
Curcumin	Sigma Life Sciences, St. Louis, USA
Cytochrome c	Sigma Life Sciences, St. Louis, USA

D

Dimethyl sulphoxide, DMSO   Sigma Life Sciences, St. Louis, USA

E

(-)-Epigallocatechin-3-gallate (EGCG)   Sigma Life Sciences, St. Louis, USA

Ethanol   Fisher Scientific, Loughborough, UK

F

Fast Green FCF   Fisher Scientific, Loughborough, UK

H

Hemin   Sigma Life Sciences, St. Louis, USA

Hexafluoroisopropanol   Sigma Life Sciences, St. Louis, USA

Hydrochloric acid, HCl   Fisher Scientific, Loughborough, UK

L

Lysozyme (hen egg)   Sigma Life Sciences, St. Louis, USA

M

Morin hydrate   Sigma Life Sciences, St. Louis, USA

Myoglobin (horse heart)   Sigma Life Sciences, St. Louis, USA

Myricetin   Sigma Life Sciences, St. Louis, USA

O

Orange G   Sigma Life Sciences, St. Louis, USA

Orcein   Sigma Life Sciences, St. Louis, USA

P

Phenol red   Fisher Scientific, Loughborough, UK

R

Resveratrol   Santa Cruz Biotech, Middlesex, UK

S

Silibinin   Sigma Life Sciences, St. Louis, USA

T

Thiabenzadole   Sigma Life Sciences, St. Louis, USA

Thioflavin T   Santa Cruz Biotech, Middlesex, UK

Tramiprosate   Santa Cruz Biotech, Middlesex, UK

U

Uranyl acetate   Sigma Life Sciences, St. Louis, USA

Ubiquitin (bovine)   Sigma Life Sciences, St. Louis, USA

W

Water   J.T.Baker, Deventer, The Netherland

2.1.3 Acquisition of IAPP fragment peptides

Human IAPP fragment peptides H_2N-24GAIL27-CO_2H (372.2 Da), H_2N-22NFGAIL27-CO_2H (633.4 Da), H_2N-$_{20}$SNNFGAIL$_{27}$-CO_2H (834.4 Da), and H_2N-20SNNFGAILSS29-CO_2H (1008.5 Da) were purchased from Protein Peptide Research (Cambridge, UK).

2.1.4 Acquisition and Synthesis of IAPP

Human and rat IAPP were synthesised, purified and kindly provided by Ping Cao, Cynthia Tu and Professor Daniel Raleigh (Stony Brook University, New York, USA) according to the following procedure :

IAPP sequences were synthesised on a 0.1 mmol or 0.25 mmol scale using a CEM Liberty peptide syntheiser, and 9-fluorenylmethoxycarbonyl (Fmoc) chemistry. Fmoc protected pseudoproline dipeptide derivatives were incorporated to facilitate the synthesis. 5-(4'- Fmoc-aminomethyl-3', 5-dimethoxyphenol) valeric acid (PAL-PEG) resin was used to generate an amidated C-terminus. Double couplings were performed for the first residue attached to the resin, pseudoprolines, all β-branched residues and all residues directly following a β-branched residue. Peptides were cleaved from the resin through the use of standard trifluoroacetic acid (TFA) methods. Crude peptides were dissolved in 20% acetic acid (*v/v*), frozen in liquid nitrogen and lyophilized. The disulphide bond was formed via oxidation by use of DMSO. Peptides were purified by reverse-phase HPLC using a Vydac C18 preparative column (10 mm x 250 mm) with buffer A, consisting of 100% H_2O and 0.045% HCl (v/v) and buffer B, composed of 80% acetonitrile, 20% H_2O and 0.045% HCl. HCl was used as the ion-pairing agent since residual TFA can cause problems with cell toxicity assays and can influence the aggregation kinetics of some amyloidogenic peptides. The identity of the pure products was confirmed by mass spectrometry using a Bruker MALDI-TOF MS. Analytical HPLC was used to confirm the purity of the peptides before each

experiment. This is an important control because deamidation alters the aggregation of hIAPP (185, 186).

2.1.5 Purification of Aβ40

The Aβ40 purification protocol was developed and performed by Rachel A. Mahood (The Astbury Centre for Structural Molecular Biology, Faculty of Biological Sciences, University of Leeds, UK), as follows.

Recombinant expression of Aβ40 results in an additional N-terminal methionine (Aβ(M40), refered to as Aβ40 throughout the thesis) (187). Aβ40 was expressed in BL21 [DE3] pLysS cells (Agilent) from a PetSac vector, kindly provided by Dominic Walsh (Brigham & Women's Hospital, Boston, USA) and Sara Linse (Lund University, Sweden) (187). Cells were grown at 37 °C in LB media, containing ampicillin (100 μg/mL) and chloramphenicol (25 μg/mL). Expression of Aβ40 was induced by the addition of 0.5 mM isopropyl-β-D-thiogalacto-pyranoside at an OD_{600} of 0.5, followed by a 3 h incubation at 37 °C. Cells were collected by centrifugation (Beckman-Coulter JLA 8.1, 6000 g, 15 min, 4 °C) and purified using a modified protocol provided by Walsh *et al*. (187). Briefly, cells were disrupted in 10 mM Tris-HCl, 1 mM EDTA, pH 8.5, containing 20 μg/mL DNase, 1 mM phenylmethanesulfonyl fluoride and 2 mM benzamidine. The suspension was stirred at 4 °C for 1 h before homogenization and sonication (30 s, 4 W). The extract was then centrifuged (Beckman-Coulter JA 25.5, 20,000 g, 15 min, 4 °C). The pellet was resuspended in 10 mM Tris-HCl, pH 8.5, containing 8 M urea and sonicated to dissolve the inclusion bodies. The suspension was centrifuged again and the supernatant collected, diluted 1:4 in 10 mM Tris-HCl buffer and agitated gently with Q Sepharose Fast Flow resin (GE Healthcare, Amersham, Bucks, UK.) for 30 min. After washing the resin with buffer containing 0 mM NaCl and then 25 mM NaCl, peptide-enriched fractions were eluted with buffer containing 125 mM NaCl, dialysed into 50 mM ammonium bicarbonate, pH 8.0 and lyophilized. Semi-purified Aβ(M1-40) was resolubilized in 50 mM Tris-HCl containing 7 M GuHCl, pH 8.5 at a concentration of approximately 10 mg/mL and purified by size exclusion

chromatography (HiLoad Superdex 75 26/60 column, GE Healthcare, Amersham, Bucks, UK) in 50 mM ammonium bicarbonate, pH 8.0, before finally lyophilizing and storing at -20 °C.

2.2 Mass spectrometry

All analyses were performed on a Synapt HDMS quadrupole time-of-flight mass spectrometer (Micromass UK Ltd., Waters Corpn., Manchester, U.K.), equipped with a Triversa (Advion Biosciences, Ithaca, NY, U.S.) automated nano-ESI interface. All samples were analysed by positive ionisation nanoESI (nESI). Data were processed by use of MassLynx v4.1 and Driftscope software supplied with the mass spectrometer. The m/z scale was calibrated with aq. CsI clusters (1 mg/ml, *m/z* range 200-10000). CCSs were estimated following IMS-MS calibration using the denatured proteins equine cytochrome c, hen egg lysozyme (disulphide bridge-reduced), horse heart myoglobin and bovine ubiquitin (10 μM in 50:40:10, v/v/v, acetonitrile, water, acetic acid), in addition to a range of peptides generated by trypsin proteolysis of equine cytochrome c and alcohol dehydrogenase, as described previously (20, 188).

2.2.1 ESI-MS to detect oligomers of hIAPP peptide fragments

2.2.1.1 Sample preparation

Lyophilized peptides H_2N-24GAIL27-CO_2H (372.2 Da), H_2N-22NFGAIL27-CO_2H (633.4 Da), H_2N-$_{20}$SNNFGAIL$_{27}$-CO_2H (834.4 Da), and H_2N-20SNNFGAILSS29-CO_2H (1008.5 Da) were dissolved in DMSO at concentrations of 5 mM. After 24 h incubation at 25 °C, stock solutions were diluted into 20 mM ammonium acetate, pH 6.8, to a final concentration of 100 μM for MS analysis.

2.2.1.2 ESI-MS analysis

A capillary voltage of 1.7 kV and a nitrogen nebulizing gas pressure of 0.8 psi. The following instrument parameters were used: cone voltage 170 V; source temperature 60 °C; backing pressure 4.2 mBar; ramped travelling wave height 4–20 V; travelling wave speed 400 m/s; IMS nitrogen gas flow 20 mL/min; IMS cell pressure 0.55 mBar. The cone voltage was optimized to transmit the higher order peptide oligomers; the CCS of the oligomers did not alter over the range 30–170 V.

2.2.2 ESI-MS to detect oligomers of hIAPP, rIAPP and Aβ40

2.2.2.1 Sample preparation

Lyophilised hIAPP and rIAPP samples were dissolved in DMSO to a concentration of 3.2 or 5 mM. After 24 h incubation at 25 °C, stock solutions were diluted in 200 mM ammonium acetate, pH 6.8, to give a final peptide concentration of 32/50 µM for mass spectrometry analysis. The final concentration of DMSO was 1 % (*v/v*). Lyophilised Aβ40 was dissolved at 32 µM in 200 mM ammonium acetate, pH 6.8, 1 % DMSO (*v/v*). The Aβ40 peptide samples were centrifuged at 13,000 rpm, 4 °C for 10 min before analysis. All samples were incubated at 25 or 37 °C in 96-well plates (Corning Costar 3915, Corning Life Sciences, Amsterdam, The Netherlands) with or without agitation (600 rpm).

2.2.2.2 ESI-MS analysis

A capillary voltage of 1.7 kV and a nitrogen nebulizing gas pressure of 0.8 psi were used. The following instrumental parameters were used: cone voltage 30–100 V; source temperature 60 °C; backing pressure 4.0 mBar; ramped traveling wave

height 7–20 V; traveling wave speed 400 m/s; IMS nitrogen gas flow 20 mL/min; IMS cell pressure 0.55 mBar. The cone voltage was optimized to transmit the higher order peptide oligomers; the CCS of the oligomers did not alter over the range 30–100 V. For ESI-IMS-MS time course experiments, 50 μM peptide samples were incubated in 20/100/200/500 mM ammonium acetate buffer, pH 6.8, 1 % DMSO) for 24 h. 10 μL volumes were removed from each solution and infused into the mass spectrometer for analysis via a Triversa automated nano-ESI interface (Advion Biosciences, Ithaca, NY, USA).

2.2.3 ESI-MS to detect ligand binding to hIAPP, rIAPP and Aβ40

hIAPP, rIAPP or Aβ40 (32/50 μM) were dissolved in 20 or 200 mM ammonium acetate (pH 6.8) containing 32/50 μM (1:1 molar ratio small molecule:peptide) or 320/500 μM (10:1 molar ratio small molecule:peptide) of small molecule. For analysis of these samples by nESI-MS, a sampling cone voltage of 30 V was used to preserve protein-ligand interactions, and a backing pressure of 1.6 mbar was applied.

Please note 32 and 320 μM are used in **Chapter 4** and 50 and 500 μM are used in **Chapter 5** and **Chapter 6.**

2.2.4 MS/MS

2.2.4.1 Collision induced unfolding (CIU) MS/MS of hIAPP and rIAPP monomers

CIU-MS/MS experiments were performed using the quadrupole analyser to select monomeric ions of hIAPP or rIAPP. Increasing collision energy was applied to the trap collision cell in 10 V increments from 10 to 100 V until the ions unfold,

observed in extracted ion mobility plots. The dependence of the ion arrival time distribution (ATD) versus increasing the trap energy (used to affect CIU) was examined.

2.2.4.2 Collision induced dissociation (CID) MS/MS of hIAPP and rIAPP oligomers

CID-MS/MS experiments were performed using the quadrupole analyser to select isobaric *m/z* ions representing the dimer and tetramer, separating these ions in the IMS device and performing CID in the transfer collision cell prior to the ToF analyser (the pressure in the collision cell was kept constant). Increasing collision energy was applied to the transfer collision cell in 10 V increments from 10 to 100 V until the oligomers ions were completely dissociated into monomer ions.

2.2.4.3 Collision induced dissociation (CID) MS/MS of hIAPP and Aβ40 dimers

CID-MS/MS experiments were performed using the quadrupole analyzer to select isobaric *m/z* ions representing the dimer 5+ ions and performing CID in the trap collision cell prior to the IMS device and ToF analyser. Increasing collision energy was applied to the trap collision cell in 10 V increments from 10-100 V until the oligomer ions were completely dissociated into monomer ions.

2.2.4.4 Collision induced dissociation (CID) MS/MS of ligand-bound hIAPP

CID-MS/MS was carried out in the trap collision cell of the mass spectrometer. The quadrupole analyser was used to select ions that represented ligand-bound monomer complexes and increasing collision energy was applied to the trap

collision cell in 10 V increments from 10 to 100 V until the ligands were completely dissociated from the monomer ions. Quantification of precursor ion intensity relative to total ion intensity was calculated using area under peaks.

2.3 Molecular modelling of peptide oligomers

The molecular modelling detailed in this section was performed by Hlengisizwe Ndlovu (School of Physics & Astronomy, University of Leeds).

The different sized models were built from the PDB coordinates of a model of the structure of SNNFGAILSS fibrils generated using ssNMR constraints (88). In this structure, SNNFGAILSS forms fibrils in which constituent β-sheets are organised in a parallel structure of protofibrils consisting of a pair of two peptide-long β-sheets (88). The parallel model was chosen arbitrarily as the difference in CCS between parallel and anti-parallel aggregates would be too small to be distinguishable by ESI-IMS-MS. The Nucleic Acid Builder (NAB) software package (189) was used to extend the length and width of the fibril by translating and joining copies of the template, allowing a variety of models with distinct dimensions to be built. The models were comprised of single β-sheets with a range of 1 to 30 peptides, double β-sheets with a range of 2 to 30 peptides, triple β-sheets with 3 to 30 peptides and finally quadruple β-sheets ranging from 4 to 28 peptides. In all cases the 4.7 Å inter-peptide β-strand distance was maintained. Missing hydrogen atoms, unresolved in the ssNMR derived coordinates, were added automatically via the LEAP module of the AMBER11 package (190). The models were then refined to remove steric clashes by multi-step energy minimization in the NAMD2.7b1 software package utilising the Amberff99sb forcefield (191, 192). CCSs were calculated on the energy minimized structures using an in-house projection approximation method (20), with the default parameters for the number of projection angles and the gas radius used.

2.4 *In vitro* techniques

2.4.1 Transmission electron microscopy

Transmission electron microscope images were acquired on a *JEOL* JEM-*1400* transmission electron microscope (JEOL Ltd., Tokyo, Japan) after incubating 32/50 μM protein (rIAPP, hIAPP and Aβ40) solutions in the presence or absence of 320 or 500 μM small molecules for 5 days at 25/37 °C. Carbon grids were prepared by irradiating under UV light for 30 min and staining with 4 % (*w/v*) uranyl acetate solution.

2.4.2 Thioflavin T fluorometry

100 μL samples containing 100 μM thioflavin T and 32/50 μM protein in 20/200 mM ammonium acetate, pH 6.8 and a 1 % (*v/v*) final concentration of DMSO were prepared in a 96-well plate and sealed with clear sealing film (Corning Costar 3915, Corning Life Sciences, Amsterdam, The Netherlands). Plates were incubated in a FLUOstar OPTIMA plate reader for 5 days at 25/37 °C with or without agitation (600 rpm), as indicated in each figure. Fluorescence was excited using a 440 ± 5 nm filter, and emission intensity was measured using a 485 ± 5 nm filter.

2.4.3 Nephelometry

Nephelometry was used to determine the extent of aggregation in rat and human IAPP peptide samples. For these experiments, the samples were prepared as described above (**Section 2.4.2**), except that ThT was not included. In each experiment readings were taken every 5 min, from 2 min to 50 h. 100 μL of 50 μM peptide samples were added to the wells of a flat-bottomed 96-well plate (CoStar, UK). To avoid evaporation and condensation, the plates were sealed with transparent, hydrophobic and gas permeable plastic films (Breathe Easy, Sigma

Aldrich) during incubation and measurement. A NEPHELOstar Galaxy laser-based microplate nephelometer (BMG LABTECH, Germany) was used to monitoring the turbidity of the samples over time.

2.4.4 Fibril Depolymerisation

Mixed samples containing a 1:1 molar ratio of hIAPP:rIAPP or hIAPP:Aβ40 were prepared by diluting 3.2 or 5 mM stock solutions of each peptide in DMSO 100-fold into 20 or 200 mM ammonium acetate, pH 6.8, to a final concentration of each peptide of 32 or 50 μM in 1% (v/v) DMSO for MS analysis. After 7.5 hours or 5 days of incubation at 25 or 37 °C and 600 rpm, mixed samples were centrifuged in a Beckman ultracentrifuge at 300,000 g for 45 min. Fibrillar samples in the pellet were depolymerised by incubation in 100 % (v/v) HFIP for 24 h at 25 °C, 200 rpm in 200 μL Eppendorf tubes. Samples were air-dried with nitrogen gas and then re-dissolved in 50:40:10 ($v/v/v$) acetonitrile/water/acetic acid, and fibril constituent peptides were identified by ESI-MS (**Section 2.2**).

2.4.5 Selecting novel small molecules for analysis of fibrillation inhibition

Compounds were selected for analysis by Charlotte H. Revill and Dr. Richard J. Foster (University of Leeds). The structure of each of the five query molecules (vanillin, resveratrol, curcumin, chloronaphthoquinine-tryptophan and epigallocatechin-3-gallate (EGCG)) was minimised to the lowest energy conformer using LigPrep (193). The minimised conformers were used as the query scaffold for virtual screening of an in-house library of 50,000 structurally diverse, novel small molecules using Rapid Overlay of Chemical Structures (ROCS) (194). ROCS is a 3D method that matches the shape of a molecule to the shape of the query molecule. ROCS also incorporates pharmacophoric features in assessing overlays

such that the *ROCS Combiscore* in ROCS measures the similarity of the matched shapes as well as the matched pharmacophoric features. Virtual hits were pooled and ranked according to the *ROCS Combiscore* parameter and 20 of the top 100 compounds selected for screening based on a qualitative assessment of structural diversity. This subset of 20 compounds chosen (**Chapter 5 Table 5.2**, referred to as molecules **11-30**) were then screened against hIAPP (and later Aβ40), along with a further 10 compounds (molecules **31-40**) which have been reported previously to inhibit aggregation by other amyloidogenic polypeptides (**Chapter 5 Table 5.2**).

3 Monitoring oligomer formation from self-aggregating amylin peptides using ESI-IMS-MS

3.1 Introduction

The work described in this Chapter has been published in reference (101).

The structure of small peptide systems has been studied extensively by IMS-MS, facilitated by both their commercial availability (3, 23, 46, 101, 106, 188, 195) and the rapid and efficient nature of modern peptide synthesis methods (196). Small peptides often serve as model systems for the interactions that occur in larger proteins and protein complexes (197, 198) and enable the structural impact of alterations in protein primary sequence to be investigated (188, 196-198). In-depth IMS and modelling studies have led to the understanding of the structures adopted by peptides in the gas-phase, thus enabling comparisons to be drawn between gas- and solution-phase structures. The application of IMS methods to peptide systems is not limited to monomeric species. Indeed, many peptide sequences, particularly those implicated in amyloid disease, form large oligomeric aggregates, via self-assembly of secondary structure elements, that are amenable to study using ESI-IMS-MS (**Chapter 1 Section 1.14**). β-sheet peptide systems have been reported frequently as models for amyloid proteins, often constituting core amyloidogenic sequences from longer proteins and polypeptides (37, 199). One advantage of studying smaller peptide fragments of larger amyloid proteins by IMS is that it enables higher order oligomers to be observed, which is often not the case for the corresponding proteins from which they are derived (106). Oligomers of fibril-competent peptide fragments can be observed and monitored over time under fibril-forming conditions and their estimated CCSs compared with modelled structures to provide insights into the assembly pathways of these sequences (46, 106).

Here ESI-IMS-MS analyses of oligomers populated during the assembly of peptides from the amyloidogenic core of the human IAPP sequence are described (**Figure 3-**

1). Intact hIAPP contains several functional regions: residues 1-19 comprise the N-terminal region that is involved in membrane binding, residues 20-29 are essential for amyloidosis (200), and residues 30-37 form the C-terminal region that aids amyloid formation (109, 201) (**Chapter 1 Section 1.10**). The ability of the full-length IAPP to form amyloid fibrils in different species has been linked directly to the sequence variability of residues 20-29 ($_{20}$SNNFGAILSS$_{29}$ in hIAPP), suggesting that this region of the peptide is in part responsible for the self-aggregating properties of the polypeptide (200). This is supported by the observation that the peptide fragment 20-29 (SNNFGAILSS) is highly amyloidogenic *in vitro* and forms amyloid-like fibrils readily in isolation that have a β-sheet morphology typical of amyloid (118, 199). The shortest IAPP sequence capable of forming amyloid-like fibrils is $_{22}$NFGAIL$_{27}$, whereas the sequence $_{23}$FGAIL$_{27}$ forms short, ribbon-like structures, and the four-amino acid peptide $_{24}$GAIL$_{27}$ is not capable of fibril or higher-order aggregate formation, even at a monomer concentration of 25 mM (199).
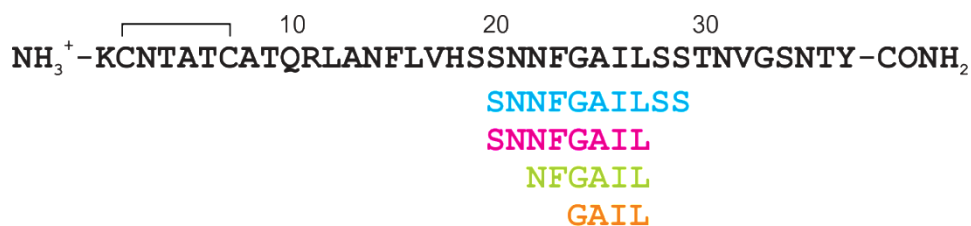
Figure 3-1. Human islet amyloid polypeptide (hIAPP) sequence and the associated peptide fragments used in this study. Residues 20–29 (SNNFGAILSS) comprise the amyloidogenic core (200) .

The interesting sequence and length dependency of amyloid fibril formation observed for IAPP and its fragments provides an ideal model system for studying the mechanism by which amyloid fibrils are formed from soluble monomers. MS-based techniques are ideally suited to separating mixtures of heterogeneous non-covalent oligomeric species in the early stages of fibril formation (6, 94) and furthermore, individual structural analysis of these oligomers is enabled using IMS-MS. Recent studies have shown that both drift tube IMS and TWIMS have the capability to evaluate the shapes of oligomeric states in amyloid proteins and

polypeptides (48, 93, 98). The shortest region of hIAPP that has been shown to form fibrils, $_{22}$NFGAIL$_{27}$, was chosen for study alongside two other amyloid competent sequences, the entire amyloid core, $_{20}$SNNFGAILSS$_{29}$ and a peptide intermediate in size, $_{20}$SNNFGAIL$_{27}$. Additionally, the tetrapeptide that is incapable of fibril formation, $_{24}$GAIL$_{27}$ was chosen as a control (**Figure 3-1**).

Characterisation of the structures of early oligomers may provide potential therapeutic targets for inhibiting the formation of amyloid fibrils in diseases such as T2DM. In this chapter, ESI-IMS-MS experiments are performed alongside conventional techniques for studying amyloid including the measurement of fibril formation kinetics using ThT fluorescence and determination of the final fibril morphology using negative stain TEM. These data combine to provide a model for the assembly mechanism of amyloid structures formed from the hIAPP core region.

3.2 Results

3.2.1 Fibril formation from IAPP peptide fragments

Four peptides from the amyloidogenic core region of hIAPP were used in this study: $H_2N\text{-}_{24}GAIL_{27}\text{-}CO_2H$ (372.2 Da), $H_2N\text{-}_{22}NFGAIL_{27}\text{-}CO_2H$ (633.4 Da), $H_2N\text{-}_{20}SNNFGAIL_{27}\text{-}CO_2H$ (834.4 Da), and $H_2N\text{-}_{20}SNNFGAILSS_{29}\text{-}CO_2H$ (1008.5 Da), purchased from Protein Peptide Research (Cambridge, UK). Self-assembly of $_{20}SNNFGAILSS_{29}$, $_{20}SNNFGAIL_{27}$ and $_{22}NFGAIL_{27}$, all known to aggregate into amyloid fibrils, was studied alongside the non-assembling tetrapeptide fragment $_{24}GAIL_{27}$ which was used as a control (**Figure 3-1**).
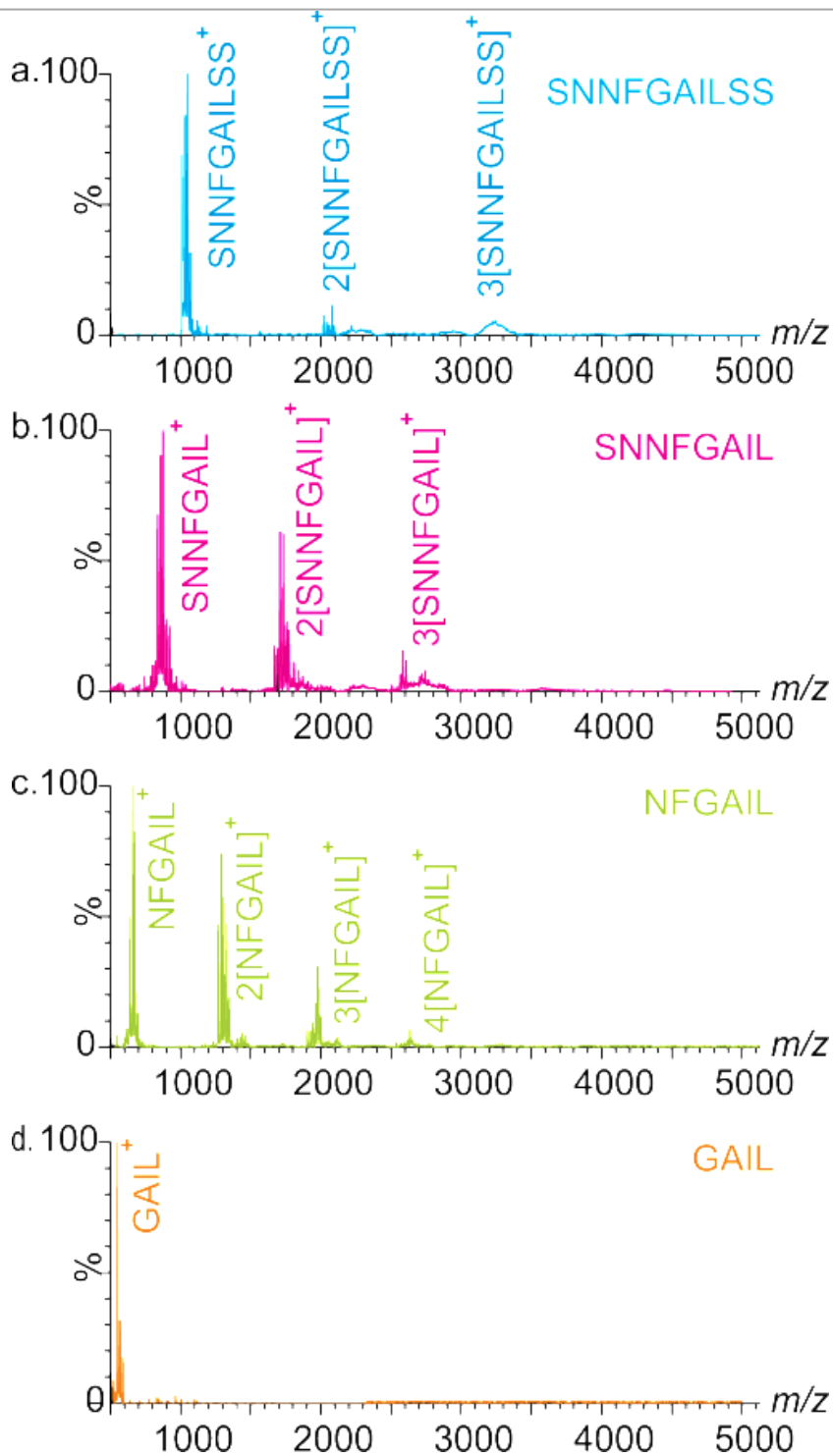
Figure 3-2. *ESI-mass spectra for (a) $_{20}$SNNFGAILSS$_{29}$, (b) $_{20}$SNNFGAIL$_{27}$, (c) $_{22}$NFGAIL$_{27}$ and (d) $_{24}$GAIL$_{27}$ demonstrating the purity of the peptides and showing the singly charged monomer (and oligomers) observed 2 min after dilution of each peptide (100 μM) into 20 mM ammonium acetate (pH 6.8, 25 °C). Oligomers are denoted as '2' for dimer, '3' for trimer and so on. All ions annotated are singly charged. Peaks are broad due to presence of sodium and potassium adducts.*

After confirming the molecular mass and purity of each of the peptides (

Figure 3-2) the generation of fibrils from solutions of the peptides in volatile, mass spectrometry-compatible solvents and buffers was verified. For this procedure, lyophilised peptides were dissolved in dimethyl sulphoxide (DMSO), used as a disaggregating solvent to avoid the presence of pre-aggregated peptide seeds (202). After 24h, the peptide solutions were diluted 50-fold with ammonium acetate (20 mM, pH 6.8) for fibril growth analyses. ThT fluorescence was used to monitor fibril growth over a 5 day period from samples contained in 96-well plates at 25 °C with agitation (600 rpm) (**Chapter 2 Section 2.4.2**), and ESI-MS spectra were acquired for each peptide during this time. After 5 days, an aliquot of each sample was removed to confirm the presence of fibrils using negative stain TEM. **Figure 3-3**a shows the time course of fibril formation for $_{20}$SNNFGAILSS$_{29}$, $_{20}$SNNFGAIL$_{27}$ and $_{22}$NFGAIL$_{27}$, monitored by the increase in the fluorescence of ThT over time. The ThT data demonstrated rapid fibril formation kinetics for each of the three IAPP peptide fragments $_{20}$SNNFGAILSS$_{29}$, $_{20}$SNNFGAIL$_{27}$ and $_{22}$NFGAIL$_{27}$ within 1-2 hours without an obvious lag-time, whilst no amyloid formation was detected for the control peptide $_{24}$GAIL$_{27}$. These results are consistent with earlier studies by Kapurniotu and co-workers (199) who reported the kinetic profiles of aggregation for these small, highly amyloidogenic peptides to proceed with negligible lag-times. Similar, rapid aggregation kinetics have been observed by others monitoring fibril growth from an hIAPP 8-37 construct (203).

Electron micrographs taken after five days of incubation confirmed the presence of polymorphic fibrillar aggregates for each of the three amyloidogenic peptides under the conditions employed (**Figure 3-3**b i-iii), and the absence of aggregated material for the control peptide, $_{24}$GAIL$_{27}$ (**Figure 3-3**b iv).
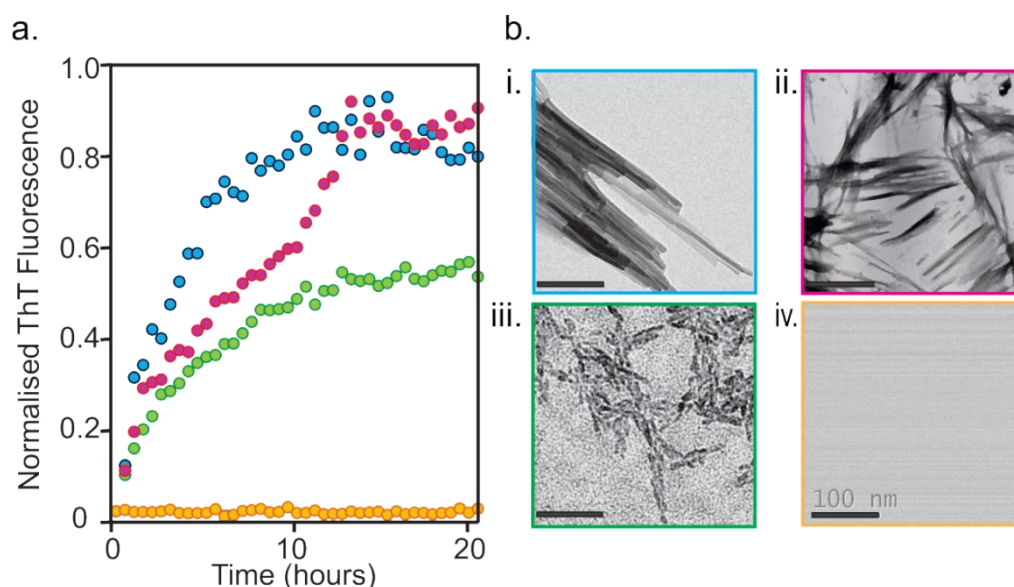
Figure 3-3. *Fibril formation from hIAPP peptide fragments. a) Monitoring amyloid fibril formation using the fluorescence of thioflavin T (ThT) for $_{20}$SNNFGAILSS$_{29}$ (blue), $_{20}$SNNFGAIL$_{27}$ (pink) and $_{22}$NFGAIL$_{27}$ (green), three self-aggregating peptide fragments from the hIAPP peptide sequence. Under the conditions used (100 µM peptide, 20 mM ammonium acetate, pH 6.8, 25 °C, 600 rpm) fibril formation reaches a maximum fluorescence in 1–2 h. The non-assembling tetrapeptide fragment $_{24}$GAIL$_{27}$ (yellow) does not form fibrils under the same conditions. The data illustrated are one representative experiment from a minimum of three independent replicates, performed in triplicate. b) Negative stain transmission electron microscopy (TEM) images of i) $_{20}$SNNFGAILSS$_{29}$ (blue), ii) $_{20}$SNNFGAIL$_{27}$ (pink) and iii) $_{22}$NFGAIL$_{27}$ (green) after 5 days under the above conditions, showing the presence of fibrillar aggregates, and of iv) $_{24}$GAIL$_{27}$ (yellow) which does not form fibrils. The scale bar=100 nm.*

3.2.2 TWIMS-MS cross-section calibration for peptide systems

As discussed in **Section 1.4**, TWIMS-MS yields ATD information, but in order to obtain CCS values, calibration of the measured ATD data using standards of known CCSs is required. The IMS-MS spectra of these calibrants must be recorded with the

same IMS parameters as the analyte (such as the height and velocity of the voltage waves), as these influence the arrival time and hence the obtained CCS (16). Determination of small peptide cross-sections by TWIMS-MS is enabled by the availability of drift tube IMS peptide CCS values obtained from tryptic digests of protein standards e.g. equine cytochrome c, which can be found in Clemmer's cross- section library (www.indiana.edu/~clemmer/Research).

Figure 3-4 shows a three dimensional Driftscope plot (*m/z vs.* drift time *vs.* intensity) of ions from equine cytochrome c following digestion with trypsin. Many tryptic peptides are detected and measured from a single digest thus enabling a peptide calibration to be achieved rapidly following analysis of a single ESI-IMS mass spectrum. Tryptic peptides are observed as singly and doubly-charged ions with a wide range of peptide sizes and yield many calibration data points that cover a wide range of reduced CCS (CCS') values (**Figure 3-4**).
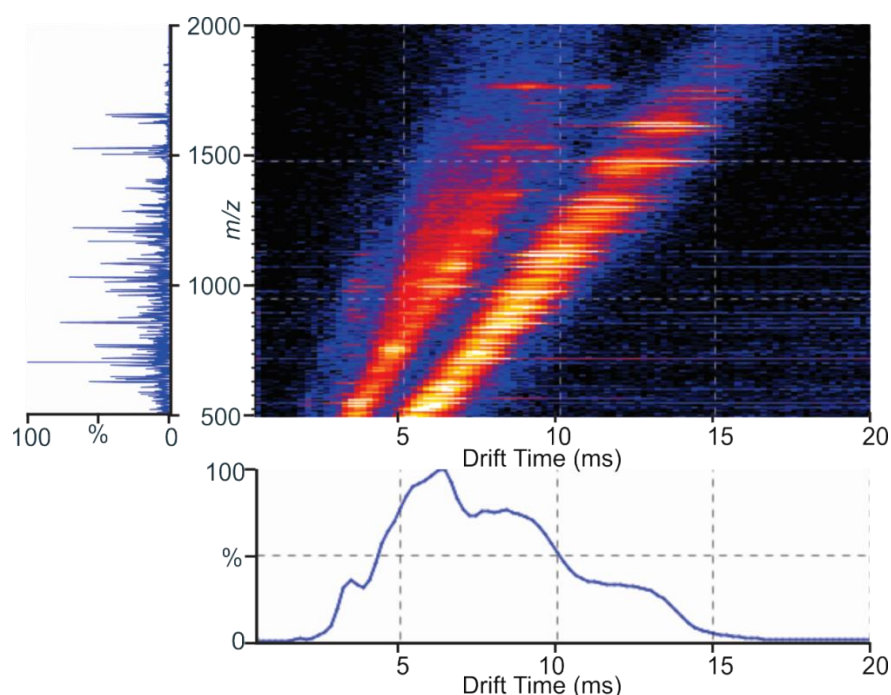
Figure 3-4. *Calibration of TWIMS-MS device three dimensional Driftscope plot (m/z vs. drift time) of ions produced from a tryptic digest of equine cytochrome c (2 hours at 37 °C using 1:50 (w/w) enzyme:substrate). The m/z spectrum is shown along the y axis, and TWIMS chromatogram along the x axis.*

61

The cytochrome c calibration shown in **Figure 3-5** covers a relatively wide range of CCS' values observed in tryptic peptides, particularly at low mobilities, subsequently facilitating the analysis of larger peptide oligomers, such as those observed during the process of amyloid fibril formation.
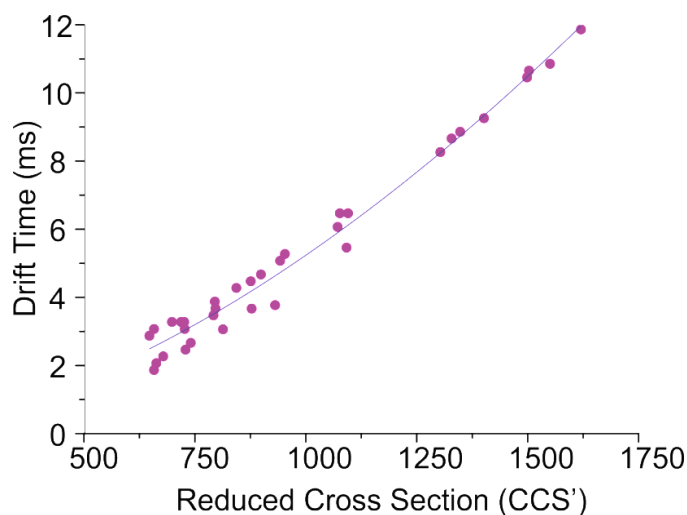
Figure 3-5. *ESI-TWIMS-MS drift time calibration curve. ESI-TWIMS-MS drift time calibration using tryptic peptides derived from equine cytochrome c, analysed using a 7-20V travelling wave ramp. An allometric (y=A'x^B) fit is applied to the data to yield reduced cross-sections from drift time measurements.*

3.2.3 ESI-IMS-MS analysis of pre-fibrillar oligomers of IAPP peptides

Having confirmed that the three self-aggregating IAPP peptide fragments could form fibrils reliably under ESI-MS-compatible solution conditions, the next step was to identify and characterise the oligomers formed during the early stages of aggregation using ESI-IMS-MS. As discussed in **Chapter 1 Section 1.14**, ESI-IMS-MS is ideally suited to the characterisation of heterogeneous, lowly-populated amyloid intermediates that are intractable by most conventional biophysical methods. **Figure 3-6** presents the ESI-IMS-MS 3D Driftscope plot (m/z vs. Drift

time vs. Intensity) for $_{20}$SNNFGAILSS$_{29}$, showing the oligomers observed 2 mins after dilution of the 10-residue peptide into 20 mM ammonium acetate (pH 6.8). ESI-IMS-MS enables separation of all the oligomers present in solution, including isobaric species which give rise to ions of the same m/z in the ESI-MS spectrum. As discussed in **Chapter 1 Section 1.4**, protein conformers of the same mass and the same charge that have different shapes (e.g. extended vs. compact conformations), will have different IMS mobility and hence different drift times. More expanded structures will experience a greater number of collisions with buffer gas molecules and therefore will have longer drift times than their more compact counterparts. In the case of oligomers with the same m/z ratio, but different mass and different charge, the most highly charged species usually has the highest mobility and hence the shorter drift time. An example of this is illustrated in **Figure 3-6** for the separation of the singly charged trimer ions, the doubly charged hexamer ions and the triply charged nonamer ions originating from $_{20}$SNNFGAILSS$_{29}$, highlighted with a yellow box. These isobaric monomeric and oligomeric ions will contribute to coincident peaks on a 2-dimensional ESI-MS spectrum (

Figure 3-2a) however, when separated by IMS and visualised on a 3-dimensional Driftscope plot (**Figure 3-6**a), they each have separate peaks that are easily distinguishable. Once separated, the oligomers can be identified by the isotopic distributions of their charge states; in this case, the nonamer, with the highest number of charges, had the shortest IMS drift time (**Figure 3-6**b).
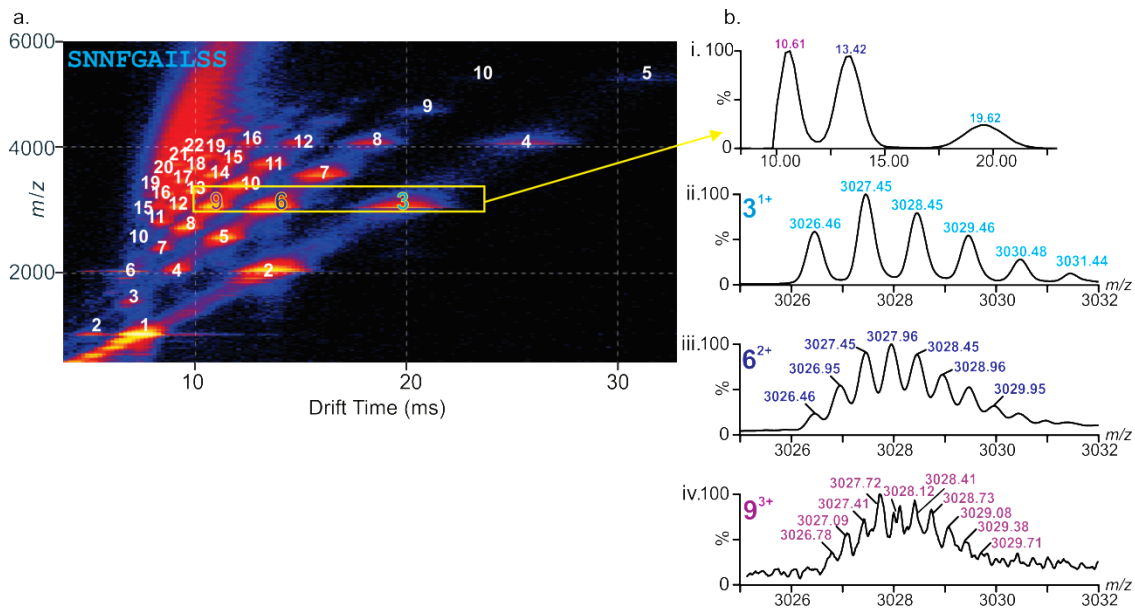
Figure 3-6. *$_{20}$SNNFGAILSS$_{29}$ forms monomer through 22-mers. a) ESI-IMS-MS 3D Driftscope plot (m/z vs. Drift time vs. Intensity) for $_{20}$SNNFGAILSS$_{29}$ showing the monomer and oligomers up to and including 22-mer. (The number adjacent to each peak represents the number of peptide subunits per oligomer e.g. 3 = trimer). b) The characterisation of oligomers contributing to the same m/z peaks is illustrated by the separation of the singly charged trimer, the doubly charged hexamer and the triply charged nonamer which generate isobaric ions at m/z 3,026-3,030. (i) the IMS-MS drift time chromatogram of m/z 3026.6 shows three peaks with drift times of 10.61, 13.42 and 19.62 ms; m/z spectra of the three peaks extracted from the driftscope chromatogram are shown in (ii) 19.62 ms, (iii) 13.42 ms, and (iv) 10.61 ms. The peaks are identified by their isotopic distributions; the peak with the shortest drift time corresponds to the triply charged nonamer (9^{3+}), as these ions have the highest number of charges and hence the highest mobility.*

The Driftscope plots (**Figure 3-7**) of the three fibril-competent peptides $_{20}$SNNFGAILSS$_{29}$, $_{20}$SNNFGAIL$_{27}$ and $_{22}$NFGAIL$_{27}$ and the non-amyloid control petide, $_{24}$GAIL$_{27}$, show the oligomers observed 2 mins after dilution into 20 mM ammonium acetate buffer, pH 6.8, concurrent with fibril formation for the amyloid competent sequences. For $_{20}$SNNFGAILSS$_{29}$, $_{20}$SNNFGAIL$_{27}$ and $_{22}$NFGAIL$_{27}$, oligomers in excess of the 20-mer were observed. For all oligomers observed using ESI-IMS-MS, their CCS values were estimated from their drift times by use of the calibration approach described in **Chapter 1 Section 1.4** . The IMS device was calibrated, as discussed in **Chapter 1 Section 1.4,** using denatured proteins (cytochrome c, lysozyme, myoglobin and ubiquitin) and a range of peptide ions (generated by trypsin proteolysis of cytochrome c and alcohol dehydrogenase) whose CCS values have been determined previously using conventional drift tube

IMS-MS (20, 188). The determined CCS values are shown in Table 3.1 for the peptides $_{20}$SNNFGAILSS$_{29}$, $_{20}$SNNFGAIL$_{27}$, and $_{22}$NFGAIL$_{27}$. The drift times observed for different oligomeric species formed from the three peptides throughout fibril assembly were within 1 % of those measured after t = 2 min, suggesting that the oligomers do not undergo any significant structural rearrangement that results in a significant change to their CCS during the assembly process. The absolute errors on the CCS estimations are ~5-8% (16, 20), however the replicated experimental values typically vary by <1%.
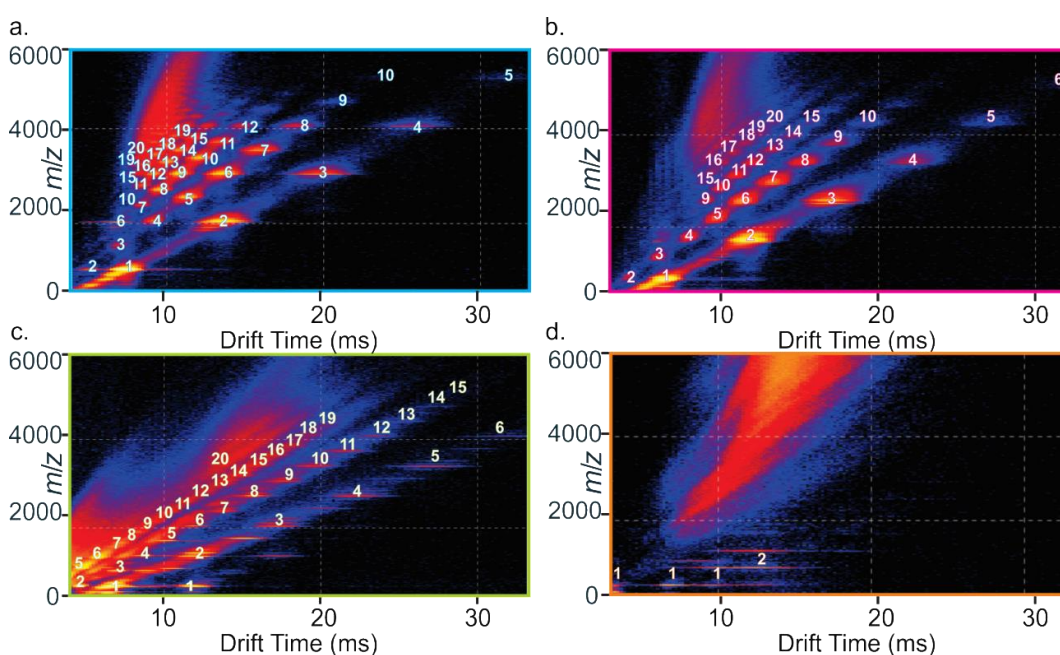
Figure 3-7. *ESI-IMS-MS 3D Driftscope plots (m/z vs. Drift time vs. Intensity) for a) $_{20}$SNNFGAILSS$_{29}$, b) $_{20}$SNNFGAIL$_{27}$, c), $_{22}$NFGAIL$_{27}$ and d) $_{24}$GAIL$_{27}$ showing the oligomers observed 2 mins after dilution of each peptide (100 μM) into 20 mM ammonium acetate (pH 6.8, 25 °C, 600 rpm). The number adjacent to each peak represents the oligomer order.*

In some cases, more than one peak was detected for a single charge state of a specific oligomer, indicating that this oligomer populates multiple conformers, each of which can be distinguished by IMS separation and hence they have a distinct CCS. The estimated CCSs of each species detected are shown in **Table 3.1** and are plotted *vs.* oligomer order in **Figure 3-8**.

a)

Oligomer Order	Charge State	Cross Sectional Area ($Å^2$)	Oligomer Order	Charge State	Cross Sectional Area ($Å^2$)
1	1	249.0	10	3	967.1
2	1	341.2	10	4	1010.0
3	1	406.8	11	3	1014.5
3	2	500.2	11	4	1054.9
4	1	460.3	12	4	1118.1
4	2	562.8	13	4	1165.6
5	1	501.1	13	5	1202.2
5	2	626.7	14	4	1218.2
6	2	682.0	14	5	1250.0
6	3	737.3	15	5	1295.5
7	2	736.4	16	5	1355.3
7	3	801.7	17	5	1406.9
8	2	782.1	18	5	1441.6
8	3	860.4	19	5	1503.4
9	4	914.3	20	5	1566.9
9	3	957.5			

b)

Oligomer Order	Charge State	Cross Sectional Area ($Å^2$)	Oligomer Order	Charge State	Cross Sectional Area ($Å^2$)
1	1	241.0	12	3	973.3
2	1	321.5	12	3	1007.7
3	1	382.4	13	3	1018.7
4	1	431.5	13	3	1031.5
5	1	471.8	14	3	1056.1
5	2	571.2	14	3	1073.2
6	2	627.2	15	4	1097.4
7	2	678.3	15	4	1124.2
8	2	724.5	16	4	1134.6
8	2	768.2	16	4	1182.6
9	2	767.0	17	4	1172.6
9	2	810.8	17	4	1218.2
10	3	805.0	18	4	1272.5
10	3	865.8	19	4	1296.0
11	3	844.4	20	4	1356.3
11	3	921.7			

c)

Oligomer Order	Charge State	Cross Sectional Area ($Å^2$)	Oligomer Order	Charge State	Cross Sectional Area ($Å^2$)
1	1	201.6	13	2	856.7
2	1	283.8	14	2	835.9
3	1	334.1	14	3	889.0
4	1	382.1	15	3	854.6
5	1	421.3	15	3	928.9
6	1	452.4	16	3	971.0
7	1	482.9	17	3	1002.4
7	2	567.9	18	3	1041.9
8	2	617.4	18	3	1103.7
9	2	656.4	19	3	1066.8
10	2	701.3	19	4	1129.8
11	2	735.0	20	4	1111.3
12	2	770.3	20	4	1152.5
13	2	805.2			

Table 3.1. *Collision cross-sectional areas of a) $_{20}SNNFGAILSS_{29,}$ b) $_{20}SNNFGAIL_{27}$, and c) $_{22}NFGAIL_{27}$ peptide oligomers (25 °C, 20 mM ammonium acetate, pH 6.8) detected by ESI-IMS-MS.*

66
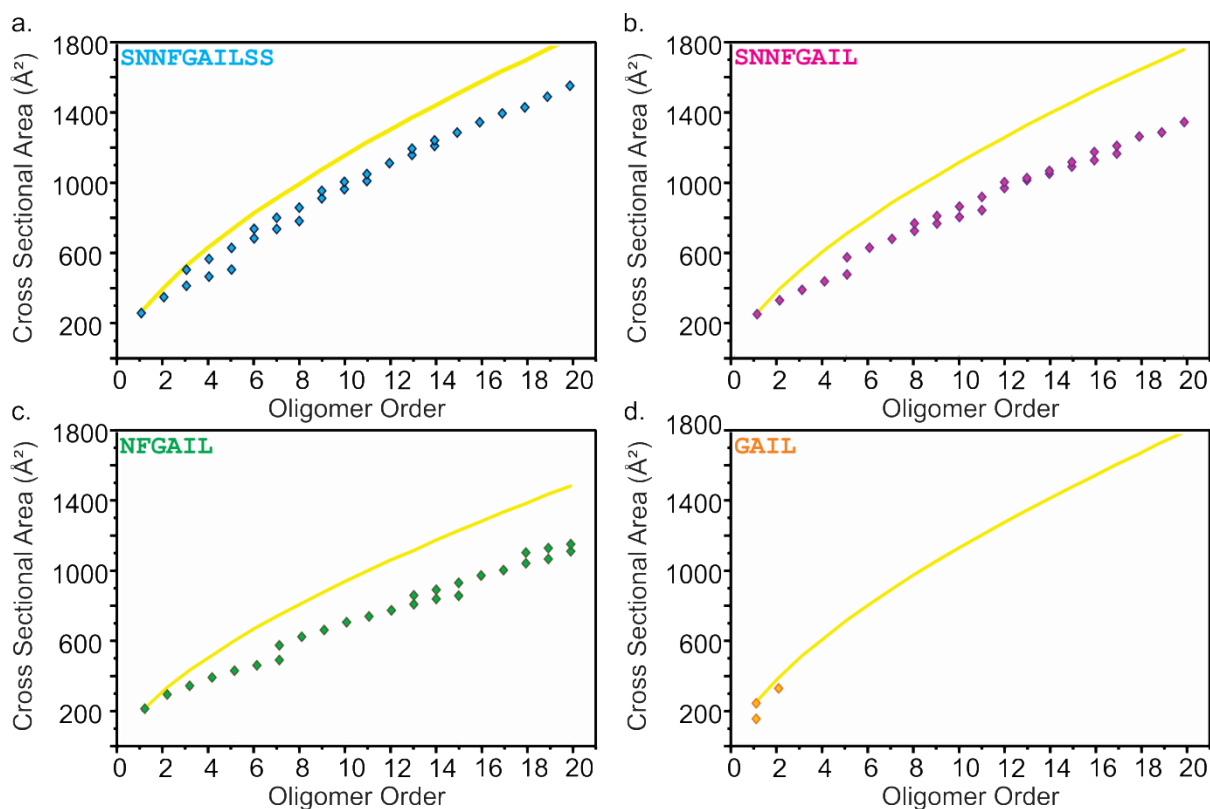
Figure 3-8*. Collision cross-section (CCS) vs. oligomer order detected for the peptides a) $_{20}$SNNFGAILSS$_{29}$, b) $_{20}$SNNFGAIL$_{27}$, c) $_{22}$NFGAIL$_{27}$, and d) $_{24}$GAIL$_{27}$. For the non-amyloidogenic peptide (d) $_{24}$GAIL$_{27}$, only the monomer and dimer are observed. The yellow line in each case represents the isotropic fit (based on the CCS of the monomer scaled by $n^{2/3}$, where n=number of peptide subunits per oligomer(46)).*

Figure 3-8 also shows an estimation of the CCS increase with molecular weight expected for the peptides calculated based on isotropic growth, in which the CCS scales from the monomer value by a factor of $n^{2/3}$ (where n is the number of peptide subunits per oligomer (46)). For all three of the fibril-competent peptides, the oligomers observed are of smaller CCS than that expected for a globular growth pattern. This result suggests that monomer units are densely packed within oligomeric species, and most likely highly ordered. The observed compactness could be a result of conformational transitions at distinct points in the aggregation pathway or the coming together of hydrophobic oligomers resulting a dense arrangement of pre-fibrillar units within a fibril. The pattern by which CCS increases with increasing oligomer order is interesting: the oligomers appear to

67

extend steadily up to a certain point before taking a step-up in size, rather than gradually increasing in CCS as oligomerisation proceeds. For example, in the case of $_{20}$SNNFGAIL$_{27}$, there is a gradual increase in CCS between monomer and pentamer; the pentamer populates two conformers, the more extended of which is the first in a new series of oligomers (pentamer to octamer), before another step up in CCS is observed. Similar step-wise self-assembly patterns were observed for the other fibril-forming peptides, $_{20}$SNNFGAILSS$_{29}$ and $_{22}$NFGAIL$_{27}$ (**Figure 3-8**a-c). The three amyloidogenic hIAPP fragments studied here exhibit transitions similar to those observed for the insulin, sup 35 and IAPP derived peptides (VEALYL, NNQQNY and SSTNVG), studied by the Bowers group (46). One explanation for the progressive behaviour observed could be the gradual transition from unstructured oligomers to β-sheets with increasing oligomer size due to increasing β-sheet content. Importantly, no oligomers higher than the dimer were detected for the non-aggregating peptide, $_{24}$GAIL$_{27}$, supporting the notion that the gas-phase oligomers observed are involved in amyloid formation.

The detection of a wide range of oligomers, each one differing from the next by a single monomer subunit, is consistent the growth mechanisms reported for other amyloid systems, for example β$_2$-microglobulin (β$_2$-m) (93) and Aβ40 (100) under certain pH and buffer conditions. In the case of β$_2$-m, at pH 3.6 and with increased ionic strength (17 μM protein at 37 °C in 150 mM ammonium formate), high-order oligomers up to at least 14-mer are observed during worm-like fibril formation (94). In the case of Aβ40, when studied by positive mode ESI-TWIMS–MS at high peptide concentrations and near-neutral pH (200 μM peptide in 10 mM ammonium acetate, pH 7.4), oligomeric species from monomer to 13-mer inclusive, together with higher order species have been observed (100). These observations are in contrast with results obtained for both β$_2$-m and Aβ40 under different conditions. Under long straight fibril-forming conditions (17 μM protein at 37 °C in 100 mM ammonium formate, pH 2.5), oligomers only as large as the tetramer have been detected for β$_2$-m (93, 94). For Aβ40 and Aβ42, assembly routes comprised of dimer and tetramer and no higher order species, and a dimer, tetramer, hexamer and dodecamer, respectively, have also been described (98).

The latter experiments were performed using negative mode ESI with a conventional drift tube (30-40 μM peptide in 25 mM ammonium acetate, pH 7.4).

In the case of larger peptides and proteins, the critical nucleus required before the final re-organisation into amyloid fibrils and the mechanism of assembly into higher order structures remain elusive. Here, using short peptide fragments derived from full length amyloid sequences, we are able to observe higher order oligomeric structures thus enabling modelling of potential assembly mechanisms, providing insights into the amyloid assembly cascade.

3.2.4 Molecular modelling of potential oligomer structures

The work presented in this section was performed by Hlengisizwe Ndlovu (School of Physics & Astronomy, University of Leeds).

As discussed in **Chapter 1 Section 1.14,** Bowers and co-workers reported recently the use of ESI-IMS-MS to determine oligomer cross-sections for a range of short-chain peptides (46, 106). A conventional drift tube IMS-MS (rather than TWIMS-MS) based study of amyloidogenic peptide sequences VEALYL, NNQQNY and SSTNVG derived from the amyloid proteins insulin, yeast sup 35 and hIAPP respectively, reported transitions from unstructured conformers to structured β-sheet oligomers (46). It was suggested that for fibril-competent peptide sequences, oligomers grow isotropically (i.e. equal growth in every dimension) up to a certain oligomer order (depending on the peptide sequence). After this point, larger structures emerge which are not consistent with isotropic self-assembly leading to a hypothesis that conformational transitions form isotropic to β-sheet-containing structures occur at different oligomer orders for different peptide systems (**Chapter 1 Section 1.14, Figure 1-15**).

In order to probe the growth mechanism observed for the hIAPP peptide fragments studied here using ESI-IMS-MS, molecular modelling was performed. The NAB molecular building tool was employed to construct β-sheet model oligomers of $_{20}$SNNFGAILSS$_{29}$ from a fibril structure of this peptide obtained from

solid state NMR (ssNMR) measurements (204). This ssNMR study hypothesised that the fibril spine consists of two β-sheet layers arranged face-to-face, with parallel hydrogen-bonded peptide β- strands within each sheet (204). On the contrary, other ssNMR studies have shown that the fibril structure is anti-parallel, while others report both parallel and anti-parallel structures (88), demonstrating the polymorphic nature of this region of hIAPP (204).

Singly, doubly, triply and quadruply stacked β-sheet model structures were generated for each oligomer order of $_{20}$SNNFGAILSS$_{29}$ between monomer and 30-mer. CCS values of the model structures were determined using a projection approximation (20). **Figure 3-9** shows the CCS values of β-sheet models for the $_{20}$SNNFGAILSS$_{29}$ oligomers of different mass. Comparison of the modelled structures with experimentally determined CCS values of $_{20}$SNNFGAILSS$_{29}$ indicates that the CCS data points obtained experimentally do not wholly fit with any one of the β-sheet models. Instead, the overall model of best fit involves a combination of the constructed β-sheet models. The obtained CCS values are consistent with a single β-sheet model between monomer and pentamer, a double β-sheet model between pentamer and decamer, a triple β-sheet model between decamer and 15-mer, and a quadruple β-sheet between 15-mer and 20-mer, as illustrated in **Figure 3-9**. The modelled β-sheet structures are all more compact than the isotropic growth model, and the ESI-IMS-MS data indicate that all oligomers above the pentamer are significantly more compact than the single β-sheet model. Together, these observations suggest that the peptides are arranging into a densely packed structure from which fibril elongation proceeds.
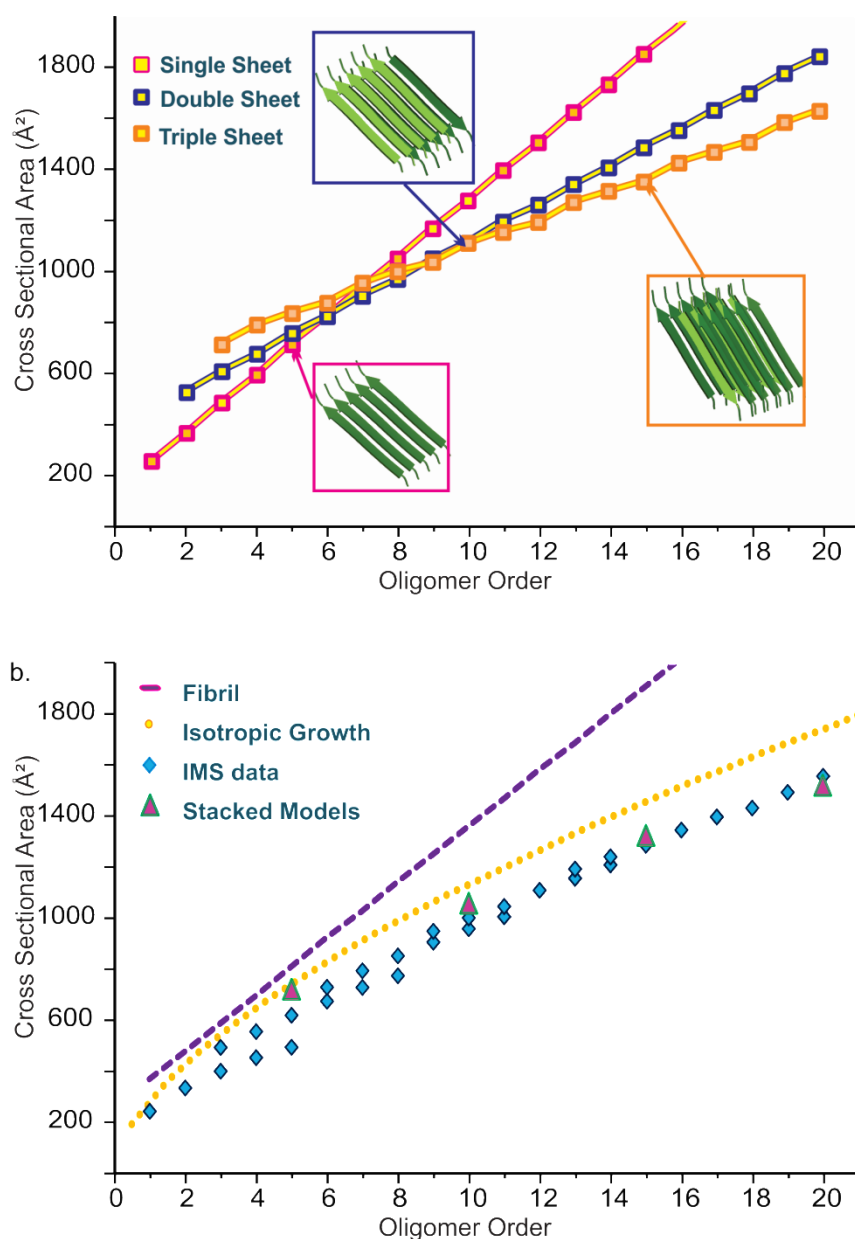
Figure 3-9*. Molecular models for hIAPP peptide oligomers a) Theoretical β-sheet models showing CCSs vs. oligomer order for the $_{20}$SNNFGAILSS$_{29}$ peptide. The structures are based upon ssNMR data of the $_{20}$SNNFGAILSS$_{29}$ peptide (204). β-sheet models were built using the NAB molecular building tool. Transformations and duplications of the structure were performed to produce single, double, triple and quadruple stranded β-sheet fibrils. b) The assembly of $_{20}$SNNFGAILSS$_{29}$ oligomers observed during fibril growth (blue diamonds) using ESI-IMS-MS is compared with the isotropic growth prediction (gold dotted line), and a predicted stacked fibril assembly (cf. Bowers et al. model where the distance between each oligomer is dimer-monomer CCS (46)) (purple dashed line). The theoretical β-sheet models are shown (red triangles) as follows: single sheet pentamer, double sheet decamer, triple sheet 15-mer and quadruple sheet 20-mer.*

Time course ESI-IMS-MS experiments were performed in order to gain measurements of oligomer CCS values for $_{20}$SNNFGAILSS$_{29}$, $_{20}$SNNFGAIL$_{27}$ and $_{22}$NFGAIL$_{27}$ over the course of fibril assembly. All of the CCSs determined for the three peptides measured over the 20 h time course of assembly were within 1 % of those measured at t = 2 min, suggesting that there is no gross structural rearrangement within the oligomers as fibrillation proceeds. This is in contrast with other published ESI-IMS-MS studies that demonstrate conformational rearrangement within amyloid oligomers over the course of assembly. For example, during the lag phase of amyloid assembly by β$_2$-microglobulin, trimeric and tetrameric oligomers become more compact and less amenable to subunit exchange (93).

3.3 Discussion

The data presented in this chapter show the applicability of TWIMS-MS to the study of both peptide structure and amyloid self-assembly. Measurement of CCS values for peptide oligomers is facilitated by the availability of conventional drift tube IMS data on denatured proteins and tryptic peptides of commercially available proteins. The applicability of TWIMS-MS to non-covalent systems makes it ideally suited to the interrogation of the oligomers occupied during amyloid fibril assembly, in terms of their relative abundances, sizes and conformations. Comparison with coarse-grain molecular models enables experimentally derived CCS values to be compared with known structures and assigned to potential growth models. TWIMS enables the observation of multiple lowly populated oligomeric states present within heterogeneous mixtures in a single spectrum thus providing multiple CCS data points for comparison with modelled structures.

In the case of the three amyloidogenic hIAPP fragments studied here, observed CCS values are consistent with single β-sheet models for low order oligomers whilst higher order oligomers are consistent with stacking of multiple sheets. Insights into the detailed mechanism of aggregation are enabled by observation and interrogation of higher order oligomeric states, particularly in $_{20}$SNNFGAILSS$_{29}$,

where oligomers up to and including n= 22 are observed. TWIMS-MS-derived CCS values indicate that initial assembly proceeds in one dimension via the formation of a single β-sheet, while two dimensional self-assembly occurs in higher-order oligomers at specific oligomer orders, observed as a separate oligomeric species that increase in size in a step-wise manner.

This study highlights the power of TWIMS-MS for studying the mechanism of self-assembly for amyloid systems, since all components of a complex mixture can be observed and their CCS measured in a single experiment. It also highlights the benefits of studying peptides as model systems for the study of protein self-assembly, given that high order species can be observed in the gas phase and growth mechanisms deduced as a result. The work in this chapter shows that when ESI-TWIMS-MS is performed in conjunction with coarse-grained modelling, a comprehensive picture of the aggregation process in self-assembling peptide systems can be gained. Application of these methods to full-length amyloidogenic peptides and proteins under physiological conditions may enable a greater understanding of the elusive mechanisms that underlie amyloid assembly. This remains a challenge, given the difficulty of maintaining non-covalent, hydrophobic interactions in the absence of solvent. Studies of intact hIAPP, Aβ40 and variants of these sequences are described in the following chapters.

4 Ion mobility spectrometry - mass spectrometry defines the oligomeric intermediates in amylin amyloid formation and the mode of action of inhibitors

4.1 Introduction

The work described in this Chapter has been published in reference (102).

In order to gain an understanding of the aggregation process of amyloid-prone peptides and proteins, the nature of oligomeric intermediates populated on- (or off-) pathway to fibrils must be interrogated. In **Chapter 3**, the high order oligomers of short peptide fragments from the amyloid core of hIAPP were investigated. Here, by exploiting the separative and investigative powers of MS coupled with IMS and CID-MS/MS, higher order oligomeric states populated by full-length, 37-residue hIAPP and rIAPP petides are described and their CCS, growth mechanism and relative gas-phase stabilities are elucidated. rIAPP is used throughout this chapter as a non-amyloidogenic control peptide, given that it is unable to fibrillate under any previously characterised conditions and rodents do not develop T2DM (114).

Previous IMS-MS-based studies have proposed structural models for the IAPP monomer (48) and dimer (47), as well as the oligomers formed during self-assembly of peptides derived from an amyloidogenic core sequence (20–29) of hIAPP (101) (**Chapter 3**). Using IMS-MS and replica-exchange molecular dynamics (REMD) simulations, Dupuis *et al.* proposed that full-length monomeric hIAPP occupies at least two conformations; both a helix–coil conformation and an extended β-hairpin conformation that has a significantly (18%) larger CCS (48). The extended hairpin structure was not significantly populated by the non-amyloidogenic rIAPP peptide, leading to the conclusion that this conformer is an amyloid precursor. In a second study, Dupuis *et al.* investigated and compared the dimeric structures populated by hIAPP and rIAPP, using IMS-MS. These data revealed that the hIAPP dimers observed are significantly more extended than

those observed for rIAPP, indicative of a higher percentage of β-sheet content formed by the assembly of extended β-hairpin-containing monomers (47). These two studies led to a proposal that a conformational transition to β-sheet-rich conformers is an early step in hIAPP self-assembly, by contrast with other reports which have suggested a transition to amyloid via helix-rich oligomers (205, 206). None of these studies, however, reported the detection or identification of higher order species. Here, hIAPP and rIAPP oligomers, monomer through hexamer, inclusively, for both peptides are described. Their relative gas phase stabilities are also investigated and the factors that determine their marked difference in amyloid propensity are discussed.

4.2 Results

4.2.1 hIAPP forms an array of oligomers early in amyloid assembly

Prior to analysis using ESI-IMS-MS, lyophilised, synthetic hIAPP and rIAPP peptides (**Figure 4-1**a) were each dissolved in 100% DMSO, to remove any pre-formed aggregates (207), for 24 h at 37 ℃. The sample was then diluted 100-fold into 20 mM ammonium acetate, pH 6.8. The distribution of oligomeric species was analysed immediately (time = 2 mins), and at various time points after dilution, using ESI-IMS-MS.

As described in **Chapter 1 Section 1.14**, ESI-IMS-MS is ideally suited to the characterisation of heterogeneous, lowly-populated, transient amyloid precursors. Previous studies (205, 208, 209) have proposed the existence of oligomeric states for hIAPP (and rIAPP) peptides. However, to date, no study has separated and/or characterised these species in detail. The data obtained using ESI-IMS-MS (**Figure 4-1**b), showed that oligomers up to, and including, hexamers are formed within 2 min of dilution of hIAPP into buffer. Here, co-populated oligomeric ions with the same *m/z* have been separated and identified individually (e.g. dimer^{3+} and tetramer^{6+}) (**Figure 4-1**b).

Consistent with previous studies from Bowers and co-workers (47, 48), multiple charge states, predominantly doubly and triply charged, and different conformers, both compact and expanded for each charge state, are observed for the hIAPP monomer. The doubly charged monomer ions, for example, occupy two distinct peaks in the IMS-MS spectrum (**Figure 4-1**b) with drift times of 7.6 and 10.6 ms. By use of the calibration approach described in **Chapter 1 Section 1.4**, the CCS of each distinct conformation can be individually assigned (**Table 4.1**). Indeed, the two conformers of the doubly charged monomer ions have CCS values that differ by ~15% (consistent with previous results by Bowers *et al.* of ~18 % (48)). Although less well-resolved, the monomer 3+ ions also exhibit two distinct

conformations, with drift times of 6.0 and 8.0 ms, ~14% different in CCS (~680 and 790 Å^2, respectively). Oligomers of hIAPP also populate a range of charge states and conformations (**Figure 4-1**), for each of which the CCS was determined (**Table 4.1**).
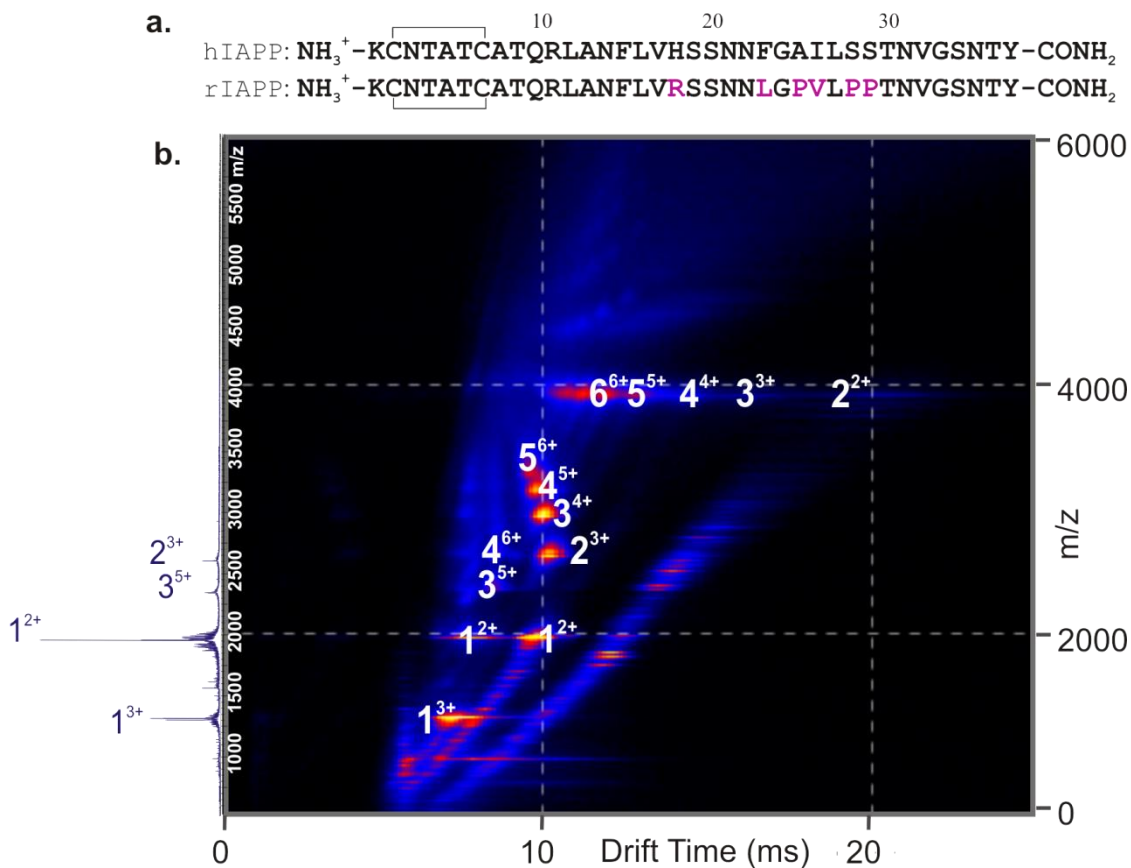
Figure 4-1. *hIAPP forms an array of oligomeric species during fibril formation. a) Comparison of hIAPP and rIAPP sequences. Both peptides have a disulfide bridge between Cys-2 and Cys-7 and have an amidated C-terminus. Residues that differ from those of the human peptide are colored pink in the rat sequence. b) ESI-IMS-MS driftscope plot of the hIAPP oligomers present 2 min after diluting the monomer to a final peptide concentration of 50 µM in 20 mM ammonium acetate, pH 6.8, 1% (v/v) DMSO. ESI-IMS-MS Driftscope plots show IMS drift time versus m/z versus intensity (z = square root scale) and the corresponding mass spectrum is shown on the left hand side. Numbers adjacent to peaks denote oligomer order, with the positive charge state of each oligomer ions in superscript. The ESI mass spectrum shows the +2 and +3 charge state ions of hIAPP monomer (labelled 1) and minor amounts of dimer and trimer (labelled 2 and 3, respectively).*

Oligomer Order	Charge State	hIAPP CCS (Å^2)	rIAPP CCS (Å^2)
1	2	513.3 (i)	509.7 (i)
1	2	606.1 (ii)	575.6 (ii)
1	3	681.6 (i)	737.3
1	3	790.4 (ii)	n/a
2	3	948.0 (i)	890.0 (i)
2	3	1019.8 (ii)	1037.7 (ii)
3	4	1252.3	1178.4
3	5	1346.3	1346.4
4	5	1537.7	1463.9
4	6	1614.7	1626.8
5	7	1927.7	1912.1
6	8	2202.6	2311.0

Table 4.1. *Experimental CCS values of hIAPP and rIAPP oligomers. CCS of hIAPP and rIAPP oligomers measured using ESI-IMS-MS (50 μM peptide), observed after 2 min incubation (37 ℃, 600 rpm, 20 mM ammonium acetate buffer, pH 6.8). Experimental error is estimated to be ± 5-8 % for all cross sections measured by use of an IMS-MS calibration (16). (i) and (ii) denote different conformers of the same ion.*

Ionic strength plays a pivotal role in determining aggregation propensities of numerous amyloid systems (210-214). Similarly, previous studies have shown that increased ionic strength increases the rate of aggregation of hIAPP (210). Consistent with these previous data, under the conditions employed, an enhanced rate of amyloid fibril formation is observed for hIAPP as the ionic strength is increased from 20 to 500 mM (**Figure 4-2**a), as determined by ThT fluorescence.

To investigate whether the formation and subsequent disappearance of oligomers of hIAPP is concomitant with the peptide assembling into amyloid fibrils, oligomerisation was studied at varying ionic strengths of the buffer, with all other conditions unchanged. The ionic-strength dependency of oligomer formation observed using ESI-IMS-MS was then compared with the rate of fibril formation, measured using ThT fluorescence. As the ionic strength of the buffer was increased, a more rapid decrease in oligomer signal intensity over time was also detected using ESI-IMS-MS (**Figure 4-2**c), concomitant with the abolishment of a lag phase of fibril assembly. This result is consistent with the oligomers observed being involved in assembly into amyloid. The gross morphology of the final fibrils

(i.e. long, straight, typical amyloid fibrils) was unchanged under all buffer conditions employed (a representative TEM image is shown (**Figure 4-2**b).

As discussed in **Chapter 1 Section 1.4** CCS values for all hIAPP oligomers observed were estimated from the ESI-IMS-MS arrival time distributions. In order to probe the structural properties of these species, their experimentally determined CCS values were compared with CCS values estimated for theoretical models including a fit assuming isotropic growth (46), a globular fit based on the average density of a protein under similar conditions (0.44 Da/$Å^3$) (62, 215) and a 'fibril' model that assumes growth in a single dimension (46). Comparison of the determined CCS values with gross structural models (**Chapter 1 Section 1.14**) suggests that hIAPP oligomers ≥4-mer in size adopt relatively extended conformations i.e. when hIAPP oligomers grow beyond a tetramer, the measured CCS values cannot be explained by isotropic or spherical growth (**Figure 4-2**d). Further, the size, order and CCS of the oligomers observed are independent of ionic strength (**Figure 4-2**d), despite being formed and consumed at different rates. These data suggest that hIAPP oligomers form relatively elongated structures, particularly at higher orders (≥4-mer). A degree of order is likely, however, given that given that the number of charges carried by each oligomer is never significantly more than its number of monomer subunits. Occupying highly unstructured conformations would result in oligomers to carrying a larger number of charges (216).
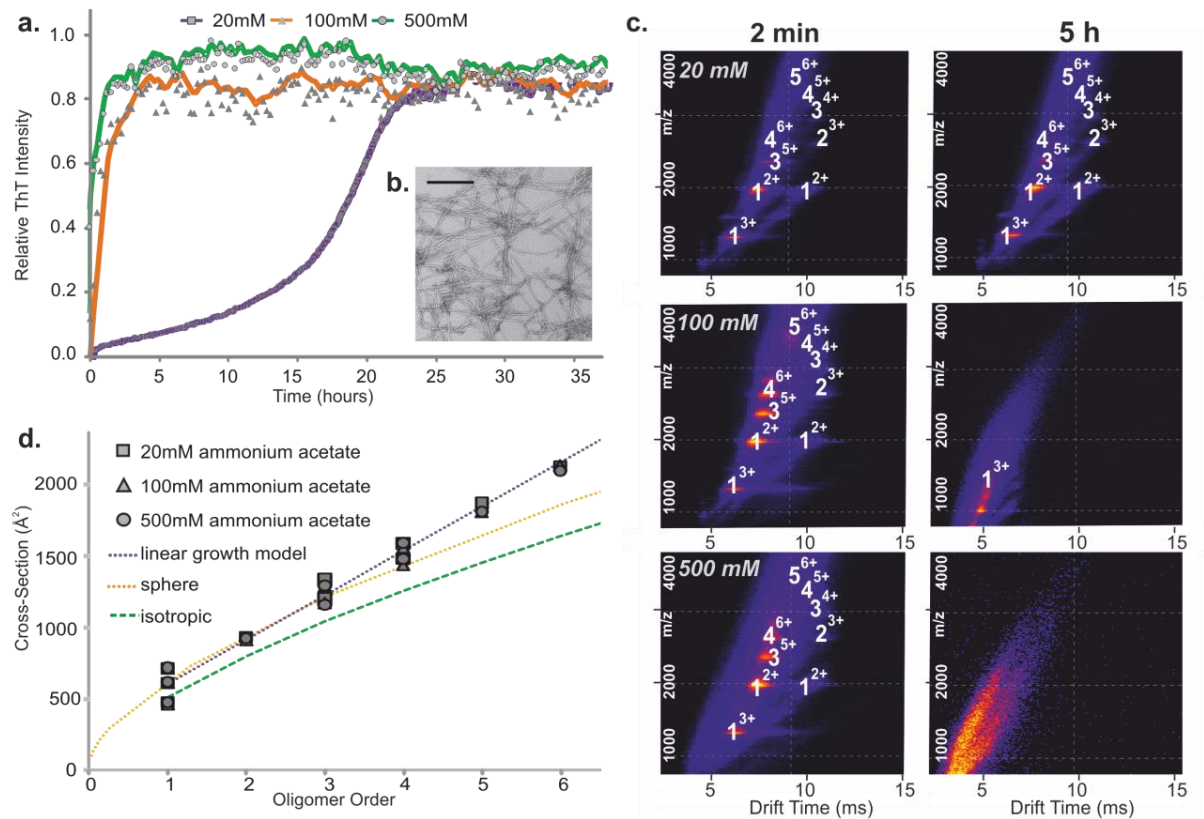
Figure 4-2. *Dependence of hIAPP oligomer and fibril formation on ionic strength. a) ThT fluorescence intensity of hIAPP (50 μM peptide, 37 ℃, 600 rpm) in 20 mM (squares/purple line), 100 mM (triangles/orange line) or 500 mM (circles/green line) ammonium acetate buffer, pH 6.8. A typical data set is shown, the experiment was performed over 5 replicates. b) The inset shows a representative negative stain TEM image of hIAPP fibrils after 5 days in 100 mM buffer (37 ℃, 600 rpm) (scale bar = 100 nm). c) ESI-IMS-MS driftscope plots of hIAPP oligomers present at t= 2 min (left hand side) and t = 5 hours (right hand side) at different ionic strengths (20 mM, 100 mM and 500 mM). d) CCSs of hIAPP oligomers measured using ESI-IMS-MS plotted versus oligomer order showing that oligomers have the same CCS regardless of ionic strength: 20 mM (squares), 100 mM (triangles) and 500 mM (circles). The orange dashed line represents a globular fit based on the average density of a protein (0.44 Da/Å³) (215); the grey dashed line represents a linear growth model (46) and the green dashed line represents an isotropic growth model (46).*

4.2.2 Non-amyloidogenic rIAPP forms a similar array of oligomers to hIAPP

As discussed in **Chapter 1 Section 1.11**, rIAPP does not form ordered amyloid fibrils under any previously characterised conditions (109). Despite its lack of amyloidogenicity, using ESI-IMS-MS, a similar array of oligomers for rIAPP was observed compared with that detected for hIAPP (**Figure 4-3**a, **Table 4.1**). Indeed, oligomers corresponding to monomer through hexamer, inclusively, were observed for the rIAPP peptide within 2 mins of dilution into buffer. Consistent with the data for hIAPP, multiple conformers are observed for the rIAPP monomer and oligomers, albeit at different relative intensities compared with those observed for hIAPP. Importantly, hIAPP monomer and oligomers consistently occupy a greater relative proportion of more expanded conformers than rIAPP (**Figure 4-4**).

Although rIAPP has been reported previously not to form amyloid fibrils (109), turbidity measurements (**Figure 4-3**b) and TEM images (**Figure 4-3**c) demontrates that under the conditions employed here (20 mM ammoumium acetate, pH 6.8, 1% DMSO (*v/v*)) rIAPP forms small globular aggregates that scatter light. Despite some aggregation, the inability of rIAPP to form amyloid under the conditions employed was confirmed by the lack of fibrils observed using TEM (**Figure 4-3**c) and the lack of ThT fluorescence increase over a 20 h incubation period (**Figure 4-3**d).

The rIAPP oligomers observed are similar in CCS, as well as size and mass, to those of hIAPP (**Table 4.1**, **Figure 4-4** & **Figure 4-5**). The vastly different amyloid competencies of the two sequences, therefore, is not solely dependent on having oligomers of different numbers of subunits and/or CCS.
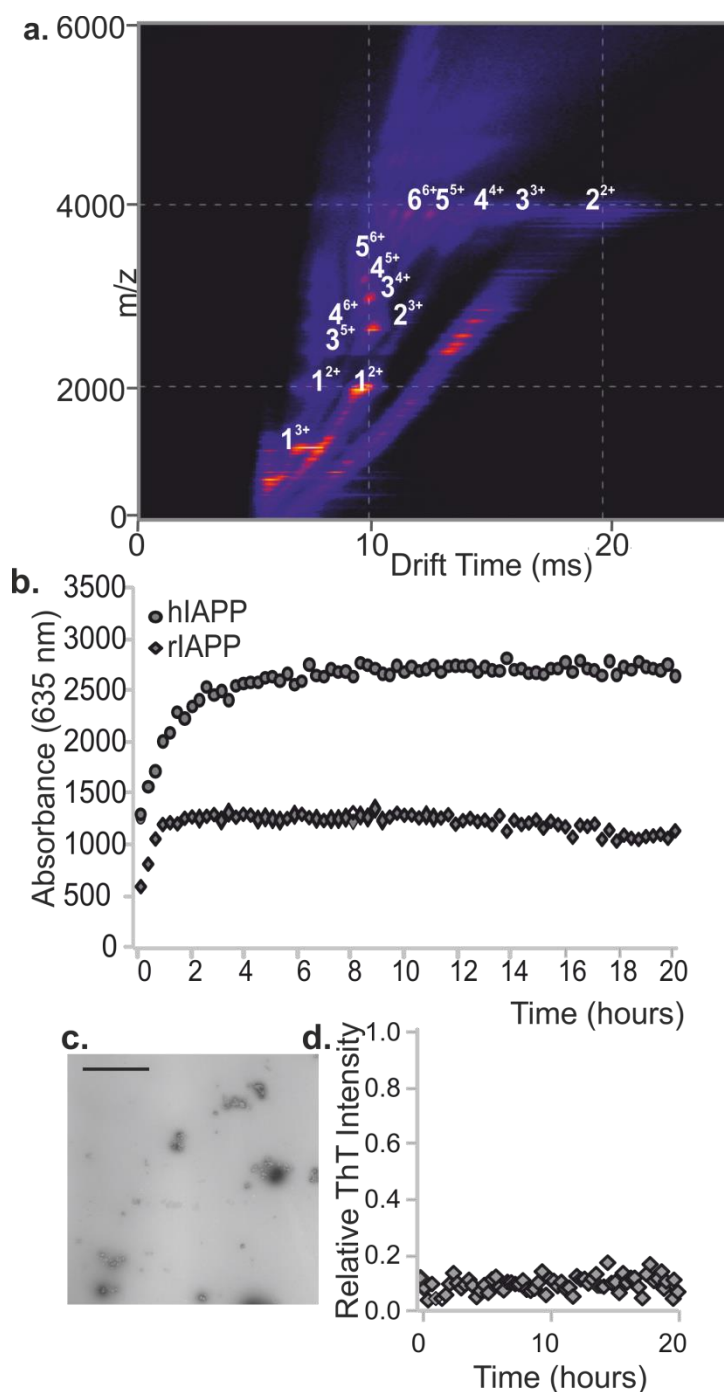
Figure 4-3. *Oligomers formed from rIAPP resemble those of hIAPP. a) ESI-IMS-MS driftscope plot of rIAPP oligomers present at 2 min after dilution into 20 mM ammonium acetate buffer, pH 6.8 to a final peptide concentration of 50 μM. The number adjacent to each peak denotes oligomer order with charge state of the oligomer in superscript. b) Aggregation of rIAPP (diamonds) and hIAPP (circles) monitored using turbidity at 635 nm. In both cases, 50 μM peptide was incubated in 20 mM ammonium acetate buffer, pH 6.8 (37 ℃, 600 rpm). A typical data set is shown, the experiment was performed over 5 replicates. c) Negative stain TEM image of rIAPP aggregates after 5 days of incubation (37 ℃, 600 rpm); scale bar = 100 nm. d) ThT fluorescence intensity of rIAPP (50μM peptide, 37 ℃, pH 6.8, 600 rpm). The data are normalized to the signal intensity of a hIAPP fibril formation end point at the same peptide concentration.*
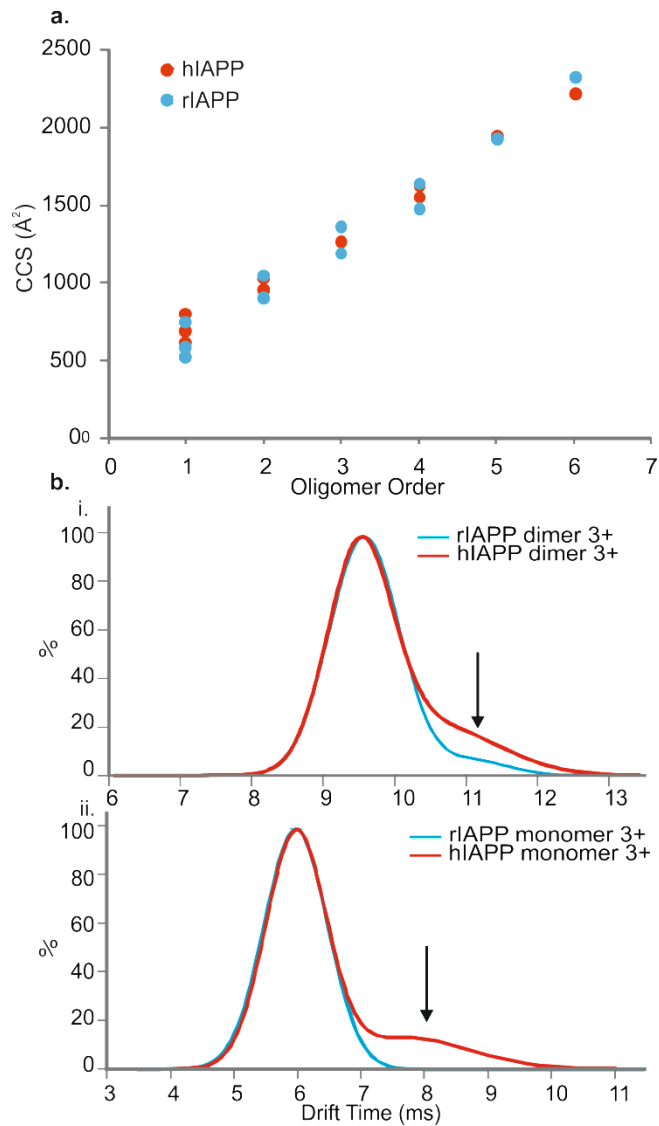
Figure 4-4*. Comparisons of hIAPP and rIAPP oligomers detected by ESI-IMS-MS. a) CCS of hIAPP oligomers (red) and rIAPP oligomers (blue) measured using ESI-IMS-MS plotted versus oligomer order. Experimental error is ± 5% for all cross sections. b) Arrival time distribution (ATD) of the hIAPP (red) and rIAPP (blue) 3+ dimer (i) and 3+ monomer (ii). The arrow highlights the second conformation of each ion.*
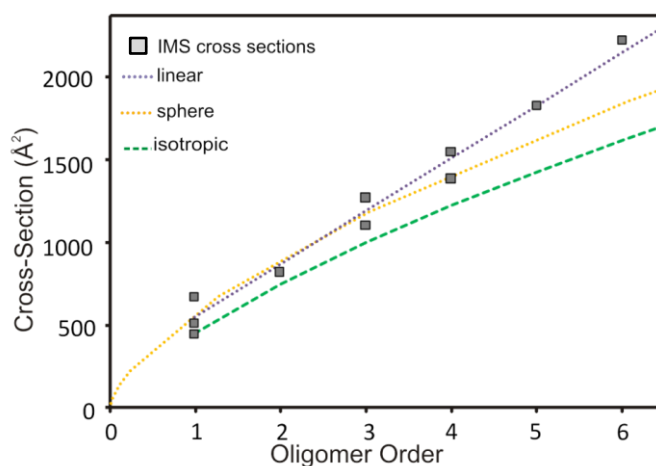
Figure 4-5. *rIAPP oligomer cross sections. CCS of rIAPP oligomers measured using ESI-IMS-MS versus oligomer order for all charge states. The orange dashed line represents a spherical growth model based on the average density of a protein (0.44 Da/Å³) (62, 215); the purple dashed line represents a linear growth model (46) and the green dashed line represents an isotropic growth model (46).*

4.2.3 CID reveals differences in gas-phase stability between hIAPP and rIAPP oligomers and monomers

As discussed in **Chapter 1 Section 1.6**, the use of hybrid instruments such as the Synapt HDMS employed here allows peptide samples to be characterised using MS/MS by CID. During CID-MS/MS experiments, precursor ions of a specific *m/z* are selected in the first mass analyser before being accelerated, collided with the buffer gas molecules and unfolded or fragmented. The energies at which the ions unfold or fragment reveals their relative gas phase stabilities (217).

To compare the stabilities of the hIAPP and rIAPP monomers, the dependence of the ATD profiles *versus* increasing the Trap energy was examined (**Figure 4-6**). Using CID-MS/MS, the triply charged hIAPP and rIAPP monomers (*m/z* 1301 and 1307, respectively) were selected using the quadrupole analyser and subjected to increasing Trap voltages in order to unfold the ions. After collisions in the Trap cell, differentially-folded ions enter the ion mobility cell and unfolding can be observed in the ion's ATD profiles. More unfolded monomeric conformers will be observed at longer drift times with respect to the more compact species. In addition, the overall profile should become wider and hence the conformational

ensemble more heterogeneous upon unfolding. The results of these experiments showed that hIAPP monomer 3+ ions unfold at lower Trap collision energies than those required for the rIAPP monomer, with hIAPP more readily converting to expanded conformers at lower trap voltages (**Figure 4-6**). At low Trap energies of 10 V, the ATD profiles of hIAPP and rIAPP monomers are narrow and exist apparently as one dominant conformation with a drift time of 6 ms and a lowly populated, more expanded conformer observed as a tail at ~10.5 ms. The latter species is more pronounced in hIAPP compared with rIAPP (**Figure 4-6**). At high Trap energies of ≥75 V, the entire ATD profile of the hIAPP 3+ monomer is shifter to longer drift times and a much larger proportion of more unfolded conformers are observed. In contrast, the rIAPP 3+ monomer ATD profile remains narrow and are indistinguishable from the ATD at 10 V when subject to high Trap energies, suggesting that it is more stable hence more resistant to gas-phase unfolding (**Figure 4-6**).
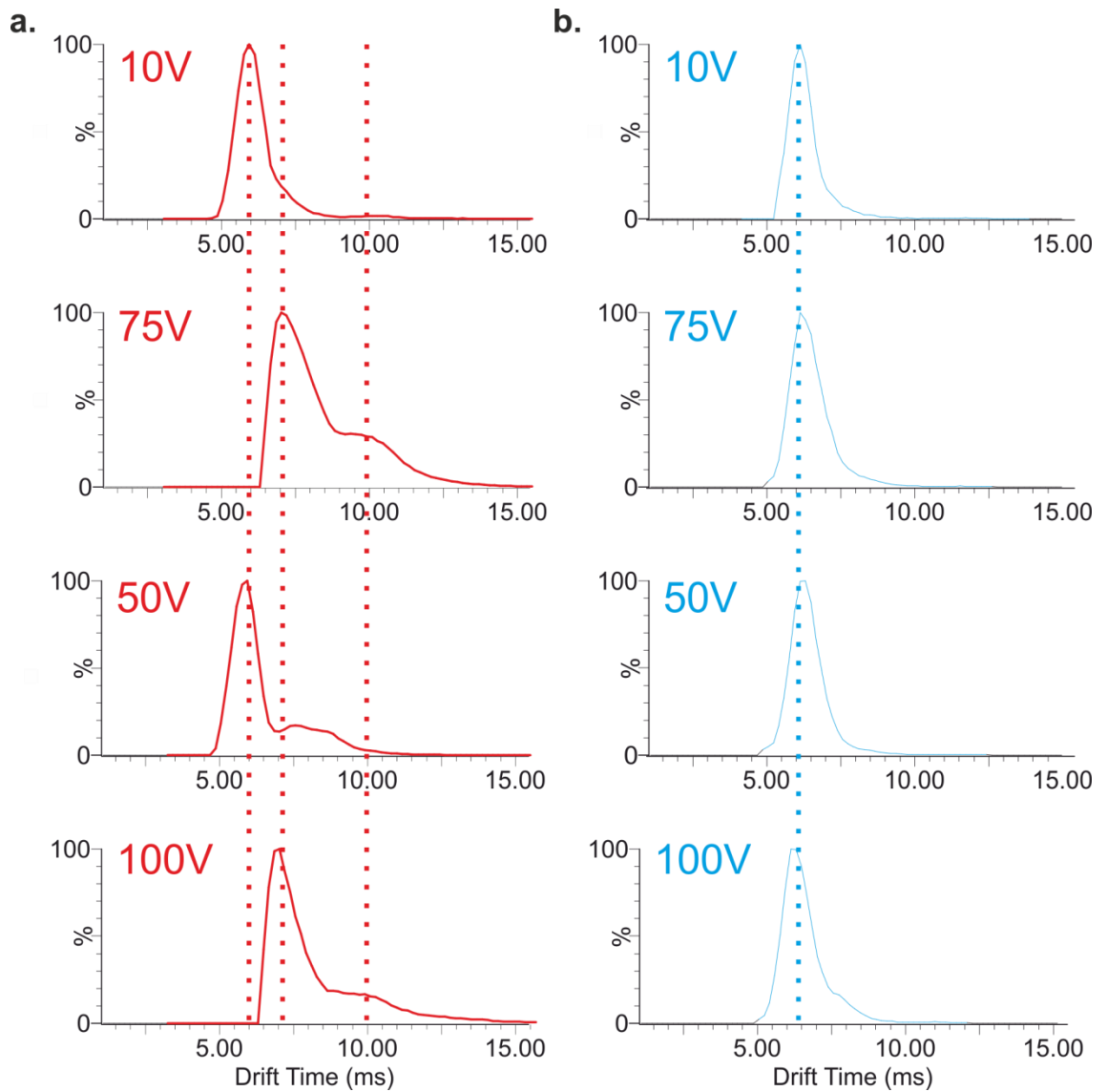
Figure 4-6. *ATDs of 3+ monomers of hIAPP (a) and rIAPP (b) at trap collision cell voltages 10 V - 100 V. A 1 Da m/z window was used in selection of ions prior to CIU.*

Next, the gas-phase stabilities of oligomers of hIAPP and rIAPP were probed to investigate whether their stability to gas-phase dissociation can be related to the differences in the ability of these sequences to form amyloid. These oligomers are not amenable to solution-phase stability assays, as they are so lowly populated. Accordingly, CID-MS/MS was utilised to provide a side-by-side comparison of the gas-phase stabilities of hIAPP and rIAPP peptides in their oligomeric states. In this experiment, ions of specific *m/z* were selected by the quadrupole analyser, followed by IMS separation of the different oligomers contributing to this *m/z*, and then sequential fragmentation of the oligomer ions in the transfer collision cell immediately prior to the time-of-flight analyser. In this instance, because ion mobility is performed before fragmentation, unfolding and/or fragmentation are not observed in ATD profiles, but instead dissociation is measured from the relative contributions of oligomer and monomeric ions to the spectra after time-of-flight analysis. In keeping with the observations for the monomeric peptides, the data revealed that hIAPP dimers have significantly lower gas-phase stabilities when compared with rIAPP dimers. hIAPP dimers were found to dissociate into monomer at an energy (40 V) which is lower than that required for the equivalent rIAPP dimers, which only began to dissociate at 70 V (**Figure 4-7**a). It is worth noting that total relative ion intensity in the CID plots is greater than one, given that the ESI-MS spectra acquired were relative to the base peak in the spectrum, giving the base peak an ion intensity of 100% thus a total ion intensity that is >100%.
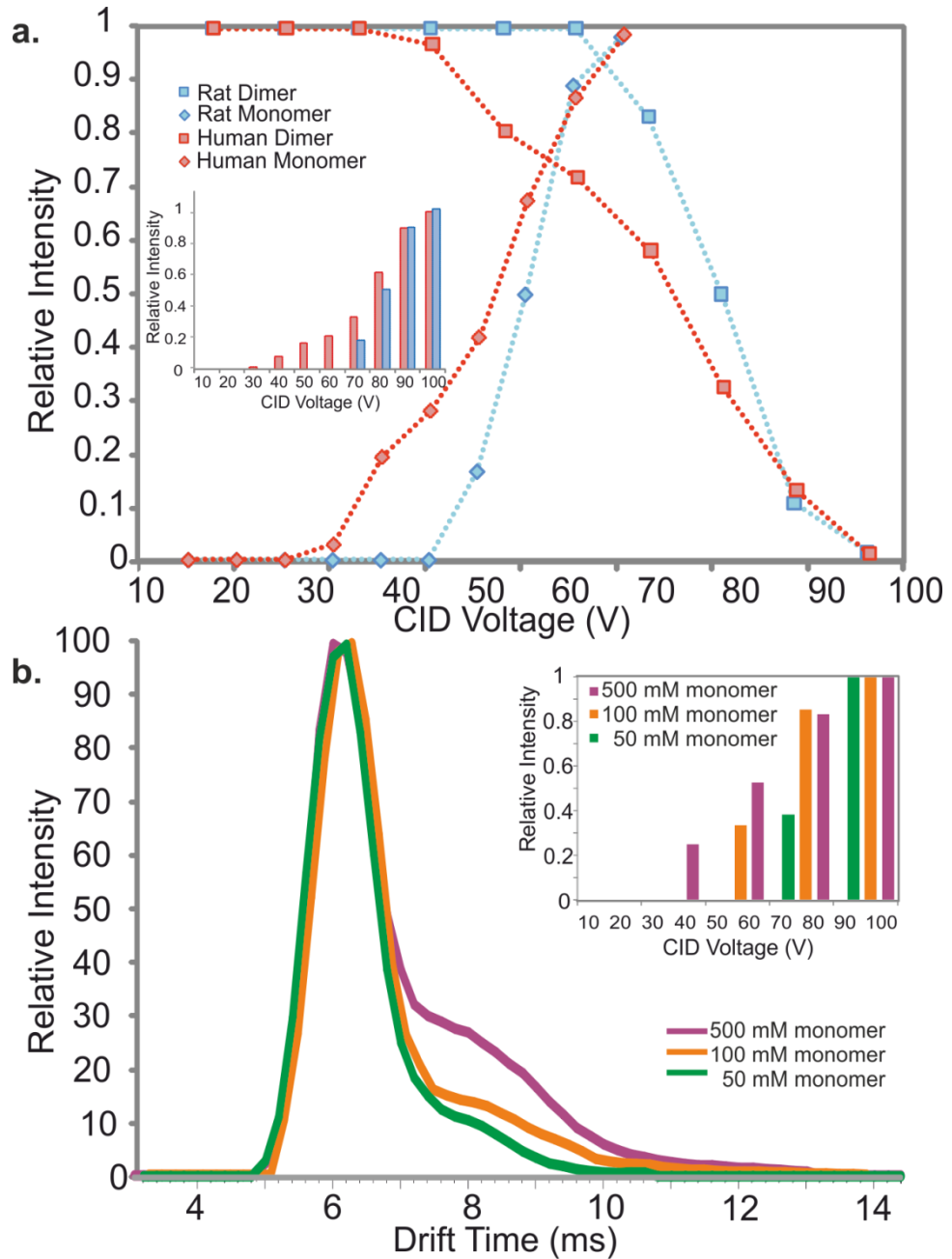
Figure 4-7. *Differences between rIAPP and hIAPP dimer and monomer stabilities in the gas-phase measured using CID. a) Collision Induced Dissociation (CID) MS/MS of rIAPP (blue) and hIAPP (red) dimers (50 µM peptide, 20 mM ammonium acetate buffer, pH 6.8). Relative intensity of the 3+ dimer ions (squares) of each peptide is plotted versus increasing ion-accelerating voltage into the transfer T-wave collision cell. Monomer ion intensity (diamonds) increases as dimers (squares) dissociate. Bar chart (inset) showing the appearance of hIAPP (red) and rIAPP (blue) monomer from dissociation of dimer ions with increasing CID voltage. b) Arrival time distributions (ATDs) of 3+ hIAPP monomer ions 2 min after dissolving into 50 mM (green), 100 mM (orange), or 500 mM (purple) ammonium acetate, pH 6.8. Bar chart (inset) showing relative intensity of monomer ions with increasing ion-accelerating voltage at different ionic strengths; 50 mM (green), 100 mM (orange), and 500 mM (purple), (25 µM peptide, 50/100/500 mM ammonium acetate buffer, pH 6.8).*
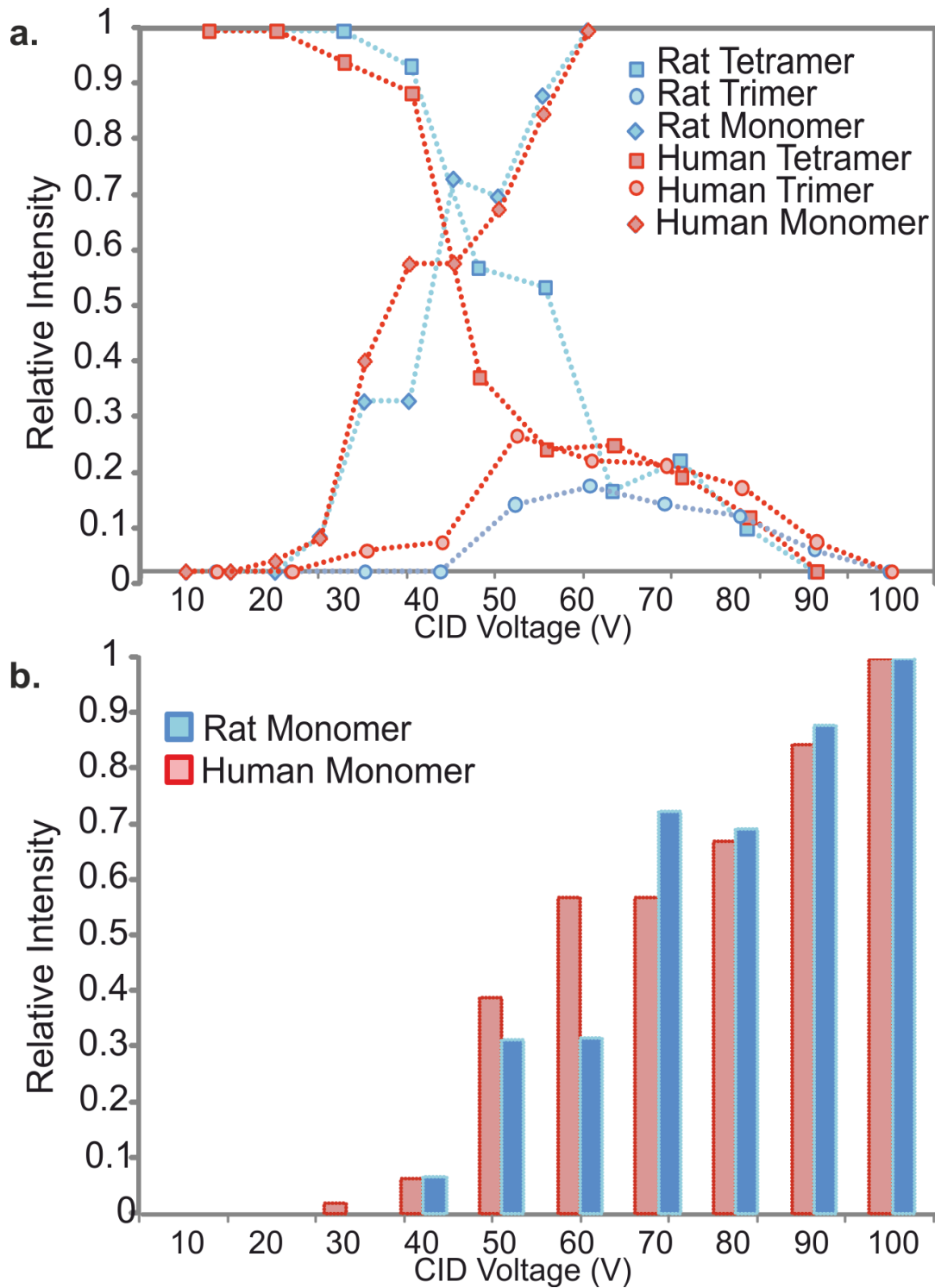
Figure 4-8. *Differences between rIAPP and hIAPP tetramer stabilities in the gas-phase measured using CID. a) MS/MS collision induced dissociation (CID) of rIAPP (blue) and hIAPP (red) tetramer ions. Relative intensity of the 6+ tetramer ion (squares) of each peptide is plotted versus increasing ion-accelerating voltage into the transfer T-wave device (CID). Monomer ion intensity (diamonds) and trimer ion intensity (circles) increase as tetramer ions (squares) become dissociated. b) Bar charts showing appearance of hIAPP (red) and rIAPP (blue) monomer from dissociation of tetramer ions with increasing CID voltage.*

The significant difference in the gas-phase stability of the dimer ions of hIAPP and rIAPP could be related to the capability of hIAPP to access amyloidogenic conformations more easily than its rIAPP counterpart. This could help towards explaining why two similar sequences that form the same size and order of oligomeric states have significantly different amyloid propensities. Consistent with this view, hIAPP monomer ions become increasingly unfolded (**Figure 4-7**b) and dimer ions become less stable in the gas-phase as the ionic strength of the buffer used is increased (**Figure 4-7**b), suggesting that high ionic strength destabilizes/unfolds oligomers and increases the rate of amyloid fibril formation. It is also possible that high ionic strength aids the formation of structurally distinct oligomers that have altered gas-phase stability, rather than merely altering the packing of monomer units within structurally similar species. This finding gives further evidence to the hypothesis that peptide gas-phase stability is correlated with the amyloid competence of IAPP. Higher order oligomeric species, including tetramer ions with six charges, also showed subtle differences in stability for the two sequences, the hIAPP tetramer^{6+} ions beginning to dissociate at 30 V whereas rat tetramer^{6+} ions remained fully associated until 40 V (**Figure 4-8**). Both the hIAPP monomer and its oligomers are, therefore, less stable than their counterparts for the rat sequence, and hIAPP becomes increasingly unstable at high ionic strengths. The results suggest, therefore, that hIAPP monomers and oligomers can accesses amyloid conformations more readily than rIAPP, and even more readily when the ionic strength of the buffer is increased.

4.2.4 Probing the mechanism of inhibition of hIAPP fibril formation with small molecules

Having identified the pre-fibrillar, oligomeric states populated by hIAPP, the next aim was to attempt to inhibit the formation of these higher order species and hence to prevent fibrillation. The mechanism of action of two known small molecule inhibitors of hIAPP fibril formation (EGCG and silibinin), therefore, was investigated using ESI-MS and ESI-IMS-MS. These compounds have been shown to prevent hIAPP fibril formation (141, 218), but the point of assembly at which they act and their mechanisms of action remained elusive. In these experiments, hIAPP (50 μM) was incubated at 37 °C in 20 mM ammonium acetate buffer, pH 6.8, in the presence of EGCG (141, 218) or silibinin (219) at molar ratios of small molecule:hIAPP of 0.1:1, 1:1 or 10:1. The monomer and oligomer populations were characterised immediately and at various time points after incubation, using ESI-IMS-MS. To complement the gas-phase analyses, fibril formation was monitored by ThT fluorescence and peptide aggregates were characterised using negative stain EM. The primary objectives here were to determine how the presence (or binding) of each small molecule affects the distribution of monomeric conformers and populations of oligomers and, whether such changes can be correlated with the inhibition of hIAPP amyloid formation, and hence to elucidate the precise mode of action of each small molecule inhibitor.

4.2.4.1 The action of EGCG on fibril formation of hIAPP probed by ESI-IMS-MS

EGCG, discussed in detail in **Chapter 1 Section 1.12**, is a polyphenol flavanol extracted from green tea that has shown promise as a generic anti-amyloid agent. EGCG has been found to redirect aggregating proteins (including hIAPP (158), α-synuclein and Aβ42 (141)) onto alternative pathways (141), or to maintain them in a monomeric state (220). It has also been shown to promote re-modelling of

mature amyloid fibrils (218), with recent work of Kelly *et al.* demonstrating that hydrophobic binding to the amyloid fibril by EGCG promotes such re-modelling (221). To identify the effects of EGCG on hIAPP aggregation, the binding capabilities of the hIAPP monomer for EGCG was investigated. The results revealed that EGCG binds to monomeric hIAPP (~10% monomer remains bound in gas phase when present at a 10-fold molar excess over peptide) (**Figure 4-9**a) and alters the equilibrium of monomer charge states present. The monomer 3+ ion becomes more highly populated in the presence of EGCG (compare **Figure 4-1**b and **Figure 4-9**a), with a change in ratio of 3+:2+ monomer in the spectra changing from ~1:2 to ~1:1.25. The observed ligand binding results in inhibition of the peptide's assembly into higher order oligomers and amyloid fibrils no longer form (**Figure 4-9**b-d). Binding of EGCG is observed to both of the charge states populated by the hIAPP monomer (2+ and 3+) (**Figure 4-9**a), and, indeed, to each monomeric conformer (both the expanded and the compact form of each charge state), (**Figure 4-10**). One or two copies of EGCG bind to one doubly-charged monomer and up three EGCG molecules bind to the triply-charged monomer, when EGCG is present at a 10-fold molar excess over hIAPP (**Figure 4-9**a). The low level of binding observed, despite complete inhibition of fibrillation (**Figure 4-9**b), is suggestive of a hydrophobic binding mechanism. It is possible that a greater proportion of the hIAPP monomers and bound by hIAPP in solution but that the ligands dissociate upon entry into the gas-phase given that hydrophobic interactions are not wholly maintained within the mass spectrometer. A hydrophobic binding mechanism, consistent with that proposed by Kelly *et al.*, may help towards explaining the ability of EGCG to inhibit a wide range of natively unfolded polypeptides and IAPP mutants (156).

ESI-IMS-MS data (**Figure 4-9**c and **Figure 4-11**) reveal that incubation with increasing molar ratios of EGCG:hIAPP prevents assembly into higher order oligomers, in a dose-dependent manner. At 0.1:1 and 1:1 molar ratios of EGCG:hIAPP, monomer through tetramer hIAPP oligomers are observed (**Figure 4-9**c), but no pentamer or hexamer (monomer through hexamer are observed in the Driftscope plot of hIAPP incubated in isolation (**Figure 4-1**b)). At a 10:1 molar ratio of EGCG:hIAPP, no species greater than monomer are observed (**Figure**

4-9c). Under the latter conditions, there is no increase in ThT fluorescence and TEM images (**Figure 4-9**d panel iii) do not show any aggregated material, indicating complete inhibition of both aggregate and amyloid formation. Together, these results demonstrate that EGCG binds to, and traps, low order species, preventing the formation of higher order oligomers. This small molecule also differentially stabilises distinct monomeric charge states of hIAPP. The result of these combined observations is that amyloid fibrils cannot form. An alternative explanation is that EGCG diverts low order oligomers of hIAPP onto other aggregation pathways that result in the formation of non-amyloid aggregates. In the latter scenario, oligomers populated must be of low abundance, low ionisation propensity, or too heterogeneous to be detected by ESI-IMS-MS.

4.2.4.2 Remodeling of mature IAPP fibrils by EGCG

In addition to its ability to interfere with amyloid assembly (141), EGCG has been shown previously to interact with pre-formed amyloid, remodelling a range of fibrils, including those formed from hIAPP (141, 158), into amorphous aggregate. Having determined the effect of EGCG on the pre-fibrillar aggregation landscape of hIAPP, the effect of this small molecule on the reverse reaction, fibril depolymerisation, was investigated. TEM was used to monitor fibril loss over time and ESI-IMS-MS was used to investigate how fibril re-modelling by EGCG alters the populations of pre-fibrillar oligomers. Fibril samples were first formed by incubation of hIAPP (50 µM) in the absence of small molecule at pH 6.8 for 5 days. A 10-fold molar excess of EGCG was then added to fibrillar samples were further incubated in 20 mM ammonium acetate buffer, pH 6.8 (37 °C, 600 rpm) for 5 days. The loss of fibrils and change in lower order species were monitored, by TEM and ESI-IMS-MS, respectively, at various time points after addition of the EGCG. Under the conditions employed, clumping of hIAPP fibrils followed by re-modelling into amorphous aggregates over a 24 h period was observed (**Figure 4-9**d iv-vi.). This remodelling is concomitant with a subtle increase in intensity of the signal arising from monomer ions, measured using ESI-IMS-MS, compared with the same sample prior to addition of EGCG (**Figure 4-11**a iv and b iv). The lack of higher order oligomers, however, suggests that fibril re-modelling by EGCG is not the reverse of amyloid formation and does not result in the re-formation of pre-fibrillar oligomeric species.
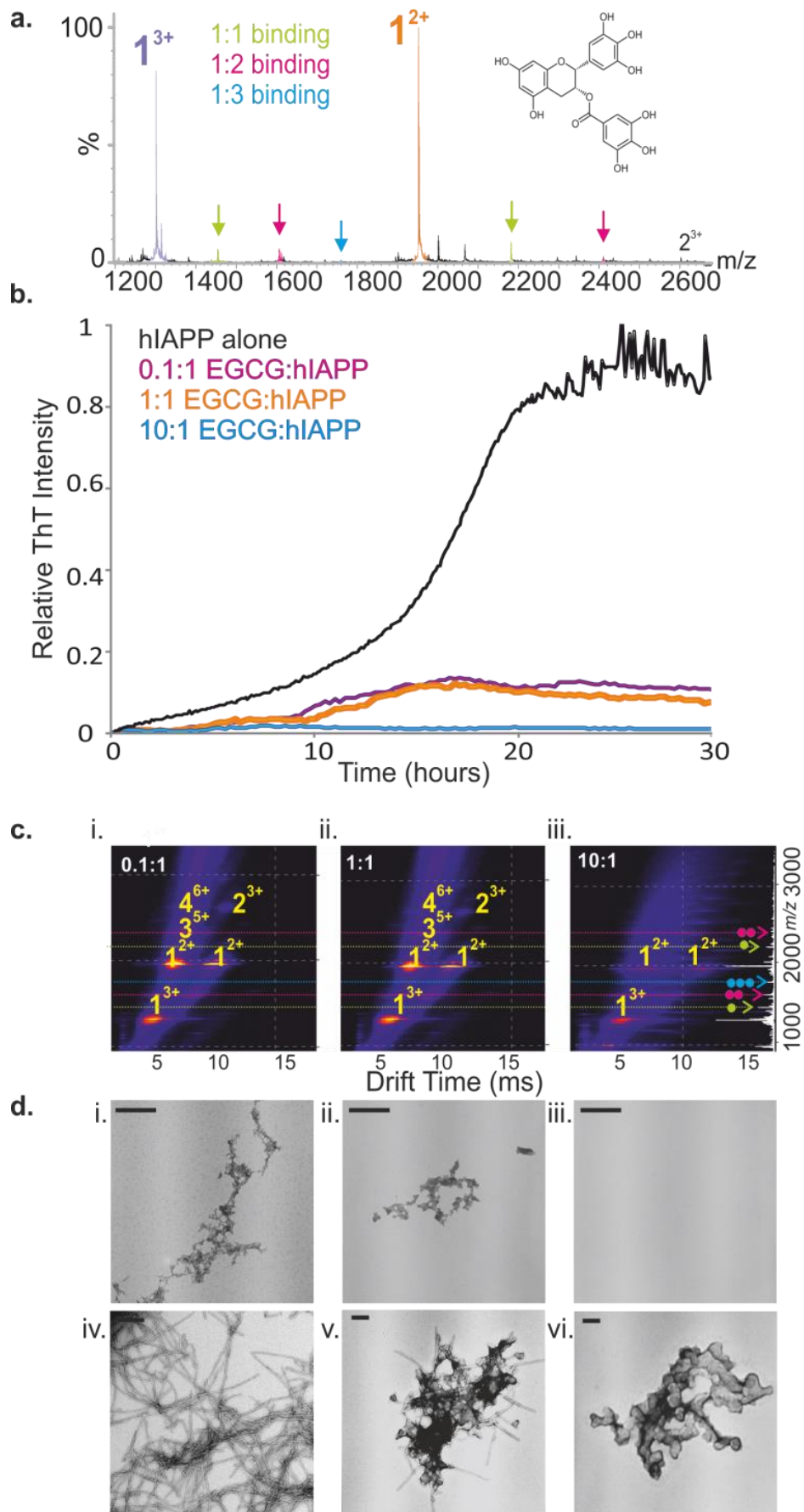
Figure 4-9. *Inhibition of hIAPP fibril formation by EGCG. a) Positive ion ESI mass spectrum showing binding of EGCG (added at 500 μM to 50 μM peptide) to both the +2 (orange) and +3 (purple) charge state ions of hIAPP monomer. Stoichiometry of binding is shown by colour: 1:1 inhibitor molecule bound to an IAPP monomer is highlighted in green, 2:1 in pink and 3:1 in blue. EGCG is shown as an inset. b) ThT fluorescence intensity of hIAPP (black) (50 μM peptide, 20 mM ammonium acetate buffer, pH 6.8, 37 °C, 600 rpm) with increasing EGCG:hIAPP molar ratios: 0.1:1 (pink) and 1:1 (orange) and 10:1 (blue). c) ESI-IMS-MS driftscope plots of hIAPP oligomers formed in the presence of (i) 0.1:1, (ii) 1:1 and (iii) 10:1 molar ratios of EGCG:peptide monomer at t= 5 hours. The number of EGCG molecules bound to each species is shown as a colored dot. d) Negative stain TEM images of hIAPP incubated with (i) 0.1:1, (ii) 1:1 and (iii) 10:1 molar ratios of EGCG for 5 days (37 °C, 600 rpm). (iv) hIAPP fibrils alone, and aggregates formed when a 10-fold molar excess of EGCG:hIAPP is added to preformed hIAPP fibrils after 5 h (v) and 24 h (vi), scale bar is 100 nm.*
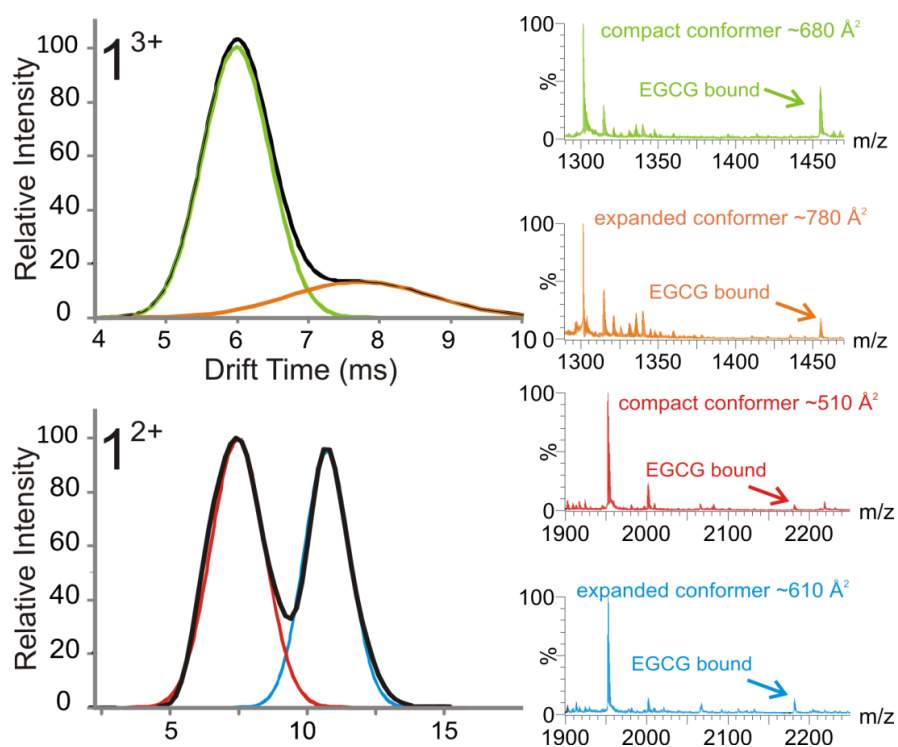
Figure 4-10. *EGCG binds to all conformers of IAPP. Arrival time distributions (ATDs) show that the 3+ monomer ions of hIAPP occupy two conformers (t_D = ~6 & 8 ms) (a i) and the 2+ monomer ion also occupies two conformers (t_D = ~7.6 & 10.6 ms) (b i). EGCG binds to the both the expanded conformer (green/red) and to the compact conformer (orange/blue) of both the 3+ and 2+ monomer ions (a and b ii-iii).*
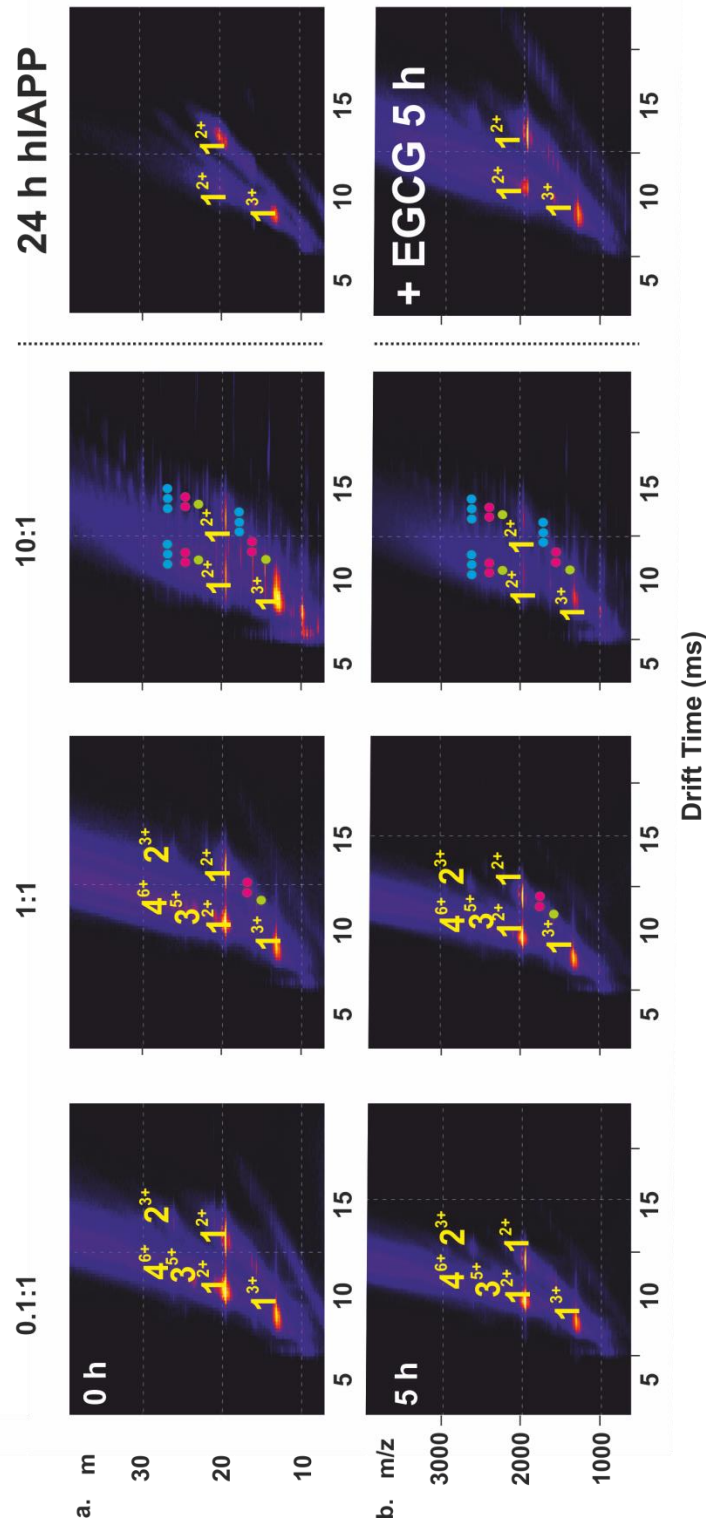
Figure 4-11. *IMS Time courses of inhibition of hIAPP oligomer formation by EGCG. Driftscope plots of hIAPP oligomers formed in the presence of 0.1:1, 1:1 or 10:1 molar ratios of EGCG at t= 2 min/'0 h' (a) and t= 5 hours (b). The right hand driftscopes shows hIAPP alone after 24 h incubation (a iv) and after subsequent addition of a 5-fold molar excess of EGCG (b iv) (ammonium acetate buffer pH 6.8, 37ºC, 600 rpm). Circles represent number of bound EGCG molecules.*

4.2.4.3 The action of silibinin on fibril formation of hIAPP probed by ESI-IMS-MS

Silibinin, a flavonol extracted from seeds of the herb milk thistle, has been proposed as a potential therapeutic for amyloidosis associated with T2DM (219). Here, the precise nature of the interaction of this small molecule with hIAPP was also probed using ESI-IMS-MS. The resulting data (**Figure 4-12**a) revealed that silibinin binds only to the 3+ charge state ions of monomeric hIAPP (~20% remaining bound in the gas phase), with no detectable binding to the 2+ charge state ions of the monomer. This preferential binding to one monomeric charge state could be indicative of the selectivity of the small molecule, or alternatively could be explained by the low abundance of the 2+ charge state in its presence. Similar to the observation in the presence of EGCG, but more pronounced, the presence of a 10:1 molar ratio of silibinin alters the equilibrium of the two different charge states of monomeric hIAPP, favoring the population of the triply-charged monomer ions. The ratio of 3+:2+ monomer in the spectra is altered from ~1:2 to ~3:1 between the absence and presence of a ten-fold molar excess of silibinin, respectively (compare **Figure 4-1** and **Figure 4-12**a). ESI-IMS-MS data indicate that silibinin prevents hIAPP oligomer formation even when present at sub-stoichiometric ratios of silibinin:hIAPP (**Figure 4-12**b and **Figure 4-13**). More specifically, detailed analysis of the ESI-IMS-MS data reveals that the binding of silibinin is only observed to the more expanded conformer of the 3+ monomer ions (**Figure 4-12**c) 5-5but does not significantly impact the ratio of monomeric conformations present. This expanded conformer (CCS=~790 Å^2) is adopted by the hIAPP monomer but not by the rIAPP monomer (**Figure 4-4**b ii.). Indeed, there is no detectable binding of silbinin to the rIAPP monomer, which lacks this conformation, when analysed under identical conditions (**Figure 4-14**). Interestingly, Bowers *et al.* have previously proposed that this expanded monomeric conformer is an on-pathway, amyloid-competent conformation which precedes the generation of extended dimers and beta-sheet rich oligomers (47, 48). Specific binding to this expanded hIAPP monomer conformation is thus consistent with the ability of silibinin to inhibit amyloid assembly. ThT data

(**Figure 4-12**d) demostrate that aggregation of hIAPP decreases significantly as the concentration of silibinin is increased, although in a 10-fold molar excess of silibinin a weak positive ThT signal is still observed (**Figure 4-12**d), likely due to the presence of small aggregates not visible by ESI-IMS-MS. TEM images indicated that incubation of monomeric hIAPP with silibinin for 5 days leads to few aggregates, with none visible by TEM when a 10-fold molar excess of silibinin:hIAPP is added (**Figure 4-12**e i-iii).

4.2.4.4 Re-modelling of mature IAPP fibrils by silibinin

Although silibinin has been shown previously to inhibit the forward reaction of amyloid assembly by hIAPP (219), unlike studies on EGCG, the interaction of silibinin with pre-formed amyloid fibrils had not been reported. Pre-formed hIAPP fibrils were incubated, therefore, with a 10-fold molar excess of silibinin and the effect of addition of the small molecule on the disassembly reaction was monitored using TEM and ESI-IMS-MS. The results showed that addition of silbinin results in the de-polymerisation of pre-formed fibrils over a 24 h time period during which time fibrils decrease in length (**Figure 4-12**e iv-vi). Concomitant with fibril depolymerisation observed by TEM, ESI-IMS-MS revealed a increase in abundance of low-order oligomeric species (**Figure 4-13**b). The re-population of hIAPP oligomers suggests that de-polymerisation may occur via oligomer release. Alternatively, monomer release may result in the rapid re-formation of oligomers in solution, i.e. the forward reaction is re-established. CCS measurements reveal that the hIAPP oligomers re-formed upon fibril de-polymerisation are comparable in size and shape to those formed during amyloid formation.
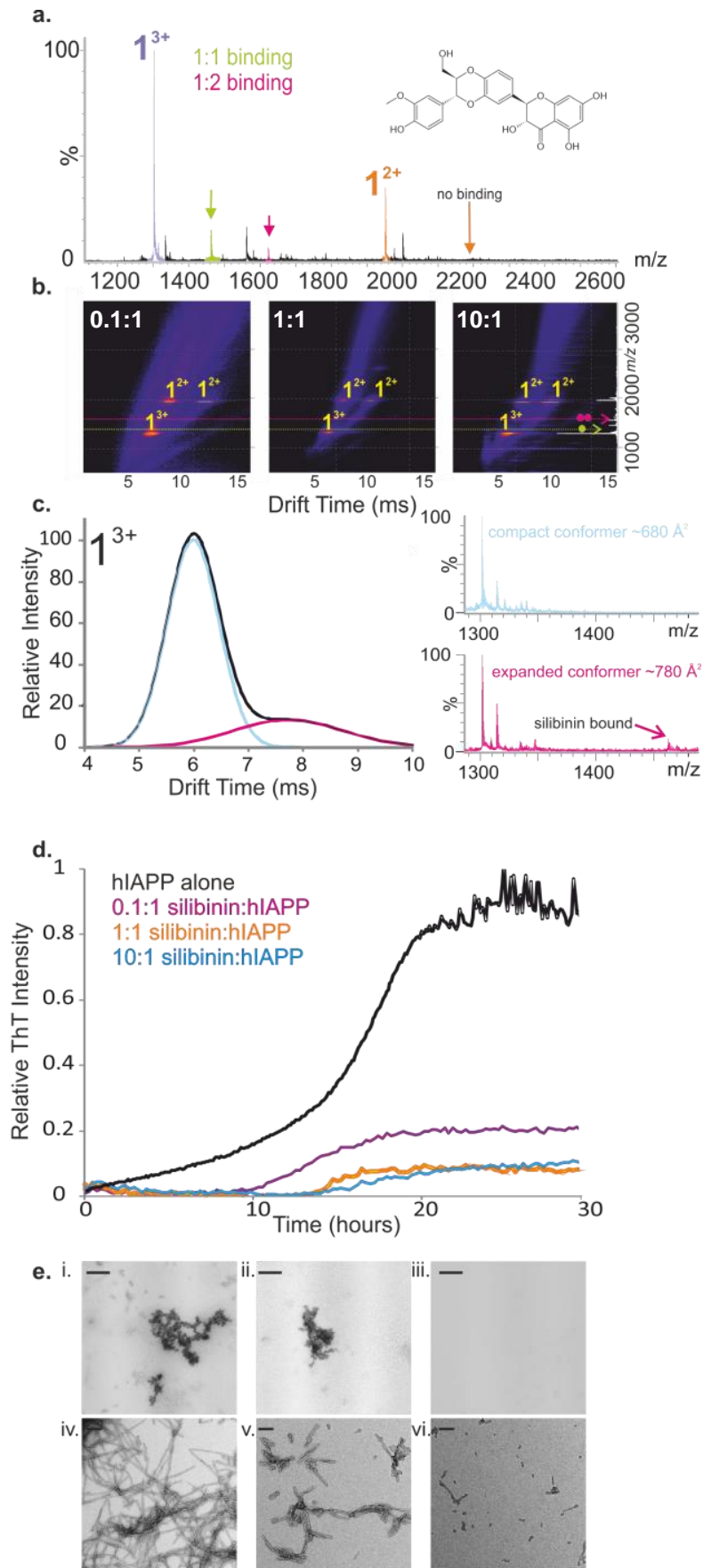
Figure 4-12. *Inhibition of hIAPP fibril formation by silibinin. a) Positive ion ESI mass spectrum showing binding of silibinin molecules (added at 500 μM to 50 μM peptide)*

to the 3+ monomer ions (purple) and absence of binding to the 2+ monomer ions (orange) at a molar ratio of silibinin:hIAPP of 10:1. The structure of silibinin is inset. b) ESI-IMS-MS driftscope plots showing the lack of hIAPP oligomers in the presence of 0.1:1, 1:1 and 10:1 molar ratios of silibinin:hIAPP at t= 5 hours. c) Arrival time distribution of 3+ monomer ions shows two conformers are present (t_D = 6 & 8 ms). Silibinin binds to the expanded conformer of the 3+ monomer ions (pink) but does not bind detectably to the compact conformer (blue). d) ThT fluorescence intensity of hIAPP (black) (50 µM peptide, 20 mM ammonium acetate buffer, pH 6.8, 37 ºC, 600 rpm) with increasing silibinin:hIAPP molar ratios: 0.1:1 (pink), 1:1 (orange) and 10:1 (blue). e) Negative stain TEM images of hIAPP incubated with (i) 0.1:1, (ii) 1:1 and (iii) 10:1 molar ratios of silibinin:hIAPP for 5 days (37 ºC, 600 rpm). Lower panels show hIAPP fibrils alone (iv) and aggregates formed when a 10-fold molar excess of silibinin:hIAPP is added to preformed hIAPP fibrils after 5 h (v) and 24 h (vi), scale bar is 100 nm.
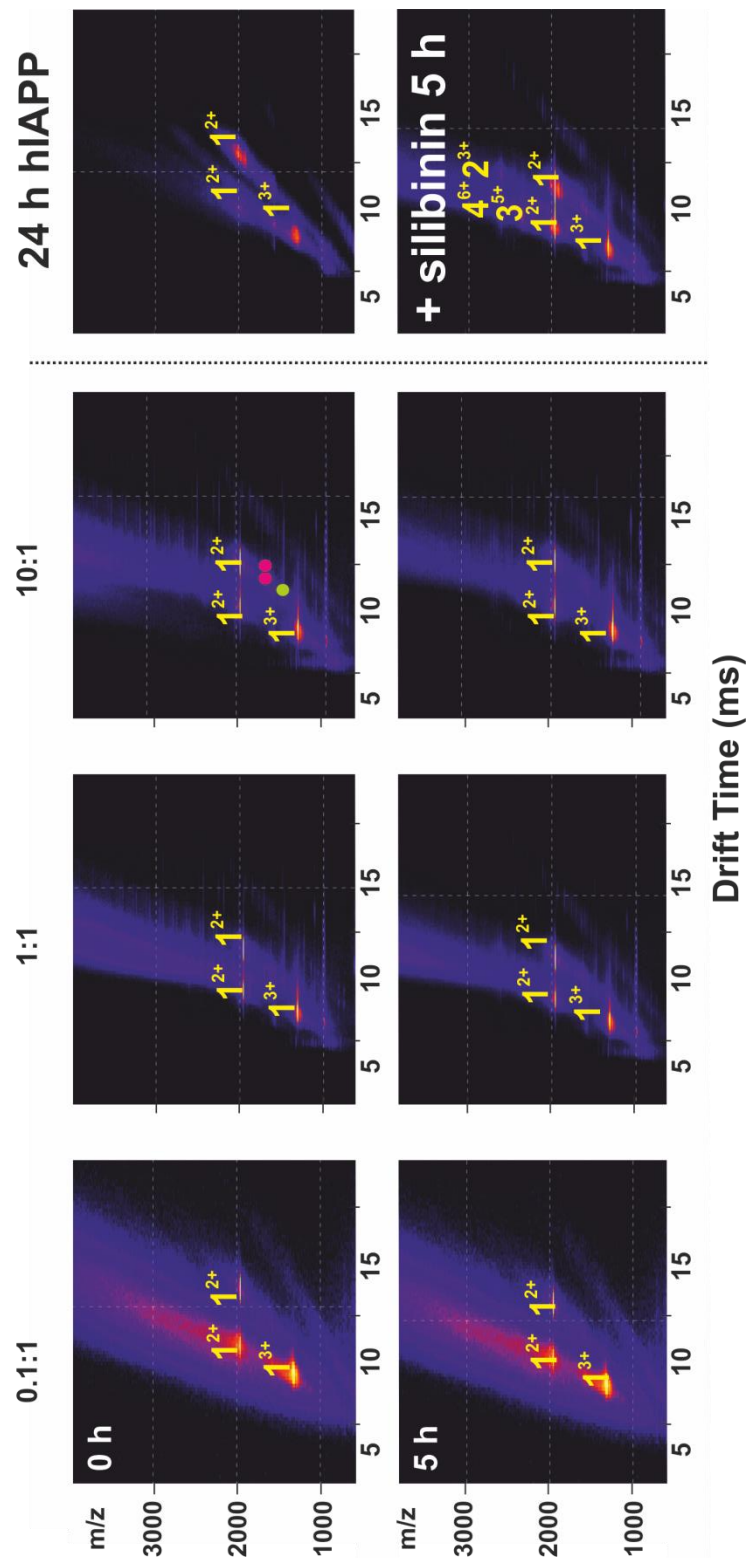
Figure 4-13. *IMS Time courses of inhibition of hIAPP oligomer formation by silibinin. Driftscope plots of hIAPP oligomers formed in the presence of 0.1:1, 1:1 or 10:1 molar ratios of silibinin at t= 2 min (a) and t= 5 hours (b). The right hand driftscope plots show hIAPP alone after 24 h incubation (a panel iv) and after subsequent addition of a 5-fold molar excess of silbinin (b panel iv) (ammonium acetate buffer pH 6.8, 37°C, 600 rpm). Circles represent number of bound silibinin molecules.*
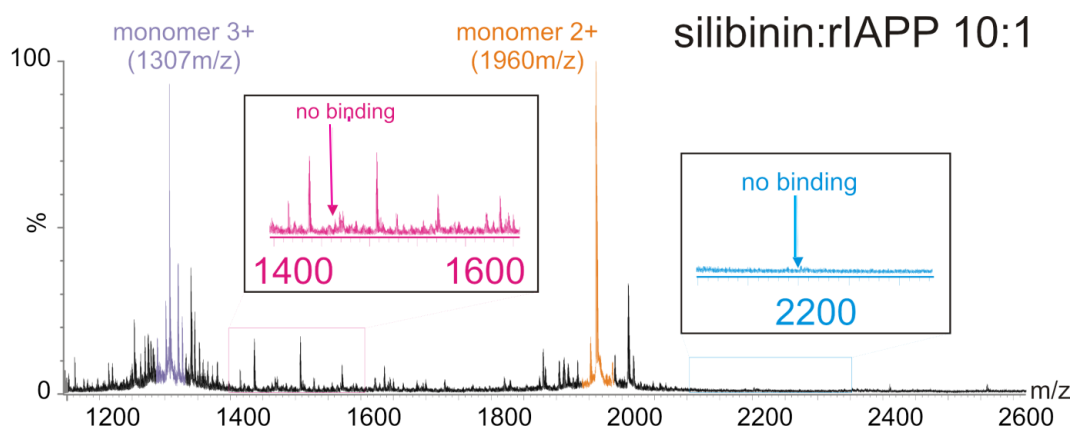
Figure 4-14*. Positive ion ESI mass spectrum showing the absence of binding of silibinin to rIAPP monomers (added at 500 µM to 50 µM peptide) to the 3+ monomer ions (purple) and to the 2+ monomer ions (orange) at a molar ratio of silibinin:rIAPP of 10:1. Zoomed regions of the spectra at which bound peaks would appear are inset.*

4.2.5 Formation of hetero-oligomers and hetero-fibrils of hIAPP and rIAPP

A range of peptide inhibitors has been developed against hIAPP (222-225). The lack of structural information available on the intermediate states occupied by the peptide has made it difficult, however, to rationalise why some are more effective than others. The rIAPP peptide has been used previously as the basis for design of an FDA approved therapy to treat T2DM (226), despite being only a moderately effective inhibitor of hIAPP amyloid formation when added at equimolar concentrations (114). A recent two-dimensional infrared spectroscopy study by Zanni *et al.* revealed that the non-amyloidogenic rIAPP peptide can become amyloid-competent in the presence of hIAPP, converting from a natively disordered rIAPP monomer into an ordered β-sheet rich complex with hIAPP (227). To determine why the rIAPP peptide is an ineffective inhibitor of hIAPP

assembly and to identify how the hIAPP-rIAPP complex forms, ESI-IMS-MS was used to study the oligomeric structures present in a mixture (1:1 molar ratio) of the two peptides.

By contrast with the decrease in oligomer populations of hIAPP observed in the presence of the two small molecule inhibitors studied in **Section 4.2.4** (EGCG and silibinin), oligomers up to, and including, hexamer are observed upon incubation of the hIAPP and rIAPP at a 1:1 molar ratio (**Figure 4-15**a), comparable with results observed when each peptide is incubated in isolation. Consistent with previous reports suggesting that the rat peptide must be present in an ~10-fold molar excess to inhibit hIAPP amyloid formation (114, 227), the presence of equimolar rIAPP does not prevent fibrillation of hIAPP under the conditions of these experiments (**Figure 4-15**b). The fibrils formed from the mixed sample were of similar morphology (long, straight) to those formed by hIAPP in isolation, as judged by TEM (**Figure 4-15**c). Mixed oligomers were observed using ESI-IMS-MS with *m/z* values corresponding to all-hIAPP, all-rIAPP and oligomers containing a mixture of hIAPP and rIAPP monomer subunits. The triply-charged dimer ions (**Figure 4-15**a, inset), for example, have an *m/z* of 2608, corresponding to one hIAPP monomer (3904 Da) and one rIAPP monomer (3921 Da), carrying three positive charges. Mixed trimers (2:1 and 1:2 hIAPP:rIAPP monomer units) and higher order oligomers were observed also, as well as homo-oligomers of both peptides. The ability to form mixed oligomers helps explain why rIAPP is inefficient at inhibiting hIAPP amyloid formation. After co-incubation of the two peptide sequences for 5 days, fibrils formed were ultra-centrifuged and depolymerised by incubation in 100% HFIP for 24 h with agitation (**Chapter 2 Section 2.4.4**). Samples were then air-dried and re-suspended in denaturing solvent (50:40:10 acetonitrile/water/acetic acid (*v/v/v*)). Crucially, the resulting mass spectra (**Figure 4-15**d i) revealed that both hIAPP and rIAPP monomer subunits are incorporated into the fibrillar state, with approximately twice as many hIAPP monomer units being incorporated into the fibrils compared with rIAPP monomers under the conditions employed. Both monomers were also found in the supernatant of the original mixed sample, with rIAPP monomers being in excess in this fraction (**Figure 4-15**d ii).
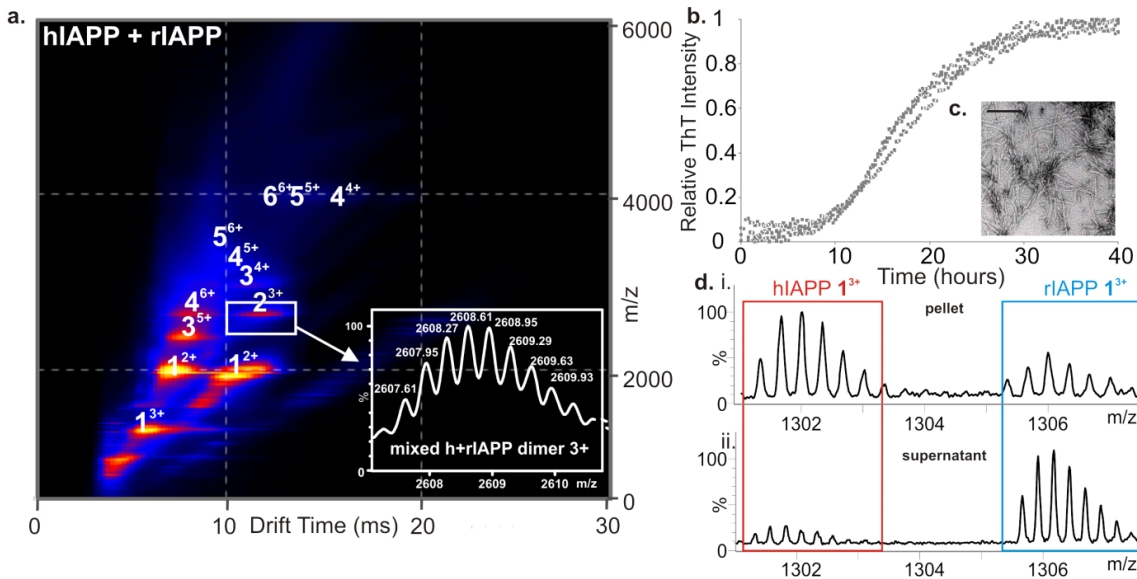
Figure 4-15. *Lack of hIAPP inhibition by rIAPP. a) ESI-IMS-MS driftscope plot of oligomers present at t= 2 min in a mixed sample of hIAPP and rIAPP at a 1:1 molar ratio (50 μM final peptide concentration, 20 mM ammonium acetate buffer, pH 6.8, 25 °C). Extracted driftscope peak shows masses corresponding to a mixed dimer of one hIAPP monomer and one rIAPP monomer (inset). b) ThT fluorescence intensity of hIAPP: rIAPP 1:1 (50 μM final peptide concentration, 20 mM ammonium acetate buffer, pH 6.8, 37 °C, 600 rpm). Data for three replicates are shown. c) Negative stain TEM image of 1:1 hIAPP: rIAPP fibrils after 5 days. Scale bar = 100 nm. d) ESI mass spectra of depolymerized fibrils showing the presence of both hIAPP and rIAPP monomer constituents in the (i) pellet and (ii) supernatant following ultracentrifugation.*

CID-MS/MS was next utilised in order to probe the stability of the hetero-oligomers formed from the 1:1 hIAPP:rIAPP mixture by subjecting the hetero-dimer and hetero-tetramer ions to increasing transfer collision cell voltages to promote gas-phase dissociation. Interestingly, the hetero-oligomers exhibited intermediate gas-phase stabilities with respect to homo-oligomers of hIAPP and rIAPP of the same mass, being less stable than rIAPP oligomers, but more stable than hIAPP oligomers (**Figure 4-16**.). The data indicate that mixing of the two sequences does not greatly perturb the amyloid competence of the human sequence but does enhance the amyloid competence of the rat sequence. The intermediate stabilities of the mixed assemblies, however, suggest a compromise in the properties of the two sequences with respect to homo-assemblies.

Taken together, therefore, the ESI-IMS-MS and CID-MS/MS data suggest that differences in gas-phase stability of monomer and low order oligomers between hIAPP and rIAPP sequences could be related to their differences in amyloid

propensity. Indeed, de-stabilisation of the monomeric or oligomeric states, either due to changes in amino acid sequence or conditions, correlates with increased amyloid propensity, as seen in the comparison of the hIAPP and rIAPP stabilities and the salt-dependence experiments, respectively.

In addition, small molecule binding to amyloidogenic hIAPP sequence prevents its assembly into fibrils by preventing oligomer assembly via binding to monomers. As a result, the aggregation pathway is diverted to alternative routes that result in the formation of low order species and/or amorphous aggregates.
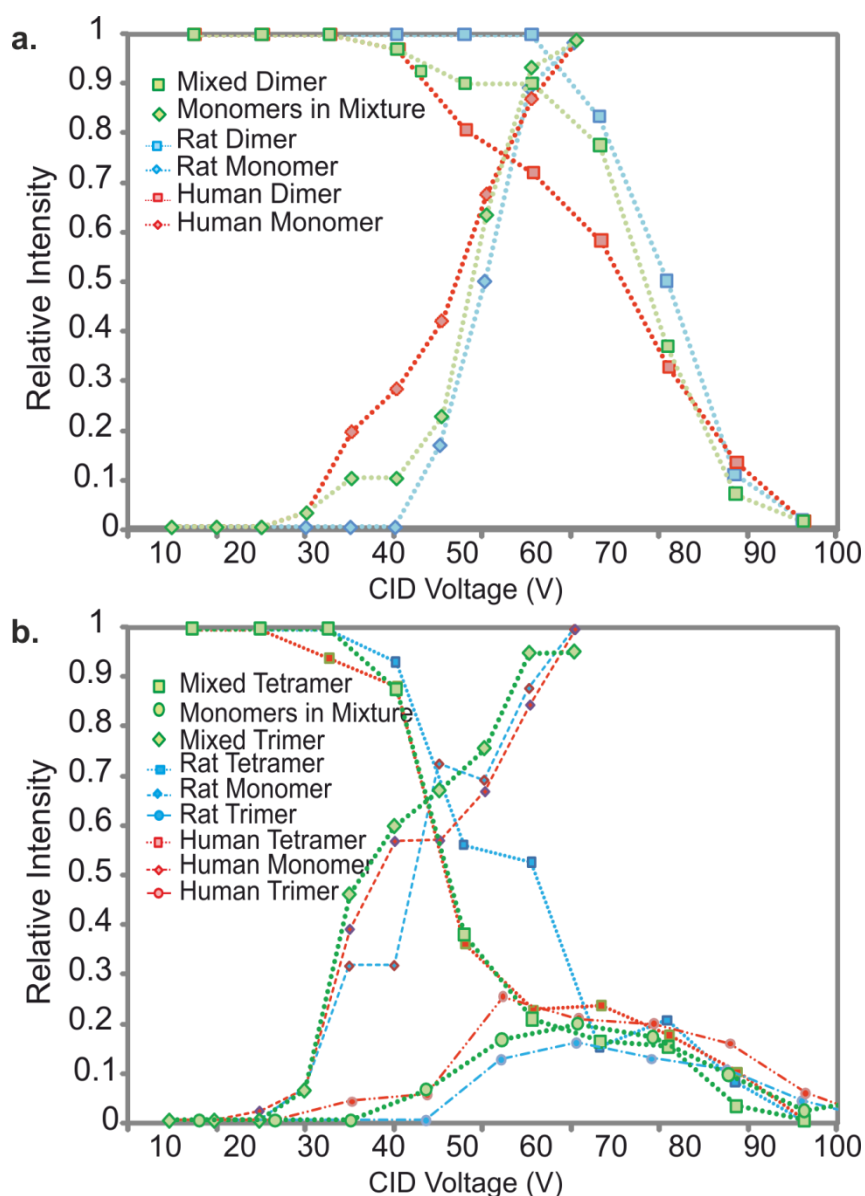
Figure 4-16. *Differences between the gas-phase stabilities of hIAPP, rIAPP and hIAPP/rIAPP mixed oligomers, measured using CID. a) Collision induced dissociation of mixed (a) dimers and (b) tetramers. a) The relative intensity of the 3+ mixed dimer ions (squares) plotted against increasing ion-accelerating voltage into the transfer T-wave device. hIAPP (red) and rIAPP (blue) are also plotted for comparison. b) The relative intensity of the mixed 6+ tetramer ions (squares) plotted against transfer voltage. Monomer (circle) and trimer (diamonds) ions appear with increasing CID voltage and trimer ion intensity subsequently decreases again as they are dissociated to monomer. In both cases mixed oligomers show intermediate stability with respect to oligomers formed from hIAPP alone and rIAPP alone.*

4.3 Discussion

The study of pre-fibrillar amyloid oligomers is a significant challenge, yet is vitally important for the unravelling of the complex mechanisms underlying protein aggregation in disease. In order to determine the specific culprits of toxicity and to design therapeutics to prevent their formation, all species on the energy misfolding and aggregation landscapes, both on- and off-pathway, must be identified and characterised. Here, using ESI-IMS-MS, oligomers of hIAPP and rIAPP have been characterised in detail for the first time, and their structures and relative gas-phase stabilities compared.

Previous IMS-MS data from Bowers and co-workers suggested that hIAPP monomer and dimer undergo a conformational transition to an extended structure early in amyloid assembly (47, 48). Here, populations of monomer through hexamer have been detected, using ESI-IMS-MS, for both peptides. The hIAPP and rIAPP oligomers may assemble via monomer addition, since every species from monomer to hexamer is observed. No further monomer association into higher order oligomers is observed for hIAPP. Fibril formation may, therefore, occur either without a population of larger oligomeric intermediates, or with higher order states being occupied that are too lowly populated, too transient or too heterogeneous to be detected by ESI-IMS-MS.

CCS calculations of hIAPP oligomers indicate that elongated species, rather than globulamers, are popluated, akin to the oligomers observed during β_2m assembly into amyloid (93). Interestingly, oligomers of rIAPP are similar in size and CCS to those of hIAPP, as judged by ESI-IMS-MS, but are significantly more stable in the gas-phase as judged by CID experiments. Although solution-phase stability cannot be directly inferred from gas-phase stability (5, 228) the difference in stability observed may help towards explaining the difference in amyloid competence of the two peptides. Assuming that a conformational change is necessary for fibril formation, the greater stability of the rIAPP peptide may impede the structural re-organisation required for amyloid assembly whereas the less stable hIAPP peptide may transition readily.

It was also revealed that hIAPP and rIAPP can form hetero-oligomeric species en route to hetero-fibrils *in vitro*, thus rationalising why rIAPP is an inefficient inhibitor of hIAPP amyloid formation. In theory, rIAPP would be expected to be a good inhibitor of hIAPP since it combines a recognition motif with a β-sheet breaker unit (114). This study highlights, therefore, the pitfalls associated with designing peptide inhibitors based on amino acid sequence.

Having characterised the hIAPP oligomers, the binding and mode of action of two potent small molecule inhibitors of hIAPP (EGCG and silibinin) have been determined using ESI-IMS-MS. Data are presented which show show that both of the two small molecule inhibitors block oligomer and fibril assembly when added to hIAPP monomer, prior to initiation of assembly.

Interestingly, the two small molecules show different binding characteristics and have different effects on the equilibrium of species present, yet both inhibit oligomerisation and fibrillation to a similar extent. EGCG was found to bind to both observed charge states of the hIAPP monomer, inhibiting early oligomer formation in a dose-dependent manner and preventing fibril formation. By contrast, silibinin was found to bind only to the most expanded conformer of the monomer 3+ ion within the dynamic ensemble of intrinsically disordered monomeric conformations, blocking oligomerisation and fibrillation. The inhibitory effect of silibinin, despite such specific binding, supports the notion of the role of the extended state of the monomer 3+ species in the fibril assembly mechanism of hIAPP. The hIAPP conformer bound by silibinin is absent in rIAPP and hence this conformer may be an important amyloid precursor. Inhibition via monomer binding may inhibit assembly directly or, alternatively, binding may create a structure that associates with other monomers to generate non-amyloidogenic aggregates. EGCG and silibinin were found to be effective as amyloid inhibitors at sub-stoichiometric concentrations, suggesting that the small molecules may bind to oligomers, as well as the monomer. Due to the low intensity of oligomers in the presence of small molecules and the known disruption of hydrophobic interactions in the gas-phase, however, binding of small molecules to oligomeric species could not be observed by ESI-IMS.

Both EGCG and silibinin alter the equilibrium of the monomeric charge states of hIAPP present, with the presence of each small molecule favouring the population of the triply-charged monomer ions. Binding to these extended species that may be direct amyloid precursors (47, 48) then prevents monomer self-assembly into amyloid. ESI-IMS-MS studies on β_2m have previously demonstrated that altering the equilibrium between different monomeric conformers can have profound effects on the assembly pathways (44), diverting protein assembly from the amyloid pathway (resulting in highly-ordered β-sheet rich fibrillar assemblies) to non-amyloid pathways (resulting in the formation of spherical/amorphous aggregates). For hIAPP, these alternative aggregation pathways are presumably kinetically or thermodynamically unfavourable in the absence of the inhibitory small molecules, but made feasible upon ligand binding to more highly charged (3+), unfolded hIAPP monomers. In addition to inhibiting the forward reaction of amyloid assembly, both EGCG and silibinin are capable of disaggregating pre-formed hIAPP amyloid fibrils. Disassembly occurs in distinguishable manners for each small molecule, with EGCG remodelling fibrils into amorphous aggregates without reformation of low order oligomers, and silibinin depolymerising fibrils and re-establishing the pre-fibrillar array of monomer plus early oligomeric species.

Early oligomeric states are widely believed to be key to protein self-assembly and subsequent toxicity in amyloid disease; therefore elucidation of their structure and dynamics of pre-amyloid oligomers is of vital importance. Here, using ESI-IMS-MS the conformational properties of hIAPP monomer and oligomeric structures have been interrogated, revealing that specific, lowly-populated hIAPP monomeric conformers are capable of binding small molecule ligands. Having identified monomer through hexameric forms of hIAPP, the effect of ligand binding on each individual species populated within heterogeneous amyloid mixtures prior to fibril formation was assessed. The experimental results obtained provide support for a route to hIAPP amyloid fibrils via monomer addition to form oligomers which have relatively elongated structures. Stability may be related to the amyloidogenicity of IAPP, given that hIAPP is less stable relative to the non-amyloidogenic rIAPP peptide. hIAPP, therefore, may more readily unfold and occupy more extended

monomer and oligomeric conformations that have increased amyloid propensity. Binding to, and stabilising amyloid-prone monomer conformations, thereby preventing their polymerisation, could be key to the mechanism of inhibition of amyloid by EGCG and silibinin.

4.4 Conclusions

The data presented herein, and previously by Bowers and co-workers (47, 48), support a hypothesis that hIAPP self-assembly into amyloid begins initially with the formation of extended structures. Binding of small molecule inhibitors to these amyloid-prone extended structures results in alteration of the distribution of conformers present and results in the inhibition of oligomerisation and fibril formation by hIAPP. The results obtained demonstrate that stability plays a role in the sequence-dependence of IAPP amyloid competence, given that oligomers of the non-amyloidogenic rat peptide are similar in size and shape to those of the human peptide, but the former oligomers are significantly more stable in the gas-phase. In addition, results are presented which demonstrate that the mixing of hIAPP and rIAPP sequences leads to co-polymerisation into hetero-oligomers and hetero-fibrils, hence rationalising the lack of inhibition of hIAPP fibril formation by rIAPP.

Having characterised in detail the monomeric and oligomeric species occupied by hIAPP and having demonstrated the suitability of ESI-IMS-MS for studying small molecule-hIAPP interactions, the project progressed toward the screening of novel inhibitors of amyloid assembly.

5 Screening and classifying small molecule inhibitors of amyloid formation using ion mobility spectrometry-mass spectrometry

5.1 Introduction

The work described in this Chapter has been published in references (182, 229).

Due to the complex mechanisms involved in amyloid diseases and the elusive nature of toxic species, commonly available therapies focus only on ameliorating the symptoms (127). There are, however, a number of promising therapeutic avenues currently being investigated, including the use of small molecule inhibitors to block and/or re-direct aberrant aggregation pathways. The ability to screen for small molecules that are able to interfere with protein aggregation, and assess their mode of action, is therefore instrumental in the quest for novel therapies against protein misfolding disorders. For folded proteins, structure-based design can be utilised in order to create small molecules able to stabilise the native state and thus prevent the conformational changes that precede protein aggregation (230-232). For aggregation-prone proteins that are intrinsically disordered, discovery of novel small molecule inhibitors of aggregation is limited to screening assays that rely on relatively low resolution techniques, such as dye binding assays. The majority of biophysical techniques available lack the sensitivity and resolution to allow detection and individual characterisation of oligomeric states occupied during aggregation and, therefore, do not allow determination of the unique pre-fibrillar protein subspecies with which the small molecule inhibitor interacts (233). Another caveat is that dye binding assays are often compromised by competitive binding of the small molecule to the dye-binding site on the protein and by inner filter effects which can interfere with the fluorescence of the dye (234, 235).

ESI-IMS-MS circumvents the disadvantages of other *in vitro* screening techniques and enables the rapid identification of small molecule inhibitors, the characterisation of their mode of action, and the identification of the individual

subspecies with which the inhibitor interacts (44, 102, 181). In this chapter, the capability of ESI-IMS-MS to screen for, and analyse, the mode of interaction of a range of small molecules is demonstrated using hIAPP and Aβ40 as examples of aggregating systems. Screening using ESI-IMS-MS has a number of advantages over conventional biophysical screening methods: it is rapid (taking <1 minute/sample), consumes low amounts of sample (~1000 molecules screened/mg protein), does not require sample labeling or immobilisation, and provides stoichiometric and conformer-specific information. In addition, colloidal inhibitors that self-aggregate and physically sequester proteins non-specifically (236), that may erroneously be classified as "hits" in other assays, are immediately identified.

While several small molecules have been shown to inhibit the fibrillation of hIAPP and/or Aβ40 *in vitro* (102, 141, 144, 152, 157, 162, 237), including EGCG and silibinin detailed in **Chapter 4**, their mechanisms of action remain largely undetermined. Using the selection of small molecules described below (**Section 5.1.1**), we demonstrate the ability of ESI-IMS-MS to differentiate and classify compounds that do not bind ('negatives'), those that bind specifically ('positives'), and those that interact non-specifically or colloidally, with hIAPP and Aβ40 (**Figure 5-1**). Furthermore, we use the method developed to screen a further thirty compounds to demonstrate that it can be implemented in a high throughput mode and, in doing so, reveal new specific inhibitors of hIAPP and Aβ40 aggregation.
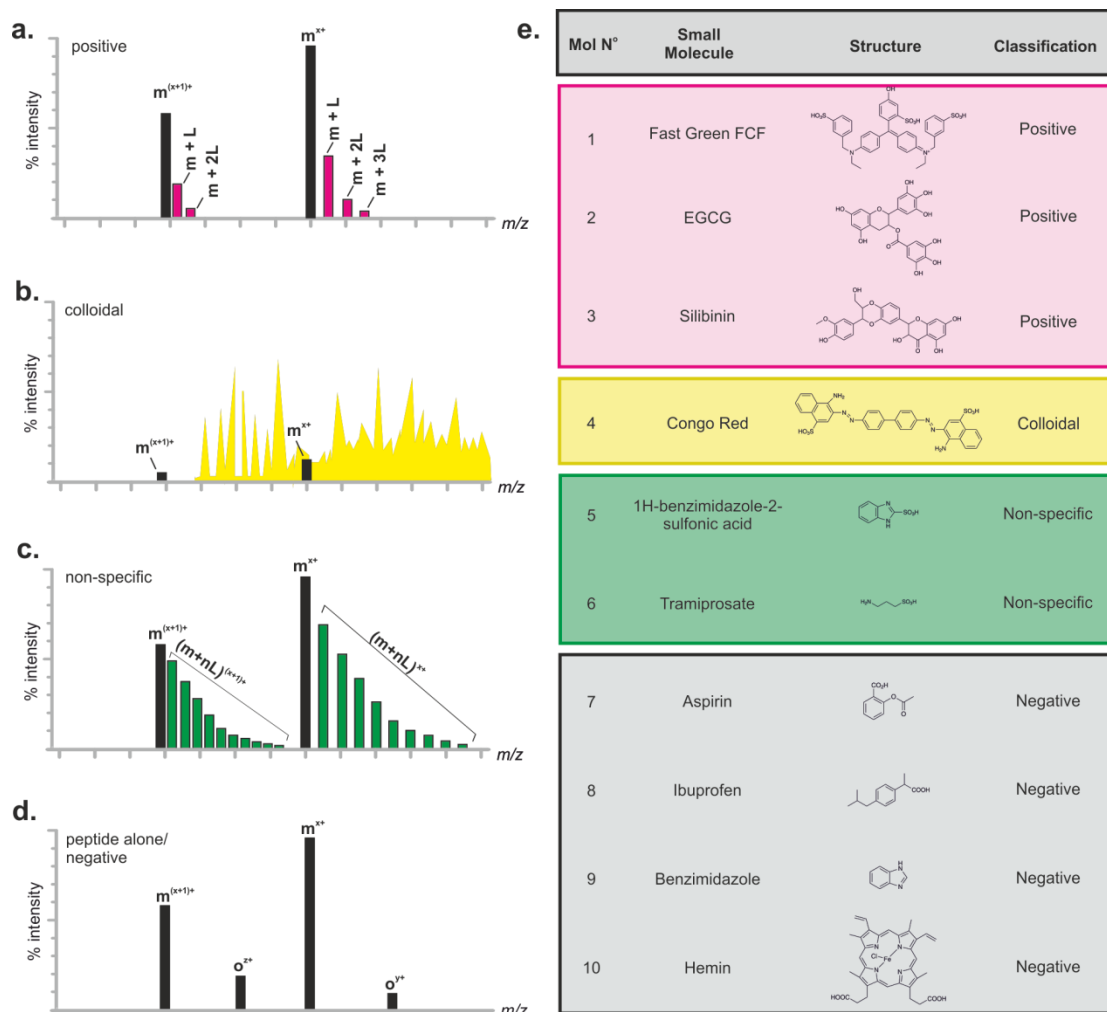
Figure 5-1. *Schematic diagram of the basis of the ESI-MS screen and a selection of the small molecules utilised for screen validation. (a-d) Schematic of expected ESI mass spectra resulting from different interactions between peptide/protein monomer (denoted m) and potential inhibitors (denoted L). Oligomers are denoted o; charge states are in superscript. (a) A specific ligand (termed 'positive') will result in a binomial distribution of bound peaks (pink)(238); (b) the presence of a colloidal inhibitor will lead to spectra containing overlapping peaks resulting from the heterogeneous self-association of the small molecule (orange peaks); (c) a non-specific ligand will bind and result in a Poisson distribution of bound peaks (green)(238); (d) the addition of a non-interacting small molecule (termed 'negative') will result in spectra similar to those of peptide alone; (e) list of ten small molecules analysed initially for inhibition of hIAPP aggregation during ESI-MS screen validation. Colours correspond to binding-mode classification by mass spectra (a-d); specific = pink, colloidal = yellow, non-specific = green, negative = grey. Figure taken from Young et al. (182).*

5.1.1 Selection of small molecules used for screen validation

'**Positives**': Fast green FCF (FG) (**1**), a triarylmethane food dye, has been shown previously to inhibit amyloid formation by hIAPP (239) and is used here as an example of inhibition by specific binding. Previous studies, described in **Chapter 4**, have shown that EGCG (102, 156, 158, 240, 241) (**2**) and silibinin (102, 219) (**3**) also act as specific inhibitors of hIAPP amyloid formation and are included here for comparison. EGCG is the most well characterised 'positive' aggregation inhibitor of a variety of proteins (e.g. α-synuclein (162), hIAPP (102, 156, 158, 240, 241) and Aβ40/42 (141, 156, 162, 181)) both *in vitro* and *in vivo* (139, 141, 156, 157, 162, 164, 242). In contrast, to our knowledge, silibinin has been reported to inhibit only hIAPP self-assembly (102, 219).

'**Colloidal**': Congo red (CR) (**4**), a dye commonly used to detect the presence of amyloid fibrils (243), was reported initially to bind to numerous protein aggregates (132, 243, 244), prevent aggregation *in vitro* (133, 245) and reduce neurotoxicity *in vivo* (246, 247). It has since been reported, however, to function via a colloidal mechanism (236). This mode of inhibition is likely due to the ability of CR to self-assemble into micelle-like species, driven by stacking of its aromatic rings (248).

'**Non-specific**': Tramiprosate (**6**) has been used as a negative control for hIAPP inhibition *in vitro* (237, 239). 1*H*-benzimidazole-2-sulfonic acid (1*H*-B-SA) (**5**), previously not assessed against hIAPP, was included in the analysis as it possesses a sulfonic acid moiety and is aromatic in nature, features known to be important for the interaction of small molecules with amyloid proteins and peptides (153).

'**Negatives**': Benzimidazole (**9**), hemin (**10**) and the non-steroidal anti-inflammatory drugs (NSAID) aspirin (**7**) and ibuprofen (**8**) contain charged and/or aromatic functional groups which are prevalent in known amyloid inhibitors, but have not been assessed previously for their interaction with hIAPP. Aspirin has been reported to inhibit fibrillogenesis of Aβ40 and Aβ42 (151, 249), and ibuprofen to reduce cognitive deficits *in vivo* and also to reduce Aβ aggregation i*n vitro* (250, 251). Benzimidazole was used in the screen described here to

determine whether the interaction observed between hIAPP and 1*H*-B-SA could result from the presence of a negatively charged sulfonated group interacting with the positively charged hIAPP in the gas-phase. Hemin has been reported previously to inhibit fibrillogenesis of Aβ (144), however, it has not been assessed for its interactions with hIAPP. The mass of molecules **1-10** are listed in **Table 5.1**.

No.	Compound	Average MW (Da)
1	Fast Green FCF ethyl-[4-[[4 -[ethyl-[(3-sulfophenyl) methyl] amino] phenyl]-(4-hydroxy-2-sulfophenyl) methylidene]-1-cyclohexa-2,5-dienylidene]-[(3-sulfophenyl) methyl] azanium	765.9
2	Silibinin (2*R*,3*R*)-3,5,7-trihydroxy-2-[(2*R*,3*R*)-3-(4-hydroxy-3-methoxyphenyl)-2-(hydroxymethyl)-2,3-dihydro-benzo[*b*][1,4]dioxin-6-yl]chroman-4-one	482.4
3	EGCG [(2*R*,3*R*)-5,7-dihydroxy-2-(3,4,5-trihydroxy-phenyl) chroman-3-yl] 3,4,5-trihydroxybenzoate	458.4
4	Congo red 4-amino-3-[4-[4-(1-amino-4-sulfonato-naphthalen-2-yl)diazenylphenyl]phenyl]diazenyl-naphthalene-1-sulfonate	652.7
5	*1H*-benzimidazole-2-sulfonic acid	198.2
6	Tramiprosate 3-Aminopropane-1-sulfonic acid	139.2
7	Aspirin 2-acetoxybenzoic acid	180.2
8	Benzimidazole 1*H*-benzimidazole	118.1
9	Ibuprofen (*RS*)-2-(4-(2-methylpropyl)phenyl)propanoic acid	206.3
10	Hemin chloro[3,7,12,17-tetramethyl-8,13-divinylporphyrin-2,18-dipropanoato(2−)]iron(III)	651.9

Table 5.1. *Molecular masses of small molecules initially screened, confirmed as MH+ ions using ESI-IMS.*

5.2 Results

5.2.1 hIAPP forms oligomeric assemblies and fibrils in absence of inhibitor

As described in detail in **Chapter 4 Section 4.2.1**, hIAPP (**Figure 5-2**a), occupies monomeric through to hexameric states, inclusively, under aggregating conditions. These oligomers, which are readily observed using ESI-MS and ESI-IMS-MS (**Figure 5-2**b&c), appear and subsequently disappear as aggregation proceeds, resulting in the formation of long straight amyloid fibrils (**Figure 5-2** inset).
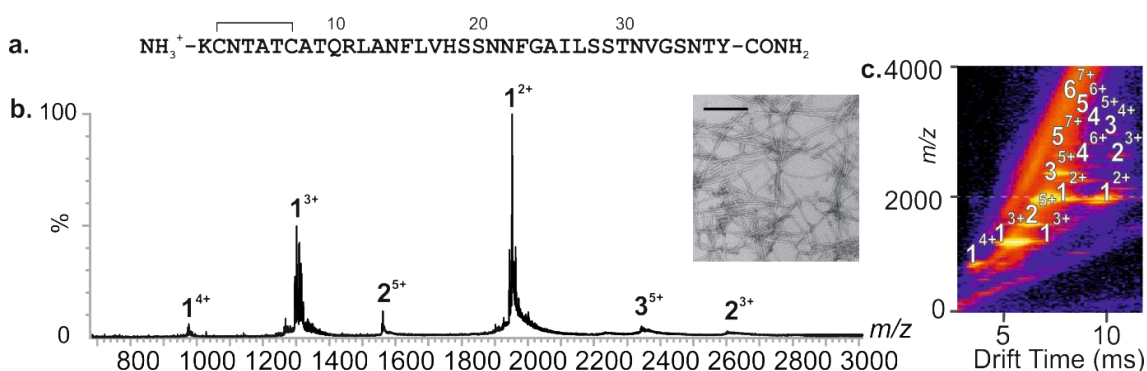
Figure 5-2. hIAPP forms an array of oligomeric species en route to long-straight amyloid fibrils. (a) Primary sequence of hIAPP. The peptide has a disulfide bridge between Cys-2 and Cys-7 and an amidated C-terminus; (b) ESI-MS mass spectrum of hIAPP. Numbers above peaks denote oligomer order, with the positive charge state of ions in superscript; (c) ESI-IMS-MS Driftscope plot of the hIAPP monomer (1) through hexamer (6), present 2 min after diluting the monomer to a final peptide concentration of 32 μM in 200 mM ammonium acetate, pH 6.8. ESI-IMS-MS Driftscope plots show IMS drift time versus mass/charge (m/z) versus intensity (z = square root scale). Inset: negative stain TEM image of hIAPP fibrils after 5 days in 200 mM ammonium acetate pH 6.8 buffer (25 °C, quiescent) (scale bar = 100 nm). Figure taken from Young et al. (182).

5.2.2 ESI-IMS-MS-based screening approach

10 compounds (**Section 5.1.1** and **Table 5.1**) were evaluated initially in order to determine their mode of action and/or inhibition of hIAPP self-assembly (**Figure 5-1**), based on their known effect on hIAPP aggregation. These compounds, or their analogues, have been proposed previously to inhibit, or not inhibit, amyloid formation, as described in **Section 5.1.1**. In each case, molar ratios of small molecule: hIAPP of 1:1 and 10:1 were used, with a hIAPP concentration of 32 μM in every case. Upon incubation of the peptide with each of the small molecules in 96-well plates, samples were infused into the mass spectrometer via an automated sampler and the monomer and oligomer populations occupied were characterised immediately. Small molecule binding modes were then observed and classified (**Section 2.2**) (**Figure 5-3**). Depending on the system, this technique can be implemented successfully to determine and rank ligand binding affinities (252-254). However, because hydrophobic interactions are not wholly maintained in the ESI-IMS-MS process, underestimation of binding affinity and/or false negative results are possible (228). For this reason, fibril formation was also monitored using ThT fluorescence and the morphologies of the resulting aggregates were assessed using negative stain TEM. The objectives of these analyses were to (i) observe interactions between amyloid peptide monomeric/oligomeric states and each small molecule; (ii) determine how these interactions affect the distribution of monomeric and oligomeric conformers populated; and (iii) elucidate whether any changes observed can be correlated with the inhibition (or lack of inhibition) of hIAPP amyloid assembly.
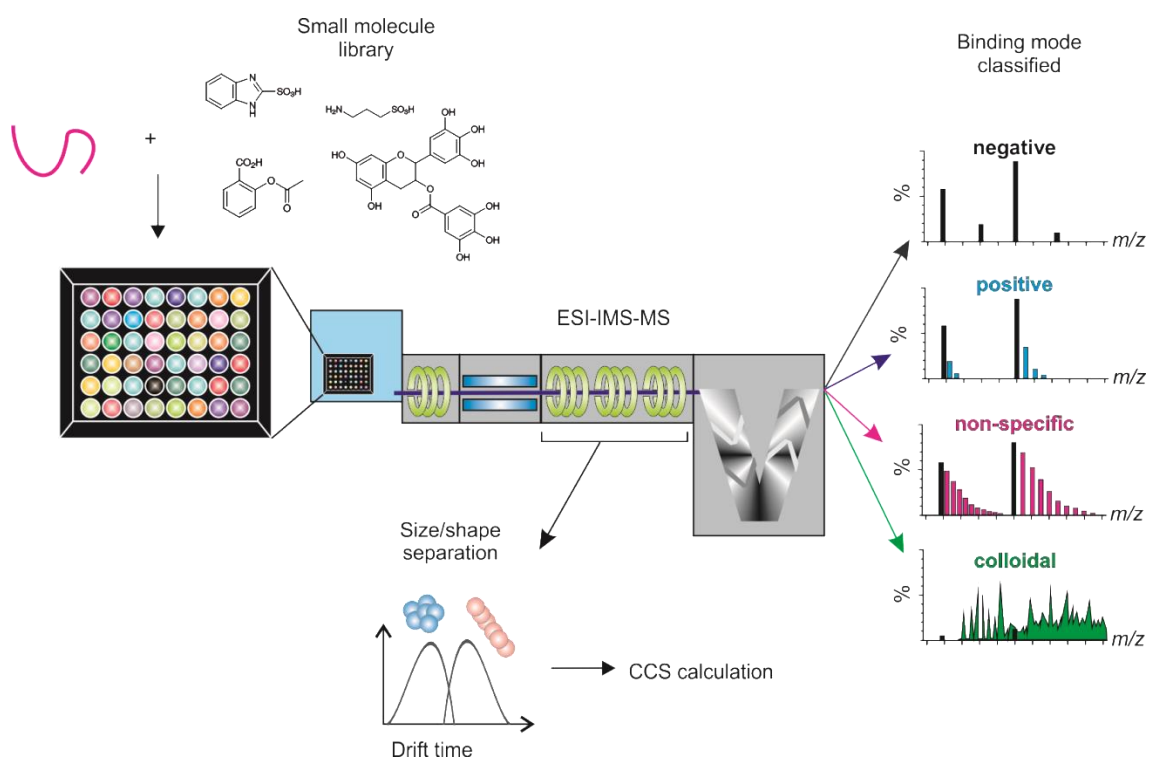
Figure 5-3. *Schematic of the ESI-IMS-MS experimental procedure. The protein of interest (pink) is mixed individually with small molecules from a compound library in 96-well plate format via a Triversa NanoMate automated nano-ESI interface, the samples are infused into the mass spectrometer, wherein separation occurs based on the mass to charge ratio (m/z) and collisional cross-sectional area (CCS). The small molecules are classified according to their protein-binding modes. Figure taken from Young et al. (229).*

5.2.3 Mode of action of a positive inhibitor of hIAPP fibril assembly

One of the 10 compounds selected for preliminary analyses (**Section 5.1.1** and **Table 5.1**) was Fast Green FCF (**1**) (FG), a known inhibitor of hIAPP fibril formation (239).

Consistent with previous reports (239), ThT fluorescence and TEM (**Figure 5-4**a,b) confirmed that FG inhibits fibril formation from hIAPP *in vitro*. The mechanism by which it inhibits assembly, however, has thus far remained elusive. Here, using ESI-IMS-MS, FG was found to bind to both the 2+ and 3+ monomer charge states of hIAPP (**Figure 5-4**c ii-iii).

121
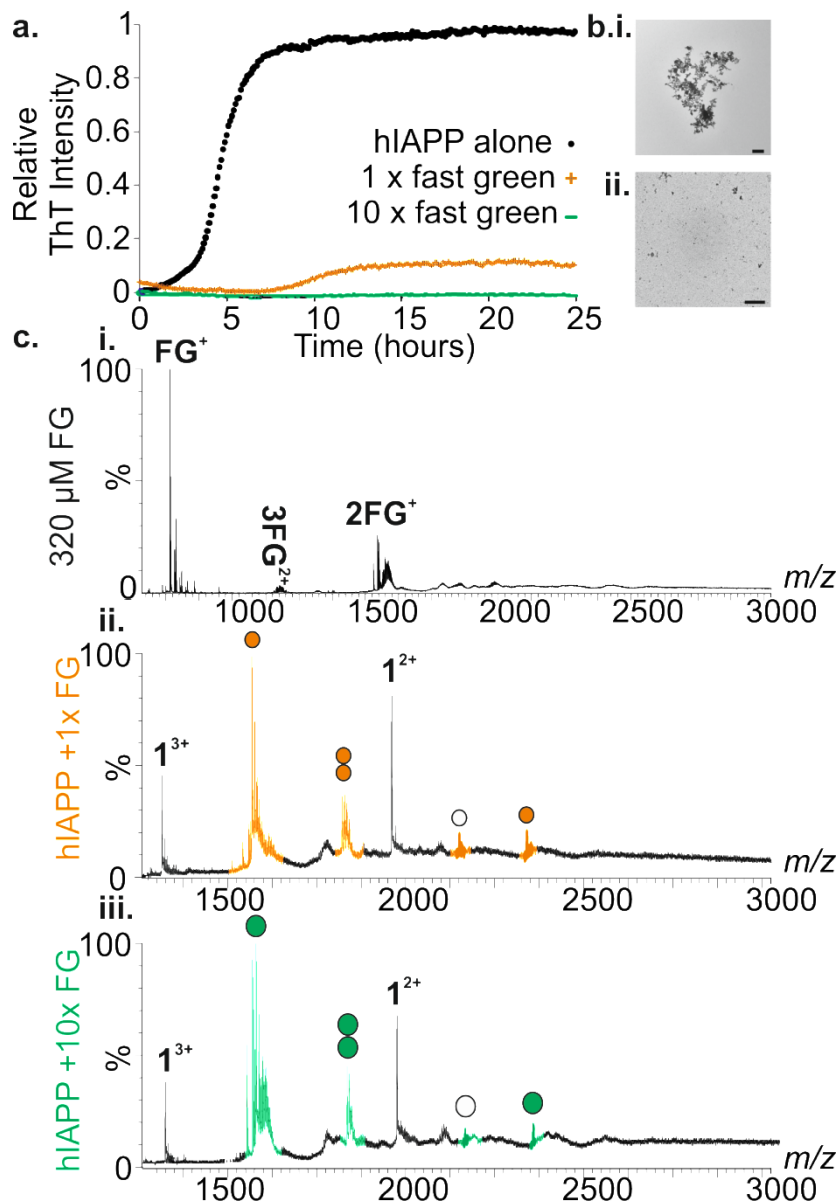
Figure 5-4. *Inhibition of hIAPP amyloid assembly by Fast Green FCF (FG). (a) ThT fluorescence intensity over time of hIAPP alone (black circles) (32 µM peptide, 200 mM ammonium acetate buffer, pH 6.8, 25 °C, quiescent) and with increasing FG:hIAPP molar ratios: 1:1 (orange) and 10:1 (green), showing dose dependant decrease in formation of ThT-postive hIAPP species upon addition of FG. (b) Negative stain TEM images of hIAPP incubated with (i) 1:1 or (ii) 10:1 molar ratios of FG:hIAPP for 5 days (25 °C, quiescent) (scale bar = 100 nm), showing lack of fibrillation and formation of small/amorphous aggregate of hIAPP in the presence of FG. (c) Positive ion ESI mass spectra showing FG alone (i), or added at 32 µM (ii), or 320 µM (iii), to hIAPP (32 µM). FG binds to the 2+ and 3+ charge state ions of hIAPP monomer (bound peaks denoted with orange or green circles; number of circles represents number of ligands bound), and to the 4+ charge state of the hIAPP dimer (bound peak denoted with white circle). This binding mode is classified as 'positive'. Figure taken from Young et al. (182).*

The work described in **Chapter 4** (102), and that of others (48), has shown that each hIAPP monomeric charge state (2+ and 3+) populates at least two conformers (extended and compact, with the more expanded structure proposed to be amyloid-prone). Analysis of the ESI-IMS-MS data reveals that FG alters the distribution of charge states and the monomeric conformers present, increasing the relative abundance of the 3+ monomer ion (**Figure 5-4**c). In addition, the proportion of compact conformers is increased compared with those observed for hIAPP alone, especially obvious for the monomer 2+ ion (**Figure 5-5**). This ion appears to be significantly compacted in the presence of FG, with dominant conformer changing in drift time from 7.05 to 6.28 ms and a new, even more compacted species emerging with a drift time of 5.25 ms (**Figure 5-5**).
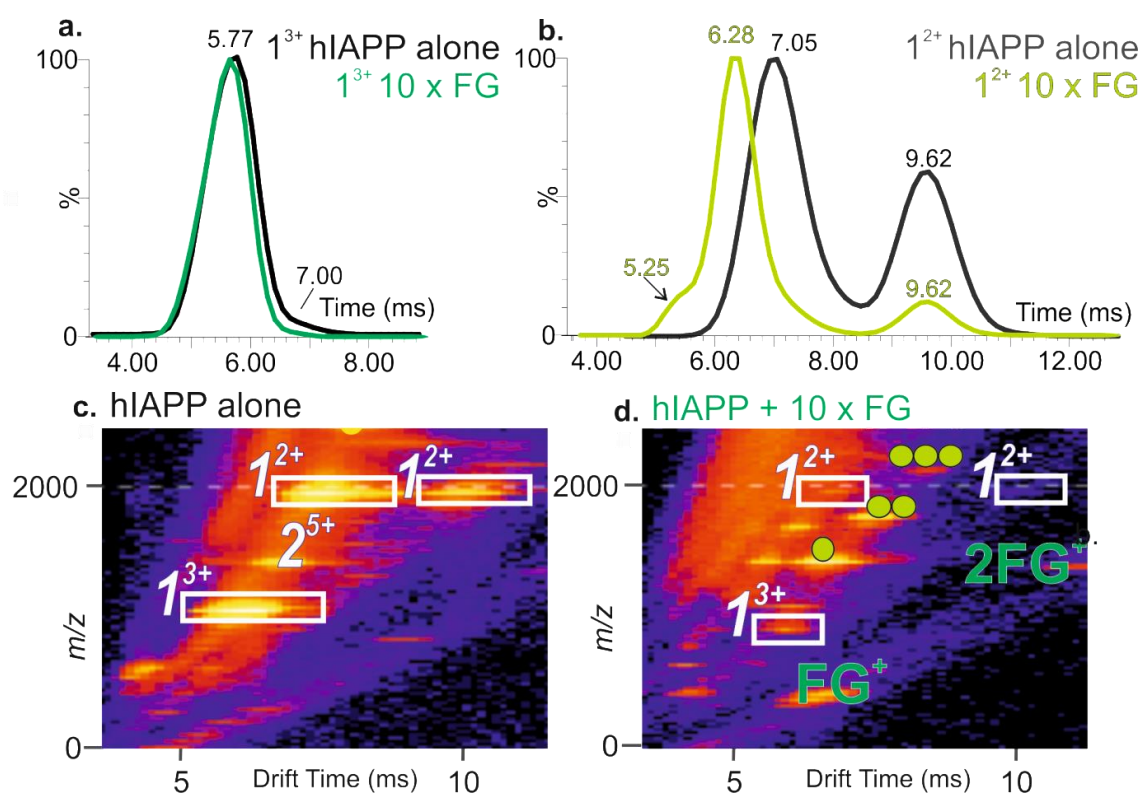
Figure 5-5. *Comparisons of hIAPP monomer drift times in the absence (black) or presence (green) of excess FG. (a) Arrival time distribution (ATD) of the hIAPP 3+ monomer ions displays one distinct conformer (drift time = ~5.8 ms) and a small component of a more extended conformation (drift time = ~7.0 ms) in the absence and presence of FG; (b) Arrival time distribution (ATD) of the hIAPP 2+ monomer ions displays two distinct conformers in the absence of FG (drift times = ~7.1 and ~9.6 ms). In the presence of FG, the hIAPP 2+ monomer displays three distinct conformers (drift times = ~5.3, ~6.3 and ~9.6 ms); (c) ESI-IMS-MS Driftscope plots of monomeric conformers observed for hIAPP alone; and (d) when FG is present at a 10-fold molar excess over hIAPP. Monomer peaks are enclosed by white boxes. Circles represent number of FG molecules bound to each species. Figure taken from Young et al. (182).*

The interaction of FG likely involves the sulfonated groups forming favorable electrostatic interactions with positively charged hIAPP at pH 6.8 (hIAPP pI $\simeq$ 8.9). Consistent with this, the extent of binding is dependent on the buffer ionic strength (**Figure 5-6**a), with a lesser extent of binding being maintained as the ionic strength of the buffer is increased from 10 mM to 100 mM.
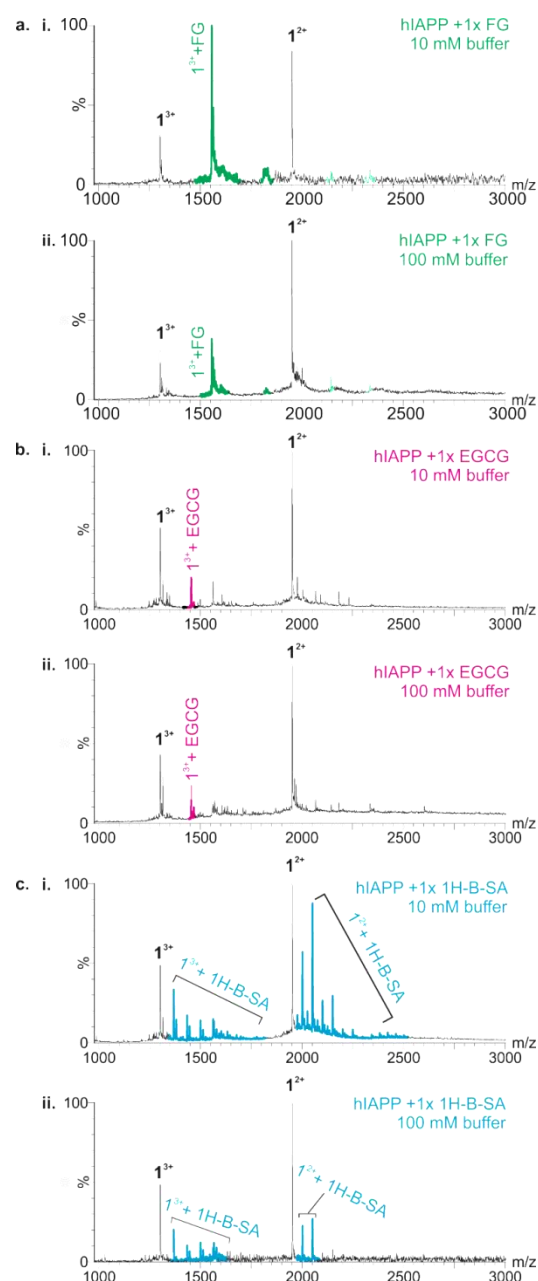
Figure 5-6. *Ionic strength dependence of ligand binding. Positive ion ESI mass spectra showing (a) FG; (b) EGCG; and (c) 1H-B-SA added at a 1:1 molar ratio to hIAPP (32 µM) in 10 mM (a. i, b. i, c. i) or 100 mM (a. ii, b. ii, c. ii) ammonium acetate buffer, pH 6.8. Ligand bound peptide peaks are highlighted in green (FG), pink (EGCG) and blue (1H-B-SA). Figure taken from Young et al. (182).*

Factors other than electrostatic complementarity must contribute to the specific binding of FG, however, as not all sulfonated small molecules are inhibitors of hIAPP amyloid assembly (**Section 5.1.1**, **Figure 5-1**e and **Figure 5-10**). For the two other known positive inhibitors described in **Chapter 4**, EGCG (102, 157) (**2**) and silibinin (102, 219) (**3**), low levels of binding are observed, despite complete inhibition of fibrillation, indicative of hydrophobic interactions playing a role in the binding interface. Unlike the hIAPP-FG interaction, this mode of binding is relatively insensitive to buffer ionic strength (**Figure 5-6**b), with comparable amounts of ligand binding being observed as the ionic strength of the buffer is increased from 10 mM to 100 mM.

5.2.4 Colloidal inhibition characterized using ESI-IMS-MS

The influence of the presence of Congo red (CR) (**4**), a known colloidal inhibitor, on the self-assembly of hIAPP was analysed next (243). At a 1:1 molar ratio of hIAPP: CR, a small increase in the rate of fibril formation was observed (**Figure 5-7**a,b), with no significant change in the monomer or oligomeric states observed in the hIAPP mass spectrum (**Figure 5-7**a-c). However, at a 10:1 molar ratio of CR: hIAPP, no fibrillation was observed (**Figure 5-7**a,b). These data are consistent with previous reports that CR promotes fibril formation in some systems at low concentrations (255) but inhibits protein self-assembly when present at high concentrations (100-200 μM)(236).
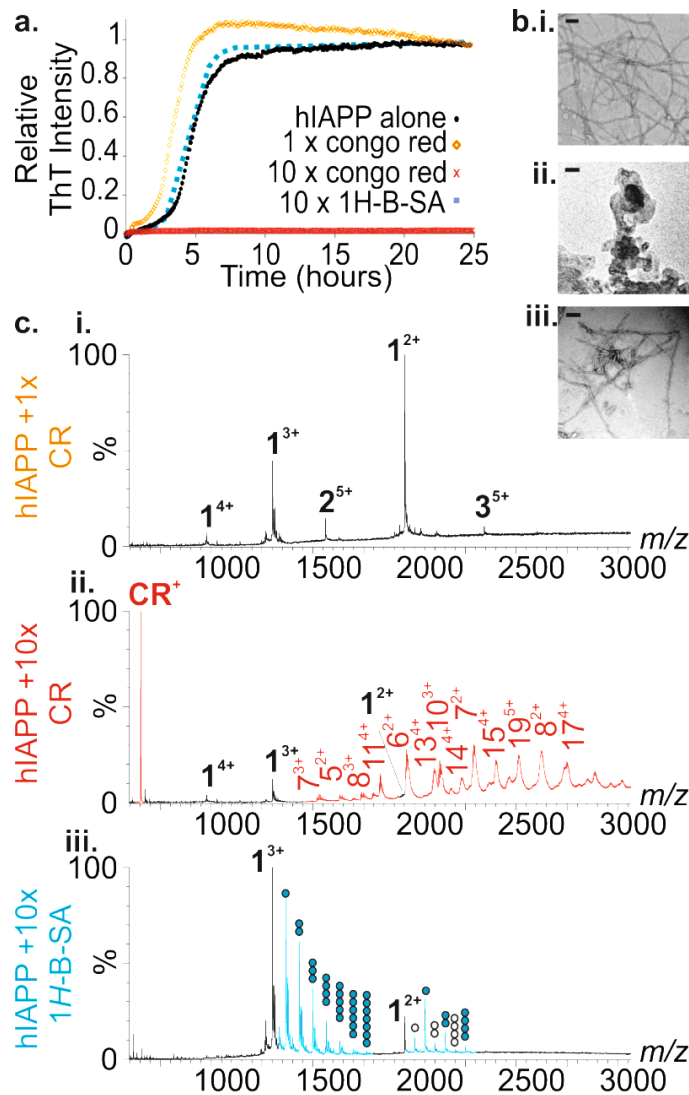
Figure 5-7. *Colloidal inhibition and non-specific binding observed using ESI-IMS. ThT fluorescence intensity of hIAPP (black) (32 μM peptide, 200 mM ammonium acetate buffer, pH 6.8, 25 °C, quiescent) with Congo red (CR):hIAPP molar ratios: 1:1 (orange) and 10:1 (red) and with 1H-benzimidazole-2-sulfonic acid (1H-B-SA):hIAPP molar ratio: 10:1 (blue). Significant inhibition of the formation of ThT-positive species is observed only in the presence of excess (10x)CR. (b) Negative stain TEM images of hIAPP incubated with 1:1 (i) or 10:1 (ii) molar ratios of CR or a 10:1 molar ratio of 1H-B-SA (iii) for 5 days (25 °C, quiescent) (scale bar = 100 nm). Fibrils are observed in the presence of equimolar CR and excess (10x) 1H-B-SA but not in the presence of excess (10x)CR. (c) Positive ion ESI mass spectra showing CR added at 32 μM (i) or 320 μM (ii) or 1H-B-SA added at 320 μM (iii), to hIAPP (32 μM). CR is not observed to bind to hIAPP when added at 32 μM (i) or 320 μM (ii), however CR self-aggregates at 320 μM (ii) (denoted n^{x+}, where n is the number of CR molecules and x is the charge state of the aggregate (red peaks). This binding mode is classified as colloidal. Multiple copies of 1H-B-SA bind to the 2+ and 3+ charge state ions of hIAPP monomer (bound peaks denoted with blue circles, number of circles represents number of ligands bound), and to the hIAPP dimer (bound peaks denoted with white circles). This binding mode is classified as non-specific. Figure taken from Young et al. (182).*

Using ESI-IMS-MS, it is possible to observe the self-association of CR at high concentrations (320 µM), with aggregates ranging in size from ~5-11 copies (**Figure 5-8**). No direct binding of CR monomer to monomeric hIAPP was observed (**Figure 5-7**c), consistent with colloidal inhibition resulting from supramolecular assemblies of CR inhibiting self-association of amyloid proteins at high ligand concentrations.
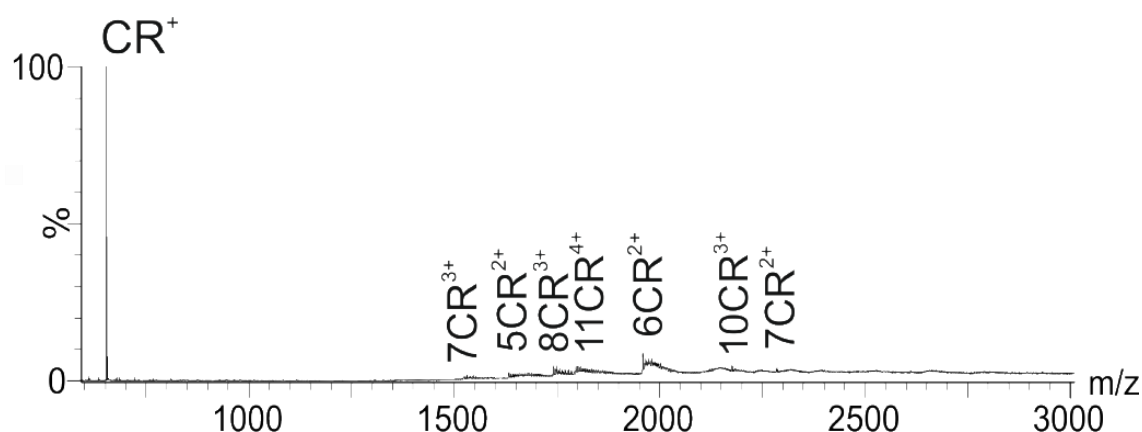
Figure 5-8. *ESI-MS spectrum of 320 µM Congo red (200 mM ammonium acetate, pH 6.8), showing self-aggregation (5- to 11-mers). Figure taken from Young et al. (182).*

5.2.5 Non-specific binding and lack of inhibition characterised using ESI-IMS-MS

Although not reported previously as an inhibitor of hIAPP amyloid formation, 1*H*-B-SA (**5**) possesses both aromatic and anionic moieties known to be important for the interaction of small molecules with amyloid proteins and peptides (153). The mass spectrum of a 10:1 molar ratio of 1*H*-B-SA and hIAPP clearly demonstrates a non-specific binding profile which results in a series of ions with multiple ligands bound, following a Poisson-like distribution (238, 252) (**Figure 5-7**c iii.). As an interaction of this type (electrostatic/hydrophilic) is often determined by charge and size complementarity, it is less sensitive to structure but can be well maintained during the ESI process (252). Further, these types of interactions can be more stable in the gas-phase than hydrophobic interactions (254), such as

127

thoseproposed between hIAPP and EGCG (**2**)(102) thus resulting in more extensive ligand-binding being observed for non-specific interactions with respect to specific interactions. Consistent with this, the ion intensity of the 1*H*-B-SA: hIAPP complex is decreased at increased ionic strength (**Figure 5-6**c), with less intense bound peaks being observed when the ionic strength of the buffer was increased from 10 mM to 100 mM. Non-specific interactions can be distinguished from specific interactions (that show a binomial distribution (238)) by comparison of the binding profiles (**Figure 5-1**a and c). To confirm annotation as a non-specific binding ligand, a second analysis performed at lower ligand: peptide ratio may be required to avoid ambiguity that may arise by specific binding of molecules forming multiply bound complexes at high ligand: peptide ratios. ThT fluorescence and TEM data confirm that the non-specific binding of 1*H*-B-SA to hIAPP does not inhibit fibril formation by the peptide (**Figure 5-7**a,b). Similarly, the mass spectrum of a 10:1 molar ratio of tramiprosate (3-amino-1-propanesulfonic acid) (**6**) and hIAPP is also indicative of a non-inhibitory, non-specific interaction, which is confirmed by TEM (**Figure 5-9**).
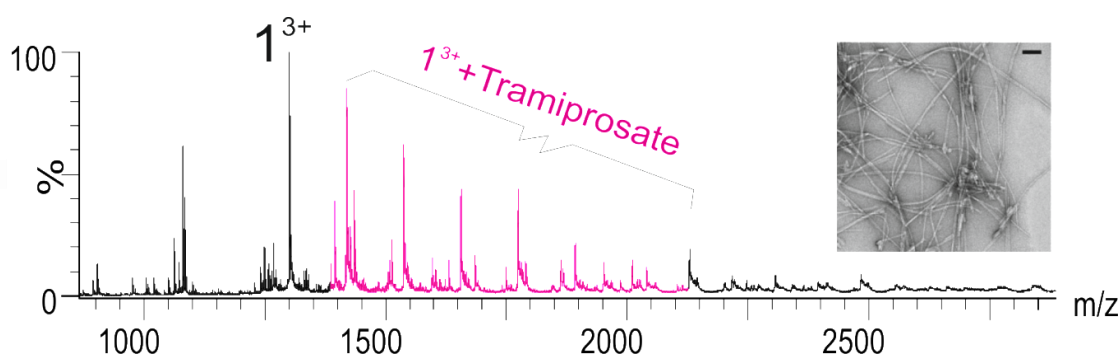
Figure 5-9. *ESI-MS spectrum of hIAPP (32 μM) in the presence of tramiprosate(320 μM). Protein-ligand bound peaks are coloured pink. Inset shows negative stain TEM image of fibrils formed by hIAPP when incubated with a 10:1 molar ratio of tramiprosate: hIAPP for 5 days (25 °C, quiescent) (scale bar = 500 nm). Figure taken from Young et al. (182). Contaminants in small molecule sample lead to peak broadening and adducts.*

Although non-specific binding interactions between ligands and the amyloid protein are encountered in some instances due the nature of the screen, a lack of any interaction between ligand and peptide is the most likely scenario in the absence of an inhibitory effect. Indeed, for the compounds aspirin (**7**), ibuprofen (**8**), benzimidazole (**9**) and hemin (**10**) (**Section 5.1.1** and **Table 5.1**), no evidence for binding to monomeric hIAPP, alteration in the monomer charge state distribution, or oligomer population, was observed using ESI-IMS-MS (**Figure 5-10**). In each case, incubation of hIAPP with an excess of a non-binding small molecule, fibrils were formed, as observed by TEM (**Figure 5-10** a-d inset). Earlier studies using CD spectroscopy and Congo red binding assays incorrectly determined that aspirin is an inhibitor of hIAPP amyloid formation (256), demonstrating the efficacy of ESI-IMS-MS in circumventing false positive results.
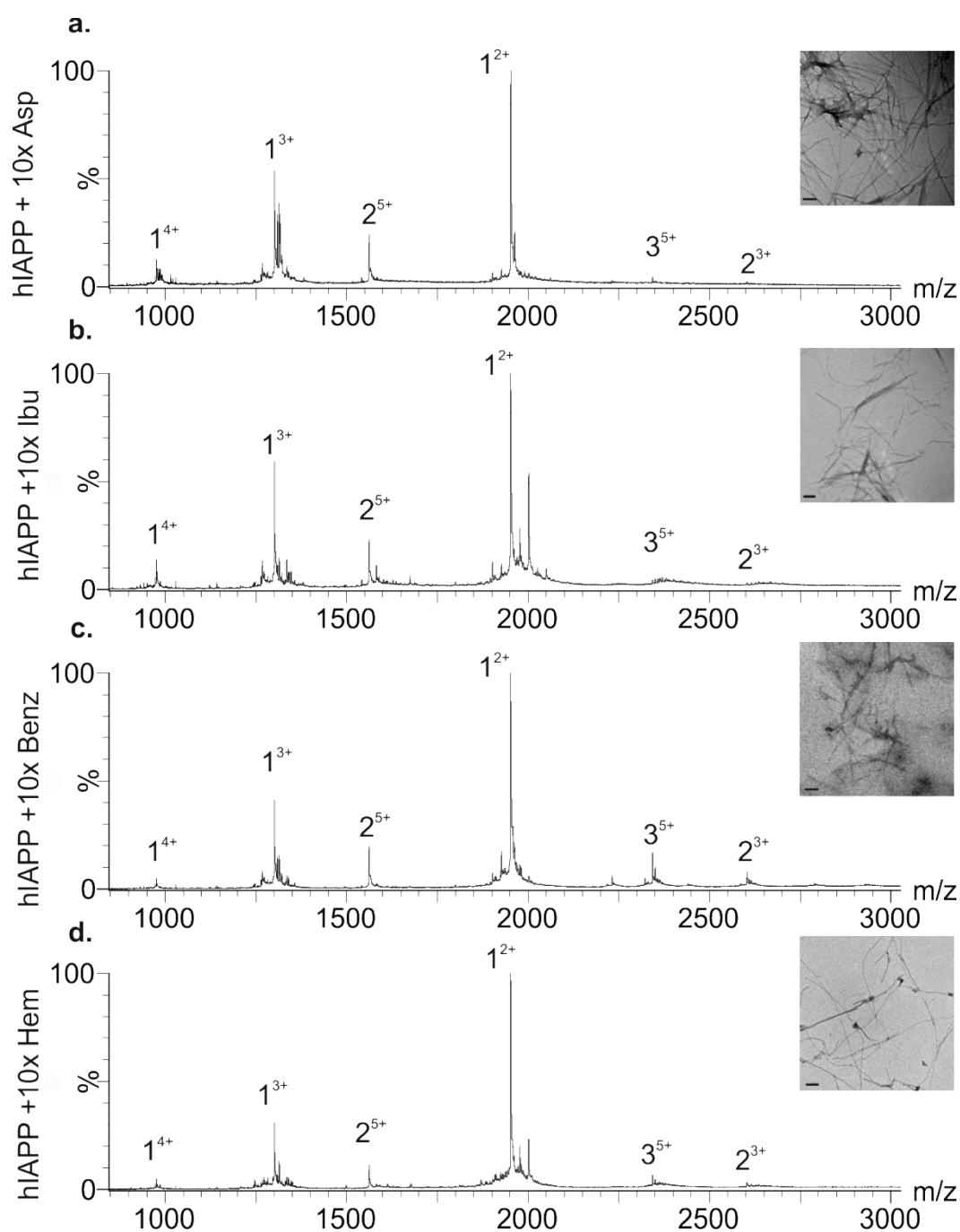
Figure 5-10. *Lack of inhibition of hIAPP amyloid assembly by (a) aspirin; (b) ibuprofen; (c) benzimidazole; and (d) hemin. Positive ion ESI mass spectra showing no observed binding when each small molecule is added at 320 μM to hIAPP peptide (32 μM). Insets: negative stain TEM images of hIAPP incubated with 10:1 molar ratios of small molecule: hIAPP for 5 days (25 °C, quiescent) (scale bar = 100 nm). Figure taken from Young et al. (182).The peak at m/z 2000 in the hIAPP + 10 x ibuprofen spectrum is an adduct that results from contaminants in the small molecule sample.*

The relationship between the structure of a small molecule, including the functional groups that it possesses, with its ability to interact with a peptide or protein of interest is not straight-forward. Indeed, predicting the inhibitory potential of small molecules against amyloid formation from their structure alone is a significant challenge, demonstrated by the fact that analogues can show significant variability in aggregation inhibition. Rifamycin SV, for example, can block fibril formation by β_2m, while other structurally similar rifamycins are ineffective (44). Similarly, derivatives of EGCG have marked differences in their inhibitory capacity (158), and no single feature of EGCG is crucial in determining inhibition (158). In order to investigate the diversity in hydrophobicity of the compounds tested and to determine whether there is any correlation with their ability to inhibit amyloid formation, the LogP value (the log of the aqueous/hydrophobic partition coefficient) of each small molecule was calculated using www.molinspiration.com software, which determines the hydrophobic parameters of the substituents (**Figure 5-11**). The LogP values of the positive inhibitors range from -4.4 (FG) to +2.2 (EGCG), demonstrating that polarity is not the only important factor required for binding to target. Both hydrophilic FG and hydrophobic EGCG inhibit hIAPP aggregation, confirming that the MS-based method for screening inhibitors is capable of observing both electrostatic and hydrophobic interactions between amyloidogenic peptides and aggregation inhibitors.
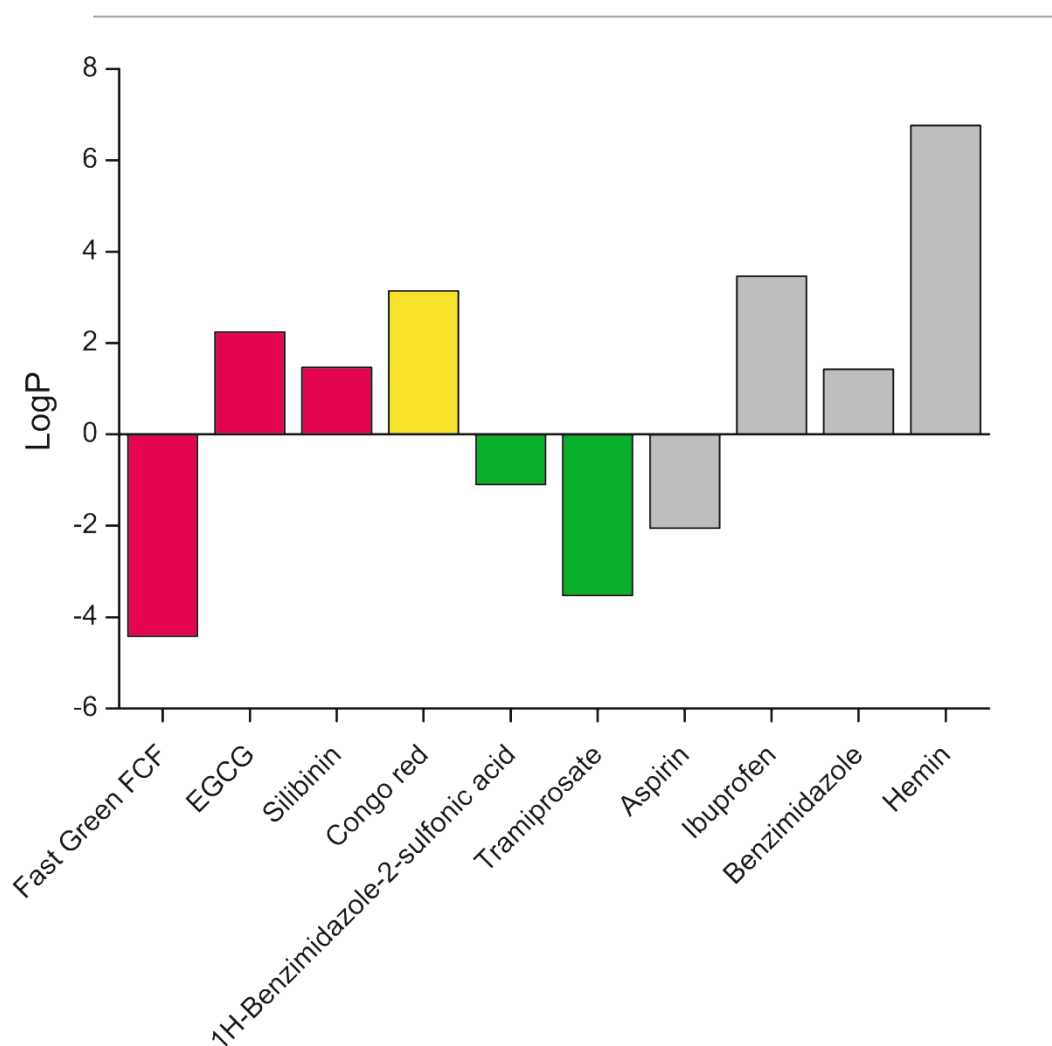
Figure 5-11. *LogP values (the log of the aqueous/hydrophobic partition coefficient) were calculated for the ten small molecules. using www.molinspiration.com software, which determines the hydrophobic parameters of the substituents. Molecules with high +ve LogP values have high hydrophobicity and molecules with high -ve LogP values are highly polar. Colours denote inhibitor classification: positive (red), colloidal (yellow), non-specific (green) and negative (grey). Figure taken from Young et al. (182).*

Further analyses using Collision Induced Dissociation (CID) MS/MS (**Section 2.2.4**) showed that the specific inhibitors bind more tightly to hIAPP than their non-specific counterparts, as judged by the gas-phase stability of the peptide-ligand complexes (**Figure 5-12**). The quadrupole analyser was used to select ligand-bound peptide ions and increasing collision energy was applied to the trap collision cell in 10 V increments from 10 to 100 V until the ligands were completely dissociated from the monomer ions. Quantification of precursor ion intensity relative to total ion intensity was calculated using area under peaks.

Indeed, 1*H*-B-SA dissociates from hIAPP at lower collision energies (10 V) than that required to dissociate either the hydrophobically bound 'positive' EGCG or the electrostatically bound 'positive' FG, which begin to dissociate after 30 and 50 V, respectively. This MS/MS method of interrogation provides an additional means of selecting ligands for further analysis after the initial screening for binding has been performed.
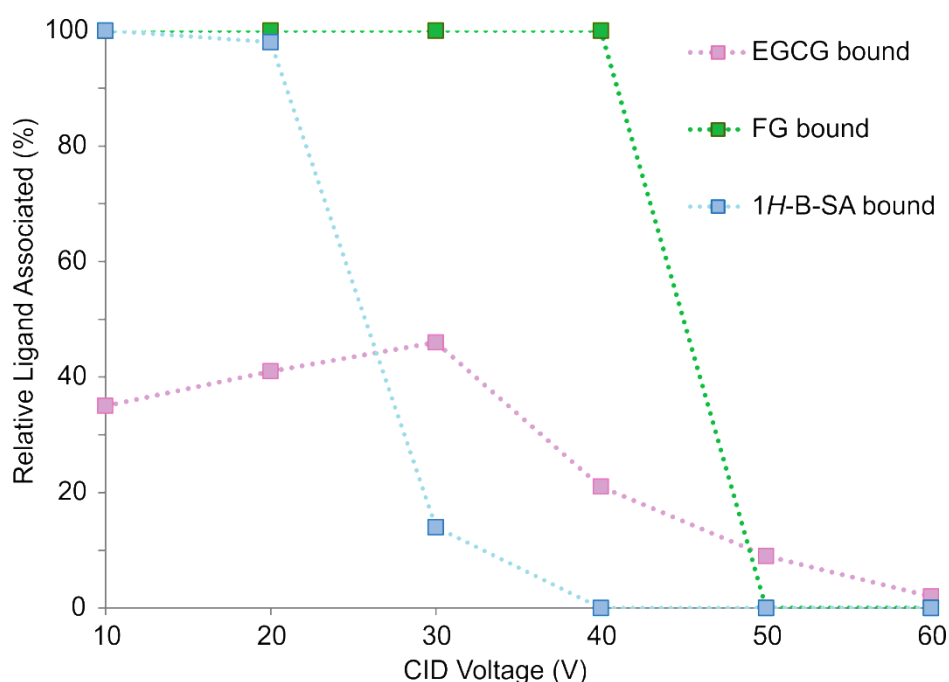
Figure 5-12. *Differences between peptide-ligand complex stabilities in the gas-phase measured using Collision Induced Dissociation (CID). CID MS/MS of FG-hIAPP (green), EGCG-hIAPP (pink) and 1H-B-SA-hIAPP (blue) complexes (32 μM peptide, 320 μM ligand, 200 mM ammonium acetate buffer, pH 6.8). Relative intensity of the 2+ monomer ions bound to ligand is plotted versus increasing ion-accelerating voltage into the trap collision cell. Percentage of ligand associated is relative to base peak in spectrum, which in the case of FG and 1-H-B-SA is ligand bound peptide and in the case of EGCG is apo-hIAPP. Figure taken from Young et al. (182).*

Arrival time distribution (ATD) plots from ESI-IMS-MS experiments also provide evidence for the type of interaction occurring. By extracting the whole-spectrum IMS-MS ATD data, observation of the average conformation of species present within a heterogenous mixture is enabled. The samples may consist of a mixture of protein-only species, ligand-only species and ligand-bound protein species. In the absence of small molecule, the hIAPP alone whole-spectrum ATD (**Figure 5-13**a) is comprised of intense peaks at short drift times (~3-10 ms) owing largely to the presence of the monomeric ions and less intense oligomeric contributions at longer drift times (~7-17 ms). With FG bound, there is a shift in the ATD plot towards more compact hIAPP monomeric protein species (compare **Figure 5-13**a and b). Additionally, there is a decrease in the oligomeric contributions at longer drift times in the presence of FG, likely due to inhibition of monomer assembly. When CR is bound, the overall ATD shifts to longer drift times (**Figure 5-13**c) due to the presence of CR aggregate and no compaction of the monomer is observed. In the presence of 1*H*-B-SA, a tail in the hIAPP monomer ATD profile is observed due to the presence of the non-specific binding (**Figure 5-13**d). There is an absence of species having longer drift times, possibly due to large amounts of non-specific binding masking signal from any lowly populated oligomeric states occupied in the presence of 1*H*-B-SA. The changes in whole-spectrum ATDs demonstrated can be explained more clearly when analysing Driftscope plots (**Section 5.2.6**) that allow unambiguous identification of every individual species present.
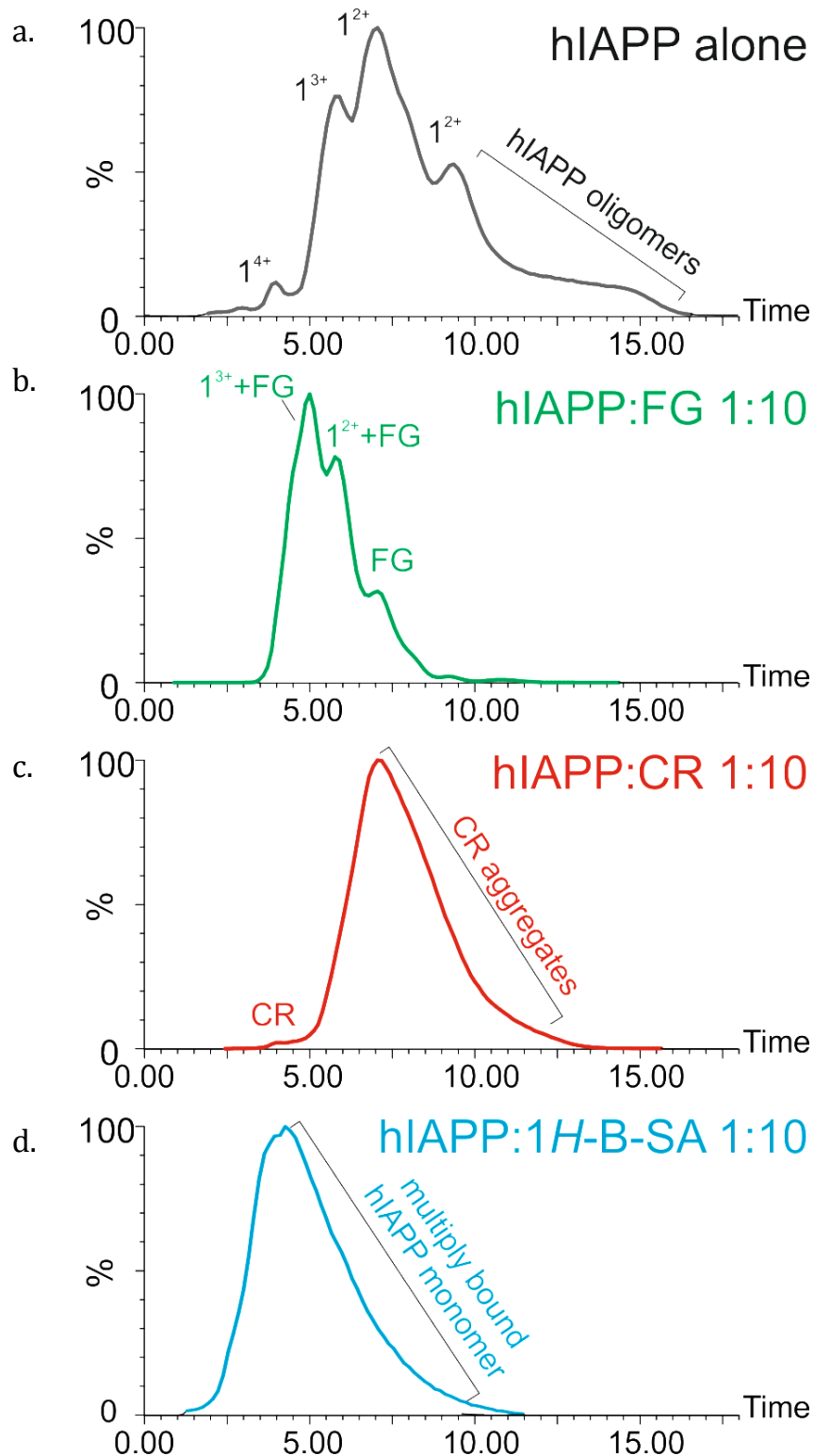
Figure 5-13. *ATDs of hIAPP in the absence or presence of inhibitors. Comparisons of whole spectra arrival time distributions (ATDs) of hIAPP (a) in the absence (grey) or presence of a 10-fold molar excess of (b) FG (green), (c) CR (red) or (d) 1H-B-SA (blue). Figure taken from Young et al. (182). A clear overall compaction of hIAPP monomeric conformations is observed in the presence of FG (b)with respect to hIAPP alone (a).*

5.2.6 Oligomer formation in the presence of small molecule inhibitors

The ability of ESI-IMS-MS to monitor oligomerisation of amyloid proteins enables the screen not only to observe binding of ligands to a protein monomer of interest, but further, to determine the impact this binding may or may not have on the higher order species populated in the aggregation landscape. Here, ESI-IMS-MS was utilised to determine the individual nature and abundance of the lowly-populated hIAPP oligomers in the presence of each class of small molecule. In the absence of small molecule, hIAPP forms monomer through hexamer, inclusively, within 2 minutes of dilution into buffer (**Figure 5-2**c) (102). In the presence of a 10-fold molar excess of a 'negative', non-interacting small molecule such as ibuprofen (**8**), the same array of oligomers is observed as for the peptide alone (**Figure 5-2**c and **Figure 5-14**a). When a 'positive' specific inhibitor (e.g. FG) (**1**) is present, binding of the small molecule to the peptide monomer is observed, with an absence of higher order hIAPP species detected (**Figure 5-14**b). This lack of oligomers is likely due to perturbation of self-assembly achieved by small molecule binding to the monomeric peptide. When a non-specific binder (e.g. 1*H*-B-SA (**5**)) is present, multiple copies of ligands (≤ seven molecules) can be seen binding to each monomeric charge state (**Figure 5-14**c), indicative of a non-specific interaction. Conversely, the spectrum of hIAPP in the presence of CR (**4**) (**Figure 5-14**d) shows a multitude of higher order species. However, the majority of these peaks have *m/z* values corresponding to multimers of CR, rather than hIAPP, resulting from self-association of the small molecule alone. Peptide monomers are observed in the spectrum, but no peptide oligomers are visible, resulting either from their low intensities compared with CR aggregates, or their absence. The ESI-IMS-MS data presented reveal clear differences between the spectral 'fingerprint' of hIAPP undergoing no interaction, specific inhibitory interactions, non-specific interactions and colloidal interactions with small molecules. 'Hits' from screens of potential small molecule inhibitors can thus be distinguished visually from negative, colloidal or non-specifically bound molecules using ESI-IMS-MS and

selected for further characterisation or optimisation based on simple categorisation of the spectral features.
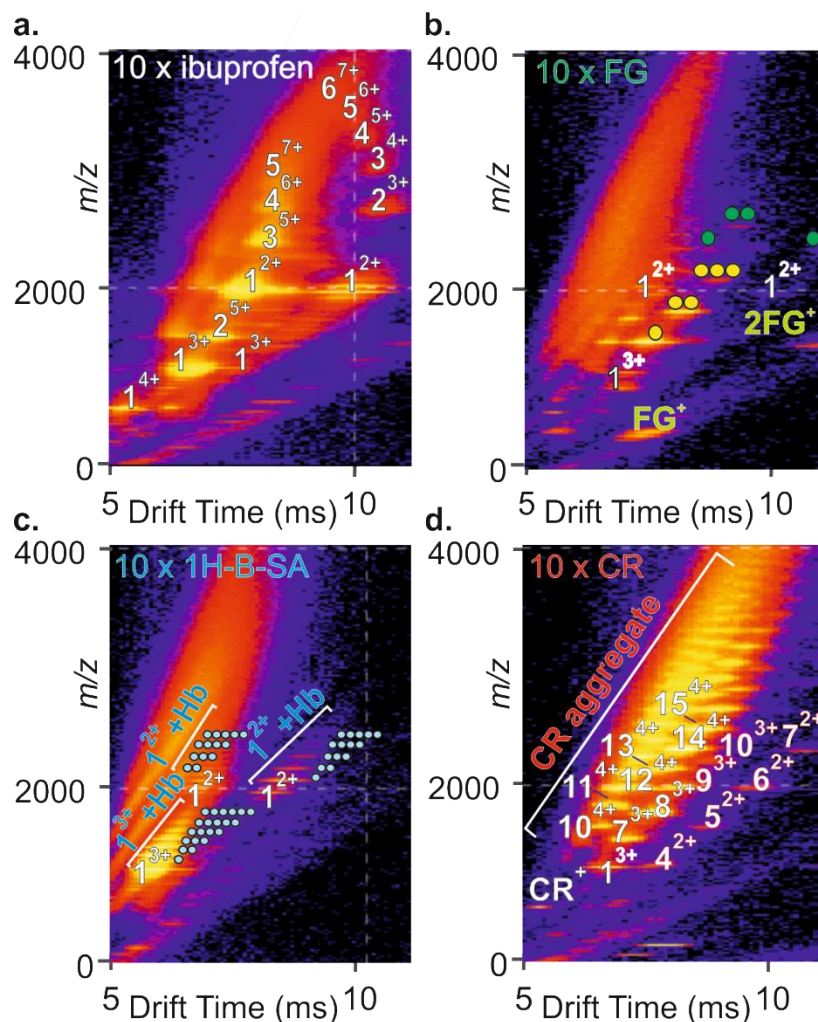
Figure 5-14. *ESI-IMS-MS demonstrates the mode of inhibition (specific/colloidal/non-specific) or lack of inhibition of hIAPP amyloid formation by small molecules. a–d, ESI–IMS–MS Driftscope plots of hIAPP and ibuprofen (a), FG (b), 1H-B-SA (Hb) (c) and CR (d) (all at 320 µM) to hIAPP (32 µM). Examples of a negative (a), a positive (b), a nonspecific (c) and a colloidal inhibitor (d) are illustrated. The numbers on the Driftscope plots indicate the oligomer order and the adjacent superscript numbers show the charge state of those ions. In b, the bound peaks are denoted with yellow (1^{3+} bound) or green (1^{2+} bound) circles (the number of circles represents the number of ligands bound); in c, the bound peaks are denoted with blue circles; in d, the colloidal aggregates are denoted nx+, where n is the number of CR molecules and x is the charge state of the aggregate. Background noise observed in Driftscope plots is a result of displaying the data on a log scale. Figure taken from Young et al. (182).*

5.2.7 Screening mixtures of small molecules using ESI-IMS-MS

To validate the high-throughput potential of this ESI-IMS-MS-based screen for small molecule interactions with aggregating proteins/peptides, several small molecules were mixed together and added to hIAPP in combination. In the mixed samples, the ability to categorise the compounds according to the simple ESI-IMS-MS 'spectral-fingerprint' analysis was assessed. These analyses test the applicability of the screen to differentiate between molecules able to bind specifically to the target protein/peptide from their non-binding or non-specific binding counterparts, when added in combination to the target peptide. This approach has two advantages: firstly, it decreases the time taken to screen a library of compounds (5-10 molecules/min rather than 1 molecule/min); secondly, in competition, the best binders as observed in the gas-phase should out-compete negative, weak or colloidal inhibitors. This method is demonstrated using FG (positive) (**1**), CR (colloidal) (**5**), 1*H*-B-SA (non-specific) (**5**) and four small molecules that do not bind to hIAPP (negative) (**7-10**). When added to hIAPP (32 µM) in combination (160 µM each small molecule), FG and CR behave as each one behaved when added individually, i.e. the 'positive' compound FG binds specifically to the target peptide and the colloidal compound CR self-associates without any specific protein interaction being observed (**Figure 5-15**a). Further, the presence of equimolar CR does not prevent FG from interacting with hIAPP, nor does the presence of equimolar FG prevent the self-association of CR. The ability of FG to bind hIAPP in the presence of mixtures of small molecules that do not bind (aspirin (**7**), ibuprofen (**8**), benzimidazole (**9**) and hemin (**10**)) was also tested. The results showed that of the five small molecules present, only FG binds to hIAPP (**Figure 5-15**b).

Figure 5-15. Screening mixtures of positive, colloidal and negative compounds. *Positive ion ESI mass spectra and corresponding ESI-IMS-MS Driftscope plots showing hIAPP peptide (32 µM) with mixtures of (a) FG (160 µM) and CR (160 µM); and (b) FG (160 µM), aspirin (160 µM), ibuprofen (160 µM), benzimidazole (160 µM) and hemin (160 µM). FG bound monomer peaks denoted with yellow (1³⁺ bound) or green (1²⁺ bound) circles and a white circle when dimer bound. Number of circles represents number of ligands bound. ESI-IMS-MS Driftscope plots are shown to the right of the corresponding spectra. Figure taken from Young et al. (182).*

Further, the presence of an excess of the non-specifically binding ligand, 1*H*-B-SA, did not perturb the 'positive' interaction between FG and hIAPP (**Figure 5-16**a). In the statistically unlikely event that two positive inhibitors are encountered in the same mixture, the molecule which binds most stably in the gas-phase should out-compete the other. This is the case when FG (**1**) and EGCG (**2**) are each added in a 5-fold molar excess to hIAPP (**Figure 5-16**b). FG and hIAPP have favourable electrostatic interactions (239), whereas EGCG is thought to bind principally via hydrophobic interactions (156). Given that electrostatic interactions are more likely to be maintained in the gas-phase over their hydrophobic counterparts, FG out-competes EGCG. The relative affinity of these two different ligands for hIAPP, therefore, cannot be deduced from these data. Thus, in order to control for the effects of the chemistry of binding determining the relative intensity of bound

peaks observed by ESI-MS (252, 253), the K_d of small molecules identified as a "hit" in a mixture of compounds should be confirmed using other biophysical methods in solution. Additionally, when a positive inhibitor is encountered, all compounds within the mixture could be re-examined against the target separately, to avoid any false-negative results.
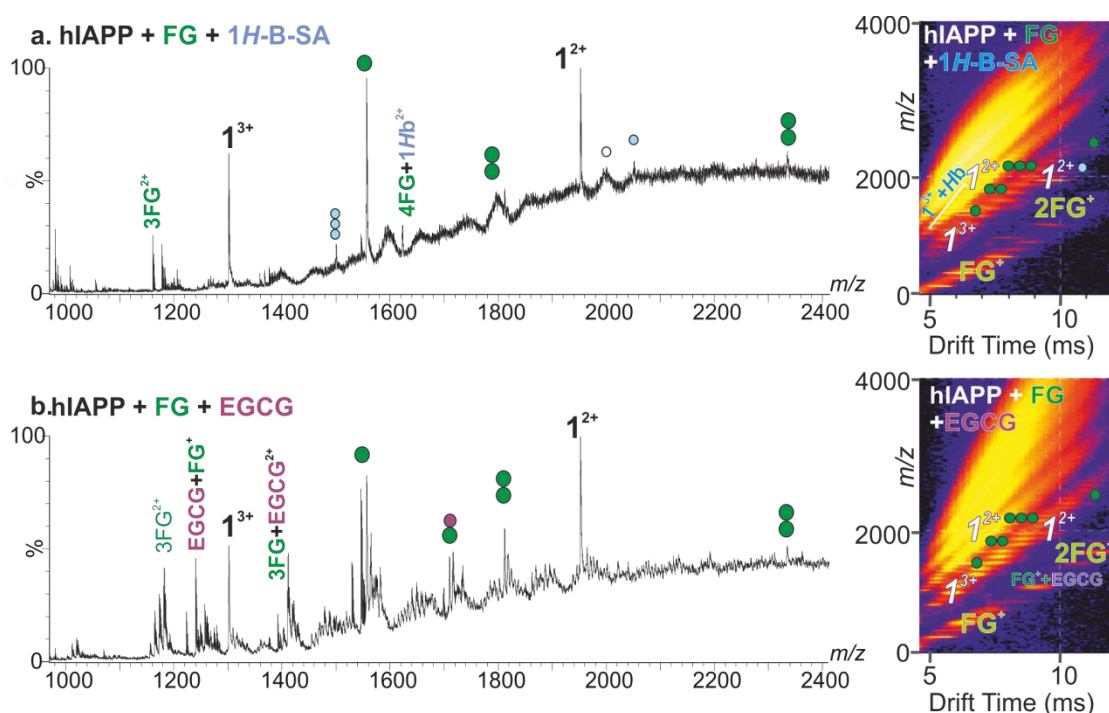
Figure 5-16. *Screening mixtures of positive and non-specific compounds. Positive ion ESI mass spectra and IMS-MS Driftscope plots showing hIAPP peptide (32 µM) in solution with mixtures of compounds. (a) hIAPP with Fast Green FCF (FG) (160 µM) and 1H-benzimidazole-2-sulfonic acid (1H-B-SA) (160 µM), FG bound monomer peaks denoted with green circles and a white circle when dimer bound, 1H-B-SA bound monomer peaks denoted with blue circles; (b) hIAPP with Fast Green FCF (160 µM) and EGCG (160 µM). FG bound monomer peaks denoted with green circles. EGCG bound peaks are denoted with purple circles. Number of circles represents number of ligands bound. Background noise observed in Driftscope plots is a result of displaying the data on a log scale. Figure taken from Young et al. (182).*

5.2.8 ESI-IMS-MS as a generic screen for amyloid inhibitors

Having demonstrated successfully the applicability of the ESI-IMS-MS-based screen to classify inhibitors of hIAPP aggregation, the same method was applied to Aβ40 assembly (257). These analyses were performed in order to assess the method developed as a generic tool for screening and classifying inhibitors of aggregating systems. The 37-residue hIAPP (**Figure 5-2**a) and 40-residue Aβ40 (**Figure 5-18**a) sequences share 25 % identity and 47 % similarity (**Figure 5-17**). The core sequences of each peptide, Aβ40 (residues 26–32) and hIAPP (residues 21–27), believed to be involved in the self-assembly of each peptide (101, 199, 258), are most similar.
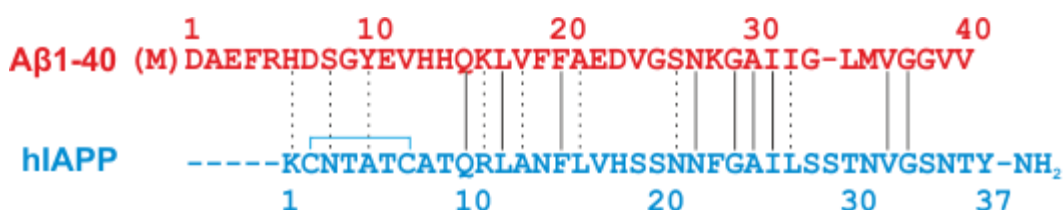
Figure 5-17. *Sequence alignment of Aβ40 and hIAPP. Recombinant expression of Aβ40 results in an additional N-terminal methionine* (187)*. The intramolecular disulfide bond in hIAPP is indicated by a blue line, and the amidated C-terminal is shown. Lines between hIAPP and Aβ40 sequences indicate exact amino acid matches, dashes indicate chemical similarity.*

Here, Aβ40 (expressed recombinantly, **Section 2.1.5**) (32 μM) was incubated alone or with tramiprosate (**6**), hemin (**10**) or EGCG (**2**) at 10:1 molar ratio of small molecule to Aβ40. Preliminary analysis of Aβ40 in isolation using ESI-MS revealed that the peptide gives rise to dominant 3+ and 4+ monomer charge state ions (**Figure 5-18**b) and oligomeric species (dimer ≥ pentamer) (**Figure 5-18**c) *en route* to long straight amyloid fibrils.

Tramiprosate (**6**) has been shown previously to inhibit Aβ40 and Aβ42 fibrillation *in vivo*, likely *via* competition with glycosaminoglycan (GAG) binding to the peptide (259, 260). The mass spectrum of a 10:1 molar ratio of tramiprosate:Aβ40 peptide (**Figure 5-18**d) indicates a non-specific interaction which may help towards explaining how tramiprosate interferes with glycosaminoglycan (GAG) binding to Aβ *in vivo* (259). ThT and TEM data reveal fibrillation in the absence and presence of tramiprosate (**6**) (**Figure 5-18**e and f ii), corroborating the findings that this interaction is non-specific and non-inhibitory. Hemin (**10**) (along with other porphyrins) has also been reported to interfere with Aβ fibrillation (144, 245). On the contrary, here, hemin has no observed effect on Aβ self-assembly, demonstrated by its inability to bind to Aβ40 as judged by ESI-MS (**Figure 5-18**d ii) and the resultant formation of Aβ40 fibrils in its presence, as judged by TEM (**Figure 5-18**f iii). Notably, no increase in ThT fluorescence is observed in the presence of hemin, presumably because the small molecule either interferes with ThT fluorescence or prevents ThT binding (**Figure 5-18**e), a common caveat of screening methods reliant on ThT data to infer inhibition. Conversely, EGCG (**2**), binds specifically to Aβ40 monomer, forming a 1:1 EGCG: Aβ40 complex (**Figure 5-18**d iii), resulting in the formation of amorphous aggregates and the absence of long straight amyloid fibrils (**Figure 5-18**e and f iv). The results demonstrate, therefore, the applicability of ESI-MS as a generic screen for inhibitors of two different amyloid systems. Further description of Aβ40 peptide oligomers and small molecule screening using Aβ40 as a target are discussed in **Section 5.2.10.2.**
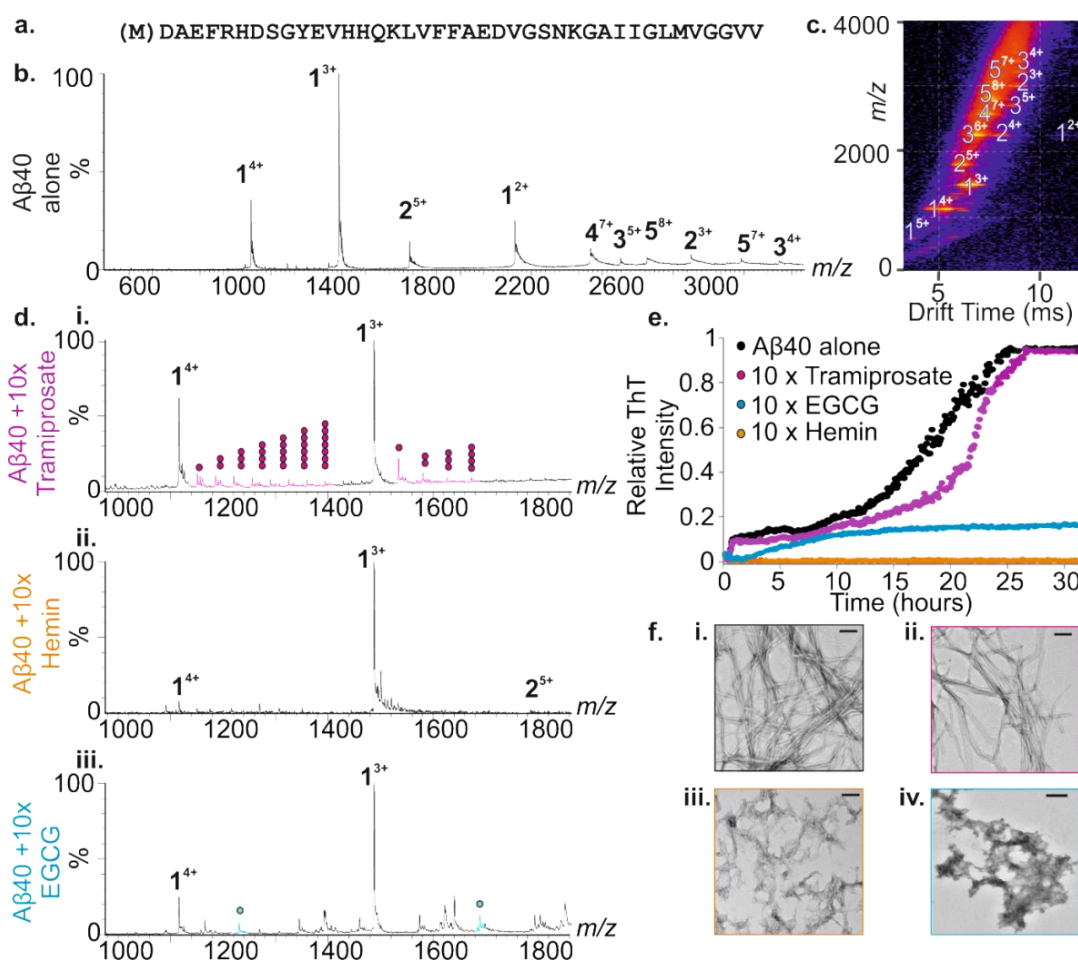
Figure 5-18. *ESI-mass spectra of Aβ40 alone and with non-specific, negative and specific binding small molecules. (a) Primary sequence of recombinantly expressed Aβ40 (with an additional methionine at the N-terminus); (b) ESI mass spectrum of Aβ40. Numbers adjacent to peaks denote oligomer order, with the positive charge state of each oligomer ions in superscript; (c) ESI-IMS-MS Driftscope plot of the Aβ40 alone (32 μM in 200 mM ammonium acetate, pH 6.8). ESI-IMS-MS Driftscope plots show IMS drift time versus m/z versus intensity (z = square root scale); (d) positive ion ESI mass spectra showing 320 μM tramiprosate (i), hemin (ii) or EGCG (iii) added to Aβ40 peptide (32 μM). Tramiprosate binds multiple copies to the 3+ and 4+ charge state ions of Aβ40 monomer (bound peaks denoted with pink circles, number of circles represents number of ligands bound). This binding mode is classified as non-specific. Hemin (ii) does not bind and is classified as negative, and EGCG (iii) binds to both the 3+ and 4+ charge state ions of Aβ40 monomer (bound peaks are denoted with blue circles) and is classified as specific. (e) ThT fluorescence intensity of Aβ40 alone (black circles) and with tramiprosate (pink circles), EGCG (blue circles) and hemin (orange circles) all present at small molecule:Aβ40 molar ratios of 10:1 (25 °C, quiescent). Significant inhibition of the formation of ThT-positive species is observed in the presence of excess EGCG and interference with ThT fluorescence is observed only in the presence of excess hemin. (f) Negative stain TEM images of Aβ40 alone (i) or incubated with 10:1 molar ratios of tramiprosate (ii), hemin (iii) or EGCG (iv) for 5 days (25 °C, quiescent); scale bar = 100 nm. Fibrils are observed by Aβ40 alone and in the presence of excess tramiprosate and hemin but not in the presence of excess EGCG. Figure taken from Young et al. (182).*

5.2.9 Focused screen for the identification of novel inhibitors of amylin amyloid formation
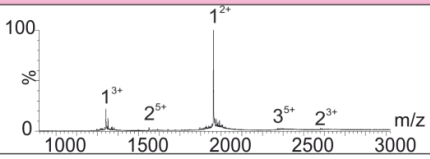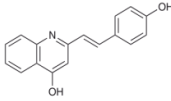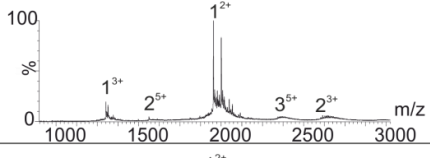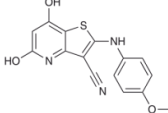
To validate further the MS-based assays and to begin screening for new inhibitors, I next performed the ESI-IMS-MS screen using a library of novel molecules (**11-30**) with structural similarity to the aggregation inhibitors previously reported (**Table 5.2**). We reasoned that a focussed screen of this type would be a rigorous test for the ESI-IMS-MS assay and indicate the suitability of this approach for high throughput screening (HTS).

The selection of compounds via virtual screening was performed by Charlotte H. Revill and Richard J. Foster (School of Chemistry, University of Leeds), as described in **Chaper 2**, **Section 2.4.5.**

Focused screening is a method well-versed in improving the hit-rate of a HTS by seeding a screening library with compounds which have a higher probability to bind to and/or inhibit the target with respect to random screening (261). This screening method uses the structural information from known bioactive ligands to identify novel compounds with similar structure, and hence greater potential for biological activity against a target of interest. For initial proof of principle experiments, five inhibitors of hIAPP and/or Aβ40 amyloid formation from the literature (vanillin (262), resveratrol (263), curcumin (264), chloronaphthoquinine-tryptophan (265) and EGCG (102)) were selected as queries from which to seed a focussed library of compounds for screening using ESI-IMS-MS. In the seeding process, each of the inhibitors is assessed for structural similarity to an in-house, structurally diverse library of 50,000 lead-like small molecules using the programme Rapid Overlay of Chemical Structures (ROCS)(194). After seeding, a subset of 20 compounds was then chosen for analysis using the comparator (ROCS Combiscore) with consideration to maximal structural diversity of the proposed screening set. This subset of 20 compounds (molecules **11-30**) were then screened against hIAPP, along with a further 10 compounds (molecules **31-40**) which have been reported to inhibit aggregation by other amyloidogenic polypeptides (**Table 5.2**). LogP values of all 30 compounds are shown in **Figure 5-19**.

Mol N°	Small Molecule	Structure	Mass Spectra	Classification
11	(2-isopropoxyphenyl) amine			Negative
12	2-[2-(4-hydroxyphenyl) vinyl]-4-quinolinol			Negative
13	5,7-dihydroxy-2-[(4-methoxyphenyl)amino] thieno[3,2-b]pyridine-3-carbonitrile			Non-specific
14	4-ethoxy-N-(4-imidazo [1,2-a] pyridin-2-ylphenyl) benzamide			Negative
15	(4-bromo-2,5-dimethoxyphenyl) amine			Negative
16	N-(3,5-dichloro-4-hydroxyphenyl)-3-ethoxybenzamide			Negative
17	[1,2,4]triazolo[1,5-a] [1,3,5]triazin-7-amine			Negative
18	5-Chloro-2-(1H-imidazol-1-yl)aniline			Negative
19	4-amino-N-(2,3-dihydro-1,4-benzodioxin-6-yl)benzamide			Negative
20	3-amino-N,N-diethyl-4,5-dimethoxy-benzamide			Negative

Table 5.2. *Focused high throughput screen (HTS) results. Molecule number 26 inhibits hIAPP aggregation by specific binding (red peaks); compounds 13, 25, 27 exhibit non-specific binding (green peaks). TEMs are shown only for compounds in which binding is observed (scale bar in nm is indicated at the foot of each TEM image). Table taken from Young et al. (182).*

145

Mol N°	Small Molecule	Structure	Mass Spectra	Classification
21	N-(3-hydroxyphenyl)-3,4-dimethoxybenzamide			Negative
22	3-amino-N-cyclopropyl-4-methoxybenzamide			Negative
23	1-{4-hydroxy-2-methyl-3-[(4-phenyl-1-piperazinyl)methyl]-6-quinolinyl}ethanone			Negative
24	3,5-dimethoxy-N-[4-(8-methylimidazo[1,2-a]pyridin-2-yl)phenyl]benzamide			Negative
25	N-(2,3-dihydro-1,4-benzodioxin-6-yl)-2-[4-{(4-methyl-6-oxo-1,6-dihydropyrimidin-2-yl)amino}piperidin-1-yl]acetamide			Non-specific
26	6-{[4-(2-fluorophenyl)-1-piperazinyl]carbonyl}-3-methyl-5H-[1,3]thiazolo[3,2-a]pyrimidin-5-one			Positive
27	1-(Adamantan-1-ylcarbonyl)-1'H-spiro[piperidine-4,2'-quinazolin]-4'(3'H)-one			Non-specific
28	N-(5-Methoxy-2-methyl-1,3-benzothiazol-4-yl)acetamide			Negative
29	1-(2,3-dimethoxybenzoyl)-4-ethylpiperazineylphenyl)-benzamide			Negative
30	N-(4-aminophenyl)-2-bromobenzamide			Negative

Table 1.2 continued

Mol N°	Small Molecule	Structure	Mass Spectra	Classification
31	**L-DOPA** (L-3,4-dihydroxyphenyl-alanine)			Negative
32	**Neocuprione** (2,9-dimethyl-1,10-phenanthroline)			Negative
23	**Lacmoid** (7-amino-2,8-bis(2,4-dihydroxyphenyl)-phenoxazin-3-one)			Negative
34	**Hematin** (hydroxy[3,7,12,17-tetramethyl-8,13-divinylporphyrin-2,18-dipropanoato(2-)(iron III))			Negative
35	**Melatonin** (N-{2-(5-methoxy-14-ind-3-yl)ethyl}acetaminde)			Negative
36	**Chloragenic acid** ((1S,3R,4R,5R)-3-{[(2Z)-3-(3,4-dihydroxyphenyl)prop-2-enoyl]oxy}-1,4,5-trihydroxycyclohexane-carboxylic acid)			Negative
37	2-Amino-methylbenzimidazole			Negative
38	2,3,4-Trihydroxybenzo-phenone			Negative
39	**Ibuprofen** ((RS)-2-(4-(2-methylpropyl)phenyl)-propanoic acid)			Negative
40	**Azure C** (3-Amino-7-(methylamino)pheno-thiazin-5-ium chloride)			Negative

Table 1.2 continued
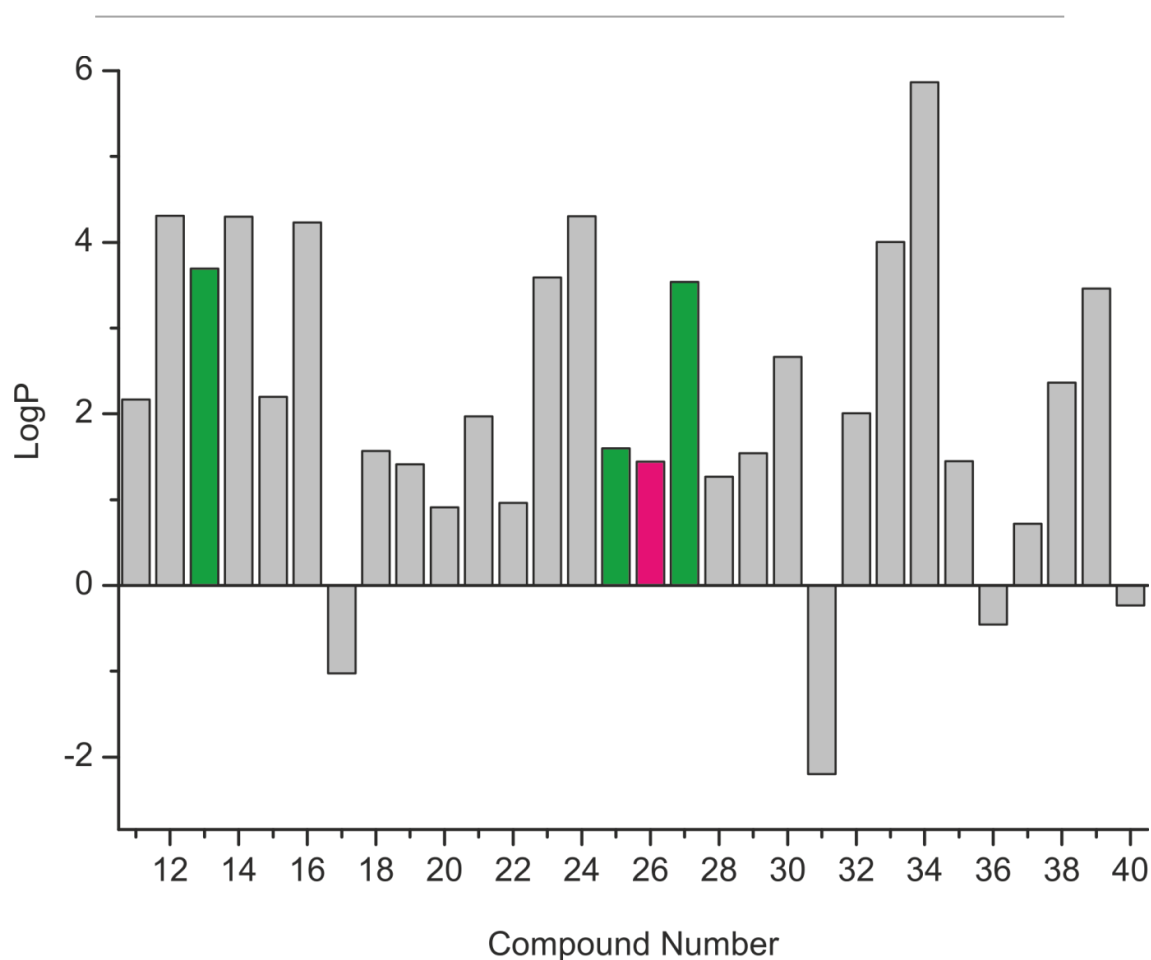
Figure 5-19. *LogP values of the 20 compounds identified from the focused screen and 10 other small molecules : LogP values (the log of the aqueous/hydrophobic partition coefficient) were calculated for the 20 small molecules identified from the focused screen (compounds 11-30) using www.molinspiration.com software, which determines the hydrophobic parameters of the substituents, plus 10 other small molecules reported to inhibit amyloid formation by other polypeptide sequences (compounds 31-40). Molecules with high +ve LogP values have high hydrophobicity. Colours denote inhibitor classification: positive (pink), non-specific (green) and negative (grey). Figure taken from Young et al. (182).*

Of these 30 compounds assayed in this screen, one was found to bind specifically and inhibit hIAPP aggregation (compound **26**), three demonstrated non-specific binding to hIAPP (compounds **13**, **25** and **27**) but a lack of inhibition, and the remainder did not bind, nor did they inhibit (**Table 5.2**). The newly discovered 'positive' inhibitor (compound **26**) is a non-obvious structural mimetic of chloronaphthoquinine–tryptophan (**Figure 5-20**), selected only as a result of focussed screening and ROCS analysis.
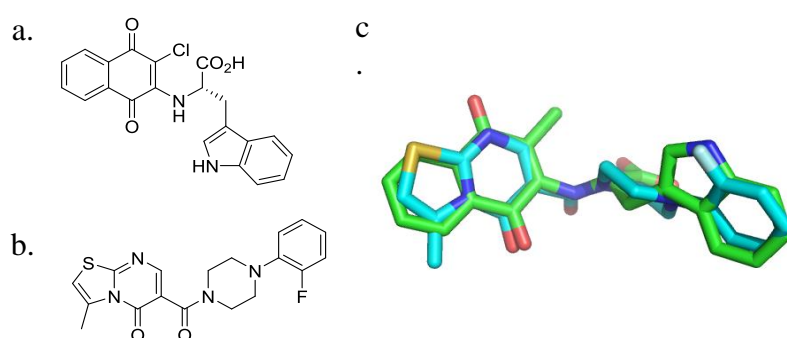
Figure 5-20. *ROCS-derived overlay of molecule number 26 with chloronaphthoquinine–tryptophan (a) Chemical structure of chloronaphthoquinine–tryptophan; (b) chemical structure of molecule number 26; (c) ROCS-derived overlay of chloronaphthoquinine–tryptophan (green sticks) and molecule number 26 (cyan sticks). Figure taken from Young et al., kindly provided by Charlotte H. Revill (School of Chemistry, University of Leeds) (182).*

In the presence of a 10-fold molar excess of compound **26**, hIAPP monomer shows evidence of specific ligand binding (**Figure 5-21**a), lack of high order oligomer formation (**Figure 5-21**b) and amorphous aggregates are formed in the absence of fibrils (**Figure 5-21** inset). These data highlight the applicability of a focused ESI-IMS-MS screen to rapidly identify novel small molecules capable of inhibiting aggregating peptides in a specific manner.
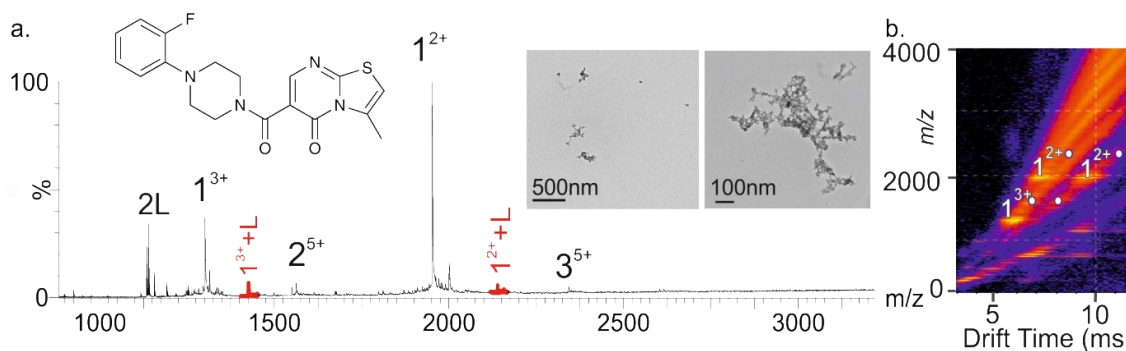
Figure 5-21. *ESI-IMS-MS analysis of 'hit' compound number 26. Inhibition of hIAPP fibril formation by compound **26**. (**a**) Positive ion ESI mass spectrum showing binding of compound **26** (6-([4-(2-fluorophenyl)-1-piperazinyl]carbonyl)-3-methyl-5H-[1,3]thiazolo[3,2-a]pyrimidin-5-one) (added at 320 μM to 32 μM peptide) to both the +2 and +3 charge state ions of hIAPP monomer (bound peaks coloured red). The structure of compound **26** and negative stain TEM images of hIAPP incubated with 10:1 molar ratios of molecule:hIAPP for 5 days (25 °C, quiescent) are inset; (**b**) ESI-IMS-MS Driftscope plot shows hIAPP species detected in the presence a 10:1 molar ratio of compound **26**:peptide monomer at t = 2 min. Bound monomer peaks are denoted with a white circle. Figure taken from Young et al. (182).*

Use of an automated sampling device enables the utility of ESI-MS to identify novel compounds from focused libraries in the form of a semi-HTS. For proof of principle, I performed analyses from a 96-well plate format, with data acquisitions of one minute per well. The results demonstrate that in doing so, spectra of high quality can be obtained in a reproducible manner (**Figure 5-22**). Using robotic automation, a minimum of 96 novel potential inhibitors could be screened per plate, consuming ~1 mg peptide thus ~1000 compounds can be screened in less than 24 hours. By assaying mixtures of five compounds in parallel, 480 molecules could be screened per plate, increasing the screening rate to ~5000 novel compounds per day.
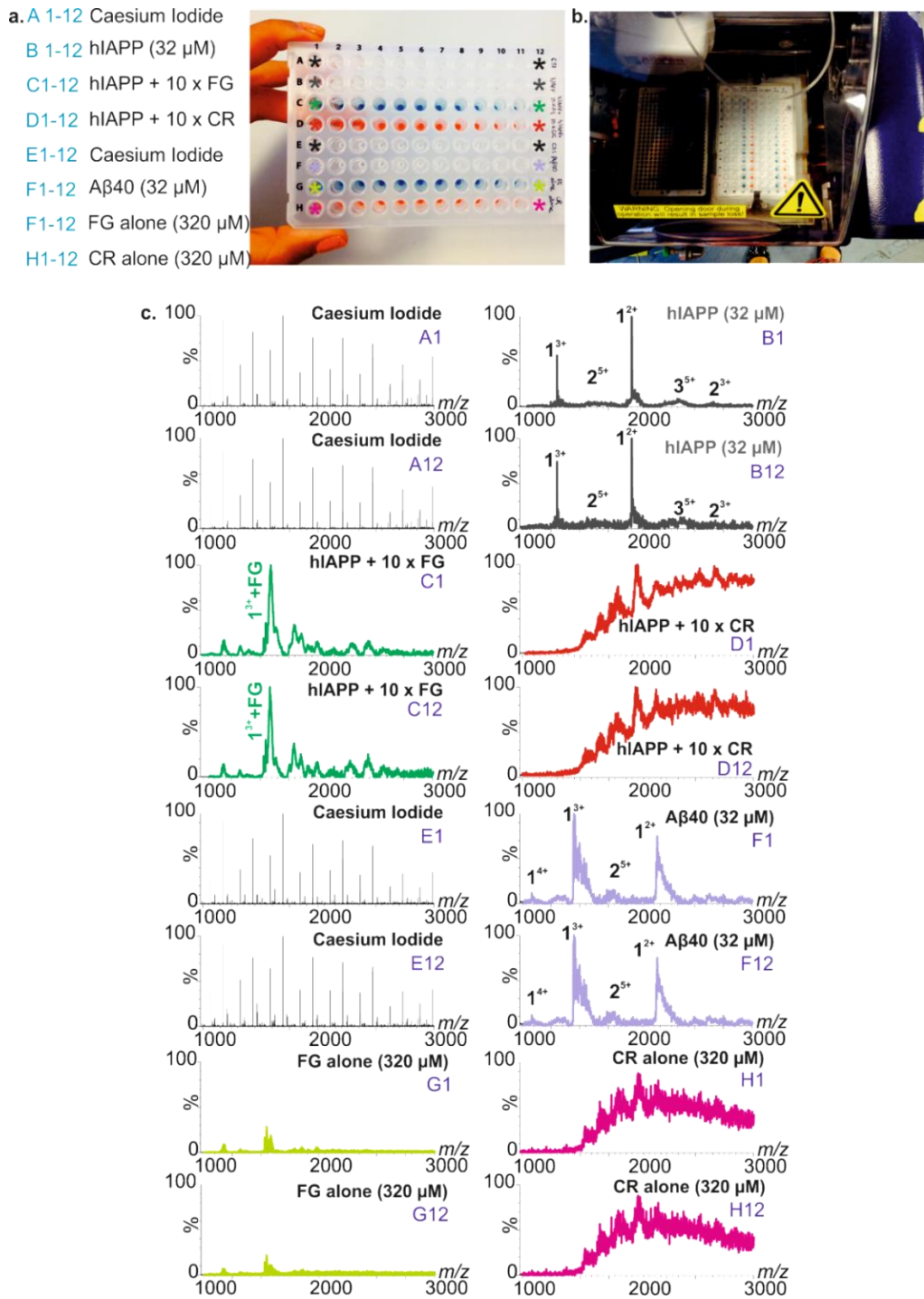
Figure 5-22. *Proof of principle 96-well plate automated semi-HTS Proof of principle 96-well plate automated semi-HTS by ESI-MS. (**a**) 10 µL samples containing aqueous CsI (A/E 1-12) for calibration, hIAPP (B1-12), hIAPP:FG (C1-12) hIAPP:CR (D1-12), Aβ40 (F1-12), FG alone (G1-12), and CR alone (H1-12) were prepared in 96-well plates. Peptide samples (32 µM) were dissolved in 200 mM ammonium acetate (pH 6.8) in the absence or presence of 320 µM small molecule; (**b**) samples were infused into the mass spectrometer via a Triversa NanoMate automated nano-ESI interface; (**c**) spectra resulting from the first and twelfth well of each row of the 96-well plate (annotated A1, A12, respectively) demonstrate the reproducibility of the assay. Figure taken from Young et al. (182).*

151

5.2.10   Screen for the inhibitors of Aβ amyloid formation

To validate further the use of MS-based assays in conjunction with focussed screening for the discovery of novel inhibitors of multiple amyloid systems, I next performed the screen of compounds **11-30**, previously assayed against hIAPP (**Section 5.2.9**), against Aβ40. This work has been published in reference (229).

5.2.10.1   Aβ40 forms an array of oligomers early in amyloid assembly

Prior to performing screening, I first investigated the higher order oligomeric states populated by Aβ40, under conditions compatible both with ESI-MS and fibril formation (as judged by TEM) (**Figure 5-23**a), and elucidated the CCSs of species formed. Aβ40 was dissolved initially in 100 % DMSO to remove any preformed aggregates and diluted 100-fold into 200 mM ammonium acetate buffer, pH 6.8 before centrifugation (13,000 g, 4 °C, 10 min) to remove any larger order species that may persist. The distribution of soluble oligomeric species was then analysed immediately (within 2 min, post centrifugation), using ESI-IMS-MS. The data obtained (**Figure 5-23**) showed that high order oligomers are formed within 10 min of dilution of Aβ40 into buffer, consistent with previous analyses (98, 100). Co-populated oligomers with the same m/z can be separated using IMS-MS, for example, the dimer[4+] and trimer[6+] ions (**Figure 2b**). Multiple charge states, predominantly triply and quadruply charged, and different conformers, both compact and expanded, are observed for the Aβ40 monomer (98, 100). Aβ40 oligomer CCSs were estimated from the ESI-IMS-MS arrival time distributions and compared with CCSs estimated for theoretical oligomer growth models (described in **Section 1.14**) including a fit assuming isotropic growth (46), a fit assuming globular oligomers based on the average density of a protein under similar conditions (0.44 Da/Å[3]) (93), and a model that assumes growth in a single dimension (linear growth) (46). CCS determination suggests that Aβ40 oligomers > trimer in size adopt relatively extended conformations rather than spherical or

152

isotropic growth conformations (**Figure 5-23**a). More detailed analysis of oligomeric structures under different solution and MS conditions is required in order to agree or disagree with any previously published growth models for this sytem (98, 100). Ultimately, under the conditions used, long, straight fibrils typical of amyloid form (**Figure 5-23 inset**).
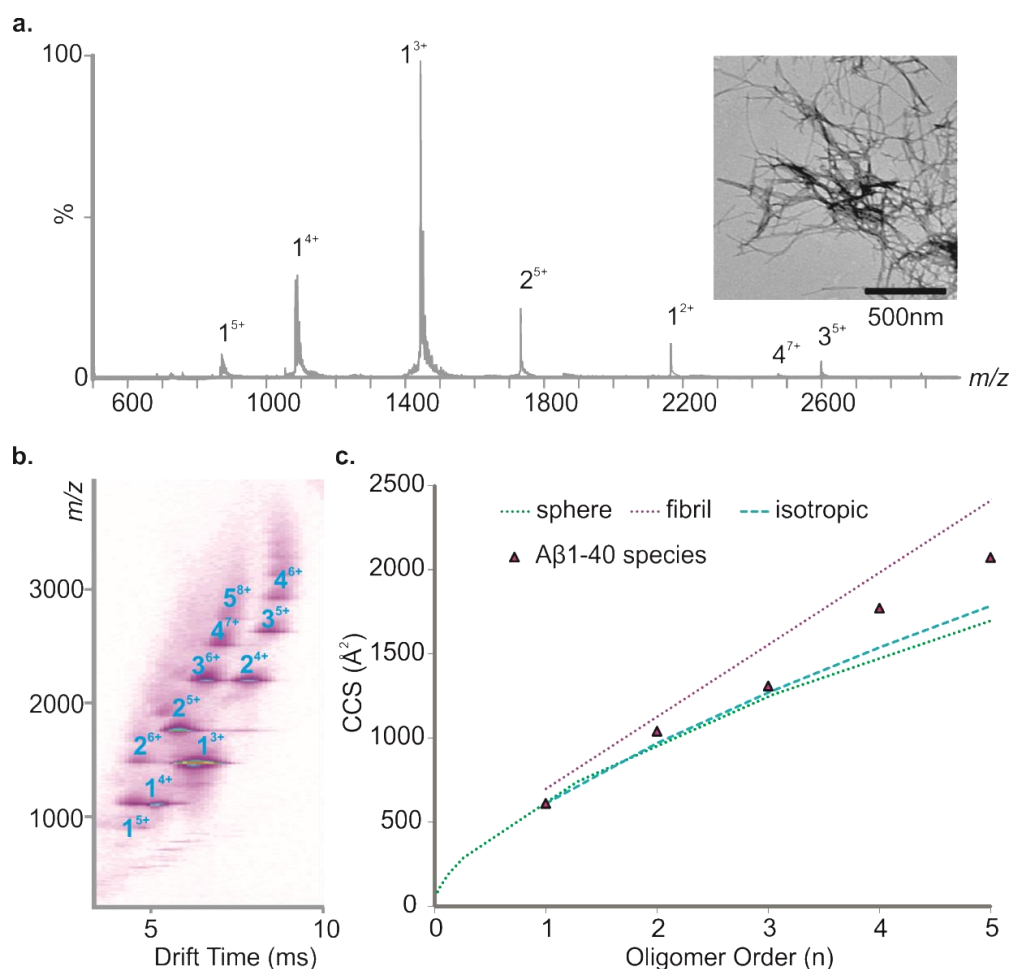
Figure 5-23. *Analysis of Aβ40 oligomer distribution and CCSs. a. ESI-MS mass spectrum of Aβ40. Numbers above peaks denote oligomer order, with the positive charge state of ions in superscript. Inset: negative stain TEM image of Aβ40 fibrils after 5 days in 200 mM ammonium acetate buffer, pH 6.8 (25 °C, quiescent) (scale bar = 500 nm). b. ESI-IMS-MS Driftscope plot of the Aβ40 oligomers present 12 min after diluting the monomer to a final peptide concentration of 32 μM in 200 mM ammonium acetate, pH 6.8, 25 °C. ESI-IMS-MS Driftscope plots show IMS drift time versus m/z versus intensity (z = square root scale); c. CCSs of Aβ40 oligomers measured using ESI-IMS-MS versus oligomer order; the CCS of the lowest charge state of each oligomer is shown (black triangles). The orange dashed line represents a fit based on globular oligomers and the average density of a protein (0.44 Da/Å³) (39), the purple dashed line represents a linear growth model (46) and the blue dashed line represents an isotropic growth model(46) (models described in detail in **Section 1.14**). Figure taken from Young et al. (229).*
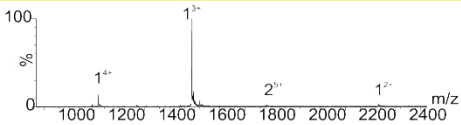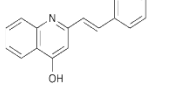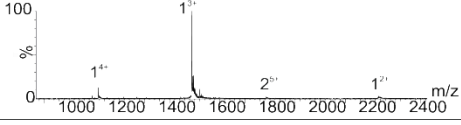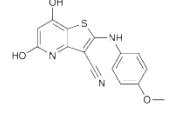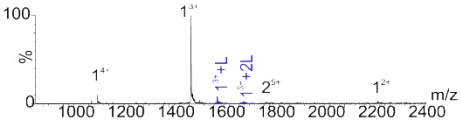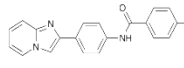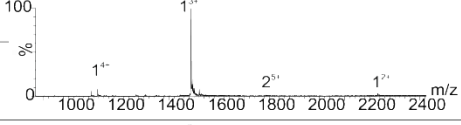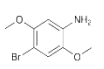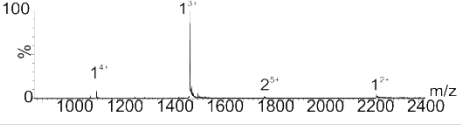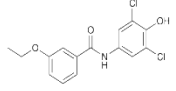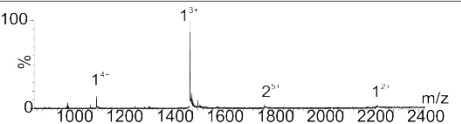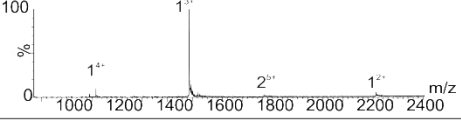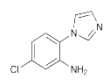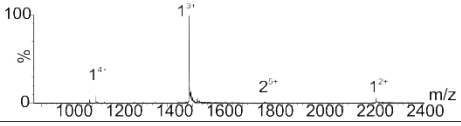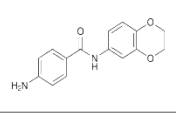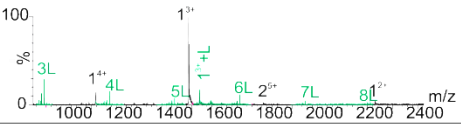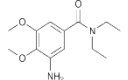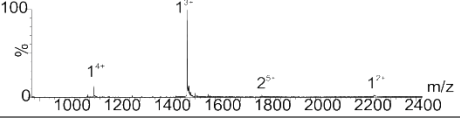
5.2.10.2   Focused screen for the identification of novel inhibitors of Aβ amyloid formation

Using the ESI-IMS-MS-based screening approach described above and in **Sections 5.2.2** and **5.2.9**, the exact same 20 compounds (**11-30**), selected by ROCS analysis (Charlotte H. Revill and Richard J. Foster, School of Chemistry) based upon their structural similarity to bioactive ligands *o*-vanillin (262), resveratrol (263), curcumin (264), chloronaphthoquinine-tryptophan (Cl-NQTrp) (265) and (-)-epigallocatechin gallate (EGCG) (102, 153) (**Table 5.3**), previously analysed for bidning to hIAPP (**Table 5.2.** Focused high throughput screen (HTS) results.), were added individually to monomeric Aβ40 and the binding mode of each was assessed by analysis of the resulting ESI-IMS-mass spectra. In parallel, the ability of the molecules to inhibit fibril formation was determined using negative stain TEM, after 5 days incubation at a 10:1 molar ratio of small molecule to Aβ40.

The compounds were categorised according to the binding mode classification system described in **Section 5.2.2**. Of the 20 compounds screened, two were found to inhibit Aβ40 aggregation (compound **13** and compound **26**, **Table 5.3** and **Figure 5-24a**), one exhibited colloidal binding (compound **19**) (**Table 5.3** and **Figure 5-24b**) and two demonstrated non-specific binding, (compounds **25** and **27**) (**Table 5.3** and **Figure 5-24c**). The remainder did not bind to Aβ40 (**Table 5.3**).

It is important to note that the ability to distinguish between specific and non-specific binding is not always straight forward. At a ten-fold molar excess of small molecule, it is conceivable that a 'positive' small molecule will bind multiple copies to its target protein. Additionally, the nature of interaction i.e. hydrophobic or electrostatic will contribute to the number of observed ligands bound, with a higher proportion of electrostatic binding being maintained in the gas-phase. In a screen of this nature, it would be beneficial to take all binding compounds forward, both those that appear initially to be specific and those that appear to be non-specific. All binders should be assayed at eqimolar concentrations with the target

peptide and EM images should be taken of the products of their incubation with the target. Only then should they be definitively classified according to this system.

Mol N°	Small Molecule	Structure	Mass Spectra	Binding mode classification	
				Aβ40	hIAPP
11	(2-isopropoxyphenyl) amine			Negative	Negative
12	2-[2-(4-hydroxyphenyl) vinyl]-4-quinolinol			Negative	Negative
13	5,7-dihydroxy-2-[(4-methoxyphenyl)amino] thieno[3,2-b]pyridine-3-carbonitrile			Positive	Non-specific
14	4-ethoxy-N-(4-imidazo [1,2-a]pyridin-2-ylphenyl) benzamide			Negative	Negative
15	(4-bromo-2,5-dimethoxyphenyl) amine			Negative	Negative
16	N-(3,5-dichloro-4-hydroxyphenyl)-3-ethoxybenzamide			Negative	Negative
17	[1,2,4]triazolo[1,5-a][1,3,5]triazin-7-amine			Negative	Negative
18	5-Chloro-2-(1H-imidazol-1-yl)aniline			Negative	Negative
19	4-amino-N-(2,3-dihydro-1,4-benzodioxin-6-yl)benzamide			Colloidal	Negative
20	3-amino-N,N-diethyl-4,5-dimethoxybenzamide			Negative	Negative

Table 5.3. *Focused high throughput screen (HTS) results. Mass spectra labels indicate number of ligands (L) bound to each charge state of Aβ40. Binding modes as determined from the mass spectra are denoted as positive, negative, non-specific or colloidal. Molecule numbers 13 and 26 exhibit positive (specific) binding to Aβ40 (purple peaks); compounds 25 and 27 exhibit non-specific binding (pink peaks) and compound 19 exhibits colloidal binding (green peaks; each multimer of the small molecule is denoted nL, where n=oligomer number. The interaction of each small molecule with hIAPP is also shown (182). Table taken from Young et al. (229).*

Mol N°	Small Molecule	Structure	Mass Spectra	Binding mode classification	
				Aβ40	hIAPP
21	N-(3-hydroxyphenyl)-3,4-dimethoxybenzamide			Negative	Negative
22	3-amino-N-cyclopropyl-4-methoxybenzamide			Negative	Negative
23	1-{4-hydroxy-2-methyl-3-[(4-phenyl-1-piperazinyl)methyl]-6-quinolinyl}ethanone			Negative	Negative
24	3,5-dimethoxy-N-[4-(8-methylimidazo[1,2-a]pyridin-2-yl)phenyl]benzamide			Negative	Negative
25	N-(2,3-dihydro-1,4-benzodioxin-6-yl)-2-[4-{((4-methyl-6-oxo-1,6-dihydropyrimidin-2-yl)amino}piperidin-1-yl]acetamide			Non-specific	Non-specific
26	6-{[4-(2-fluorophenyl)-1-piperazinyl]carbonyl}-3-methyl-5H-[1,3]thiazolo[3,2-a]pyrimidin-5-one			Positive	Positive
27	1-(Adamantan-1-ylcarbonyl)-1'H-spiro[piperidine-4,2'-quinazolin]-4'(3'H)-one			Non-specific	Non-pecific
28	N-(5-Methoxy-2-methyl-1,3-benzothiazol-4-yl)acetamide			Negative	Negative
29	1-(2,3-dimethoxybenzoyl)-4-ethylpiperazineylphenyl)-benzamide			Negative	Negative
30	N-(4-aminophenyl)-2-bromobenzamide			Negative	Negative

Table 5.3 continued

Despite interacting with Aβ40, non-specific and colloidal binding of small molecules to target proteins is not useful therapeutically. The newly discovered inhibitors, compound **13** and compound **26** are structurally similar to, but chemically distinct (as determined by ROCS Combiscore), from the known inhibitors of Aβ40 aggregation, resveratrol (263) and Cl-NQTrp (265), respectively (**Figure 5-25**). In the presence of a 10-fold molar excess of either compound, Aβ40 shows evidence of specific ligand binding and depletion of higher order oligomers such that only dimers and trimers are observed. Neither of the latter species is detected to bind the small molecule. TEM analysis confirms that fibril formation is inhibited and amorphous or short fibrillar aggregates accumulate (**Figure 5-24**a). The low levels of binding observed for the 'positive' inhibitors, despite complete inhibition of fibrillation, are consistent with the fact that hydrophobic interactions are not wholly maintained in the gas-phase. Similar low levels of binding have been observed for 'positive' inhibitors of hIAPP, including EGCG (102). Gas-phase analysis of hydrophobic interactions between protein and ligands could lead to underestimation of binding affinity and/or false negative results (254).
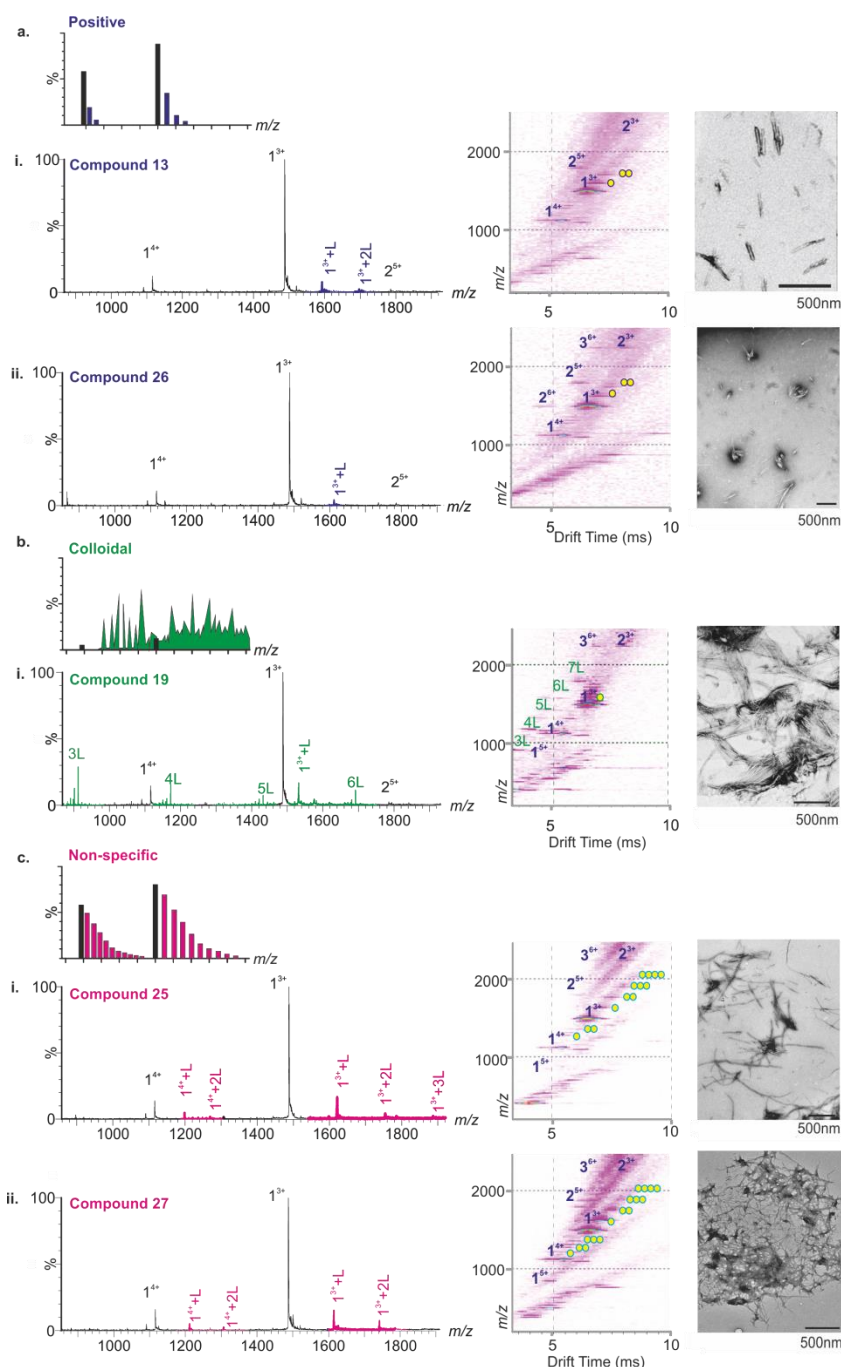
Figure 5-24. *Positive, colloidal and non-specific binding molecules from focused HTS. a) Molecule numbers 13 (i) and 26 (ii) exhibit 'positive' (specific) binding to Aβ40 monomer (purple peaks) according to the ESI-IMS-MS classification system and negative stain TEM images of Aβ40 incubated with 10:1 molar ratios of molecule: Aβ40 for 5 days in 200 mM ammonium acetate buffer, pH 6.8 (25 °C, quiescent) show the absence of fibrils after incubation. b) Compound 19 (i) exhibits colloidal binding to itself (peaks denoted + nL where n is the number of small molecules present in the aggregate) and to Aβ40 (green peaks). c) Compounds 25 (i) and 27 (ii) exhibit non-specific binding to Aβ40 (pink peaks). Compounds 19, 25 and 27 fail to prevent fibrillation of Aβ40 (scale bar in nm is indicated at the foot of each TEM image). Circles in ESI-IMS-MS Driftscope images indicate the number of small molecules bound to each ion. Figure taken from Young et al. (229).*

Remarkably, 18 of the 20 lead compounds screened exhibit similar interactions with human islet amyloid polypeptide (hIAPP) (182) and Aβ40 (**Table 5.3**). The two exceptions are compound **13** (specific binding to Aβ40, non-specific binding to hIAPP (182)) (**Table 5.3**) and compound **19** (colloidal binding in the presence of Aβ40, no binding in the presence of hIAPP (182)) (**Table 5.3**). Interestingly, compound **26** binds specifically to both hIAPP and Aβ40, and inhibits fibrillation of both peptides *in vitro* (182). Although hIAPP and Aβ40 share only 25 % sequence identity and 47 % sequence similarity (**Figure 5-17**), the core sequences of both, believed to key for self-assembly (4, 40), share 57 % identity and 86 % similarity (NNFGAIL in hIAPP, SNKGAII in Aβ40). The ability of compound **26** to interrupt the fibrillation process of both these peptides suggests that this small molecule may be either interacting directly with these comparable amyloidogenic sequences, or with an early oligomeric species with interaction interfaces common to both fibrillation pathways.

Combined with previous success in the discovery of new inhibitors of hIAPP aggregation (**Section 5.2.9**) (182), I envision that ESI-IMS-MS will play a pivotal role in future compound discovery in the anti-amyloid therapeutic field as a whole.
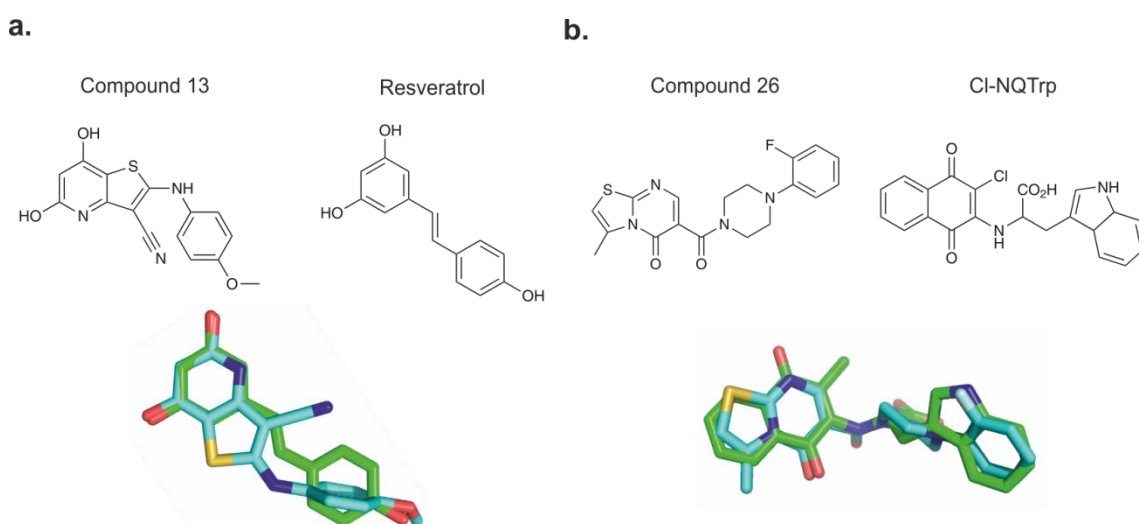
Figure 5-25. *Structural comparison of Aβ40 inhibitors with their parent compounds in ROCS analysis. a. Compound **13** (blue) and the parent molecule resveratrol (green). b. Compound **26** (blue) and the parent molecule Cl-NQTrp (green). Figure taken from Young et al. (229).*

5.3 Conclusions

The data presented in this chapter demonstrate the utility of ESI-IMS-MS as a HTS for inhibitors of self-assembly from amyloid proteins. This approach allows rapid identification of protein-ligand interactions, using microliter sample volumes and milligrams of protein, and provides information-rich data concerning the identity of the interacting species (monomer or oligomer), the nature of binding (specific, non-specific or colloidal) and the effect of the ligand on protein aggregation (monomer binding, shift in monomer equilibrium, disassembly of oligomers). The use of IMS in conjunction with ESI-MS serves further to allow a reliable and easily interpretable visual screen based purely on the appearance of 3D Driftscope plots, without requiring complex data analysis. The results establish this method as a powerful tool with unique analytical capability for the discovery of small molecule leads in the anti-amyloid drug discovery field. Additionally, novel inhibitors of both hIAPP and Aβ40 aggregation have been identified based on analysis of a library of small molecules, illustrating the potential of this method as a HTS.

6 Concluding remarks and future directions

Inhibition of aberrant protein aggregation is a vital step towards alleviating some of the developed world's most prevalent diseases, ranging from neurodegenerative disorders including AD to systemic diseases including T2DM. These amyloid diseases share the key pathological hallmark of large fibrillated structures known as amyloid plaques that form as a result of the accumulation of misfolded/aggregated peptides and proteins (89, 266). The current hypothesis in the amyloid field is that prefibrillar intermediates (rather than mature fibrils), either low molecular weight soluble oligomers or higher order prefibrillar aggregates, are the agents of toxicity (66, 72, 267, 268).

The principle achievements of this thesis was the characterisation of the transient oligomeric species present during the lag-phase of amyloid fibril formation of hIAPP and the observation of the alterations in the aggregation landscape in the presence of small molecule inhibitors. The thesis focussed primarily on interrogating the amyloidogenic peptide hIAPP associated with T2DM, and the Aβ40 peptide associated with AD has been probed as a secondary system. The aims were accomplished by applying a range of synergistic mass spectrometry-based approaches, including ESI-MS to observe protein-ligand binding, ESI-IMS-MS to interrogate co-populated oligomeric states occupied during amyloid assembly and ESI-IMS-MS-CID fragmentation to determine the stability of protein-protein and protein-ligand complexes. Combined, these techniques have yielded significant insights into the mechanisms of hIAPP fibril formation *in vitro* and have lead to new methods for identifying novel inhibitors of amyloid assembly using ESI-IMS-MS. The work presented demonstrates that ESI-IMS-MS can facilitate the identification and analysis of protein-ligand interactions required for amyloid inhibition thereby offering new avenues for the development of novel therapeutic strategies to circumvent fibrillation and/or cytotoxicity in amyloid disease.

Firstly, this thesis showed the capability of ESI-IMS-MS to probe the mechanism of amyloid assembly from both short fragment peptides derived from amyloid sequences (**Chapter 3**) and full length amyloidogenic peptides (**Chapter 4**). The data in **Chapter 3**, demonstrate that when ESI-IMS-MS is performed in conjunction

with coarse-grained modelling, a comprehensive picture of the aggregation process in self-assembling peptide systems can be gained. In **Chapter 4**, oligomers from an otherwise intractable amyloid system, IAPP, are identified and characterised in detail for the first time. From the ESI-MS and ESI-IMS-MS data presented, it remained unclear as to whether the subtle differences observed in the structure and relative abundances of hIAPP and rIAPP oligomers could account for their stark differences in amyloidogenicity. MS/MS experiments were performed and revealed significant differences in the gas-phase stabilities of the two peptides both in the monomeric and oligomeric states, which may explain the striking differences in their aggregation landscapes. In **Chapter 4,** the use of mass spectrometry-based techniques to study amyloid inhibition is also demonstrated, which inspired the development of the screening method detailed in **Chapter 5.**

Having characterised amyloid oligomers formed from several peptides, the next aim was to prevent the formation of these, and any other potentially toxic species. One approach to prevent aggregation of amyloid proteins is the use of small molecules that bind specifically to the protein of interest, and inhibit the initial stages of misfolding and/or aggregation (269-271). IAPP and Aβ40, along with many aggregation-prone peptides and proteins, are intrinsically disordered, and, therefore their structural intricacies remain elusive and screening against the monomer poses a significant challenge (272). As discussed in **Chapter 1** and **Chapter 5**, a number of techniques are inappropriate to use in isolation when screening for small molecule inhibitors of aggregation. By relying too heavily on dye binding studies, for example, several groups have mistakenly identified 'inhibitors' of aggregation, whereby in fact, the 'hits' were only interfering with the dye binding to the fibril (273, 274). The ESI-IMS-MS method described (**Chapter 5**), demonstrates that a number of these claimed inhibitors do not, in fact, have any effect on amyloid assembly. Significantly, the ESI-IMS-MS-based method is able to differentiate between specific inhibitors of protein aggregation and non-specifically or colloidally interacting molecules (**Chapter 5**). ESI-IMS-MS enables observation of multimeric species resulting from self-assembly of compounds as well as protein-only oligomers and protein-ligand complexes, all within one spectrum. This is an important requirement of an inhibitor screen, as any molecule

that erroneously and/or non-specifically interacts with the protein of interest is not an appropriate therapeutic. Other studies have identified inhibitors of protein aggregation, albeit using >20-fold molar excess of small molecule inhibitor: protein (273-275). The use of such high concentrations of potentially inhibitory compounds can lead to physical perturbation of protein aggregation in a colloidal manner. Colloidal inhibitors are identified rapidly and disregarded in the ESI-IMS-MS-based screen, due to the direct observation of their self-assembly. This approach, therefore, has the potential to identify lead compounds which specifically bind to monomeric amyloid precursor proteins and eliminate unsuitable molecules in the early stages of screening, thus increasing the throughput of small molecule drug discovery.

The amyloid cascade underlies more than fifty human disorders (64). Both social and economic burdens associated with amyloid disease are increasing exponentially with our ageing population and increasingly sedentary lifestyles. As such, the ability to screen large numbers of potential aggregation inhibitors against a diverse range of protein targets is paramount. The ESI-IMS-MS method described is rapid, effective, uses only µL sample volumes and has been shown to be applicable to multiple amyloid systems. Furthermore, the data in **Chapter 5** demonstrate that the assay is amenable to automation in the form of an HTS, which results in increased throughput (~5000 compounds/ day) and reduced protein requirements (~ 1 mg/ 5000 compounds). Further automation of the assay is crucial to exploiting its full potential, particular in terms of data interpretation, which may be amenable to pattern recognition analysis. As such, this is to be investigated within the laboratory, over the coming months.

To date, only one successful small molecule therapeutic, Tafamadis, that specifically targets a protein aggregation disorder has been developed (276-278). With increasing resources now being directed towards the detection of compounds as new therapeutics with the potential to interfere with amyloid cascade, cures for some of the world's most debilitating diseases world may become available in the future. The challenges of developing such therapies, however, are not limited merely to the identification of molecules that inhibit protein aggregation. Once identified, these compounds must be developed into stable drug formulations that

164

maintain the potency of the original lead compound. A further challenge in the case of neurodegenerative diseases, such as AD, is that any drug candidate will have the formidable task of needing to cross the blood-brain-barrier. Moreover, many anti-amyloid therapies have failed in clinical trials, largely because the drugs are administered too late in the patient's disease progression (279). If early detection was implemented, prior to the manifestation of symptoms, the preventative therapies could be administered prior to the onset of irreparable damage. Given the multifaceted nature of amyloid diseases, it is unlikely that a single therapeutic avenue will provide the 'silver bullet'. However, rapid identification of aggregation inhibitors is a first, and vital step towards therapeutic intervention into such devastating disorders. The ESI-IMS-MS-based method described here may prove a valuable tool towards achieving these goals, by allowing direct identification of small molecule inhibitors of amyloid assembly.

References

1. DOLE, M. Molecular beams of Macroions. *J. Chem. Phys.*, 1968, **49**(3), pp.2240-2249.
2. FENN, J.B., M. MANN, C.K. MENG, S.F. WONG and C.M. WHITEHOUSE. Electrospray ionization for mass spectrometry of large biomolecules. *Science*, 1989, **246**(4926), pp.64-71.
3. HILLENKAMP, F. and M. KARAS. Mass spectrometry of peptides and proteins by matrix-assisted ultraviolet laser desorption/ionization. *Methods Enzymol.*, 1990, **193**, pp.280-95.
4. MEHMOOD, S., T.M. ALLISON and C.V. ROBINSON. Mass spectrometry of protein complexes: from origins to applications. *Ann. Rev. Phys. Chem.*, 2015, **66**, pp.453-74.
5. MARCOUX, J. and C.V. ROBINSON. Twenty years of gas phase structural biology. *Structure*, 2013, **21**(9), pp.1541-50.
6. WOODS, L.A., S.E. RADFORD and A.E. ASHCROFT. Advances in ion mobility spectrometry-mass spectrometry reveal key insights into amyloid assembly. *BBA - Gen. Sub.*, 2013, **1834**(6), pp.1257-68.
7. PRINGLE, S.D., K. GILES, J.L. WILDGOOSE, J.P. WILLIAMS, S.E. SLADE, K. THALASSINOS, R.H. BATEMAN, M.T. BOWERS and J.H. SCRIVENS. An investigation of the mobility separation of some peptide and protein ions using a new hybrid quadrupole/travelling wave IMS/oa-ToF instrument. *Int. J. Mass Spectrom.*, 2007, **261**(1), pp.1-12.
8. GRIFFITHS, W.J., A.P. JONSSON, S. LIU, D.K. RAI and Y. WANG. Electrospray and tandem mass spectrometry in biochemistry. *Biochem. J.*, 2001, **355**(Pt 3), pp.545-61.
9. KARAS, M., M. GLUCKMANN and J. SCHAFER. Ionization in matrix-assisted laser desorption/ionization: singly charged molecular ions are the lucky survivors. *J. Mass Spectrom.*, 2000, **35**(1), pp.1-12.
10. IRIBARNE, J.V. and B.A. THOMSON. On the evaporation of small ions from charged droplets. *J. Chem. Phys.*, 1976, **64**(6), pp.2287–2294.
11. BENESCH, J.L., B.T. RUOTOLO, D.A. SIMMONS and C.V. ROBINSON. Protein complexes in the gas phase: technology for structural genomics and proteomics. *Chem. Rev.*, 2007, **107**(8), pp.3544-67.
12. YUE, X., S. VAHIDI and L. KONERMANN. Insights into the mechanism of protein electrospray ionization from salt adduction measurements. *J. Am. Soc. Mass Spectrom.*, 2014, **25**(8), pp.1322-31.
13. WILM M, M.M. Analytical properties of the nanoelectrospray ion source. *Anal. Chem.*, 1996, **68**(1), pp.1-8.
14. FENN, J.B. Electrospray wings for molecular elephants (Nobel lecture). *Angew. Chem. Int. Ed.*, 2003, **42**(33), pp.3871-94.
15. GUO, J.P., T. ARAI, J. MIKLOSSY and P.L. MCGEER. Abeta and tau form soluble complexes that may promote self aggregation of both into the insoluble forms observed in Alzheimer's disease. *Proc. Natl. Acad. Sci.*, 2006, **103**(6), pp.1953-8.
16. RUOTOLO, B.T., J.L. BENESCH, A.M. SANDERCOCK, S.J. HYUNG and C.V. ROBINSON. Ion mobility-mass spectrometry analysis of large protein complexes. *Nat. Protoc.*, 2008, **3**(7), pp.1139-52.

17. UETRECHT, C., R.J. ROSE, E. VAN DUIJN, K. LORENZEN and A.J. HECK. Ion mobility mass spectrometry of proteins and protein assemblies. *Chem. Soc. Rev.*, 2010, **39**(5), pp.1633-55.

18. VERBECK, G.F., B.T. RUOTOLO, H.A. SAWYER, K.J. GILLIG and D.H. RUSSELL. A fundamental introduction to ion mobility mass spectrometry applied to the analysis of biomolecules. *J Biomol. Tech.*, 2002, **13**(2), pp.56-61.

19. KANU, A.B., P. DWIVEDI, M. TAM, L. MATZ and H.H. HILL, JR. Ion mobility-mass spectrometry. *J. Mass Spectrom.*, 2008, **43**(1), pp.1-22.

20. SMITH, D.P., T.W. KNAPMAN, I. CAMPUZANO, R.W. MALHAM, J.T. BERRYMAN, S.E. RADFORD and A.E. ASHCROFT. Deciphering drift time measurements from travelling wave ion mobility spectrometry-mass spectrometry studies. *Eur. J. Mass Spectrom.*, 2009, **15**(2), pp.113-30.

21. SHVARTSBURG, A.A. and R.D. SMITH. Fundamentals of Traveling Wave Ion Mobility Spectrometry. *Anal. Chem.*, 2008, **80**(24), pp.9689-9699.

22. GILES, K., S.D. PRINGLE, K.R. WORTHINGTON, D. LITTLE, J.L. WILDGOOSE and R.H. BATEMAN. Applications of a travelling wave-based radio-frequency-only stacked ring ion guide. *Rapid Commun. Mass Spectrom.*, 2004, **18**(20), pp.2401-14.

23. VALENTINE, S.J., A.E. COUNTERMAN, C.S. HOAGLUND, J.P. REILLY and D.E. CLEMMER. Gas-phase separations of protease digests. *J. Am. Soc. Mass Spectrom.*, 1998, **9**(11), pp.1213-6.

24. CLEMMER, D.E.H., R. R.; JARROLD, M. F. Naked Protein Conformations: Cytochrome c in the Gas Phase. *J. Am. Chem. Soc.*, 1995, **117**, pp.10141-10142.

25. MESLEH, M.F., J.M. HUNTER, A.A. SHVARTSBURG, G.C. SCHATZ and M.F. JARROLD. Structural information from ion mobility measurements: Effects of the long-range potential (vol 100, pg 16082, 1996). *J Phys. Chem. A*, 1997, **101**(5), pp.968-968.

26. SHVARTSBURG, A.A. and M.F. JARROLD. An exact hard-spheres scattering model for the mobilities of polyatomic ions. *Chem. Phys. Lett.*, 1996, **261**(1-2), pp.86-91.

27. BLEIHOLDER, C., T. WYTTENBACH and M.T. BOWERS. A novel projection approximation algorithm for the fast and accurate computation of molecular collision cross sections (I). Method. *Int. J Mass Spectrom.*, 2011, **308**(1), pp.1-10.

28. STEPHENS, W. Pulsed Mass Spectrometer with Time Dispersion. *Bull. Am. Phys. Soc.*, 1946, **21**(2), p.22.

29. WILEY, W.C. and I.H. MCLAREN. Time-Of-Flight Mass Spectrometer with Improved Resolution. *Rev. of Sci. Instrum.*, 1955, **26**(12), p.1150.

30. BROWN, R.S. and J.J. LENNON. Mass resolution improvement by incorporation of pulsed ion extraction in a matrix-assisted laser desorption/ionization linear time-of-flight mass spectrometer. *Anal. Chem.*, 1995, **67**(13), pp.1998-2003.

31. MAMYRIN, B.A., V.I. KARATAEV, D.V. SHMIKK and V.A. ZAGULIN. Mass-Reflectron a New Nonmagnetic Time-of-Flight High-Resolution Mass-Spectrometer. *Zh Eksp Teor Fiz+*, 1973, **64**(1), pp.82-89.

32. DEHOFFMANN, E. Tandem mass spectrometry: A primer. *J. Mass Spectrom.*, 1996, **31**(2), pp.129-137.

33. SHUKLA, A.K. and J.H. FUTRELL. Tandem mass spectrometry: dissociation of ions by collisional activation. *J. Mass Spectrom.*, 2000, **35**(9), pp.1069-1090.

34. ROSTOM, A.A. and C.V. ROBINSON. Disassembly of intact multiprotein complexes in the gas phase. *Curr. Opin. Struct. Biol.*, 1999, **9**(1), pp.135-41.

35. NIU, S. and B.T. RUOTOLO. Collisional unfolding of multiprotein complexes reveals cooperative stabilization upon ligand binding. *Protein Sci.*, 2015, **24**(8), pp.1272-81.

36. WYSOCKI, V.H., K.A. RESING, Q.F. ZHANG and G.L. CHENG. Mass spectrometry of peptides and proteins. *Methods*, 2005, **35**(3), pp.211-222.

37. CHOWDHURY, S.K., V. KATTA and B.T. CHAIT. Electrospray ionization mass spectrometric peptide mapping: a rapid, sensitive technique for protein structure analysis. *Biochem. Biophys. Res. Commun.*, 1990, **167**(2), pp.686-92.

38. KALTASHOV, I.A. and A. MOHIMEN. Estimates of protein surface areas in solution by electrospray ionization mass spectrometry. *Anal. Chem.*, 2005, **77**(16), pp.5370-9.

39. LORENZEN, K., A.S. OLIA, C. UETRECHT, G. CINGOLANI and A.J. HECK. Determination of stoichiometry and conformational changes in the first step of the P22 tail assembly. *J. Mol. Biol.*, 2008, **379**(2), pp.385-96.

40. UETRECHT, C., C. VERSLUIS, N.R. WATTS, W.H. ROOS, G.J.L. WUITE, P.T. WINGFIELD, A.C. STEVEN and A.J.R. HECK. High-resolution mass spectrometry of viral assemblies: Molecular composition and stability of dimorphic hepatitis B virus capsids. *Proc. Natl. Acad. Sci.*, 2008, **105**(27), pp.9216-9220.

41. BERESZCZAK, J.Z., M. HAVLIK, V.U. WEISS, M. MARCHETTI-DESCHMANN, E. VAN DUIJN, N.R. WATTS, P.T. WINGFIELD, G. ALLMAIER, A.C. STEVEN and A.J.R. HECK. Sizing up large protein complexes by electrospray ionisation-based electrophoretic mobility and native mass spectrometry: morphology selective binding of Fabs to hepatitis B virus capsids. *Anal. Bioanal. Chem.*, 2014, **406**(5), pp.1437-1446.

42. KNAPMAN, T.W., V.L. MORTON, N.J. STONEHOUSE, P.G. STOCKLEY and A.E. ASHCROFT. Determining the topology of virus assembly intermediates using ion mobility spectrometry-mass spectrometry. *Rapid Commun. Mass Spectrom.*, 2010, **24**(20), pp.3033-3042.

43. HECK, A.J.R. Ion mobility mass spectrometry applied to virus structure and assembly. *Abstr. Pap. Am. Chem. Soc.*, 2010, **240**.

44. WOODS, L.A., G.W. PLATT, A.L. HELLEWELL, E.W. HEWITT, S.W. HOMANS, A.E. ASHCROFT and S.E. RADFORD. Ligand binding to distinct states diverts aggregation of an amyloid-forming protein. *Nat. Chem. Biol.*, 2011, **7**(10), pp.730-9.

45. GESSEL, M.M., S. BERNSTEIN, M. KEMPER, D.B. TEPLOW and M.T. BOWERS. Familial Alzheimer's disease mutations differentially alter amyloid β-protein oligomerization. *ACS Chem. Neurosci.*, 2012, **3**(11), pp.909-918.

46. BLEIHOLDER, C., N.F. DUPUIS, T. WYTTENBACH and M.T. BOWERS. Ion mobility-mass spectrometry reveals a conformational conversion from random assembly to β-sheet in amyloid fibril formation. *Nat. Chem.*, 2011, **3**(2), pp.172-7.

47. DUPUIS, N.F., C. WU, J.E. SHEA and M.T. BOWERS. The amyloid formation mechanism in human IAPP: dimers have β-strand monomer-monomer interfaces. *J. Am. Chem. Soc.*, 2011, **133**(19), pp.7240-3.

48. DUPUIS, N.F., C. WU, J.E. SHEA and M.T. BOWERS. Human islet amyloid polypeptide monomers form ordered beta-hairpins: a possible direct amyloidogenic precursor. *J. Am. Chem. Soc.*, 2009, **131**(51), pp.18283-92.

49. BERNSTEIN, S.L., D. LIU, T. WYTTENBACH, M.T. BOWERS, J.C. LEE, H.B. GRAY and J.R. WINKLER. Alpha-synuclein: stable compact and extended monomeric structures and pH dependence of dimer formation. *J. Am. Soc. Mass Spectrom.*, 2004, **15**(10), pp.1435-43.

50. SINZ, A. The advancement of chemical cross-linking and mass spectrometry for structural proteomics: from single proteins to protein interaction networks. *Expert Rev. Proteomics*, 2014, **11**(6), pp.733-43.

51. SINZ, A. Chemical cross-linking and mass spectrometry to map three-dimensional protein structures and protein-protein interactions. *Mass Spectrom. Rev.*, 2006, **25**(4), pp.663-82.

52. RAND, K.D., M. ZEHL and T.J. JORGENSEN. Measuring the hydrogen/deuterium exchange of proteins at high spatial resolution by mass spectrometry: overcoming gas-phase hydrogen/deuterium scrambling. *Acc. Chem. Res.*, 2014, **47**(10), pp.3018-27.

53. RAND, K.D., S.D. PRINGLE, J.P. MURPHY, 3RD, K.E. FADGEN, J. BROWN and J.R. ENGEN. Gas-phase hydrogen/deuterium exchange in a traveling wave ion guide for the examination of protein conformations. *Anal. Chem.*, 2009, **81**(24), pp.10019-28.

54. DILL, K.A. and H.S. CHAN. From Levinthal to pathways to funnels. *Nat. Struc. Biol.*, 1997, **4**(1), pp.10-9.

55. DOBSON, C.M. Protein-misfolding diseases: Getting out of shape. *Nature*, 2002, **418**(6899), pp.729-730.

56. CHITI, F. and C.M. DOBSON. Protein misfolding, functional amyloid, and human disease. *Ann. Rev. Biochem.*, 2006, **75**, pp.333-66.

57. HARTL, F.U. and M. HAYER-HARTL. Converging concepts of protein folding *in vitro* and *in vivo*. *Nat. Struc. Mol. Biol.*, 2009, **16**(6), pp.574-581.

58. BROCKWELL, D.J. and S.E. RADFORD. Intermediates: Ubiquitous species on folding energy landscapes? *Curr. Opin. Struct. Biol.*, 2007, **17**(1), pp.30-37.

59. DOBSON, C.M. Protein folding and misfolding. *Nature*, 2003, **426**(6968), pp.884-90.

60. STEFANI, M. and C.M. DOBSON. Protein aggregation and aggregate toxicity: new insights into protein folding, misfolding diseases and biological evolution. *J Mol.Med.*, 2003, **81**(11), pp.678-99.

61. VENDRUSCOLO, M., J. ZURDO, C.E. MACPHEE and C.M. DOBSON. Protein folding and misfolding: a paradigm of self-assembly and regulation in complex biological systems. *Philos. Transact. A Math. Phys. Eng. Sci.*, 2003, **361**(1807), pp.1205-22.

62. SIPE, J.D., M.D. BENSON, J.N. BUXBAUM, S.-I. IKEDA, G. MERLINI, M.J.M. SARAIVA and P. WESTERMARK. Nomenclature 2014: Amyloid fibril proteins and clinical classification of the amyloidosis. *Amyloid*, 2014, **21**(4), pp.221-224.

63. ROSS, C., POIRIER, M.,. Protein aggregation and neurodegenerative disease. *Nat. Med.*, 2004, **10**, pp.S10-S17.

64. SIPE, J.D., M.D. BENSON, J.N. BUXBAUM, S.-I. IKEDA, G. MERLINI, M.J.M. SARAIVA and P. WESTERMARK. Amyloid fibril protein nomenclature: 2012

recommendations from the Nomenclature Committee of the International Society of Amyloidosis. *Amyloid*, 2012, **19**(4), pp.167-170.

65. VENDRUSCOLO, M., T.P. KNOWLES and C.M. DOBSON. Protein solubility and protein homeostasis: a generic view of protein misfolding disorders. *Cold Spring Harb. Perspect. Biol.*, 2011, **3**(12).

66. KAYED, R., E. HEAD, J.L. THOMPSON, T.M. MCINTIRE, S.C. MILTON, C.W. COTMAN and C.G. GLABE. Common structure of soluble amyloid oligomers implies common mechanism of pathogenesis. *Science*, 2003, **300**(5618), pp.486-489.

67. NORRBY, E. Prions and protein folding diseases. *J. Internal Med.*, 2011, **270**(1), pp.1-14.

68. NOMURA, Y. Molecular approaches to the treatment, prophylaxis, and diagnosis of Alzheimer's disease. *J Pharmacol.Sci.*, 2012, **118**(3), pp.317-318.

69. JAIN, S., N. WOOD and D. HEALY. Molecular genetic pathways in Parkinson's disease: a review. *Clin. Sci.*, 2005, **109**, pp.355-364.

70. KIERNAN, M.C., S. VUCIC, B.C. CHEAH, M.R. TURNER, A. EISEN, O. HARDIMAN, J.R. BURRELL and M.C. ZOING. Amyotrophic lateral sclerosis. *Lancet*, **377**(9769), pp.942-955.

71. ROSS, C.A. and S.J. TABRIZI. Huntington's disease: from molecular pathogenesis to clinical treatment. *Lancet Neurol.*, 2011, **10**(1), pp.83-98.

72. WESTERMARK, P., A. ANDERSSON and G.T. WESTERMARK. Islet amyloid polypeptide, islet amyloid, and diabetes mellitus. *Physiol. Rev.*, 2011, **91**(3), pp.795-826.

73. SHIKAMA, Y., J.-I. KITAZAWA, N. YAGIHASHI, O. UEHARA, Y. MURATA, N. YAJIMA, R. WADA and S. YAGIHASHI. Localized amyloidosis at the site of repeated insulin injection in a diabetic patient. *Intern. Med.*, 2010, **49**(5), pp.397-401.

74. TEOH, C., M.W. GRIFFIN and G. HOWLETT. Apolipoproteins and amyloid fibril formation in atherosclerosis. *Protein Cell*, 2011, **2**(2), pp.116-127.

75. MERLINI, G., R.L. COMENZO, D.C. SELDIN, A. WECHALEKAR and M.A. GERTZ. Immunoglobulin light chain amyloidosis. *Exp. Rev. Hematol.*, 2014, **7**(1), pp.143-156.

76. PETTERSSON, T., Y. KONTTINEN and C. MAURY. Treatment strategies for amyloid A amyloidosis. *Exp. Opin. Pharmacother.*, 2008, **9**(12), pp.2117-2128.

77. SMITH, D., A. ASHCROFT and S. RADFORD. Hemodialysis-related amyloidosis. *In:* M. RAMIREZ-ALVARADO, J. KELLY and C. DOBSON, eds. *Protein misfolding diseases: current and emerging principles and therapies*. Hoboken, New Jersey: John Wiley & Sons, Inc., 2010.

78. GRANEL, B., S. VALLEIX, J. SERRATRICE, P. CHÉRIN, A. TEXEIRA, P. DISDIER, P. WEILLER and G. GRATEAU. Lysozyme amyloidosis: report of 4 cases and a review of the literature. *Medicine*, 2006, **85**(1), pp.66-73.

79. HYUNG, S.J., C.V. ROBINSON and B.T. RUOTOLO. Gas-phase unfolding and disassembly reveals stability differences in ligand-bound multiprotein complexes. *Chem. Biol.*, 2009, **16**(4), pp.382-90.

80. ADAMCIK, J. and R. MEZZENGA. Study of amyloid fibrils via atomic force microscopy. *Curr. Opin. Colloid. In.*, 2012, **17**(6), pp.369-376.

81. SERPELL, L.C. Alzheimer's amyloid fibrils: structure and assembly. *Bba-Mol Basis Dis*, 2000, **1502**(1), pp.16-30.

82. BENDITT, E.P., N. ERIKSEN and C. BERGLUND. Congo red dichroism with dispersed amyloid fibrils, an extrinsic cotton effect. *Proc. Natl. Acad. Sci.*, 1970, **66**(4), pp.1044-51.

83. BAN, T., D. HAMADA, K. HASEGAWA, H. NAIKI and Y. GOTO. Direct observation of amyloid fibril growth monitored by thioflavin T fluorescence. *J. Biol. Chem.*, 2003, **278**(19), pp.16462-5.

84. HOBBS, J.R. and A.D. MORGAN. Fluorescence Microscopy with Thioflavine-T in Diagnosis of Amyloid. *J Pathol. Bacteriol.*, 1963, **86**(2), pp.437-&.

85. LADEWIG, P. Double-Refringence of the Amyloid-Congo-Red-Complex in Histological Sections. *Nature*, 1945, **156**(3951), pp.81-82.

86. BIANCALANA, M. and S. KOIDE. Molecular mechanism of Thioflavin-T binding to amyloid fibrils. *BBA - Gen. Sub.*, 2010, **1804**(7), pp.1405-12.

87. FERRONE, F. Analysis of protein aggregation kinetics. *Method Enzymol.*, 1999, **309**, pp.256-274.

88. MADINE, J., E. JACK, P.G. STOCKLEY, S.E. RADFORD, L.C. SERPELL and D.A. MIDDLETON. Structural insights into the polymorphism of amyloid-like fibrils formed by region 20-29 of amylin revealed by solid-state NMR and X-ray fiber diffraction. *J Am. Chem. Soc.*, 2008, **130**(45), pp.14990-5001.

89. WESTERMARK, P. Amyloid in the islets of Langerhans: thoughts and some historical aspects. *Ups. J. Med. Sci.*, 2011, **116**(2), pp.81-9.

90. KARAMANOS, T.K., A.P. KALVERDA, G.S. THOMPSON and S.E. RADFORD. Visualization of transient protein-protein interactions that promote or inhibit amyloid assembly. *Mol. Cell*, 2014, **55**(2), pp.214-26.

91. KUMAR, A., L.C. PASLAY, D. LYONS, S.E. MORGAN, J.J. CORREIA and V. RANGACHARI. Specific Soluble Oligomers of Amyloid-β Peptide Undergo Replication and Form Non-fibrillar Aggregates in Interfacial Environments. *J. Biol. Chem.*, 2012, **287**(25), pp.21253-64.

92. LAMBERT, M.P., A.K. BARLOW, B.A. CHROMY, C. EDWARDS, R. FREED, M. LIOSATOS, T.E. MORGAN, I. ROZOVSKY, B. TROMMER, K.L. VIOLA, P. WALS, C. ZHANG, C.E. FINCH, G.A. KRAFFT and W.L. KLEIN. Diffusible, nonfibrillar ligands derived from $A\beta_{1-42}$ are potent central nervous system neurotoxins. *Proc. Natl. Acad. Sci.*, 1998, **95**(11), pp.6448-6453.

93. SMITH, D.P., S.E. RADFORD and A.E. ASHCROFT. Elongated oligomers in beta2-microglobulin amyloid assembly revealed by ion mobility spectrometry-mass spectrometry. *Proc. Natl. Acad. Sci.*, 2010, **107**(15), pp.6794-8.

94. SMITH, A.M., T.R. JAHN, A.E. ASHCROFT and S.E. RADFORD. Direct observation of oligomeric species formed in the early stages of amyloid fibril formation using electrospray ionisation mass spectrometry. *J. Mol. Biol.*, 2006, **364**(1), pp.9-19.

95. FRIMPONG, A.K., R.R. ABZALIMOV, V.N. UVERSKY and I.A. KALTASHOV. Characterization of intrinsically disordered proteins with electrospray ionization mass spectrometry: conformational heterogeneity of alpha-synuclein. *Proteins*, 2010, **78**(3), pp.714-22.

96. LIU, Y., J.A. CARVER, A.N. CALABRESE and T.L. PUKALA. Gallic acid interacts with alpha-synuclein to prevent the structural collapse necessary for its aggregation. *Biochim. Biophys. Acta*, 2014, **1844**(9), pp.1481-5.

97. WILLIAMS, D.M. and T.L. PUKALA. Novel insights into protein misfolding diseases revealed by ion mobility-mass spectrometry. *Mass Spectrom. Rev.*, 2013, **32**(3), pp.169-87.

98. BERNSTEIN, S.L., N.F. DUPUIS, N.D. LAZO, T. WYTTENBACH, M.M. CONDRON, G. BITAN, D.B. TEPLOW, J.E. SHEA, B.T. RUOTOLO, C.V. ROBINSON and M.T. BOWERS. Amyloid-β protein oligomerization and the importance of tetramers and dodecamers in the aetiology of Alzheimer's disease. *Nat. Chem.*, 2009, **1**(4), pp.326-31.

99. ZHENG, X., M.M. GESSEL, M.L. WISNIEWSKI, K. VISWANATHAN, D.L. WRIGHT, B.A. BAHR and M.T. BOWERS. Z-Phe-Ala-diazomethylketone (PADK) disrupts and remodels early oligomer states of the Alzheimer disease Aβ42 protein. *J. Biol. Chem.*, 2012, **287**(9), pp.6084-6088.

100. KLONIECKI, M., A. JABLONOWSKA, J. POZNANSKI, J. LANGRIDGE, C. HUGHES, I. CAMPUZANO, K. GILES and M. DADLEZ. Ion mobility separation coupled with MS detects two structural states of Alzheimer's disease Abeta1-40 peptide oligomers. *J Mol. Biol.*, 2011, **407**(1), pp.110-24.

101. YOUNG, L., H. NDLOVU, T. KNAPMAN, S. HARRIS, S. RADFORD and A. ASHCROFT. Monitoring oligomer formation from self-aggregating amylin peptides using ESI-IMS-MS. *Int. J. Ion Mobil. Spectrom.*, 2013, **16**(1), pp.29-39.

102. YOUNG, L.M., P. CAO, D.P. RALEIGH, A.E. ASHCROFT and S.E. RADFORD. Ion mobility spectrometry-mass spectrometry defines the oligomeric intermediates in amylin amyloid formation and the mode of action of inhibitors. *J. Am. Chem. Soc.*, 2014, **136**(2), pp.660-70.

103. MCCAMMON, M.G., D.J. SCOTT, C.A. KEETCH, L.H. GREENE, H.E. PURKEY, H.M. PETRASSI, J.W. KELLY and C.V. ROBINSON. Screening transthyretin amyloid fibril inhibitors: characterization of novel multiprotein, multiligand complexes by mass spectrometry. *Structure*, 2002, **10**(6), pp.851-63.

104. SUSA, A.C., C. WU, S.L. BERNSTEIN, N.F. DUPUIS, H. WANG, D.P. RALEIGH, J.-E. SHEA and M.T. BOWERS. Defining the molecular basis of amyloid inhibitors: human islet amyloid polypeptide–insulin interactions. *J. Am. Chem. Soc.*, 2014, **136**(37), pp.12912-12919.

105. NETTLETON, E.J., P. TITO, M. SUNDE, M. BOUCHARD, C.M. DOBSON and C.V. ROBINSON. Characterization of the oligomeric states of insulin in self-assembly and amyloid fibril formation by mass spectrometry. *Biophys. J.*, 2000, **79**(2), pp.1053-65.

106. GRABENAUER, M., C. WU, P. SOTO, J.E. SHEA and M.T. BOWERS. Oligomers of the prion protein fragment 106-126 are likely assembled from beta-hairpins in solution, and methionine oxidation inhibits assembly without altering the peptide's monomeric conformation. *J. Am. Chem. Soc.*, 2010, **132**(2), pp.532-9.

107. ABEDINI, A. and A.M. SCHMIDT. Mechanisms of islet amyloidosis toxicity in type 2 diabetes. *FEBS Lett.*, 2013, **587**(8), pp.1119-1127.

108. WESTERMARK, P., C. WERNSTEDT, E. WILANDER, D.W. HAYDEN, T.D. O'BRIEN and K.H. JOHNSON. Amyloid fibrils in human insulinoma and islets of Langerhans of the diabetic cat are derived from a neuropeptide-like protein

also present in normal islet cells. *Proc. Natl. Acad. Sci.*, 1987, **84**(11), pp.3881-3885.

109. WESTERMARK, P., A. ANDERSSON and G.T. WESTERMARK. Islet amyloid polypeptide, islet amyloid, and diabetes mellitus. *Physiol. Rev.*, 2011, **91**(3), pp.795-826.

110. YAN, L.M., M. TATAREK-NOSSOL, A. VELKOVA, A. KAZANTZIS and A. KAPURNIOTU. Design of a mimic of nonamyloidogenic and bioactive human islet amyloid polypeptide (IAPP) as nanomolar affinity inhibitor of IAPP cytotoxic fibrillogenesis. *Proc Natl Acad Sci U S A*, 2006, **103**(7), pp.2046-51.

111. MAREK, P., A.M. WOYS, K. SUTTON, M.T. ZANNI and D.P. RALEIGH. Efficient microwave-assisted synthesis of human islet amyloid polypeptide designed to facilitate the specific incorporation of labeled amino acids. *Org Lett*, 2010, **12**(21), pp.4848-51.

112. SARAOGI, I., J.A. HEBDA, J. BECERRIL, L.A. ESTROFF, A.D. MIRANKER and A.D. HAMILTON. Synthetic alpha-helix mimetics as agonists and antagonists of islet amyloid polypeptide aggregation. *Angew Chem Int Ed Engl*, 2010, **49**(4), pp.736-9.

113. WESTERMARK, P., U. ENGSTROM, K.H. JOHNSON, G.T. WESTERMARK and C. BETSHOLTZ. Islet amyloid polypeptide: pinpointing amino acid residues linked to amyloid fibril formation. *Proc Natl Acad Sci U S A*, 1990, **87**(13), pp.5036-40.

114. CAO, P., F. MENG, A. ABEDINI and D.P. RALEIGH. The ability of rodent islet amyloid polypeptide to inhibit amyloid formation by human islet amyloid polypeptide has important implications for the mechanism of amyloid formation and the design of inhibitors. *Biochem.*, 2010, **49**(5), pp.872-81.

115. TENIDIS, K., M. WALDNER, J. BERNHAGEN, W. FISCHLE, M. BERGMANN, M. WEBER, M.L. MERKLE, W. VOELTER, H. BRUNNER and A. KAPURNIOTU. Identification of a penta- and hexapeptide of islet amyloid polypeptide (IAPP) with amyloidogenic and cytotoxic properties. *J Mol Biol*, 2000, **295**(4), pp.1055-71.

116. MENG, F., D.P. RALEIGH and A. ABEDINI. Combination of kinetically selected inhibitors in trans leads to highly effective inhibition of amyloid formation. *J. Am. Chem. Soc.*, 2010, **132**(41), pp.14340-2.

117. YAN, L.M., M. TATAREK-NOSSOL, A. VELKOVA, A. KAZANTZIS and A. KAPURNIOTU. Design of a mimic of nonamyloidogenic and bioactive human islet amyloid polypeptide (IAPP) as nanomolar affinity inhibitor of IAPP cytotoxic fibrillogenesis. *Proc. Nat. Acad. Sci.*, 2006, **103**(7), pp.2046-51.

118. MORIARTY, D.F. and D.P. RALEIGH. Effects of sequential proline substitutions on amyloid formation by human amylin20-29. *Biochem.*, 1999, **38**(6), pp.1811-8.

119. CAO, P., A. ABEDINI, H. WANG, L.H. TU, X. ZHANG, A.M. SCHMIDT and D.P. RALEIGH. Islet amyloid polypeptide toxicity and membrane interactions. *Proc. Natl. Acad. Sci.*, 2013, **110**(48), pp.19279-84.

120. SAKAGASHIRA, S., H.J. HIDDINGA, K. TATEISHI, T. SANKE, T. HANABUSA, K. NANJO and N.L. EBERHARDT. S20G mutant amylin exhibits increased in vitro amyloidogenicity and increased intracellular cytotoxicity compared to wild-type amylin. *Am. J. Pathol.*, 2000, **157**(6), pp.2101-9.

121.   TU, L.H., A.L. SERRANO, M.T. ZANNI and D.P. RALEIGH. Mutational analysis of preamyloid intermediates: the role of his-tyr interactions in islet amyloid formation. *Biophys. J.*, 2014, **106**(7), pp.1520-7.

122.   LEE, V.M.Y. Amyloid binding ligands as Alzheimer's disease therapies. *Neurobiology of Aging*, 2002, **23**(6), pp.1039-1042.

123.   MINATI, L., T. EDGINTON, M. GRAZIA BRUZZONE and G. GIACCONE. Reviews: Current concepts in Alzheimer's disease: A multidisciplinary review. *Am. J. Alzheimers Dis. Other Demen.*, 2009, **24**(2), pp.95-121.

124.   LANDAU, M., M.R. SAWAYA, K.F. FAULL, A. LAGANOWSKY, L. JIANG, S.A. SIEVERS, J. LIU, J.R. BARRIO and D. EISENBERG. Towards a pharmacophore for amyloid. *PLoS Biol.*, 2011, **9**(6), p.e1001080.

125.   MAK, J.C.W. Potential role of green tea catechins in various disease therapies: Progress and promise. *Clin. Exp.Pharmacol. Physiol.*, 2012, **39**(3), pp.265-273.

126.   BULAWA, C.E., S. CONNELLY, M. DEVIT, L. WANG, C. WEIGEL, J.A. FLEMING, J. PACKMAN, E.T. POWERS, R.L. WISEMAN, T.R. FOSS, I.A. WILSON, J.W. KELLY and R. LABAUDINIÈRE. Tafamidis, a potent and selective transthyretin kinetic stabilizer that inhibits the amyloid cascade. *Proc. Natl. Acad. Sci.*, 2012.

127.   HAMLEY, I.W. The amyloid beta peptide: a chemist's perspective. Role in Alzheimer's and fibrillization. *Chem. Rev.*, 2012, **112**(10), pp.5147-5192.

128.   PORAT, Y., A. ABRAMOWITZ and E. GAZIT. Inhibition of amyloid fibril formation by polyphenols: structural similarity and aromatic interactions as a common inhibition mechanism. *Chem. Biol. Drug Des.*, 2006, **67**(1), pp.27-37.

129.   LORENZO, A. and B.A. YANKNER. Beta-amyloid neurotoxicity requires fibril formation and is inhibited by Congo red. *Proc. Natl. Acad. Sci.*, 1994, **91**(25), pp.12243-12247.

130.   POLI, G., W. PONTI, G. CARCASSOLA, F. CECILIANI, L. COLOMBO, P. DALL'ARA, M. GERVASONI, M.L. GIANNINO, P.A. MARTINO, C. POLLER, S. VILLA and M. SALMONA. *In vitro* evaluation of the anti-prionic activity of newly synthesized Congo red derivatives. *Arzneim.-Forsch.*, 2003, **53**(12), pp.875-888.

131.   MISHRA, R., B. BULIC, D. SELLIN, S. JHA, H. WALDMANN and R. WINTER. Small-molecule inhibitors of islet amyloid polypeptide fibril formation. *Angew. Chem. Int. Ed.*, 2008, **47**(25), pp.4679-4682.

132.   WU, C., J. SCOTT and J.-E. SHEA. Binding of Congo red to amyloid protofibrils of the Alzheimer $A\beta_{9-40}$ peptide probed by molecular dynamics simulations. *Biophys. J.*, 2012, **103**(3), pp.550-557.

133.   TURNELL, W.G. and J.T. FINCH. Binding of the dye Congo red to the amyloid protein pig insulin reveals a novel homology amongst amyloid-forming peptide sequences. *J. Mol. Biol.*, 1992, **227**(4), pp.1205-1223.

134.   KIM, Y.-S., T.W. RANDOLPH, M.C. MANNING, F.J. STEVENS and J.F. CARPENTER. Congo red populates partially unfolded states of an amyloidogenic protein to enhance aggregation and amyloid fibril formation. *J. Biol. Chem.*, 2003, **278**(12), pp.10842-10850.

135.   PALHANO, F.L., J. LEE, N.P. GRIMSTER and J.W. KELLY. Toward the molecular mechanism(s) by which EGCG treatment remodels mature amyloid fibrils. *J. Am. Chem. Soc.*, 2013, **135**(20), pp.7503-7510.

136.   MENG, F., A. ABEDINI, A. PLESNER, C.B. VERCHERE and D.P. RALEIGH. The flavanol (-)-epigallocatechin 3-gallate inhibits amyloid formation by islet

amyloid polypeptide, disaggregates amyloid fibrils, and protects cultured cells against IAPP-induced toxicity. *Biochem.*, 2010, **49**(37), pp.8127-8133.

137.   CAO, P. and D.P. RALEIGH. Analysis of the inhibition and remodeling of islet amyloid polypeptide amyloid fibers by flavanols. *Biochem.*, 2012, **51**(13), pp.2670-2683.

138.   YOUNG, L.M., P. CAO, D.P. RALEIGH, A.E. ASHCROFT and S.E. RADFORD. Ion mobility spectrometry–mass spectrometry defines the oligomeric intermediates in amylin amyloid formation and the mode of action of inhibitors. *J. Am. Chem. Soc.*, 2013, **136**(2), pp.660-670.

139.   FERREIRA, N., M.J. SARAIVA and M.R. ALMEIDA. Natural polyphenols inhibit different steps of the process of transthyretin (TTR) amyloid fibril formation. *FEBS Lett.*, 2011, **585**(15), pp.2424-2430.

140.   HUDSON, S.A., H. ECROYD, F.C. DEHLE, I.F. MUSGRAVE and J.A. CARVER. (−)-Epigallocatechin-3-gallate (EGCG) maintains κ-casein in its pre-fibrillar state without redirecting its aggregation pathway. *J. Mol. Biol.*, 2009, **392**(3), pp.689-700.

141.   EHRNHOEFER, D.E., J. BIESCHKE, A. BOEDDRICH, M. HERBST, L. MASINO, R. LURZ, S. ENGEMANN, A. PASTORE and E.E. WANKER. EGCG redirects amyloidogenic polypeptides into unstructured, off-pathway oligomers. *Nat. Struc. Mol. Biol.*, 2008, **15**(6), pp.558-66.

142.   AISEN, P.S. The development of anti-amyloid therapy for alzheimer's disease: From secretase modulators to polymerisation inhibitors. *CNS Drugs*, 2005, **19**(12), pp.989-996.

143.   TANIGUCHI, S., N. SUZUKI, M. MASUDA, S.-I. HISANAGA, T. IWATSUBO, M. GOEDERT and M. HASEGAWA. Inhibition of heparin-induced Tau filament formation by phenothiazines, polyphenols, and porphyrins. *J. Biol. Chem.*, 2005, **280**(9), pp.7614-7623.

144.   HOWLETT, D., P. CUTLER, S. HEALES and P. CAMILLERI. Hemin and related porphyrins inhibit β-amyloid aggregation. *FEBS Lett.*, 1997, **417**(2), pp.249-251.

145.   ONO, K., K. HASEGAWA, H. NAIKI and M. YAMADA. Curcumin has potent anti-amyloidogenic effects for Alzheimer's β-amyloid fibrils *in vitro*. *J Neurosci. Res.*, 2004, **75**(6), pp.742-750.

146.   JIANG, T., X.-L. ZHI, Y.-H. ZHANG, L.-F. PAN and P. ZHOU. Inhibitory effect of curcumin on the Al(III)-induced $A\beta_{42}$ aggregation and neurotoxicity *in vitro*. *Biochim. Biophys. Acta*, 2012, **1822**(8), pp.1207-1215.

147.   DAVAL, M., S. BEDROOD, T. GURLO, C.-J. HUANG, S. COSTES, P.C. BUTLER and R. LANGEN. The effect of curcumin on human islet amyloid polypeptide misfolding and toxicity. *Amyloid*, 2010, **17**(3-4), pp.118-128.

148.   SPARKS, S., G. LIU, K.J. ROBBINS and N.D. LAZO. Curcumin modulates the self-assembly of the islet amyloid polypeptide by disassembling α-helix. *Biochem. Biophys. Res. Commun.*, 2012, **422**(4), pp.551-555.

149.   PANDEY, N., J. STRIDER, W. NOLAN, S. YAN and J. GALVIN. Curcumin inhibits aggregation of α-synuclein. *Acta Neuropathol.*, 2008, **115**(4), pp.479-489.

150.   BORANA, M.S., P. MISHRA, R.R.S. PISSURLENKAR, R.V. HOSUR and B. AHMAD. Curcumin and kaempferol prevent lysozyme fibril formation by modulating aggregation kinetic parameters. *BBA - Proteins Proteomics*, 2014, **1844**(3), pp.670-680.

151. HARRIS, J.R. *In vitro* fibrillogenesis of the amyloid β$_{1–42}$ peptide: cholesterol potentiation and aspirin inhibition. *Micron*, 2002, **33**(7–8), pp.609-626.

152. PORAT, Y., Y. MAZOR, S. EFRAT and E. GAZIT. Inhibition of islet amyloid polypeptide fibril formation: a potential role for heteroaromatic interactions. *Biochem.*, 2004, **43**(45), pp.14454-62.

153. PORAT, Y., A. ABRAMOWITZ and E. GAZIT. Inhibition of amyloid fibril formation by polyphenols: structural similarity and aromatic interactions as a common inhibition mechanism. *Chem. Biol. Drug. Des.*, 2006, **67**(1), pp.27-37.

154. MASUDA, M., M. HASEGAWA, T. NONAKA, T. OIKAWA, M. YONETANI, Y. YAMAGUCHI, K. KATO, S.-I. HISANAGA and M. GOEDERT. Inhibition of α-synuclein fibril assembly by small molecules. *FEBS Lett.*, 2009, **583**(4), pp.787-791.

155. CHENG, B., H. GONG, H. XIAO, R.B. PETERSEN, L. ZHENG and K. HUANG. Inhibiting toxic aggregation of amyloidogenic proteins: A therapeutic strategy for protein misfolding diseases. *Biochem. Biophys. Res. Commun.*, 2013, **1830**(10), pp.4860-4871.

156. PALHANO, F.L., J. LEE, N.P. GRIMSTER and J.W. KELLY. Toward the molecular mechanism(s) by which EGCG treatment remodels mature amyloid fibrils. *J. Am. Chem. Soc.*, 2013, **135**(20), pp.7503-10.

157. MENG, F., A. ABEDINI, A. PLESNER, C.B. VERCHERE and D.P. RALEIGH. The flavanol (-)-epigallocatechin 3-gallate inhibits amyloid formation by islet amyloid polypeptide, disaggregates amyloid fibrils, and protects cultured cells against IAPP-induced toxicity. *Biochem.*, 2010, **49**(37), pp.8127-33.

158. CAO, P. and D.P. RALEIGH. Analysis of the inhibition and remodeling of islet amyloid polypeptide amyloid fibers by flavanols. *Biochem.*, 2012, **51**(13), pp.2670-83.

159. AHMAD, E., A. AHMAD, S. SINGH, M. ARSHAD, A.H. KHAN and R.H. KHAN. A mechanistic approach for islet amyloid polypeptide aggregation to develop anti-amyloidogenic agents for type-2 diabetes. *Biochimie*, 2011, **93**(5), pp.793-805.

160. JIANG, L., C. LIU, D. LEIBLY, M. LANDAU, M. ZHAO, M.P. HUGHES, D.S. EISENBERG and J. KURIYAN. Structure-based discovery of fiber-binding compounds that reduce the cytotoxicity of amyloid beta. *eLife*, 2013, **2**, p.e00857.

161. ARMSTRONG, A.H., J. CHEN, A.F. MCKOY and M.H. HECHT. Mutations that replace aromatic side chains promote aggregation of the Alzheimer's Aβ peptide. *Biochem.*, 2011, **50**(19), pp.4058-4067.

162. BIESCHKE, J., J. RUSS, R.P. FRIEDRICH, D.E. EHRNHOEFER, H. WOBST, K. NEUGEBAUER and E.E. WANKER. EGCG remodels mature α-synuclein and amyloid-β fibrils and reduces cellular toxicity. *Proc. Natl. Acad. Sci.*, 2010, **107**(17), pp.7710-7715.

163. FERREIRA, N., M.J. SARAIVA and M.R. ALMEIDA. Epigallocatechin-3-gallate as a potential therapeutic drug for TTR-related amyloidosis: "*in vivo*" evidence from FAP mice models. *PLoS ONE*, 2012, **7**(1), p.e29933.

164. CHOI, Y.-T., C.-H. JUNG, S.-R. LEE, J.-H. BAE, W.-K. BAEK, M.-H. SUH, J. PARK, C.-W. PARK and S.-I. SUH. The green tea polyphenol (−)-epigallocatechin gallate

attenuates β-amyloid-induced neurotoxicity in cultured hippocampal neurons. *Life Sci.*, 2001, **70**(5), pp.603-614.

165. CEGELSKI, L., J.S. PINKNER, N.D. HAMMER, C.K. CUSUMANO, C.S. HUNG, E. CHORELL, V. Ã...BERG, J.N. WALKER, P.C. SEED, F. ALMQVIST, M.R. CHAPMAN and S.J. HULTGREN. Small-molecule inhibitors target *Escherichia coli* amyloid biogenesis and biofilm formation. *Nat. Chem. Biol.*, 2009, **5**(12), pp.913-919.

166. TUROVEROV, K.K., I.M. KUZNETSOVA and V.N. UVERSKY. The protein kingdom extended: Ordered and intrinsically disordered proteins, their folding, supramolecular complex formation, and aggregation. *Prog.Biophys. Mol. Biol.*, 2010, **102**(2-3), pp.73-84.

167. MCGLINCHEY, R.P., T.L. YAP and J.C. LEE. The yin and yang of amyloid: insights from alpha-synuclein and repeat domain of Pmel17. *Phys. Chem. Chem. Phys.*, 2011, **13**(45), pp.20066-75.

168. BORYSIK, A.J., S.E. RADFORD and A.E. ASHCROFT. Co-populated conformational ensembles of beta2-microglobulin uncovered quantitatively by electrospray ionization mass spectrometry. *J. Biol. Chem.*, 2004, **279**(26), pp.27069-77.

169. STEFANIS, L. alpha-Synuclein in Parkinson's Disease. *Cold Spring Harb. Perspect. Med.*, 2012, **2**(2).

170. FLOEGE, J. and G. EHLERDING. Beta-2-microglobulin-associated amyloidosis. *Nephron*, 1996, **72**(1), pp.9-26.

171. VLAD, C., K. LINDNER, C. KARREMAN, S. SCHILDKNECHT, M. LEIST, N. TOMCZYK, J. RONTREE, J. LANGRIDGE, K. DANZER, T. CIOSSEK, A. PETRE, M.L. GROSS, B. HENGERER and M. PRZYBYLSKI. Autoproteolytic fragments are intermediates in the oligomerization/aggregation of the Parkinson's disease protein alpha-synuclein as revealed by ion mobility mass spectrometry. *ChemBioChem*, 2011, **12**(18), pp.2740-4.

172. SMITH, D.P., K. GILES, R.H. BATEMAN, S.E. RADFORD and A.E. ASHCROFT. Monitoring copopulated conformational states during protein folding events using electrospray ionization-ion mobility spectrometry-mass spectrometry. *J. Am. Soc. Mass Spectrom.*, 2007, **18**(12), pp.2180-90.

173. LUCA, S., W.M. YAU, R. LEAPMAN and R. TYCKO. Peptide conformation and supramolecular organization in amylin fibrils: constraints from solid-state NMR. *Biochem.*, 2007, **46**(47), pp.13505-22.

174. HILTON, G.R. and J.L.P. BENESCH. Two decades of studying non-covalent biomolecular assemblies by means of electrospray ionization mass spectrometry. *J. R. Soc. Interface*, 2012, **9**(70), pp.801-816.

175. RUOTOLO, B.T. and C.V. ROBINSON. Aspects of native proteins are retained in vacuum. *Curr Opin Chem Biol*, 2006, **10**(5), pp.402-408.

176. RUOTOLO, B.T., K. GILES, I. CAMPUZANO, A.M. SANDERCOCK, R.H. BATEMAN and C.V. ROBINSON. Evidence for Macromolecular Protein Rings in the Absence of Bulk Water. *Science*, 2005, **310**(5754), pp.1658-1661.

177. BUSH, M.F., Z. HALL, K. GILES, J. HOYES, C.V. ROBINSON and B.T. RUOTOLO. Collision cross sections of proteins and their complexes: a calibration framework and database for gas-phase structural biology. *Anal. Chem.*, 2010, **82**(22), pp.9557-65.

178. SMITH, D.P., S.E. RADFORD and A.E. ASHCROFT. Elongated oligomers in β2-microglobulin amyloid assembly revealed by ion mobility spectrometry-mass spectrometry. *Proc. Natl. Acad. Sci.*, 2010, **107**(15), pp.6794-6798.

179. SMITH, D.P., K. GILES, R.H. BATEMAN, S.E. RADFORD and A.E. ASHCROFT. Monitoring Copopulated Conformational States During Protein Folding Events Using Electrospray Ionization-Ion Mobility Spectrometry-Mass Spectrometry. *J Am Soc Mass Spectrom*, 2007, **18**(12), pp.2180-2190.

180. SMITH, D.P., L.A. WOODS, S.E. RADFORD and A.E. ASHCROFT. Structure and Dynamics of Oligomeric Intermediates in β2-Microglobulin Self-Assembly. *Biophys. J.*, 2011, **101**(5), pp.1238-1247.

181. HYUNG, S.J., A.S. DETOMA, J.R. BRENDER, S. LEE, S. VIVEKANANDAN, A. KOCHI, J.S. CHOI, A. RAMAMOORTHY, B.T. RUOTOLO and M.H. LIM. Insights into antiamyloidogenic properties of the green tea extract (-)-epigallocatechin-3-gallate toward metal-associated amyloid-β species. *Proc. Natl. Acad. Sci.*, 2013, **110**(10), pp.3743-8.

182. YOUNG, L.M., J.C. SAUNDERS, R.A. MAHOOD, C.H. REVILL, R.J. FOSTER, L.H. TU, D.P. RALEIGH, S.E. RADFORD and A.E. ASHCROFT. Screening and classifying small-molecule inhibitors of amyloid formation using ion mobility spectrometry-mass spectrometry. *Nat. Chem.*, 2015, **7**(1), pp.73-81.

183. LIU, Y.Q., L.H. HO, J.A. CARVER and T.L. PUKALA. Ion Mobility Mass Spectrometry Studies of the Inhibition of Alpha Synuclein Amyloid Fibril Formation by (-)-Epigallocatechin-3-Gallate. *Aust. J Chem.*, 2011, **64**(1), pp.36-40.

184. GRABENAUER, M., S.L. BERNSTEIN, J.C. LEE, T. WYTTENBACH, N.F. DUPUIS, H.B. GRAY, J.R. WINKLER and M.T. BOWERS. Spermine binding to Parkinson's protein alpha-synuclein and its disease-related A30P and A53T mutants. *J. Phys. Chem. B*, 2008, **112**(35), pp.11147-54.

185. NILSSON, M.R., M. DRISCOLL and D.P. RALEIGH. Low levels of asparagine deamidation can have a dramatic effect on aggregation of amyloidogenic peptides: Implications for the study of amyloid formation. *Protein Sci.*, 2002, **11**(2), pp.342-349.

186. DUNKELBERGER, E.B., L.E. BUCHANAN, P. MAREK, P. CAO, D.P. RALEIGH and M.T. ZANNI. Deamidation accelerates amyloid formation and alters amylin fiber structure. *J. Am. Chem. Soc.*, 2012, **134**(30), pp.12658-12667.

187. WALSH, D.M., E. THULIN, A.M. MINOGUE, N. GUSTAVSSON, E. PANG, D.B. TEPLOW and S. LINSE. A facile method for expression and purification of the Alzheimer's disease-associated amyloid β-peptide. *FEBS J.*, 2009, **276**(5), pp.1266-1281.

188. VALENTINE, S.J., A.E. COUNTERMAN and D.E. CLEMMER. A database of 660 peptide ion cross sections: use of intrinsic size parameters for bona fide predictions of cross sections. *J. Am. Soc. Mass Spectrom.*, 1999, **10**(11), pp.1188-211.

189. MACKE, T.J. and D.A. CASE. Modeling unusual nucleic acid structures. *In:* N. LEONTES and J. SANTALUCIA, eds. *Molecular Modeling of Nucleic Acids*. Washington, DC: American Chemical Society, 1998, pp.379-393.

190. CASE, D.A., T.E. CHEATHAM, 3RD, T. DARDEN, H. GOHLKE, R. LUO, K.M. MERZ, JR., A. ONUFRIEV, C. SIMMERLING, B. WANG and R.J. WOODS. The Amber biomolecular simulation programs. *J Comput. Chem.*, 2005, **26**(16), pp.1668-88.

191. PHILLIPS, J.C., R. BRAUN, W. WANG, J. GUMBART, E. TAJKHORSHID, E. VILLA, C. CHIPOT, R.D. SKEEL, L. KALE and K. SCHULTEN. Scalable molecular dynamics with NAMD. *J Comput. Chem.*, 2005, **26**(16), pp.1781-802.

192. HORNAK, V., R. ABEL, A. OKUR, B. STROCKBINE, A. ROITBERG and C. SIMMERLING. Comparison of multiple Amber force fields and development of improved protein backbone parameters. *Proteins*, 2006, **65**(3), pp.712-25.

193. *Maestro* [CD-ROM]. LLC, NY, USA: Schrödinger, 2014-2.

194. *Rapid Overlay of Chemical Structures (ROCS)* [CD-ROM]. Santa Fe, NM, USA: OpenEye, Scientific Software.

195. ROEPSTORFF, P. and J. FOHLMAN. Proposal for a common nomenclature for sequence ions in mass spectra of peptides. *Biomed. Mass Spectrom.*, 1984, **11**(11), p.601.

196. KALETA, D.T. and M.F. JARROLD. Peptide pinwheels. *J Am. Chem. Soc.*, 2002, **124**(7), pp.1154-5.

197. JIN, L., P.E. BARRAN, J.A. DEAKIN, M. LYON and D. UHRIN. Conformation of glycosaminoglycans by ion mobility mass spectrometry and molecular modelling. *Phys. Chem. Chem. Phys.*, 2005, **7**(19), pp.3464-71.

198. THALASSINOS, K., M. GRABENAUER, S.E. SLADE, G.R. HILTON, M.T. BOWERS and J.H. SCRIVENS. Characterization of phosphorylated peptides using traveling wave-based and drift cell ion mobility mass spectrometry. *Anal. Chem.*, 2009, **81**(1), pp.248-54.

199. TENIDIS, K., M. WALDNER, J. BERNHAGEN, W. FISCHLE, M. BERGMANN, M. WEBER, M.L. MERKLE, W. VOELTER, H. BRUNNER and A. KAPURNIOTU. Identification of a penta- and hexapeptide of islet amyloid polypeptide (IAPP) with amyloidogenic and cytotoxic properties. *J Mol. Biol.*, 2000, **295**(4), pp.1055-71.

200. WESTERMARK, P., U. ENGSTRÖM, K.H. JOHNSON, G.T. WESTERMARK and C. BETSHOLTZ. Islet amyloid polypeptide: pinpointing amino acid residues linked to amyloid fibril formation. *Proc. Nat. Acad. Sci.*, 1990, **87**(13), pp.5036-40.

201. ZHAO, J., X. YU, G. LIANG and J. ZHENG. Structural polymorphism of human islet amyloid polypeptide (hIAPP) oligomers highlights the importance of interfacial residue interactions. *Biomacromolecules*, 2011, **12**(1), pp.210-20.

202. ABEDINI, A., G. SINGH and D.P. RALEIGH. Recovery and purification of highly aggregation-prone disulfide-containing peptides: application to islet amyloid polypeptide. *Anal. Biochem.*, 2006, **351**(2), pp.181-6.

203. WILTZIUS, J.J., S.A. SIEVERS, M.R. SAWAYA, D. CASCIO, D. POPOV, C. RIEKEL and D. EISENBERG. Atomic structure of the cross-beta spine of islet amyloid polypeptide (amylin). *Protein Sci.*, 2008, **17**(9), pp.1467-74.

204. NIELSEN, J.T., M. BJERRING, M.D. JEPPESEN, R.O. PEDERSEN, J.M. PEDERSEN, K.L. HEIN, T. VOSEGAARD, T. SKRYDSTRUP, D.E. OTZEN and N.C. NIELSEN. Unique identification of supramolecular structures in amyloid fibrils by solid-state NMR spectroscopy. *Angew. Chem. Int. Ed.*, 2009, **48**(12), pp.2118-21.

205. KUMAR, S. and A.D. MIRANKER. A foldamer approach to targeting membrane bound helical states of islet amyloid polypeptide. *Chem. Commun.*, 2013, **49**(42), pp.4749-51.

206. WILLIAMSON, J.A. and A.D. MIRANKER. Direct detection of transient alpha-helical states in islet amyloid polypeptide. *Protein Sci.*, 2007, **16**(1), pp.110-7.

207. ABEDINI, A., G. SINGH and D.P. RALEIGH. Recovery and purification of highly aggregation-prone disulfide-containing peptides: application to islet amyloid polypeptide. *Anal Biochem*, 2006, **351**(2), pp.181-6.

208. HEBDA, J.A., I. SARAOGI, M. MAGZOUB, A.D. HAMILTON and A.D. MIRANKER. A peptidomimetic approach to targeting pre-amyloidogenic states in type II diabetes. *Chem. Biol.*, 2009, **16**(9), pp.943-50.

209. LARSON, J.L., E. KO and A.D. MIRANKER. Direct measurement of islet amyloid polypeptide fibrillogenesis by mass spectrometry. *Protein Sci.*, 2000, **9**(2), pp.427-31.

210. MAREK, P.J., V. PATSALO, D.F. GREEN and D.P. RALEIGH. Ionic strength effects on amyloid formation by amylin are a complicated interplay among Debye screening, ion selectivity, and Hofmeister effects. *Biochem.*, 2012, **51**(43), pp.8478-90.

211. JAIN, S. and J.B. UDGAONKAR. Salt-induced modulation of the pathway of amyloid fibril formation by the mouse prion protein. *Biochem.*, 2010, **49**(35), pp.7615-24.

212. FUJIWARA, S., F. MATSUMOTO and Y. YONEZAWA. Effects of salt concentration on association of the amyloid protofilaments of hen egg white lysozyme studied by time-resolved neutron scattering. *J Mol. Biol.*, 2003, **331**(1), pp.21-8.

213. CASTELLETTO, V., I.W. HAMLEY, C. CENKER and U. OLSSON. Influence of salt on the self-assembly of two model amyloid heptapeptides. *J. Phys. Chem. B*, 2010, **114**(23), pp.8002-8.

214. BOSSIS, F. and L.L. PALESE. Amyloid beta(1-42) in aqueous environments: effects of ionic strength and E22Q (Dutch) mutation. *Biochim. Biophys. Acta*, 2013, **1834**(12), pp.2486-93.

215. SMITH, D.P., S.E. RADFORD and A.E. ASHCROFT. Elongated oligomers in beta2-microglobulin amyloid assembly revealed by ion mobility spectrometry-mass spectrometry. *Proc Natl Acad Sci U S A*, 2010, **107**(15), pp.6794-8.

216. COLE, H.L., J.M. KALAPOTHAKIS, G. BENNETT, P.E. BARRAN and C.E. MACPHEE. Characterizing early aggregates formed by an amyloidogenic peptide by mass spectrometry. *Angew Chem Int Ed Engl*, 2010, **49**(49), pp.9448-51.

217. WELLS, J.M. and S.A. MCLUCKEY. Collision-induced dissociation (CID) of peptides and proteins. *Methods Enzymol.*, 2005, **402**, pp.148-85.

218. MENG, F., A. ABEDINI, A. PLESNER, C.B. VERCHERE and D.P. RALEIGH. The flavanol (-)-epigallocatechin 3-gallate inhibits amyloid formation by islet amyloid polypeptide, disaggregates amyloid fibrils, and protects cultured cells against IAPP-induced toxicity. *Biochemistry*, 2010, **49**(37), pp.8127-33.

219. CHENG, B., H. GONG, X. LI, Y. SUN, X. ZHANG, H. CHEN, X. LIU, L. ZHENG and K. HUANG. Silibinin inhibits the toxic aggregation of human islet amyloid polypeptide. *Biochem. Biophys. Res. Commun.*, 2012, **419**(3), pp.495-9.

220. HUDSON, S.A., H. ECROYD, F.C. DEHLE, I.F. MUSGRAVE and J.A. CARVER. (-)-epigallocatechin-3-gallate (EGCG) maintains kappa-casein in its pre-fibrillar

state without redirecting its aggregation pathway. *J Mol Biol*, 2009, **392**(3), pp.689-700.

221. PALHANO, F.L., J. LEE, N.P. GRIMSTER and J.W. KELLY. Toward the Molecular Mechanism(s) by which EGCG Treatment Remodels Mature Amyloid Fibrils. *J Am Chem Soc*, 2013.

222. YAN, L.M., M. TATAREK-NOSSOL, A. VELKOVA, A. KAZANTZIS and A. KAPURNIOTU. Design of a mimic of nonamyloidogenic and bioactive human islet amyloid polypeptide (IAPP) as nanomolar affinity inhibitor of IAPP cytotoxic fibrillogenesis. *Proceedings of the National Academy of Sciences of the United States of America*, 2006, **103**(7), pp.2046-51.

223. MENG, F., D.P. RALEIGH and A. ABEDINI. Combination of kinetically selected inhibitors in trans leads to highly effective inhibition of amyloid formation. *J Am Chem Soc*, 2010, **132**(41), pp.14340-2.

224. KAPURNIOTU, A., A. SCHMAUDER and K. TENIDIS. Structure-based design and study of non-amyloidogenic, double N-methylated IAPP amyloid core sequences as inhibitors of IAPP amyloid formation and cytotoxicity. *J Mol Biol*, 2002, **315**(3), pp.339-50.

225. GILEAD, S. and E. GAZIT. Inhibition of amyloid fibril formation by peptide analogues modified with alpha-aminoisobutyric acid. *Angew Chem Int Ed Engl*, 2004, **43**(31), pp.4041-4.

226. HOLLANDER, P.A., P. LEVY, M.S. FINEMAN, D.G. MAGGS, L.Z. SHEN, S.A. STROBEL, C. WEYER and O.G. KOLTERMAN. Pramlintide as an adjunct to insulin therapy improves long-term glycemic and weight control in patients with type 2 diabetes: a 1-year randomized controlled trial. *Diabetes Care*, 2003, **26**(3), pp.784-90.

227. MIDDLETON, C.T., P. MAREK, P. CAO, C.C. CHIU, S. SINGH, A.M. WOYS, J.J. DE PABLO, D.P. RALEIGH and M.T. ZANNI. Two-dimensional infrared spectroscopy reveals the complex behaviour of an amyloid fibril inhibitor. *Nat Chem*, 2012, **4**(5), pp.355-60.

228. DYACHENKO, A., M. GOLDFLAM, M. VILASECA and E. GIRALT. Molecular recognition at protein surface in solution and gas phase: Five VEGF peptidic ligands show inverse affinity when studied by NMR and CID-MS. *Biopolymers*, 2010, **94**(6), pp.689-700.

229. YOUNG, L.M., J.C. SAUNDERS, R.A. MAHOOD, C.H. REVILL, R.J. FOSTER, A.E. ASHCROFT and S.E. RADFORD. ESI-IMS–MS: A method for rapid analysis of protein aggregation and its inhibition by small molecules. *Methods*, 2015, **in press,** http://dx.doi.org/10.1016/j.ymeth.2015.05.017.

230. GRIMSTER, N.P., S. CONNELLY, A. BARANCZAK, J. DONG, L.B. KRASNOVA, K.B. SHARPLESS, E.T. POWERS, I.A. WILSON and J.W. KELLY. Aromatic sulfonyl fluorides covalently kinetically stabilize transthyretin to prevent amyloidogenesis while affording a fluorescent conjugate. *J. Am. Chem. Soc.*, 2013, **135**(15), pp.5656-68.

231. KLABUNDE, T., H.M. PETRASSI, V.B. OZA, P. RAMAN, J.W. KELLY and J.C. SACCHETTINI. Rational design of potent human transthyretin amyloid disease inhibitors. *Nat. Struc. Mol. Biol.*, 2000, **7**(4), pp.312-321.

232. CONNELLY, S., S. CHOI, S.M. JOHNSON, J.W. KELLY and I.A. WILSON. Structure-based design of kinetic stabilizers that ameliorate the transthyretin amyloidoses. *Curr. Opin. Struct. Biol.*, 2010, **20**(1), pp.54-62.

233. HAMRANG, Z., N.J.W. RATTRAY and A. PLUEN. Proteins behaving badly: emerging technologies in profiling biopharmaceutical aggregation. *Trends Biotechnol.*, 2013, **31**(8), pp.448-458.

234. MENG, F., P. MAREK, K.J. POTTER, C.B. VERCHERE and D.P. RALEIGH. Rifampicin does not prevent amyloid fibril formation by human islet amyloid polypeptide but does inhibit fibril thioflavin-T interactions: Implications for mechanistic studies of β-cell death. *Biochem.*, 2008, **47**(22), pp.6016-6024.

235. BUELL, A.K., C.M. DOBSON, T.P. KNOWLES and M.E. WELLAND. Interactions between amyloidophilic dyes and their relevance to studies of amyloid inhibitors. *Biophys. J.*, 2010, **99**(10), pp.3492-7.

236. FENG, B.Y., B.H. TOYAMA, H. WILLE, D.W. COLBY, S.R. COLLINS, B.C.H. MAY, S.B. PRUSINER, J. WEISSMAN and B.K. SHOICHET. Small-molecule aggregates inhibit amyloid polymerization. *Nat. Chem. Biol.*, 2008, **4**(3), pp.197-199.

237. MENG, F. and D.P. RALEIGH. Inhibition of glycosaminoglycan-mediated amyloid formation by islet amyloid polypeptide and proIAPP processing intermediates. *J. Mol. Biol.*, 2010, **406**(3), pp.491-502.

238. DAUBENFELD, T., A.P. BOUIN and G. VAN DER REST. A deconvolution method for the separation of specific versus nonspecific interactions in noncovalent protein-ligand complexes analyzed by ESI-FT-ICR mass spectrometry. *J. Am. Soc. Mass Spectrom.*, 2006, **17**(9), pp.1239-48.

239. MENG, F., A. ABEDINI, A. PLESNER, C.T. MIDDLETON, K.J. POTTER, M.T. ZANNI, C.B. VERCHERE and D.P. RALEIGH. The sulfated triphenyl methane derivative acid fuchsin is a potent inhibitor of amyloid formation by human islet amyloid polypeptide and protects against the toxic effects of amyloid formation. *J. Mol. Biol.*, 2010, **400**(3), pp.555-66.

240. KAMIHIRA-ISHIJIMA, M., H. NAKAZAWA, A. KIRA, A. NAITO and T. NAKAYAMA. Inhibitory mechanism of pancreatic amyloid fibril formation: Formation of the complex between tea catechins and the fragment of residues 22–27. *Biochem.*, 2012, **51**(51), pp.10167-10174.

241. ENGEL, M.F.M., C.C. VANDENAKKER, M. SCHLEEGER, K.P. VELIKOV, G.H. KOENDERINK and M. BONN. The polyphenol EGCG inhibits amyloid formation less efficiently at phospholipid interfaces than in bulk solution. *J. Am. Chem. Soc.*, 2012, **134**(36), pp.14781-14788.

242. HUDSON, S.A., H. ECROYD, F.C. DEHLE, I.F. MUSGRAVE and J.A. CARVER. (-)-epigallocatechin-3-gallate (EGCG) maintains kappa-casein in its pre-fibrillar state without redirecting its aggregation pathway. *J. Mol. Biol.*, 2009, **392**(3), pp.689-700.

243. KHURANA, R., V.N. UVERSKY, L. NIELSEN and A.L. FINK. Is Congo red an amyloid-specific dye? *J. Biol. Chem.*, 2001, **276**(25), pp.22715-22721.

244. ROTERMAN, I., M. KRÓL, M. NOWAK, L. KONIECZNY, J. RYBARSKA, B. STOPA, B. PIEKARSKA and G. ZEMANEK. Why Congo red binding is specific for amyloid proteins - model studies and a computer analysis approach. *Med. Sci. Monit.*, 2001, **7**(4), pp.771-784.

245. NECULA, M., R. KAYED, S. MILTON and C.G. GLABE. Small molecule inhibitors of aggregation indicate that amyloid β oligomerization and fibrillization pathways are independent and distinct. *J. Biol. Chem.*, 2007, **282**(14), pp.10311-10324.

246. LORENZO, A. and B.A. YANKNER. Beta-amyloid neurotoxicity requires fibril formation and is inhibited by congo red. *Proc. Natl. Acad. Sci.*, 1994, **91**(25), pp.12243-12247.

247. POLLACK, S.J., I.I.J. SADLER, S.R. HAWTIN, V.J. TAILOR and M.S. SHEARMAN. Sulfonated dyes attenuate the toxic effects of β-amyloid in a structure-specific fashion. *Neurosci. Lett.*, 1995, **197**(3), pp.211-214.

248. MALTSEV, A.S., A. GRISHAEV and A. BAX. Monomeric α-synuclein binds Congo red micelles in a disordered manner. *Biochem.*, 2012, **51**(2), pp.631-42.

249. THOMAS, T., T.G. NADACKAL and K. THOMAS. Aspirin and non-steroidal anti-inflammatory drugs inhibit amyloid-β aggregation. *Neuroreport*, 2001, **12**(15), pp.3263-3267.

250. LIM, G.P., F. YANG, T. CHU, P. CHEN, W. BEECH, B. TETER, T. TRAN, O. UBEDA, K.H. ASHE, S.A. FRAUTSCHY and G.M. COLE. Ibuprofen suppresses plaque pathology and inflammation in a mouse model for Alzheimer's disease. *J. Neurosci.*, 2000, **20**(15), pp.5709-5714.

251. MCKEE, A.C., I. CARRERAS, L. HOSSAIN, H. RYU, W.L. KLEIN, S. ODDO, F.M. LAFERLA, B.G. JENKINS, N.W. KOWALL and A. DEDEOGLU. Ibuprofen reduces Aβ, hyperphosphorylated tau and memory deficits in Alzheimer mice. *Brain Res.*, 2008, **1207**(0), pp.225-236.

252. SUN, N., J. SUN, E.N. KITOVA and J.S. KLASSEN. Identifying nonspecific ligand binding in electrospray ionization mass spectrometry using the reporter molecule method. *J. Am. Soc. Mass Spectrom.*, 2009, **20**(7), pp.1242-50.

253. SUN, J., E.N. KITOVA, W. WANG and J.S. KLASSEN. Method for distinguishing specific from nonspecific protein-ligand complexes in nanoelectrospray ionization mass spectrometry. *Anal. Chem.*, 2006, **78**(9), pp.3010-8.

254. WANG, W., E.N. KITOVA and J.S. KLASSEN. Influence of solution and gas phase processes on protein-carbohydrate binding affinities determined by nanoelectrospray Fourier transform ion cyclotron resonance mass spectrometry. *Anal. Chem.*, 2003, **75**(19), pp.4945-55.

255. KIM, Y.S., T.W. RANDOLPH, M.C. MANNING, F.J. STEVENS and J.F. CARPENTER. Congo red populates partially unfolded states of an amyloidogenic protein to enhance aggregation and amyloid fibril formation. *J. Biol. Chem.*, 2003, **278**(12), pp.10842-50.

256. THOMAS, T., G.T. NADACKAL and K. THOMAS. Aspirin and diabetes: inhibition of amylin aggregation by nonsteroidal anti-inflammatory drugs. *Exp. Clin. Endocr. Diab.*, 2003, **111**(1), pp.8-11.

257. SIPE, J.D., M.D. BENSON, J.N. BUXBAUM, S. IKEDA, G. MERLINI, M.J. SARAIVA, P. WESTERMARK and N.C.O.T.I.S.O. AMYLOIDOSIS. Amyloid fibril protein nomenclature: 2012 recommendations from the Nomenclature Committee of the International Society of Amyloidosis. *Amyloid*, 2012, **19**(4), pp.167-70.

258. PETKOVA, A.T., Y. ISHII, J.J. BALBACH, O.N. ANTZUTKIN, R.D. LEAPMAN, F. DELAGLIO and R. TYCKO. A structural model for Alzheimer's β-amyloid fibrils based on experimental constraints from solid state NMR. *Proc. Natl. Acad. Sci.*, 2002, **99**(26), pp.16742-16747.

259. AISEN, P., S. GAUNTHIER, B. VELLAS, R. BRIAND, D. SAUMIER and J. LAURIN. Alzhemed: A potential treatment for Alzheimer's disease. *Curr. Alzheimer Res.*, 2007, **4**, pp.473-478.

260. GERVAIS, F., J. PAQUETTE, C. MORISSETTE, P. KRZYWKOWSKI, M. YU, M. AZZI, D. LACOMBE, X. KONG, A. AMAN, J. LAURIN, W.A. SZAREK and P. TREMBLAY. Targeting soluble Aβ peptide with Tramiprosate for the treatment of brain amyloidosis. *Neurobiol. Aging*, 2007, **28**(4), pp.537-547.

261. VALLER, M.J. and D. GREEN. Diversity screening versus focussed screening in drug discovery. *Drug Discov. Today*, 2000, **5**(7), pp.286-293.

262. DE FELICE, F.G., M.N.N. VIERA, L.M. SARAIVA, J.D. FIGUEROA-VILLAR, J. GARCIA-ABREU, R. LIU, L. CHANG, W.L. KLEIN and S.T. FERREIRA. Targeting the neurotoxic species in Alzheimer's disease: inhibitors of Aβ oligomerization. *FASEB J.*, 2004, **18**(12), pp.1366-1372.

263. LADIWALA, A.R.A., J.C. LIN, S.S. BALE, A.M. MARCELINO-CRUZ, M. BHATTACHARYA, J.S. DORDICK and P.M. TESSIER. Resveratrol selectively remodels soluble oligomers and fibrils of amyloid Aβ into off-pathway conformers. *J. Biol. Chem.*, 2010, **285**(31), pp.24228-24237.

264. YANG, F., G.P. LIM, A.N. BEGUM, O.J. UBEDA, M.R. SIMMONS, S.S. AMBEGAOKAR, P.P. CHEN, R. KAYED, C.G. GLABE, S.A. FRAUTSCHY and G.M. COLE. Curcumin inhibits formation of amyloid β oligomers and fibrils, binds plaques, and reduces amyloid *in vivo*. *J. Biol. Chem.*, 2005, **280**(7), pp.5892-5901.

265. SCHERZER-ATTALI, R., R. PELLARIN, M. CONVERTINO, A. FRYDMAN-MAROM, N. EGOZ-MATIA, S. PELED, M. LEVY-SAKIN, D.E. SHALEV, A. CAFLISCH, E. GAZIT and D. SEGAL. Complete phenotypic recovery of an Alzheimer's disease model by a quinone-tryptophan hybrid aggregation inhibitor. *PLoS ONE*, 2010, **5**(6), p.e11101.

266. YATES, D. and D.M. MCLOUGHLIN. The molecular pathology of Alzheimer's disease. *Psychiatry*, 2008, **7**(1), pp.1-5.

267. KIM, H.-J., S.-C. CHAE, D.-K. LEE, B. CHROMY, S.C. LEE, Y.-C. PARK, W.L. KLEIN, G.A. KRAFFT and S.-T. HONG. Selective neuronal degeneration induced by soluble oligomeric amyloid beta protein. *FASEB J.*, 2003, **17**(1), pp.118-120.

268. LAST, N.B., E. RHOADES and A.D. MIRANKER. Islet amyloid polypeptide demonstrates a persistent capacity to disrupt membrane integrity. *Proc. Natl. Acad. Sci. U. S. A.*, 2011, **108**(23), pp.9460–9465.

269. KROTH, H., A. ANSALONI, Y. VARISCO, A. JAN, N. SREENIVASACHARY, N. REZAEI-GHALEH, V. GIRIENS, S. LOHMANN, M.P. LOPEZ-DEBER, O. ADOLFSSON, M. PIHLGREN, P. PAGANETTI, W. FROESTL, L. NAGEL-STEGER, D. WILLBOLD, T. SCHRADER, M. ZWECKSTETTER, A. PFEIFER, H.A. LASHUEL and A. MUHS. Discovery and structure activity relationship of small molecule inhibitors of toxic β-amyloid$_{-42}$ fibril formation. *J. Biol. Chem.*, 2012, **287**(41), pp.34786-34800.

270. NIE, Q., X.-G. DU and M.-Y. GENG. Small molecule inhibitors of amyloid β peptide aggregation as a potential therapeutic strategy for Alzheimer's disease. *Acta Pharma. Sin.*, 2011, **32**(5), pp.545-551.

271. WEI, L., P. JIANG, W. XU, H. LI, H. ZHANG, L. YAN, M.B. CHAN-PARK, X.-W. LIU, K. TANG, Y. MU and K. PERVUSHIN. The molecular basis of distinct aggregation

pathways of islet amyloid polypeptide. *J. Biol. Chem.*, 2011, **286**(8), pp.6291-6300.

272.   BULAWA, C.E., S. CONNELLY, M. DEVIT, L. WANG, C. WEIGEL, J.A. FLEMING, J. PACKMAN, E.T. POWERS, R.L. WISEMAN, T.R. FOSS, I.A. WILSON, J.W. KELLY and R. LABAUDINIÈRE. Tafamidis, a potent and selective transthyretin kinetic stabilizer that inhibits the amyloid cascade. *Proc. Natl. Acad. Sci. U. S. A.*, 2012, **109**, pp.9629-9634.

273.   AITKEN, J.F., K.M. LOOMES, B. KONARKOWSKA and G.J.S. COOPER. Suppression by polycyclic compounds of the conversion of human amylin into insoluble amyloid. *Biochem. J.*, 2003, **374**(3), pp.779-784.

274.   WU, C., H. LEI, Z. WANG, W. ZHANG and Y. DUAN. Phenol red interacts with the protofibril-like oligomers of an amyloidogenic hexapeptide NFGAIL through both hydrophobic and aromatic contacts. *Biophys. J.*, 2006, **91**(10), pp.3664-3672.

275.   PORAT, Y., Y. MAZOR, S. EFRAT and E. GAZIT. Inhibition of islet amyloid polypeptide fibril formation: a potential role for heteroaromatic interactions. . *Biochem.*, 2004, **43**(45), pp.14454-14462.

276.   JOHNSON, S.M., S. CONNELLY, C. FEARNS, E.T. POWERS and J.W. KELLY. The transthyretin amyloidoses: from delineating the molecular mechanism of aggregation linked to pathology to a regulatory-agency-approved drug. *J. Mol. Biol.*, 2012, **421**(2–3), pp.185-203.

277.   RAZAVI, H., S.K. PALANINATHAN, E.T. POWERS, R.L. WISEMAN, H.E. PURKEY, N.N. MOHAMEDMOHAIDEEN, S. DEECHONGKIT, K.P. CHIANG, M.T.A. DENDLE, J.C. SACCHETTINI and J.W. KELLY. Benzoxazoles as transthyretin amyloid fibril inhibitors: synthesis, evaluation, and mechanism of action. *Angew. Chem. Int. Ed.*, 2003, **42**(24), pp.2758-2761.

278.   HAMMARSTRÖM, P., R.L. WISEMAN, E.T. POWERS and J.W. KELLY. Prevention of transthyretin amyloid disease by changing protein misfolding energetics. *Science*, 2003, **299**(5607), pp.713-716.

279.   MILLER, G. Stopping Alzheimer's before it starts. *Science*, 2012, **337**(6096), pp.790-792.